CRANFIELD UNIVERSITY

Ewa M Jakubczyk

Effect of sodium rich pretreatments and processing conditions on microstructure and property evolution of sodium cobalt oxide thermoelectric materials

School of Applied Sciences

PhD thesis

Supervisor:
Prof. Robert Dorey
Dr Chris Sansom

CRANFIELD UNIVERSITY
SCHOOL OF APPLIED SCIENCES
DEPARTMENT OF MANUFACTURING AND MATERIALS

PhD Thesis

Ewa M. Jakubczyk

Effect of sodium rich pretreatments and processing conditions on microstructure and property evolution of sodium cobalt oxide thermoelectric materials

Supervisor: Prof. Robert Dorey and Dr Chris Sansom
June 2014

© Cranfield University 2014. All rights reserved. No part of this publication may be reproduced without the written permission of the copyright owner.

…Nothing in life
is to be feared, it
is only to be
understood…

~ Maria Curie

ABSTRACT

Global environmental and sustainability issues have led to a growth in interest in oxide based thermoelectric materials. Sodium cobalt oxide, which presents low toxicity, is one of the most promising p-type thermoelectric materials for high temperature power generation applications. However, reproducibility and ease of manufacture limits its common use.

$NaCo_2O_4$ bulk ceramic materials were prepared from powders synthesized using a solid state reaction (SSR) and sol gel (SG) method. The effect of time and temperature of treatment were investigated in order to determine their influence on microstructure and physical properties.

The effects of three different Na-enriching pretreatments were evaluated with respect to microstructural evolution and their impact on thermoelectric and electric behaviour of the materials. Such modifications were found to be a critical factor affecting the microstructure of the bulk ceramic materials. The Na-rich pretreatments were found to improve density by up to 15%, increase electrical conductivity and help to compensate for Na loss at high sintering temperatures. The thermoelectric figure of merit ZT was found to increase for Na-rich pretreatment samples due to increases in Seebeck coefficient and low thermal conductivity. The highest value of ZT was found to be for the infiltration pretreatment where the value of 0.025 was observed at 350K. Na rich pretreatments, when compared with unpretreatment samples, reduces thermal conductivity by up to 35%, electrical resistivity by up to 67%, increases Seebeck coefficient by up to 23% and as a consequence increases ZT for ball milling preatreatment by 28%, for mixing preatreatment by 71% and for infiltrating by 250%.

A range of films were also produced using a spin coating technique, with thicknesses ranging from 200 nm, for single sol gel layers, up to ~ 32µm for 4 (ink + 2 sol layers) structures. Several factors such as: process conditions, substrates, surfactant and base components used, were investigated in order to improve the quality of films. Process conditions were found to be a critical factor affecting the quality of films. The use of sol infiltration of each layer and a higher preheated temperature were found to reduce surface roughness by up to 23%. The films showed good electrical resistivity ranging from 260 to 500 µΩcm. The lowest value of electrical resistivity was found to be for films annealed at 700ºC.

ACKNOWLEDGEMENTS

I feel so incredibly grateful to everyone who made this PhD possible.

I would like to express my sincere appreciation and gratitude to my great supervisors Prof. Robert Dorey and Dr Chris Sansom who gave me an opportunity to conduct this research at Cranfield University. Their continuous supervision, encouragement and enthusiastic guidance had shaped me during these years of study. Thanking for all your help, every tip and knowledge gained.

I would like to express my gratitude to Dr Christine Kimpton, Dr. Xianwei Liu, Andy Stallard and Matthew Taunt and all the other members of the Materials Department for their support, patience, useful discussions and sharing of knowledge.

I wish to thank all my colleagues Ola, Zsuzanna, Rebecca, Alice, Dominika, Kasia, Ash, Alex, Vlad, Nathan, Matt and Tony and all other members of the Nanotechnology Centre who created a perfect workplace for me.

Very special thanks to my best friend Kinga, Ania and Ewa for their endless trust, help and support.

I'm indebted to my parents Krystyna and Jozef who raised me with love, discipline, hard work, humour and most of all in belief that everything is possible - even dream can come true. I would like to thank my sister Justyna, my brother Adam and my relatives for all their love and for always being there for me.

I would like to express special indebtedness to my beloved daughter Kaja for her love, dedication, understanding and trust. This work would not be completed without you.

TABLE OF CONTENTS

LIST OF FIGURES

LIST OF TABLES

LIST OF EQUATIONS

LIST OF ABBREVIATIONS

T	Temperature (hot side/ cold side; subscripts h,c)
σ	Electrical conductivity
ρ	Electrical resistivity
α	Seebeck coefficient
V	Voltage
k_B	Boltzman constant
g_1,g_2	Electronic degeneracy
y	Carrier concentration
e	Absolute value of electron charge
Q	Absorbed/released heat
Π	Pelteir coefficient
Γ_{th}	Thomson coefficient
I	Current flow
Θ	Absorption/generation heat
zT	Thermoelectric figure of merit
κ	Thermal conductivity (lattice and electron; subscripts lattice, el)
L	Lorenz number
C_v	Specific heat per unit
V_s	Velocity of sound
l_{ph}	the average distance a phonon moves
PF	Power factor
TE	Thermoelectric
TEG	Thermoelectric generator
NASA	The National Aeronautics and Space Administration
RTG	Radioisotope thermoelectric generators
SNAP	Systems for Nuclear Auxiliary Power
CCS	Climate-control seats
DOS	Density of states
ITO	Indium-Tin-Oxide
Sp	Spin
Con	Configuration
Deg	Degeneracy
CAC	The citric acid complex process
HHP	The hot pressing technique
RTGG	The reactive template grain growth
PC	Polymerized complex method
SG	Sol gel method

SSR	Solid state reaction
TGA	Thermogravimetric analyser
CVD	Chemical vapour deposition
PVD	Physical vapour deposition
CN	Pore coordination number (critical value subscript c)
INF	Infiltration preatreatment
M	Mixing pretraetment
BM	Ball milling preatretment
SGBM	Sol gel ball milling preatreatment
p	Density
m	Mass
V_l	Volume
XRD	X-ray diffraction
SEM	Scanning electron microscope
EDX	The Energy Dispersive X-Ray Spectroscope
TEM	Transmission electron microscopy
pO_2	Partial oxygen pressure
OAG	Oxide-assisted growth
Θ	Incident angle of X-ray

Chapter 1 Introduction

Helping to meet the energy needs of contemporary life has become the target of many areas of research. Obtaining energy from natural sources as well as energy recovery, is a rapidly expanding field. Harvesting energy from heat is especially attractive as more than half of all the energy generated by mankind is lost as waste heat. The possibility to harvest even a small part of this waste heat could have a giant impact on energy efficiency. The use of environment friendly technologies and alternatives for the recovery of waste heat is the subject of much research. Therefore thermoelectric materials, which convert heat into electricity, have attracted much attention. The increased level of interest in thermoelectric materials is reflected not only in the search for materials with increased thermoelectric efficiency near to room temperatures for applications such as electric refrigerators, air conditioners and power generators, but also high temperature materials for industrial and military applications.

The efficiency of thermoelectric devices is dependent on the properties of the materials used and is evaluated by figure of merit ZT. Despite much research the efficiency of thermoelectrics remains relatively low with a figure of merit in around 1.5. Figure 1 shows a comparison of the efficiency of thermoelectric materials with different values of ZT as a function of temperature. The thermoelectric generated efficiency mainly depends on ZT and the operating temperature (difference between the cold and hot side of thermoelectric generator). Good thermoelectric materials should have a high Seebeck coefficient and electrical conductivity coupled with a low thermal conductivity. With higher operating temperature the thermoelectric generator efficiency and Carnot efficiency can be improved. Therefore materials which can be used at higher temperatures are of interest in the automotive industry, mainly for conversion of “waste” heat from internal combustion engines, due to possibility of extracting energy more efficiently at high temperatures.

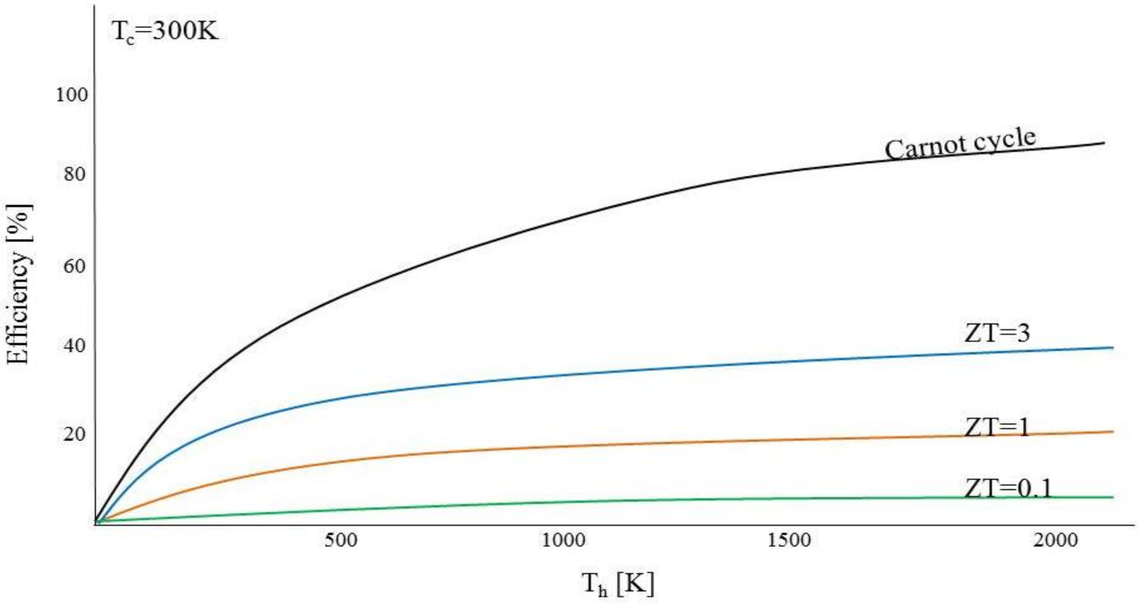

Figure 1 The maximum thermoelectric generator efficiency [%] shown as a function of T_h (for T_c=300K) with a comparison of different average of figure of merit and the Carnot efficiency.

Layered complex metal oxides have been found to be promising, environment friendly materials that can be used in power generation applications and which can operate at high temperatures. Among them, sodium cobalt oxides have been paid attention since the late 1990's. The layered cobalt oxides exhibit metallic behaviour connected with a large Seebeck coefficient resulting in high thermoelectric efficiencies. Sodium cobalt oxide compounds have been found to have a much higher carrier concentration[1] than in some thermoelectric materials such as Bi_2Te_3 and PbTe. Additionally Bi_2Ti_3 and PbTe are not attractive, especially for high temperature applications, because they can easily melt, decompose or vaporize at elevated temperatures[2] (< 800 ºC). For these reasons sodium cobalt oxide, which also presents low toxicity, is being considered as an attractive future commercial thermoelectric applications.

Often small crystal or microstructural differences strongly influence changes in physical properties. In most case the structural changes are dependent on the synthesis method used when processing the material. Recently, a number of methods including solid state reaction (SSR)[3], polymerized complex[1], sol gel[4] and mechanical grinding and spark plasma sintering[5] have been reported for producing $Na_xCo_yO_z$. The good thermoelectric behaviour is due to the layered structure where Na is sandwiched between CoO_2 layers and where the CoO_2 is an electrically conductive layer and the Na layer acts as an insulator. The instability of the material caused by Na evaporation is one of the major problems when trying to maintain the appropriate stoichiometric ratio.

To achieve dense ceramic materials, the use of high temperature sintering is required. When lowering the temperature of sintering the materials produced become more porous and less homogeneous. For sodium cobalt oxide the increase of sintering temperature results in loss of Na which leads to increased thermal conductivity and reduced Seebeck coefficient. Manufacturing the cobaltites requires a well-defined preparation method to obtain a homogeneous and dense bulk material.

To date, the values of ZT obtained for polycrystalline bulk sodium cobalt oxide is relatively low (ZT=1[6]). Further improvements could be achieved through microstructural modifications and a repeatable preparation method for creating nanostructured materials.

1.1 Aim and objectives

The aim of this project is to develop an inexpensive, reproducible processing route to create a high temperature thermoelectric material. To achieve this aim, the following objectives were determined.

The objectives involve the synthesis, production and characterisation of sodium cobalt oxide powders as a high temperature thermoelectric material.

1. Determine the influence of time and temperature on microstructure and composition of sodium cobalt oxide.
2. Evaluate the influence of a powder synthesis route on microstructure and composition of material.
3. Develop a Na rich pre-treatment process to minimize Na loss.
4. Evaluate the influence of processing and powder synthesis on thermal and electrical properties.

1.2 Thesis structure

This thesis is structured as eight chapters of which this is the first.

In Chapter two the background literature is presented. The first section of Chapter 2 provides a review of the thermoelectric phenomena with particular attention paid to semiconductors as good and promising thermoelectric materials. The second part concerns a review of the sodium cobaltites, discussing the history, synthesis techniques, lattice structure and physical properties.

Chapter three, methodology, contains a description of the experimental procedures used in this work.

Chapter four contains a description of a solid state reaction synthesis method used to produce the powder. Particular attention is paid to the influence of the temperature and time on the resulting product. The later part of this chapter is dedicated to the production of pellets and the effect of temperature and time on the production of pellets.

The effect of time and temperature on the production of NaOH pre-treated samples is described in Chapter five. Particular attention is paid to three different Na rich pre-treatments and their influence on the thermoelectric properties of material.

Chapter six contains a description of the sol gel synthesis method to produce powder and bulk material. The later part of this chapter is dedicated to the Na rich pre-treatment and its influence on the thermoelectric properties.

The development of sodium cobalt films and the influence of different substrates, dispersants and processing temperatures are discussed in Chapter seven.

Chapter 8 contains a description of sodium cobalt oxide nanostructures which was developed during this work.

The thesis ends with Chapter 9 which summarises the main conclusions of this work as well as proposing future work.

Chapter 2 Literature review

2.1 Literature review on thermoelectrics

Thermoelectricity refers to the phenomena by which thermal energy is directly converted into electricity. This transformation takes place without intermediaries of moving parts such as turbines or working fluids. Further, the phenomenon of transformation works bidirectionally.

2.1.1 Thermoelectric effects

2.1.1.1 Seebeck coefficient

In 1822 the German physicist J. T. Seebeck found that two metals at different temperatures in a closed loop produce a voltage. He described this phenomenon and named it "the magnetic polarization of metals and ores produced by a temperature difference". The discovery was followed by a series of research works carried out by Ampere, Biot, Savart, Laplace and many others. These studies, and particularly Ampere's hypothesis, confirmed the phenomena to be electric rather than magnetic in nature[7],[8].

The principle of the Seebeck effect can be understood according to the operation of a thermocouple within a temperature gradient. A temperature difference applied across thermoelectric materials causes charge carriers in the material to diffuse from the hot side to the cold side. In thermoelectric materials there are two different types of mobile carriers; electrons for n-type materials and holes for p-type materials. In the case of n-type materials exposed to the temperature gradient ΔT, the electrons at the hot end will have more energy than equivalent electrons at the cold end. This means that the hot side electrons will move faster to the cold end, at the same time the electrons from the cold end will move slowly. As a consequence a negative charge will be established at the cold side. By analogy, for p-type materials which conduct positive charges (holes), the cold end will become positively charged. The direction of current flow in the circuit is opposite to the direction of flow of the electrons. The induced voltage is strongly dependant on the temperature difference between the hot and cold sides and is given by the

$$V = \int_{T_c}^{T_h} \alpha(T)dT$$ Equation 1

Equation 1.

where T_h and T_c is the absolute temperature of the hot and cold side, respectively, α is the Seebeck coefficient (also called thermopower or thermoelectric power). The generated voltage can be expressed by Equation 2 which also simply describes the Seebeck coefficient.

$$\alpha = -\frac{\Delta \mathrm{V}}{\Delta T}$$ Equation 2

The value of α for n-type materials is negative and for p-type materials is positive. By combining the p- and n- type materials in a thermoelectric element, known as thermoelectric couple, the opposite signs of generated thermoelectomotive force (TMF)-voltage can be combined.

Another method to calculate the thermopower, proposed in 1961 by Heikes is a formula for high temperature[9], and modified by Koshibea[10,11] in 2000, takes into consideration the conduction band and carrier concentration, and is given by Equation 3

$$\alpha = -\frac{k_B}{e}\ln(\frac{g_1}{g_2}\frac{y}{1-y})$$ Equation 3

Where g_1 and g_2 are electronic degeneracy, y is the carrier concentration, e absolute value of electron charge and k is the Boltzman constant.

2.1.1.2 Peltier effect

Thermoelectricity is strongly connected with another effect which was discovered in 1834 by J.C.A. Peltier who found the reverse of the Seebeck effect. When the voltage is passing through metals an accompanying decrease and increase in temperature of the solids can be observed. The absorbed or released heat Q is proportional to the current passed through conductor and can be given by Equation 4.

$$Q = \Pi I \qquad \text{Equation 4}$$

where Π is a Peltier coefficient, and I current flow.

2.1.1.3 Thomson Effect

In the late 1850's one of the founders of thermodynamics, W. Thomson (later Lord Kelvin) established the relationship between the Seebeck and Peltier effects and simultaneously discovered a third phenomenon known as the Thomson effect. Thomson described and published his theory of the thermoelectric phenomena consisting of absorption or generation of heat Θ by the application of current I passing through a homogeneous conductor which is exposed to a temperature gradient. The heat is proportional to the electric current and at the same time to the temperature gradient dT according to Equation 5

$$\Theta = \Gamma_{th} IdT \qquad \text{Equation 5}$$

where r_{th} is the Thomson coefficient. W. Thomson demonstrated that the Thomson coefficient is related by thermodynamics to the Seebeck coefficient in following relationship (Equation 6):

$$\frac{d\alpha}{dT} = \frac{\Gamma_{th}}{T} \qquad \text{Equation 6}$$

He showed also that the Peltier effect is closely related to Seebeck effect and can be described by Equation 7:

$$\Pi = \alpha T \qquad \text{Equation 7}$$

where T is the absolute temperature of the junction, α Seebeck coefficient and Π Peltier effect.

2.1.1.4 Figure of Merit ZT

The concept of the 'figure of merit' ZT, was developed in 1949 by Abram Fedorovich Ioffe (1956) as a modern theory of thermoelectricity. He described this quantity as the most important characteristic of the thermoelements in his book Semiconductor Thermoelements and Thermoelectric Cooling[7] and defined it by Equation 8:

$$Z = \frac{\alpha^2}{\rho \kappa} \qquad \text{Equation 8}$$

where α is the Seebeck coefficient (thermoelectric power), ρ is the specific electrical resistivity and κ is the specific thermal conductivity[7].

As the properties used (α, σ, κ) in the thermoelectric figure of merit are a function of temperature therefore the temperature should also be taken into account in the above equation. For this reason in the literature the dimensionless figure of merit is described by Equation 9:

$$ZT = \frac{\alpha^2 \, \sigma T}{\kappa} \qquad \text{Equation 9}$$

where α is the Seebeck coefficient, σ electrical conductivity, T temperature and κ thermal conductivity.

2.1.1.5 Thermal conductivity

In the formula of figure of merit besides the thermoelectric coefficients the thermal conductivity plays an important role. The heat transfer by conduction involves transfer of energy through a material without any motion of the material as a whole. In a crystalline solid, heat can be carried by the electronic contribution κ_{el} (motion of charge carriers), and the lattice component $\kappa_{lattice}$. Hence the total thermal conductivity κ is a sum of the electric and lattice components as presented below (Equation 10).

$$\kappa = \kappa_{lattice} + \kappa_{el}$$ Equation 10

The electronic contribution is strongly related to Wiedemann-Franz law and depends on the carrier concentration (Equation 11):

$$L = \frac{\kappa}{\sigma T} = \frac{\pi^2 k^2}{3e^2} = 2.45x10^{-8}\, {}^{W\Omega}/_{K^2}$$ Equation 11

where L is the Lorenz factor.

Lattice conductivity is the dominant factor of conductivity for insulators, while for metals the electron conductivity is the main factor. For semiconductors the lattice conductivity has a stronger effect than the electron part. The lattice conductivity is determined by the phonon mean free path, phonon velocity and the heat capacity, and is distributed in the three dimensional space through the crystal lattice as in Equation 12:

$$\kappa_{lattice} = \frac{1}{3} C_v V_s\, l_{ph}$$ Equation 12

where C_v is the specific heat per unit volume, V_s velocity of sound and l_{ph} is the average distance a phonon moves before being interfere. The changes in κ at increasing temperatures depend on the dominant action occurring in the lattice because with increasing temperature the speed of movement of free electrons increases. In lattices at low temperatures the mean free path of the phonon is subordinate to the defect concentration and size of the grain.

Each material is characterized by specific value of carrier concentration with dependent α, ρ and κ. This dependence for conventional thermoelectric materials is shown in Figure 2.

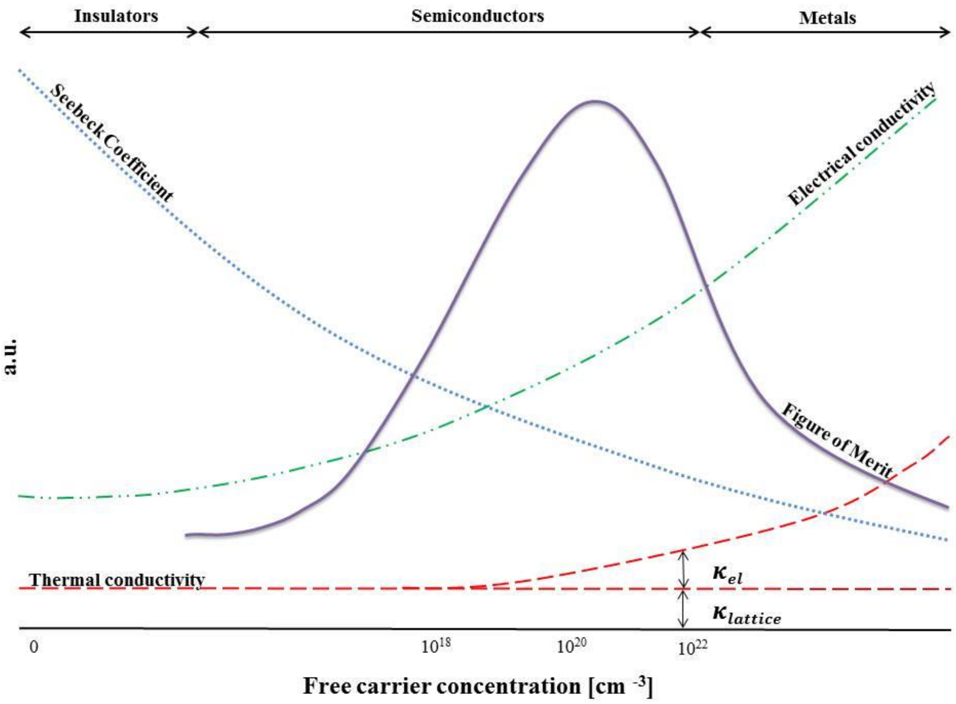

Figure 2 Seebeck coefficient, electrical conductivity and thermal conductivity as a function of carrier concentration for thermoelectric materials.

2.2 Improvement of efficiency of thermoelectric materials

A good thermoelectric material should have a large Seebeck coefficient and at the same time high electrical conductivity but according to Figure 2 both properties depend on carrier concentration in different ways. A large value of Seebeck coefficient can be obtained when the Fermi level is below the conduction band while the high electric conductivity can be achieved when Fermi level is in the conduction band. The power factor (PF) has a maximum when the F_l is close to the conduction band edge. The power factor gives an optimum value for electrical conductivity and Seebeck coefficient according to Equation 13:

$$PF = \sigma\alpha^2 \qquad \text{Equation 13}$$

Another fact which should be considered is that the electrical conductivity and thermal conductivity are related to each other. The electron carrier allows electrons to flow easy also tend to be good at conducting heat. As a result the temperature gradient across a material is decreased and the efficiency decrease. Therefore one strategy to improve efficiency is to lower the lattice thermal conductivity while not interfering with the electronic properties.

There are a range of strategies applied for lowering κ_{lattice} most of them based on photon scattering mechanisms. Thermal conductivity can be significantly reduced by introducing interfaces[12] or increasing interfacial scattering by introducing nano-size particles[13]. Another possibility is to introduce disorder in the lattice due to the presence of different sizes of atoms. Low phonon energies are exhibited by materials composed of heavy elements (e.g. Pb, Bi or Te) which have high atomic weights. The significant reduction of specific heat per unit volume C_v is noted for a complex crystal structure as for pervoskite-type characterized by many atoms per unit cell.

In order to improve the efficiency of thermoelectric materials and maximize the value of ZT improvement of the remaining quantities should be also consider.

The improvement of Seebeck coefficient relates to changes in the band structure (energy-levels) by higher density states near Fermi level due to Quantum Confinement effects.

With reduction of the polarity of covalent bonding the improvement of the electrical conductivity may be achieved. The electrical conductivity increases along with the increase mobility of charge carriers. Support of the transport speed can be obtained by introduction of metal (metallic) nano-particles, or by optimal doping concentration.

2.2.1 Thermoelectric materials, properties and applications.

2.2.1.1 Thermoelectric applications

The phenomenon of thermoelectricity is used for many devices which are capable to generating electricity from temperature differences. The devices are small, cheap, quiet, accurate and reliable. There are many examples of thermoelectric materials, some of which were developed many years ago and are now very well established. Materials discovered in the 1990’s require further research and development. As materials capable of harvesting the thermal losses in systems, they possess great potential for use in the real-world applications, especially in applications where maintenance-free operation is essential including energy harvesting in industry, space or military applications.

A wide range of thermoelectric materials have been reported which are used in various fields, from materials generating energy from the human body[14,8], to the high temperature devices used in space by NASA[15].

Thermoelectrics have been used in a nuclear thermoelectric generator system (SNAP) Systems for Nuclear Auxiliary Power, in which thermal energy was supplied to a thermogenerator by a small nuclear reactor or radioactive materials. For long duration space missions, long-term electricity supplies are the basis for the well-being of such missions. A solution for this requirement is the use of radioisotope thermoelectric generators (RTG). The radioactive decay of a radioactive element is accompanied by release of thermal energy which is converted to electricity by the RTG (Figure 3). This phenomena was used in over 44 spacecraft over the past 40 years[15]. An example of a good radioisotope is plutonium 238 (238Pu) which is characterised by a low level of radiation emission and a satisfactory long half-life estimated to be ~ 88 years.

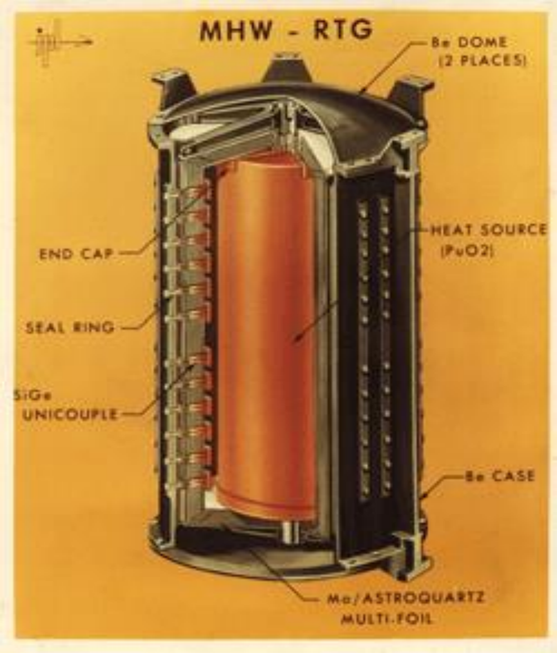

Figure 3 Schematic of radioisotope thermoelectric generators (RTG) used in Voyager deep space probe[16].

Thermoelectric devices can be used in internal combustion vehicles in which only 25% of the fuel energy is efficiently converted, while the rest of fuel energy is lost as waste heat. The biggest portion of the lost energy is through the exhaust gas. However, in this case the difficulties of installing the TE technology are high. However, TEG$_S$ can be used in car air conditioning systems, and thus can improve their efficiency. An excellent example a TE application can be the climate-control seats (CCS) which are powered by TE technique. The CCS is characterised by rapid heating in winter and cooling in summer of car seats[17]. Thermoelectric generators also are used in electric cars, to maintain the heat release from the engine[18,19]. In addition to the above applications of thermoelectric materials, there are, among others: coolers for food, portable fridges and cooling components of medical devices.

Hence the applications for the thermoelectric technologies described above shows that they can be used in various differing fields of interest whilst at the same time adhering to the standards of environmental protection agencies[47].

2.2.1.2 Thermoelectric Materials

The past fifty years have seen the increased development as well as interest in on expanding range of thermoelectric materials. Figure 4 illustrates the scope of the historical development of thermoelectric materials.

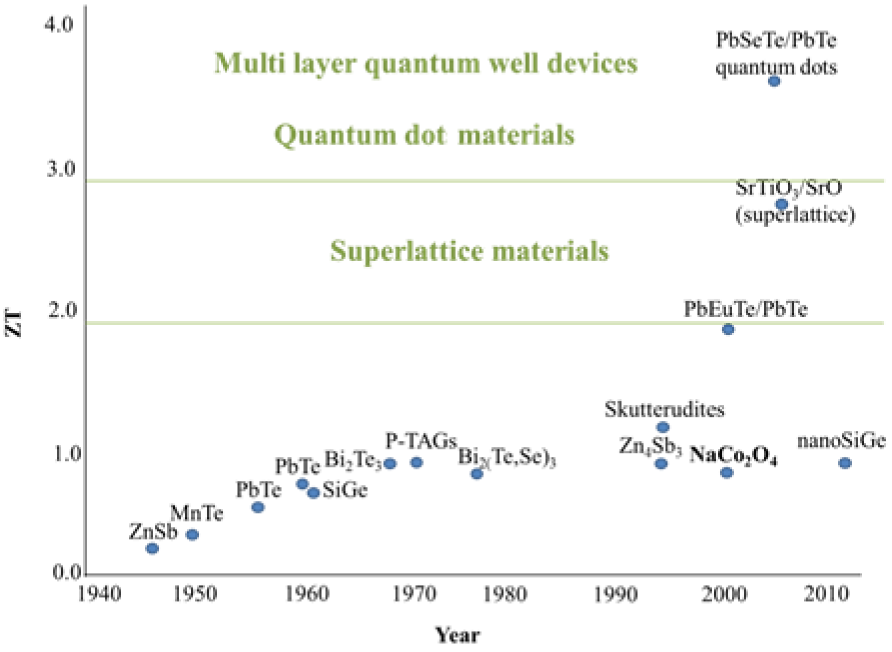

Figure 4 Overview of the historical development of thermoelectric materials[20].

In today’s TE devices, the alloys of Bi_2Te_3 and Sb_2Te_3, which present good ZT values especially at low temperatures, are used at temperatures around 450K[21].

The compounds from group VI named as tellurides, such as; PbTe, GeTe or SnTe are usually applied for power generation in the intermediate temperature range (i.e. 500-900 K). Most of these materials show values of ZT ~0.8. One of the most popular thermoelectric materials is Bi_2Te_3[22]. The highest value of *ZT* > 1 have been found for both n- and p-type materials in $AgSbTe_2$ alloys. In the same temperature range the alloy $(GeTe)_{0.85}(AgSbTe_2)_{0.15}$, which is commonly referred to as TAGS, shows a maximum ZT of > 1.2 but this material has only been successfully used in long-term TEGs[23] as a p-type.

For the high temperature (i.e.>1000K) TEG applications, the SiGe alloys are used as n- and p-type (Figure 5) materials.

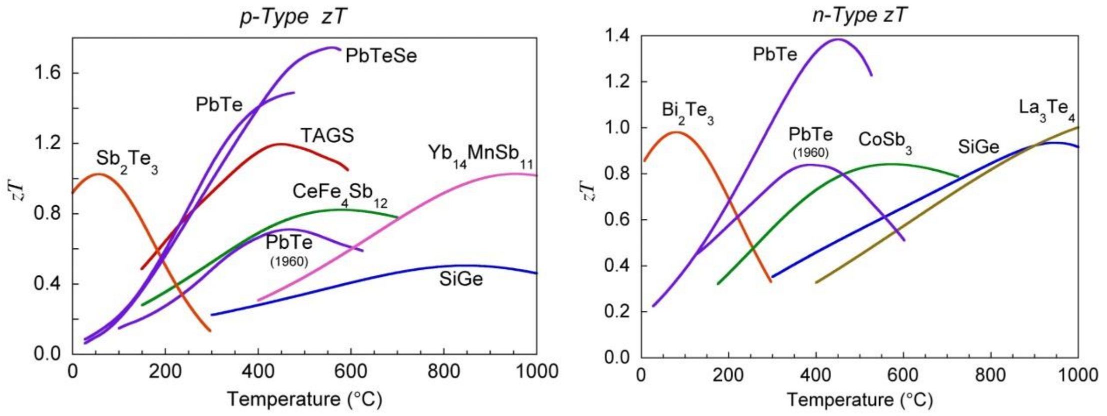

Figure 5 Figure of merit ZT for p and n-type state of art commercial materials. Figure adapted from[8]. (TAGS: $(AgSbTe_2)_{1-x}(GeTe)_x$)

Thermoelectric materials containing elements of group IV are primarily silicides and derivatives of germanium. One of the best examples of such materials in use is that of SiGe which is used by NASA[15] in thermal generators which process heat energy from radio isotopic units to power deep space probes[15,**Error! Bookmark not defined.**].

The most common forms of mono-and polycrystalline silicides are produced by techniques such as Czochralski or Bridgman, hot-pressing, sintering or melting. Germanium crystals are most often doped with various metals such as silicon, boron, and phosphorus[24].

Group V element thermoelectric materials are those based on arsenic, antimony or bismuth[25,26,27,28].

Thermoelectric materials originating from Group VI are derivatives of selenium and tellurium. These materials have been the most commonly used since the 1960s and form the basis for most of the commercial applications developed today[29,30,31,32].

For many years, scientists who have been studying the thermoelectric properties of materials have neglected oxide materials[33,34,35,36,37]. At present there are several well-known oxide compositions which possess good thermoelectric properties, mainly of p-type conductivity. These compositions are characterised by metallic type electrical resistivity. However, finding suitable materials for conductive n-type materials presented many difficulties[38, 39, 40, 41, 42].

Currently, the best performance materials are thermoelectric semiconductors. Therefore, most of the world's research has focused on them. Forming newer and more complex compositions, which are characterized by slightly better parameters. As a consequence, these new semiconductors are becoming more expensive, requiring more complex production processes and it is important to find low cost thermoelectric materials with good properties and using simpler production technology.

2.2.1.3 Semiconductor thermoelectrics

Semiconductors present many advantages as thermoelectrics which can be visualized by considering the band theory of solids. Every atom has its own bond structure (stationary state). Each of the energy levels is filled by electrons or remains empty. In the case of multiple atoms in close proximity (i.e. a solid) the energy levels (filled and empty) are shifted due to the neighboring atoms. In materials, when a large numbers of atoms are brought together the levels (the available energy states) form continuous bands of energy rather than discrete stationary states (as in the case of free atoms) (Figure 6).

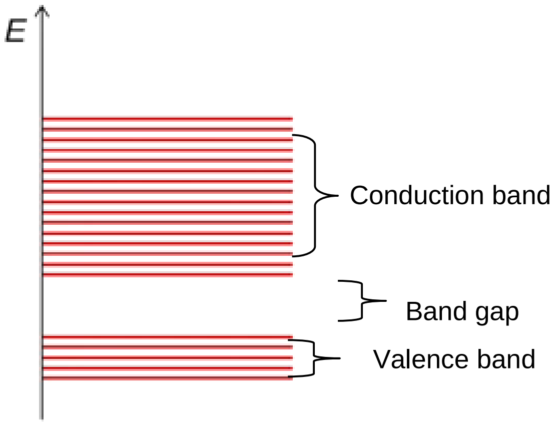

Figure 6 The energy level at absolute temperature with division into 2 bands (conduction + valence)[43].

The position of these bands defines the characteristic of each type of material as shown in Figure 7.

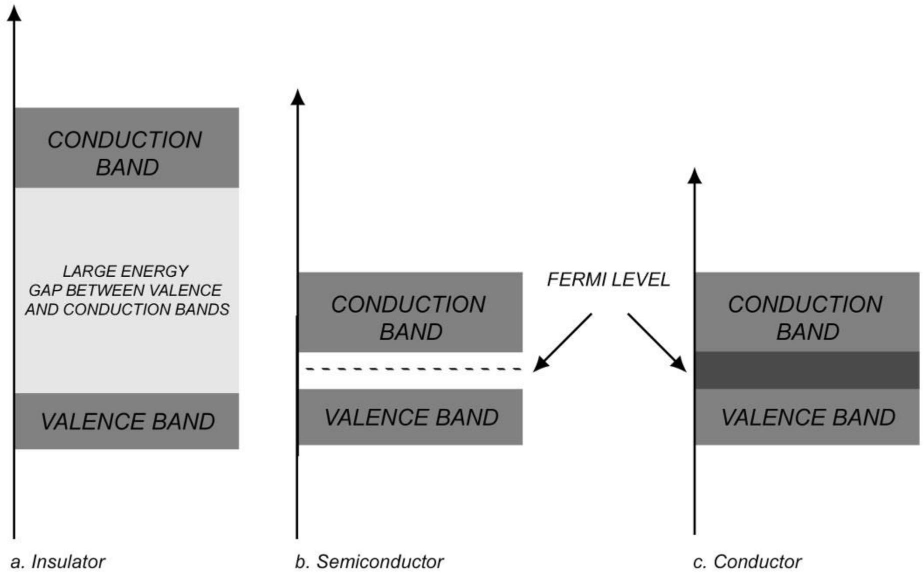

Figure 7 The energy level a) with a large band gap between valence and conduction bands typical for insulators, b) small energy gap typical for semiconductors and c) the overlap of conducting and valence band for metals[43],[44].

An important parameter in band theory is the Fermi level, which is identified in Figure 7. The Fermi energy is characterised by the amount of energy required for an electron to move from the valence band to the Fermi level. Consequently the position of the Fermi level with the relation to the conduction band is a crucial factor in determining the transport properties of the material. A semiconductor seems to be an ideal candidate for thermoelectrics. Since the valence band is not overlapping the conducting band as in case of metals and because the band gap is smaller than for insulators it can be overcome by electrons. The advantage of using of semiconductors may be the fact that the conductive properties can be easily controlled by doping. Two types of material can be obtained by adding other atoms. The “impurities” can change the carrier concentration and behave as donors or acceptors. The donor doping creates n-type materials with electrons as charge carrier, and the acceptors has holes as a carrier because they accept an electron from the filled valence band[43]. The changes of electron or holes concentration in semiconductors are presented schematically in Figure 8.

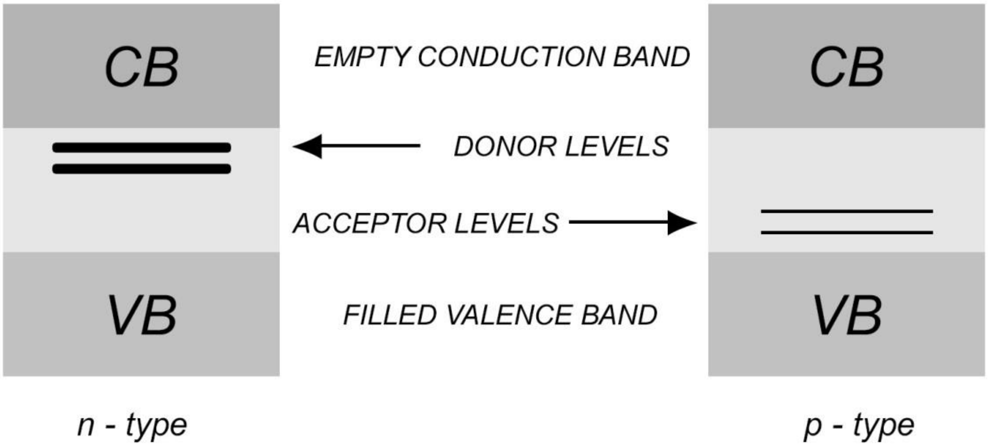

Figure 8 Change of electrons or holes concentration in semiconductors.

Taking into account the Fermi function f(E) which demonstrates that the available energy level could be occupied and is determined by temperature. The Fermi function has a form given by Equation 14:

$$f(E) = \frac{1}{e^{\frac{(E-E_F)}{kT}} + 1} \qquad \text{Equation 14}$$

where T is the absolute temperature, k is Boltzmann's constant and e is the electron charge. When at absolute zero temperature f (E)=0 and the state is not occupied, meaning that there are no electrons above the valence band and there are no available energy states in the band gap. If the temperature is greater than 0K some of the electrons have energies above the Fermi level[45] (overcoming the energy barrier). With increasing temperature some electrons can jump to the conducting band and promote an electric current[46]. This phenomenon is shown schematically in Figure 9

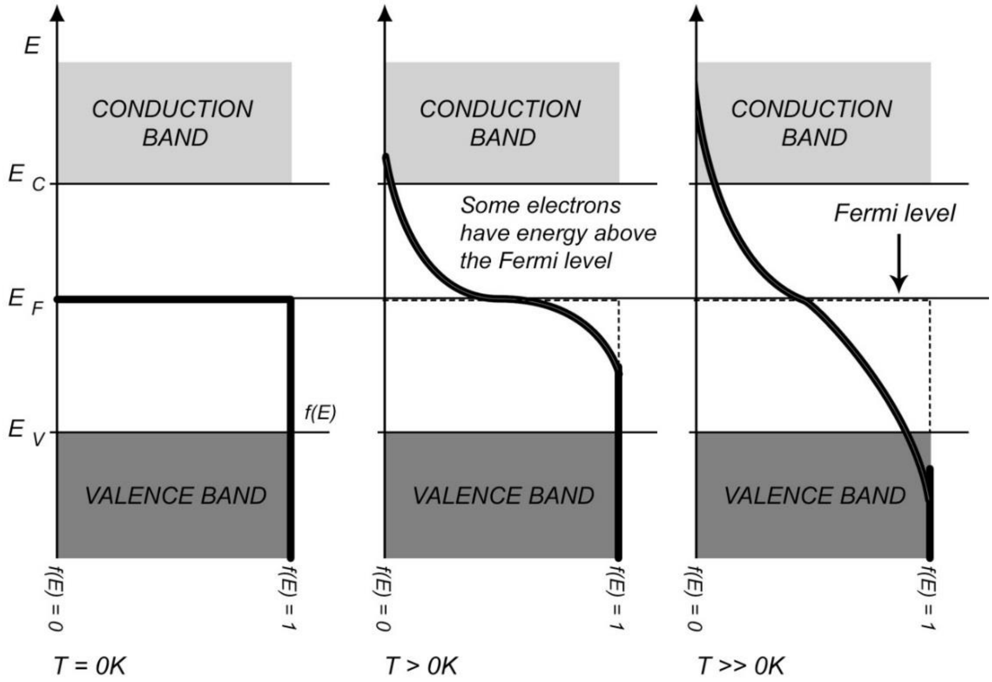

Figure 9 Schematic illustration of the changes at the Fermi level (states above Fermi level =n-type and states below Fermi level= p-type). The number of available energy states must be accounted for determine how many electrons reach the conduction band, the so call electron density of states (DOS).

At this point it should be noted that the three thermoelectric parameters (α, σ, κ) are related to the density of states (DOS) at the Fermi level EF as a function of the carrier concentration. A large value of Seebeck coefficient is achieved for semiconductors with a high density of states at the Fermi level, which at the same time indicates an interdependence of thermopower and carrier concentration. The generated voltage in case of metals is commonly less than 50 μV/K while for semiconductors this factor can be increased up to hundreds of μV/K[47].

2.2.1.4 Oxide semiconductors.

There is a large group of oxide semiconductors with both n and p conduction types including: p-type CuO, n-type MnO_3, p-type NiO[48], n-type WO_3, n-type TiO_2 and SnO_2. Since the 1960's, when the first papers appeared with descriptions of SnO_2[49], this oxide semiconductor has been described by many research groups to have thermoelectric properties after adding an additional element. The SnO_2-based ceramics doped with Al, substituting Al^{3+} for Sn^{4+}, show an increased sheet resistance of the films as reported by Moharrami et al.[50]. The thermoelectric measurements show that the doping levels change the behaviour from n-type to the p-type[50]. The higher Seebeck coefficient of -341 μV/ K was obtained for 30 at.% Al-doping level. The nanocomposite TiO_2/SnO_2 exhibits n-type behavior and a power factor of 70 $\mu W/m^2K$ at 1000ºC[51]. Other SnO_2-based ceramics with the Nd-, Hf-or Bi-doping, $Sn_{0.97}Sb_{0.01}Zn_{0.01}M_{0.01}O_2$, where M = Nd, Hf or Bi, were investigated. The power factor was enhanced due to increased electrical conductivity and Seebeck coefficient with Bi-doping[52] .

The oxide based materials were overlooked in the world's research until 1997 with a report of $Na_xCo_2O_4$ with good thermoelectric performance[53]. In comparison to conventionally known materials, the oxide thermoelectric materials can be non-toxic, cost-efficient and oxidation resistant in air. Oxide materials exhibit a strong interplay between spin, charge and lattice[61].

Promising oxide thermoelectric materials include $SrTiO_3$, $CaMnO_3$ based perovskites, ZnO with different kinds of doping, and also cobaltites which will be described later in this chapter. The complex oxide Indium-Tin-Oxide (ITO) is one of the highest mobility oxides used in a wide range of industrial applications (e.g. transparent electrodes). The highest value of ZT for this complex oxide was 0.06. Increase of ZT up to 0.45[54] at 1273K are achieved by addition of Ge to In_2O_3 with the substitution of Ge^{4+} for In^{3+} and fine particle size reducing thermal conductivity for the composition of $In_{1.8}Ge_{0.2}O_3$ [54]. In_2O_3 films doped with Pd (6vol%) showed a 65% increase of thermoelectric power factor (450 $\mu W/mK^2$) compared to the pure In_2O_3 films[55] at 1000°C. For $SrTiO_3$ the power factor was found to be around 600 $\mu W/mK^2$ at 630K and 1040 $\mu W/mK^2$ for doped sample $Sr_{0.9}Y_{0.1}TiO_3$ at the same condition[41]. La-doped $SrTiO_3$ films exhibit a large Seebeck coefficient up to 980 μV/K and the power factor of 390 $\mu W/mK^2$ [34]. A high conductivity is reported for perovskite-type $La_{1-x}Sr_xCrO_3$[56] with the positive Seebeck coefficient value of 200-300 μV/K up to 1800°C. The reported ZT value for complex $La_{0.85}Sr_{0.15}CrO_3$ was 0.14 at 1600K[57]. Similar conduction was reported for another perovskite-type oxide $CaMnO_3$ with the increased power factor (200 $\mu W/mK^2$) through substitution of Ca with

Bi $(Ca_{0.9}Bi_{0.1})MnO_3$[58]. $Ca(Mn_{0.19}In_{0.1})O_3$ was reported to achieve a ZT of 0.16 at 900°C. For a low temperature applications (300K) $La_{1-x}Sr_xCuO_{3-y}$ exhibits a decrease of positive Seebeck coefficient from 400 μV/K to 40 μV/K with the Sr level[25]. Good performance with a ZT value of 0.35 at 1000K is shown for polycrystalline Nb-doped perovskite $SrTiO_3$[59].

In ZnO-based thermoelectric materials increased mobility of carrier is achieved by reduction of ionicity of the metal-oxygen bond. Pure bulk ZnO is a n-type semiconductor, with Al doping showing enhancement in electrical conductivity together with a change to more metallic behaviour. Maximum thermoelectric performance was reported for the composition $Zn_{0.8}Al_{0.2}O$[60]. $Zn_{1-x}Al_xO$ within the range of $x = 0 – 0.1$[61] shows large mobility of carriers but the high thermal conductivity decreases the thermoelectric performance. The reduction of thermal conductivity of ZnO based material can be achieved by the use of elements heavier then Al e.g. Ga, In[62] or adding MgO[63]. The highest value of ZT for n-type bulk material was reported at 1273K with a value of 0.65 for $Zn_{0.96}Al_{0.02}Ga_{0.02}O$[64]. Ohta et al.[37] described an amorphous oxide semiconductor (ASO) superlattice composed of layers of amorphous-In-Zn-O and amorphous-In-Ga-Zn-O with increasing value of Seebeck coefficient strongly correlated with the thickness of layers, and the value of 73 μV/K which is 4 times bigger than that of the bulk material[37].

Rare-earth orthochromites ($RCrO_3$, where R = La, Pr, Nd, Gd, Sm, and Eu)[65] have reported electrical conductivities at room temperature in the range between 10^{-7} to 10^{-5} Ω^{-1} cm^{-1}, and values of 10^{-2} Ω^{-1} cm^{-1} near 1000 K.

There are several known compositions of oxides with mixed valence ions which can be classified into different groups:

- $LiMn_2O_4$ mixed valence (Mn^{3+}/Mn^{4+}) spinel with reported thermopower of -73 μV /K at high temperatures (1100 K)[66],
- spinel cobalt manganese $Mn_{3-x}Co_xO_4$ where the author mention about conduction due to Mn^{3+}/Mn^{4+} [67],

The alkaline-earth doped perovskite type oxides include:

- $CaMn_{1-x}Ru_xO_{3-\delta}$ with the mixed valence Mn^{3+}/Mn^{4+} and Ru^{5+},
- $(Ba,Sr)Pb_3$ with the mixed valence of Pb^{2+}/Pb^{4+},

- Rare earth cuprates with superconductor behaviour $Bi_2Sr_2CaCu_2O_{8+\delta}$ (Bi^{3+}/Bi^{5+}, Cu^{+}/Cu^{2+}),
- or semiconducting $YBa_2(Cu,Mn)_3O_{7-\delta}$ (Cu^{+}/Cu^{2+}),
- layered type cobaltites with the mixed valence Co^{3+}/Co^{4+} (described in the next part of this chapter),
- Spinel-structured oxides $Li_{1-x}Mn_{2-x}O_4$ with mixed valence Mn^{3+}/Mn^{4+} or mixed valence Co^{2+}/Co^{3+} in the case of $Ni_xMn_{1-x}Co_{2-2x}O_4$.

A. I. Klyndyuk[68] investigated p-type semiconductor of holmium barium cobaltocuprates with Seebeck coefficient of 220 μV/K at 500K.

An overview of a range thermoelectric materials with operating temperature is shown in Figure 10.

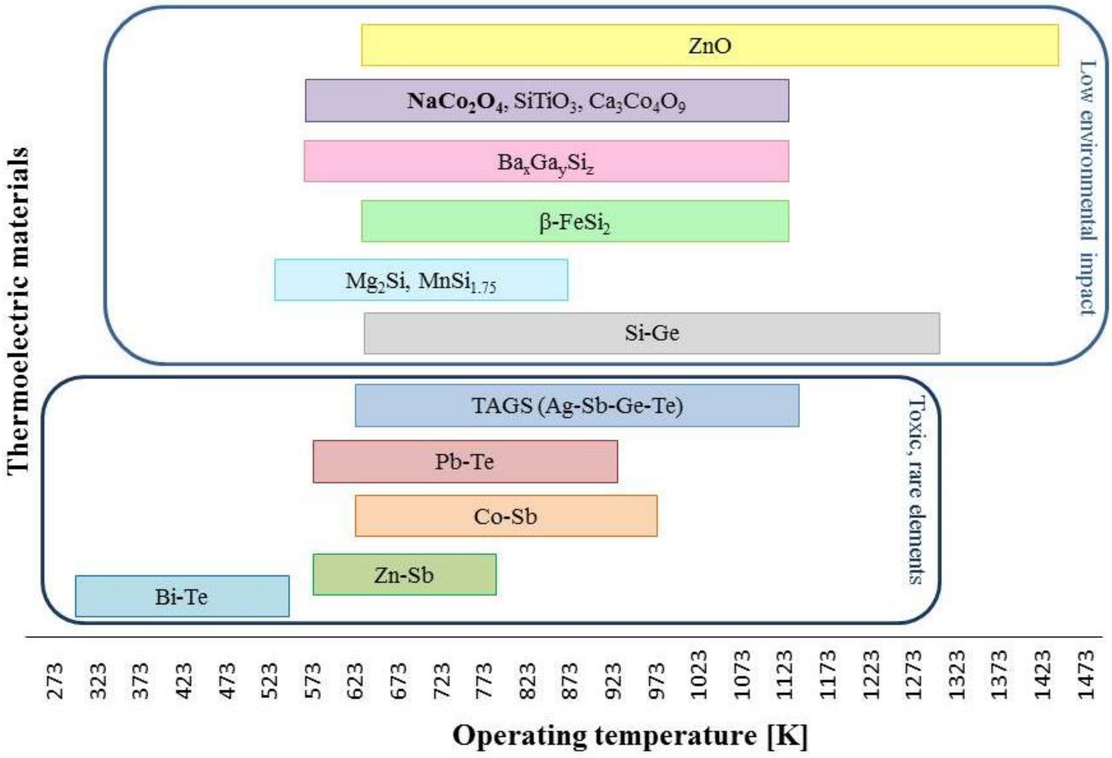

Figure 10 The overview on discovered and recorded operating temperature of typical thermoelectric materials and their environmental impact[47].

2.2.1.4.1 Cobalt oxide p-type semiconductor

Cobalt oxide materials have generated a lot of interest due to a wide range of properties exhibited including: electrical, magnetic[69] and transport[70]. The properties of p-type semiconductors are a result of the presence of electron holes. These holes are the carriers of charge which appear as a result of deficiency of metal, or in case of excess oxygen. The conduction of p-type semiconductors has properties intermediate between insulators (10^{14} to 10^{22} $\Omega\cdot$cm) and good conductors (10^{-6} to 10^{-5} $\Omega\cdot$cm)[71] with the amount and type of semiconductivity depending on the ambient oxygen pressure[72].

The cobalt oxide materials have attracted growing attention due to their high metallic electrical conductivity, which was observed in compounds such as $NaCoO_2$, $Bi_2Sr_2Co_2O_9$, $Ca_3Co_4O_9$, $Tl_{0.4}(Sr_{0.9}O)_{1.12}CoO_2$[73]and $Ho_{0.9}Ca_{0.1}CoO_3$[17], and their high thermoelectric performance.

Many Co oxide materials were discovered in the 1990's -2000's include $Ca_3Co_4O_9$[74], $(Ca_2CoO_3)_{0.62}CoO_2$[75], $[(Ca_{1-x}Sr_x)_2CoO_3]\rho CoO_2$[76] and $[Ca2(Co_{0.65}Cu_{0.35})_2O_4]_{0.63}CoO_2$ [77].

The Co- oxides are described as misfit layers of CoO_2 hexagonal conducting layers and the rock-salt type block layers. The a and c axes of those two layers are similar while the b-axis are different. Nevertheless in the literature[78] the general structure for layered cobalt oxides containing these two type of sublattices can be found. The general formula is presented as $((MO)_n)^{RS}(CoO_2)_{bRS/bH}$, where M is Pb, Hg, Bi, Ca, Tl or Sr atoms, n is the number of rock-salt layer ($_{bRS/bH}$ the subscripts RS= rock-salt and H-hexagonal layers). For example Ca based cobalt oxide for which n=3 (three RS layers) will take the form $(Ca_2CoO_3)^{RS}(CoO_2)_{bRS/bH.}$ The misfit layered Co oxides exhibit similar properties with differences in chemical properties. The thermopower was found to be between 80~160 μV/K at room temperature, with a CoO_2 layer resistivity of 5~30 mΩcm, and thermal conductivity of 1-2 W/mK. The very good thermoelectric properties are the result of the unusual layer structure.

More complex compounds of cobalt include: $Bi_{2.2-x}Pb_xSr_2CoO_y$, $Ca_{3-x}Bi_xCo_4O_9$[79], $Bi_{1.5}Pb_{0.5}Ca_{2-x}M_xCo_2O_{8+\delta}$[80], $Ni_xMn_{1-x}Co_{2-2x}O_4$[81] and $NiCo_2O_4$[82]. Cobaltite compounds can be characterized by negative or positive Seebeck coefficients depending on the dopant[83]. For the $LaCoO_3$ system the Seebeck coefficient can be p and n-type depending on doping. Doping with Sr^{2+} produces p-type behavior whereas n-type is obtained with the use of Ti^{4+}, Ce^{4+} or Sn^{4+} [84].

2.3 Sodium cobaltites

2.3.1 Introduction to Sodium cobalt oxides

In 1997 Terasaki[53] identified $NaCo_2O_4$ as a high temperature semiconductor with a high Seebeck coefficient and an impressively high electrical conductivity[85]. Sodium cobalt oxide is defined as a layered 3*d*-transition metal oxide belonging to the A_xMY_2 type compounds where A is an alkaline metal, M is a transition metal and Y represents O, S or Se. Ito et al.[5,86] noted that sodium cobalt oxide can occur with three types of structure depending on the level of sodium. The P3 type of structure is characterised for β-phase where sodium level is $1.1 \leq x \leq 1.2$, O3 type structure for α-phase with sodium level of $1.8 \leq x \leq 2.0$. The best electrical properties are found for a P2 type structure for a γ-phase which is characterised by a sodium level of $1.0 \leq x \leq 1.4$. This phase shows metallic conductivity[86], and has a larger Seebeck coefficient than the other known phases[87]. The compound is often also described as $NaCoO_2$. The structure of $NaCoO_2$ was investigated in the temperature range of 600-700°C in 1997 by Froussier. Froussier discovered the existence of four crystallographic phases as a function of Na α-Na_xCoO_2 ($0.9 \leq x \leq 1.0$), α'-$Na_{0.75}CoO_2$, β-Na_xCoO_2 ($0.55 \leq x \leq 0.60$) and γ-$Na_xCo_yO_2$ ($x < 1.0$, $y \leq 1.0$; $0.55 \leq x$ or $y \leq 0.74$)[88]. For all phases sodium is sandwiched between edge-sharing CoO_6 octahedra layers along the c-axis direction. The sodium cobalt oxide has excellent thermoelectric properties due to its unusual crystal structure[89], which will be detailed in the later part of this chapter. The γ-phase of $NaCo_2O_4$ is build up of layers[90]. The unit contains a sheet of edge-sharing CoO_6 octahedral with Na layers between the CoO_2 sheets[91]. Jansen and Hoppe[92] assigned a $P6_322$ crystal structure with a=02843 and c=1.081 lattice parameter. The sequence of the CoO_2 layers determines the number of sheets in a unit cell. There are two or three alkali layers per unit cell. The structure types are explicitly recognized by Na synchronization type and number of layers per unit cell; hence the α, α' and β phase exhibit the three-layer structures, while the γ-phase has a two-layer structure. Where the α-phase has a O3 structure (O refers to octahedral synchronization of Na ions and 3 is the number of layers which repeat) α’ phase has the ʹO3 structure (monoclinic deformation of O3 phase) β the prismatic P3 structure and γ is the prismatic two layer structure[93].

Similar to the copper based layered high temperature superconductors (HTSCs), the layered sodium cobalt oxides exhibit superconductivity[94] in a hydrated form. The behaviour is much more complex in sodium cobalt oxide so that the origins of superconducting behaviour is still unclear.

2.3.2 Structure dependence and atomic relations.

By changing the Na content using different chemical reactions it was found that sodium cobalt oxide changes behaviour from superconductors to metallic. A wide range of behaviour, ranging from semiconductor to metallic, has been reported for sodium cobalt oxide dependant on the level of sodium and is shown in the composition property map in Figure 11.

The variations in properties of sodium cobalt oxide are dependent on the sodium content as shown in Figure 11. However, studies have also shown that changes in the structure of the material are accompanied by a change in relative position of atoms to each other in the crystal lattice. Na ions can occupy two different atomic positions affecting the donation of electrons to the CoO_2.

For the three layered $Na_xCo_yO_z$ family the crystal structure is more complicated and occurs in the octahedral (O) or prismatic (P) coordinations with the numerical designation 1, 2, 3 which refers to the number of CoO_2 layers per unit cell. When $x=0.32$ and $x=0.92$ sodium cobalt oxide has a O3 type structure, when $x=0.6$ and $x=0.51$ have a P1 structure type and for $x=0.75$ a O1 structure. For the two layered system the P2 structure type dominates over the composition range from $x=0.3$ up to $x=1$, (except a region for $x = 0.5$).

The nomenclature of H1, H2 and H3 relate to slight differences in crystal structure within the P2 phase.

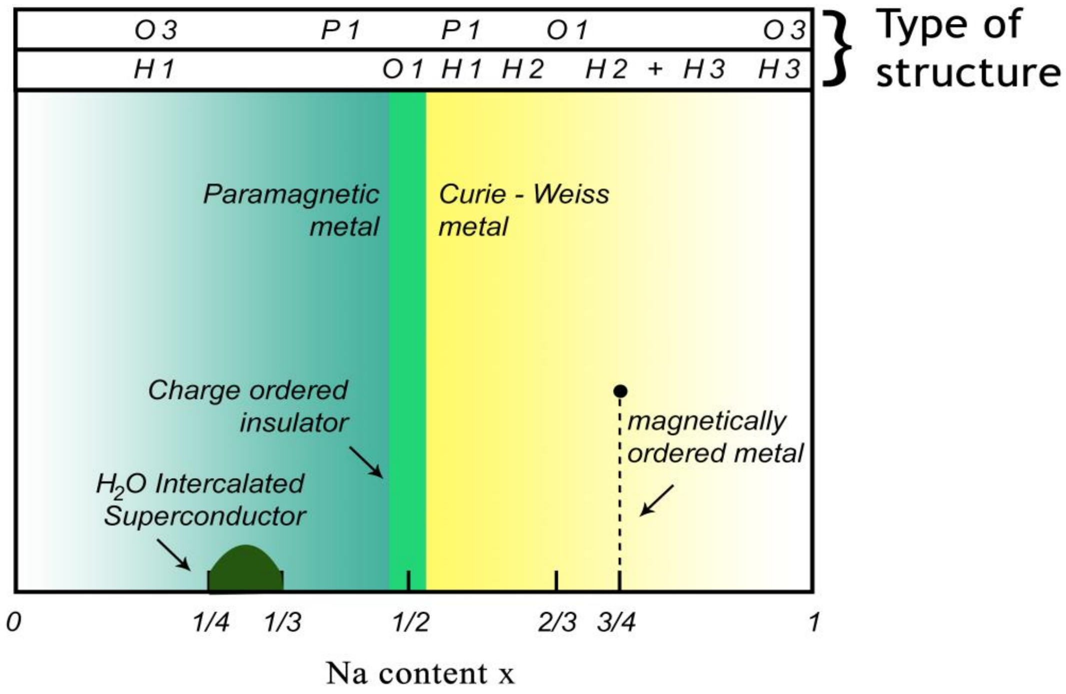

Na content / Properties	1/3	1/2	2/3	3/4	4/5	~1
α [μV/K]		100	110	160	100	105
ρ [μΩcm]	400	200		400		
PF [μW/mK^2]			25			33
κ [W/mK]		2		1.9		
Ref.	153	53	112	163	165	86

Figure 11 Electrical behaviour map of sodium cobalt oxide showing dependence on sodium level[95] and common types of structures for the two-and three-layered. (H1, H2, H3 refer to subtle differences in crystal structure within the P2 phase.)

For the two layered sodium cobalt oxide when x<1/2 the system is a paramagnetic metal with both the Na(1) and Na(2) sites being partially occupied, and the Na(2) site slightly displaced and called Na(2)’ as shown by the H1 structure. Figure 12 illustrates the three hexagonal structure types in terms of atomic positions.

For x>1/2 where the material behaves as a Curie-Weiss metal the structure shows H1 ordering. Around x=3/4 the Na structure transforms to the more ordered H2 structure where Na(2) is located in the centre of triangles. The structure remains up to x = 1 when the H3 phase exists.

When *x* ~ 0.5, the system is orthorhombic and exhibits a special charge and insulating structure, with the Na ions positioned in zigzag ordered chains[95].

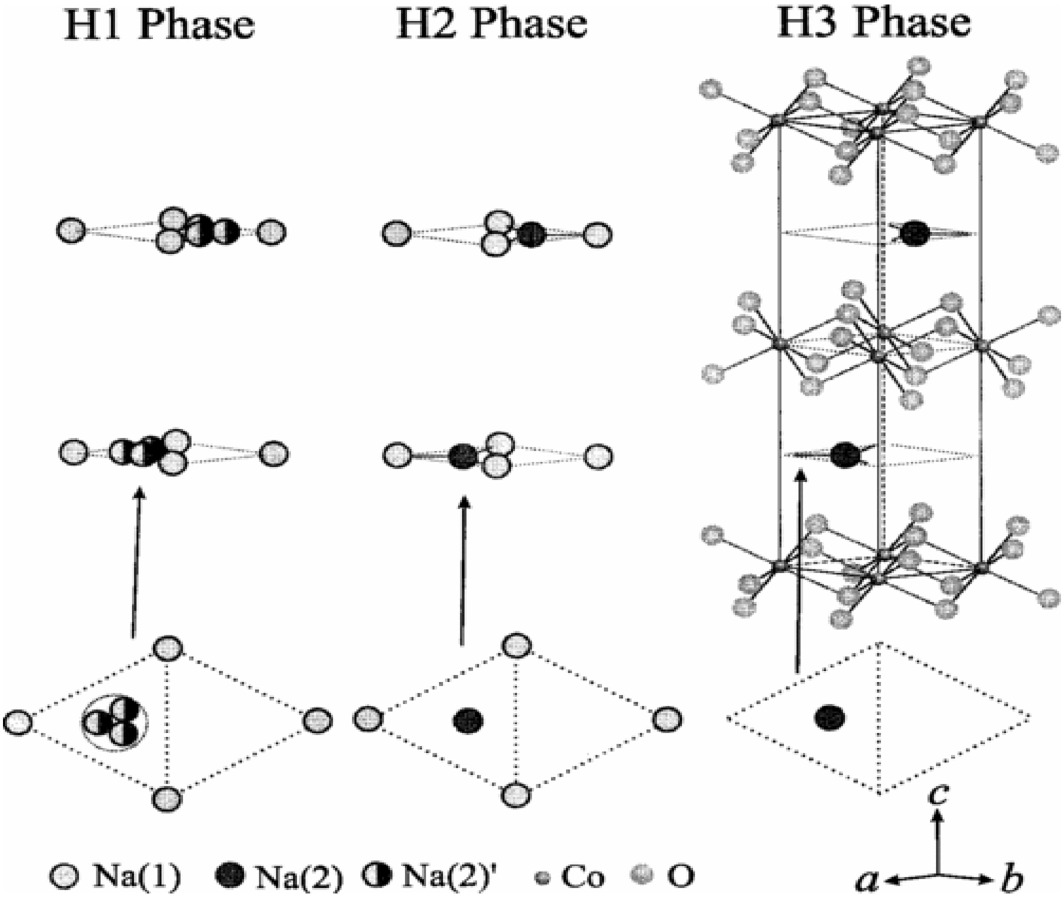

Figure 12 The three hexagonal structure types found for two layered $Na_xCo_yO_z$ with the layers of edge-shared CoO_6 octahedra and Na ions occupying ordered or disordered positions in the interspersed planes[96].

A possible structural atomic order was proposed by Zhang et al.[97] and is presented in Figure 13.

In addition to the location of sodium atoms affecting the properties of this material[95], the thickness of subsequent layers also has an effect on the behaviour which is especially visible for the three layered $Na_xCo_yO_z$. The CoO_2 layers become closer together as a result of changes in Na coordination and consequently the thickness of the NaO_2 layers changes continuously with Na content.

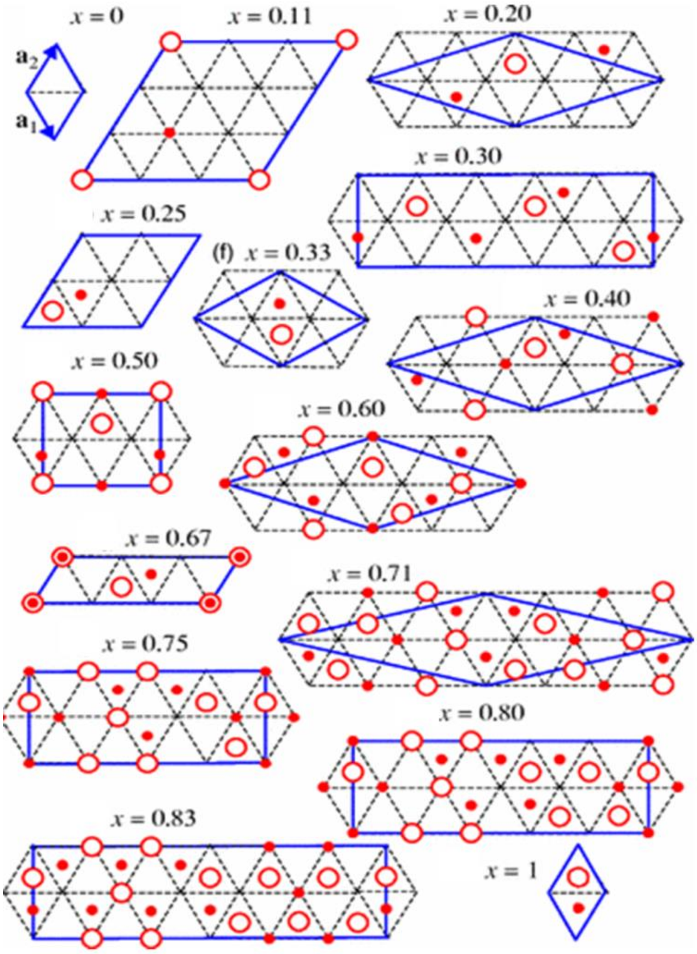

Figure 13 A possible structural atomic order for $Na_xCo_yO_z$. Blue thicker lines indicate the minimum unit cell in each case, Na(1) sites atom fall on top of the triangular lattice and Na(2) sites fall in the centre of the triangles. The dashed lines represent the projected triangular lattice of Co atoms[97].

With the changes of sodium content the changes in oxidation stage of Co (3^+, 3.5^+ and 4^+) will also affect behaviour. For the three layered structure when the sodium content decreases the Co-Co spacing also decreases and results in an increase of the oxidation state of Co from Co^{3+} for x=0.92 to $Co^{3.68+}$ for x=0.31. The studies of thickness of the CoO_2 layers suggest the redistribution of charge among different electronic orbits. Figure 14 shows that the thickness of the CoO_2 layer[93] is linked closely with the atomic coordination.

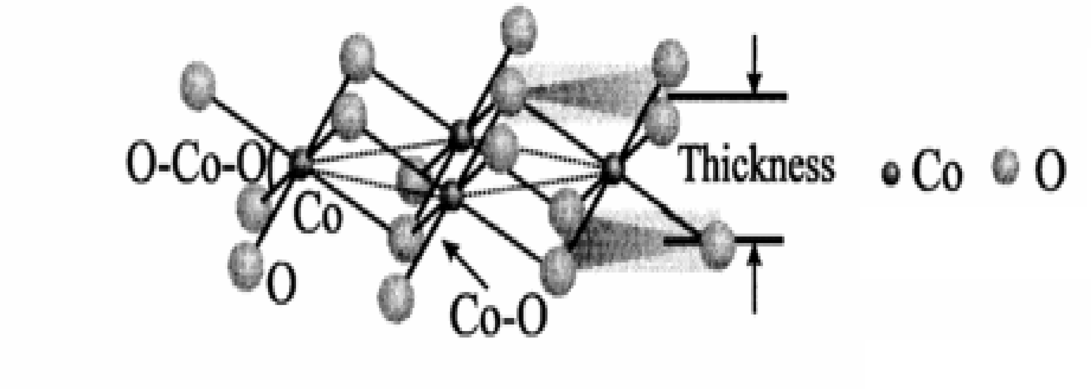

Figure 14 Detail of thickness of the CoO_2 layer[94].

There is a redistribution of charge within the CoO_2 layers dependent on the composition. In particular, for $Na_{0.75}CoO_2$ when the two and three layer sodium cobalt oxide phases are compared different electronic structure can be observed at the same atomic composition[93].

The lattice structure of the compound of sodium cobalt oxide is very diverse giving rise to a range of behaviours of this material. However this differentiated structure is not the primary focus of this thesis and so will not be discussed in further detail.

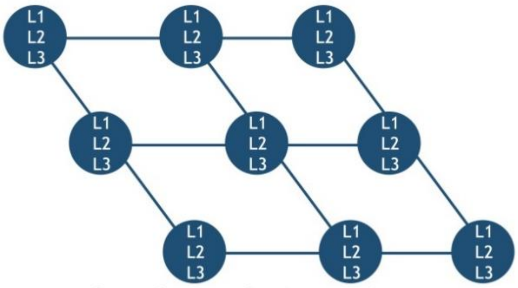

Co planes in two - layer

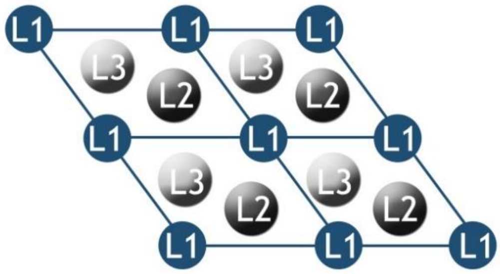

Co planes in three - layer

Figure 15 The comparison of the Co position in 2- and 3-layer variants. In the 2-layer variant the Co planes are the same in all layers. In a 3-layer variant the triangular Co planes are staged: $L_{1,}$ $L_{2,}$ L_3 represent layers[94].

2.3.3 Correlation of thermopower with electron band (electronic structure) in sodium cobalt oxides

As previously discussed the structure has a significant impact on the thermoelectric properties. The number of Na atoms, the arrangement of atoms with respect to each other, as well as the thickness of CoO layers and length of the axis, brings significant changes in the behaviour of this material. Koshibae et al.[10,11,98] modified Heikes[9] formula (Equation 3) to show that the conduction of electrons should also be taken into account.

The large carrier density (~10^{22} cm^3) for sodium cobalt oxide is due to the donation of valence electrons from Na atoms to the CoO_2 layer. The average oxidation state of the Co ion is +3.5 which means that the compound contains a mixed valence of Co with an equal amount of Co ions in the oxidation state of +3 and +4. The different arrangements of electrons are presented in Table 1.

Table 1 Description of different arrangement of electrons for Co^{+3} and Co^{+4} ions in these bands. The calculated value represented: spin-Sp, configuration-Con, degeneracy-Deg respectively.

Spin state	Co^{+3} bands	Co^{+4} bands	Calculated value for Co^{+3}	Calculated value for Co^{+4}
Low Spin State	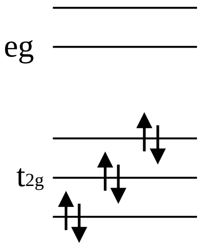	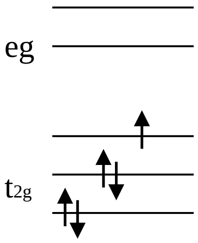	Sp=0 Con=1 Deg=1	Sp=1/2 Con=3 Deg=6
Intermediate Spin State	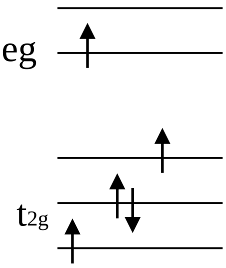	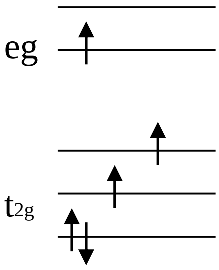	Sp=1 Con=6 Deg=18	Sp=3/2 Con=6 Deg=24
High Spin State	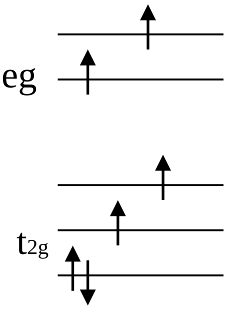	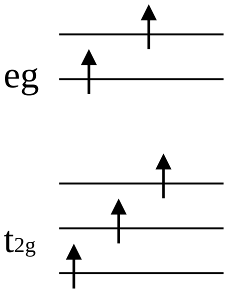	Sp=2 Con=3 Deg=15	Sp=5/2 Con=1 Deg=6

2.3.4 Synthesis of sodium cobalt oxide

A number of proposals for the synthesis of $Na_xCo_2O_4$ reported include: solid state reaction (SSR) method[3], auto-ignition route followed by an airflow shatter process[21], a citric acid complex (CAC) method and hot pressing (HHP) technique[99], a reactive template grain growth (RTGG) method[100], polymerized complex (PC) method[101], sol gel (SG) method, and a few mixed methods. However, the thermal, mechanical, electrical and magnetic properties of ceramics, metals, and composites are often improved with decreasing the particle size. Therefore, it is important to optimize a cheap and simple technology for the production of good thermoelectric material that can be used to adopt microstructures.

To date, just few methods have been reported for the preparation of thin films of $Na_xCo_2O_4$ using technique such as: electrospinning technique[102] or epitaxial deposition[103]. The spin coating method which is proposed in the present work is a cheap and fast technique which allows control of the thickness of the layers relatively easily.

The preparation of sodium cobaltate crystals characterised by high quality crystal structure is a big challenge. The chemical homogeneity and stability even of a single crystal is the largest problem. Many different methods for growing crystals have been reported such as a modified solid state reaction technique called 'rapid heat up'[1] the floating zone technique with the use of an optical furnace[154] and the flux method[53].

Methods for the production of sodium cobalt oxide nanofibers have been reported. Maensiri and Nuansing[104] described the fabrication of nanofibres by electrospinning. F. Ma et al.[147] proposed a sol-gel-based electrospinning technique to fabricate nanofibres about 10 nm in size, an order of magnitude smaller than sodium cobalt oxide powders produced by conventional sol-gel methods. In this way an enhanced figure of merit can be achieved by phonon scattering at grain boundaries and interfaces. Details of the performance are given in the following section.

2.3.5 Properties of sodium cobalt oxide

Tarasaki[99] reported a high thermopower for $NaCo_2O_4$ single crystals. This material has since appeared in various publications disclosing interesting thermoelectric properties[8]. For single crystal materials the thermopower was reported to be 100 μV/K and the electrical resistivity 200 μΩcm at 300K[53]. The resistivity has been reported to range from 200 to 600 μΩcm, and is related to the level of Na[105].

M. Ito et al.[5] disclosed $Na_xCo_2O_4$ synthesized by the polymerized complex (PC) method and reported metallic properties for x=1.7[5]. Compared to conventional SSR produced material, for which the electrical resistivity was found to be 250 μΩcm and the Seebeck coefficient 120 μV/K at 500K, material produced by the PC method exhibited a resistivity and Seebeck coefficient of 260 μΩcm and 140 μV/K, respectively. The thermal conductivity was reported as 1.79 W/mK for PC and 1.7 W/mK for SSR produced materials.

S. Katsuyama et al.[90] presented a synthesis of sodium cobalt oxide by a citric acid complex (CAC) method consolidated by hydrothermal hot pressing. The reported results show that the use of different processing conditions leads to different thermoelectric values, the results were collected and are shown in Table 2, all results were obtained at 300K.

Table 2 The Seebeck coefficient, electrical conductivity and power factor results obtained at 300K for citric acid complex (CAC) method and consolidated by the hydrothermal hot pressing method[90].

Synthesis condition	Seebeck coefficient μV/K	Electrical resistivity μΩcm	Power factor μW/mK^2
HHP untreated	145	265	800
HHP 473K,100MPa	110	325	385
HHP 473K,200MPa	120	250	580
HHP 523K,200MPa	135	235	800

K. Kurosaki et al.[106] described an elongated form of SSR synthesis and results obtained at 500K showed a thermal conductivity 3.2 W/mK, the electrical resistivity was found to be 150 μΩcm, and a Seebeck coefficient of 118 μV/K.

T. Seetwan et al.[3] obtained sodium cobalt oxide by a SSR method and reported a value of 103 μΩcm at 500K, a thermal conductivity between 3-4.7 W/mK, and Seebeck coefficient between 85-135 μV/K.

Cold high pressure compacting followed by solid state sintering was used by J.Cheng et al.[89] with results of 120 μV/K, 38 μΩcm, and 420 μW/mK^2 for Seebeck coefficient, electrical resistivity and power factor, respectively.

A power factor of 400 μW/mK^2, Seebeck coefficient of 98 μV/K and electrical conductivity of 410 S/cm was reported at 500K by S. Tajima et al.[107] after using reactive tempated grain growth methods.

X. Tang et al.[91] grew single crystals by low temperature flux method and achieved at 300K a Seebeck coefficient of 55 μV/K, and electrical resistivity of 115 μΩcm.

The further results for the SSR method presented by M.Ito and D. Furumoto[108] showed a Seebeck coefficient of 150 μV/K and electrical resistivity 380 μΩcm at 600K. For materials produced by polymerized complex method[109] a Seebeck coefficient of 150 μV/K, thermal conductivity of 1.7 W/mK, electrical resistivity of 270 μΩcm and power factor value of 0.75 μW/mK^2 were obtained at 500K. The introduction of mechanical milling of $Na_xCo_2O_4$ was found to improve electrical resistivity from 25.5 for conventional SSR samples to 360 μΩcm with the introduction of mechanical milling[110], the Seebeck coefficient increased from 120 to 130 μV/K, while the power factor was almost the same at 0.6 mW/mK^2.

K. Park et al.[111] using a SSR method obtained (at 800K) power factor of 230 μW/mK^2 with a Seebeck coefficient of 125 μV/K and 130 S/cm for electric conductivity.

L.Zhang et al.[112] used the sol-gel (SG) citrate method modified with the addition of Polyethylene glycol 400 (PEG-400) and achieved results shown in Table 3.

Table 3 Summary of results obtained for the sol-gel(SG)[112] citrate method modified with or without addition of Polyethylene glycol 400 (PEG-400)

Synthesis method	Seebeck coefficient μV/K	Electrical conductivity S/cm	Power factor 10^{-4}W/mK^2
SG	110	190	2.25
PEG-400	102	300	3.25

Comparison of γ and α phases of sodium cobalt oxide M. Mikami et al.[113] showed a difference in thermoelectric properties at 300K (Table 4),

Table 4 Comparision of result obtained by M. Mikami et al.[113].

Phase of $Na_xCo_2O_4$	Seebeck coefficient μV/K	Electrical resistivity μΩcm	Power factor $10^{-5}W/mK^2$
α	150	320	10
γ	100	120	80

Films produced by epitaxial film growth exhibited an electrical resistivity of 59 μΩcm at 100K for 275 nm thick films. The results are 1/40 of the polycrystalline bulk materials were comparable with the single crystal materials[114].

C-J. Lin et al.[115] produced γ- $Na_xCo_2O_4$ films by sol-gel spin coating method resulting in an electrical resistivity of 200 μΩcm at 300K and Seebeck coefficient of 54 μV/K, at the same temperature.

2.4 From the bulk materials to the nanoscale

In order to obtain large ZT values it is necessary to modify the three parameters (Seebeck coefficient, thermal conductivity and electrical conductivity) in conventional solid materials. One route is to modify the nanostructure of these materials to increase the value of ZT and enhance thermoelectric energy conversion[116], as the nanostructure materials exhibit unique properties which are not observed in bulk materials[117]. The enhanced properties due to nanoscale structure, affect the transport of electric charge and heat[118]. Hicks and Dresselhauss[116] described the reduction of the degrees of freedom of carriers (so-called as quantum confinement) as a result of noncontinuous energy levels. The bulk materials are considered as 0 degree of confinement. The overlapping of conduction and valence band is visible for one dimension or two dimension structures. The quantum confinement can be achieved in a thin film as in one dimension structure, or in a nanowire (two dimensions). The large quantum confinement effect is achieved by reducing the dimensionality therefore the largest thermoelectric figures of merit have been calculated for nanowire systems[119]. The reduction in thermal conductivity can also enhance ZT. It is believed that the scattering of energy carriers at surfaces and interfaces also plays an important role[120,121].

2.5 Basic overview on preparation methods

2.5.1 Solid state reactions

A wide range of chemical methods exists for the synthesis of ceramic materials. The solid state reaction is one of them. A new material is a product by interdiffusion of elements. Where starting reagents are not stable i.e. commonly used carbonates, hydroxides, oxalates, nitrates, sulfates, acetates, alkoxides or other metal salts, the new phase may be accompanied by the release of gas as a byproduct of the reaction[122].

2.5.1.1 Synthesis of polycrystalline Na_xCoO_{2-y}

Conventional solid state reaction (SSR) is a well founded technique which gives satisfactory results for the formation of $Na_xCo_yO_z$ phases. The commercial available chemicals, sodium carbonate (Na_2CO_3 - 99.9%) and cobalt oxide (Co_3O_4 -99.99%) are commonly used as a starting components for this synthesis. The powders are first mixed and pulverized to decrease the grain size and increase the homogeneity. The powder is then heat treated.

2.5.2 Formation of $NaCo_2O_4$ phase

Understanding the formation mechanisms of $NaCo_2O_4$ can lead to further optimisation of the process conditions and thus an enhancement of the thermoelectric properties. Ohtaki and Shouji presented the influence of CO_2 partial pressure on inhomogeneous Na distribution in bulk materials employing thermogravimetric analysis (TGA)[85]. Motohaski et al.[1] also investigated the phase formation using TGA where the precursors were heated in flowing oxygen. Both research teams noticed a weight loss around 100°C that was attributed to moisture evaporation. The decomposition of precursor (Na_2CO_3, Co_3O_4) components occurs between 500-750°C. Motohaski et al. described that the weight remained almost unchanged at 860°C for 12 hour and longer. The total weight loss between 500 and 750°C was found to be more than 7% while the stoichiometric composition of the raw materials should result in theoretical total weight loss around 6%. This difference in the additional weight loss can be attributed to simultaneous vaporization and total loss of Na_2CO_3.

Results described by Ohtaki and Souji[85] indicate the formation of a final phase of $NaCo_2O_4$ at 735°C in an oxidizing atmosphere. Additionally they presented results of the influence of CO_2 partial pressure showing that in pure CO_2 no reaction between the starting components was observed. Only when a low CO_2 partial pressure of 0.02 atm was observed the $NaCo_2O_4$ formation reaction was noted at 800°C. The TG results are shown in Figure 16.

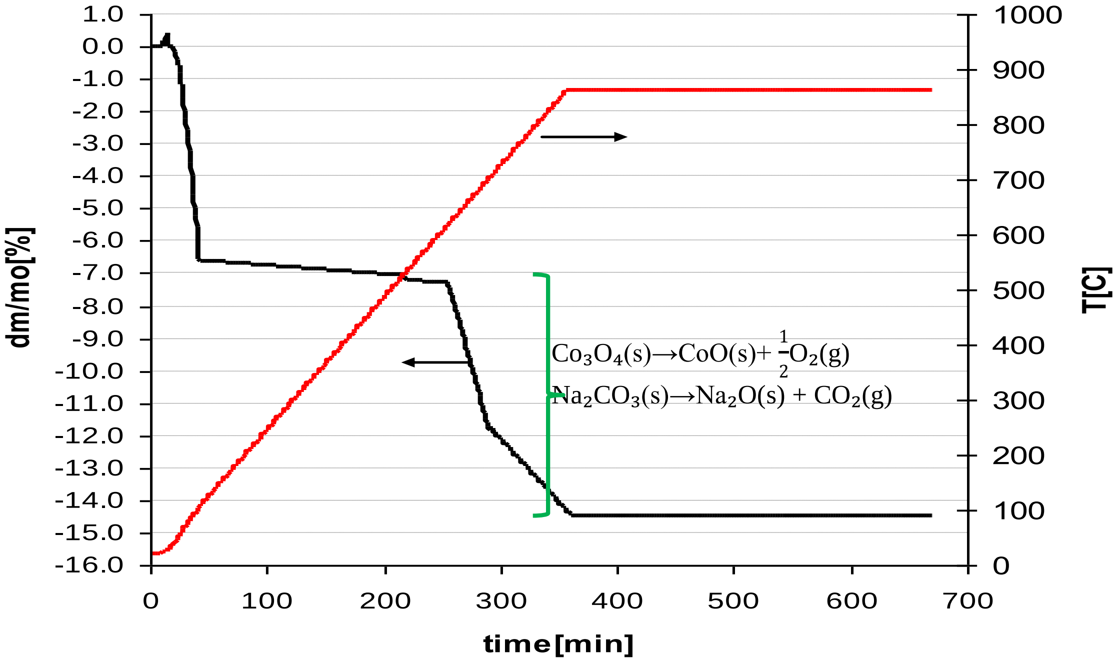

Figure 16 Thermogravimetric profiles for a reaction mixture of Co_3O_4 and Na_2CO_3 with a change in mass (and temperature) as a function of time[85].

Based on these results Motohaski et al.[1] have proposed a new technique called “rapid heat-up”. This method introduces the raw materials into a pre-heated furnace thus minimising Na evaporation.

2.6 Preparation of nanopowders

Small grain size can enhance the specific grain boundary surface area. The specific surface area also depends on the shape of the powder and can be extremely large for particles of elongated shape[123].

The techniques can be divided into two groups: physical vapour deposition (PVD) and chemical vapour deposition (CVD)[124]. In the PVD method the solid material is transformed into a gas through physical or thermal processes. Synthesis in the gas phase is a process for producing a solid under conditions of a thermodynamically unstable vapour (supersaturated). With the appropriate degree of steam supersaturation the nucleation of a solid phase occurs. This process is very quick and relatively uncontrolled. To prevent condensation, by lowering of supersaturation and hence nucleation, the system should be instantly cooled down. The resulting particles coagulate in the presence of a higher sinter temperature instead of coagulation. At lower temperatures loose agglomerates with open structures arise. The other known techniques for preparing nanoparticles in the gas phase are: spray pyrolysis, a condensation method in an inert gas, as well as the modified chemical vapor deposition. The oxide material powders can also be formed by controlled oxidation of received nanoparticles of metals or lower oxides. The process oxidation rate is determined by the degree of agglomeration of received nano particles. Through suitable selection of the synthesis parameters the formation of layers is avoided in exchange for the increased homogeneous nucleation of molecules in the gas flow. The chemical vapour deposition (CVD) is a more efficient technique PVD.

For decomposition of precursors the following techniques can be used: microwave plasma, laser pyrolysis, photothermal synthesis compulsion, and flame-chemical vapour condensation. The precursor can be supplied also in the form of droplets from a solution e.g. (spray pyrolysis, aerosol decomposition synthesis, droplet-to particle conversion).

Reacting in a liquid environment gives more possibilities than reactions in the gas phase. The advantage of reactions in the liquid environment is the good homogeneity, which affects the quality of the resulting nanopowders. However, the downside is the discontinuity of this process and lengthening of the synthesis time. In the wide range of methods for obtaining nanopowders in a liquid environment the most common are: co-precipitation, hydrothermal treatment, a microemulsion technique and sol-gel[125].

Co-precipitation is the introduction of the precipitation agent to the solution. This factor contains metal cations which are both included in the synthesized relationship. Co-precipitation products are most often metal hydroxides. These hydroxides are then calcined to obtain the desired oxide phase. The advantage is the uniformity of the obtained powder, grain size, and control of the chemical composition. The calcination process may be replaced by crystallization under hydrothermal conditions. Crystallization takes place in an aqueous medium at elevated temperatures and under pressures greater than atmospheric.

2.7 Sol Gel reactions

Sol-gel synthesis (sol-gel) is based on the slow dehydration of hydroxide from a previously prepared sol. Those reactions lead to the conversion of a sol into a gel[125]. This method makes use of the hydrolysis reaction of a metal alkoxide according to the formula (Equation 15):

$$M(OR)_n + nH_2O \rightarrow M(OH)_2 + nROH$$

Equation 15

where M is a metal atom-with a value of n-alkyl group R

Alcohols may be replaced by chelate complexes of a metal cation which stabilise and reduce its reactivity. This is useful in the synthesis of multicomponent systems, in which the differences in the rate of hydrolysis result in the formation of precipitates. Sol-gel synthesis occurs in a liquid medium at temperatures much lower than typical solid-state reactions. The basic raw materials for the synthesis of oxides are usually metal alkoxides and other compounds, e.g. chelates, esters, or combinations of organic and inorganic compounds (nitrates, chlorides, oxychlorides).

The first stage of this process is characterised by following reaction (Equation 16):

$$M(OR)_x + H_2O \rightarrow (RO)_{x-1}M - OH + ROH$$

Equation 16

The alkoxides are placed in water as a common solvent and a suitable catalyst is added. According to Equation 15 the hydrolysis of the alkoxy bond (M-OR) leads to the formation of hydroxyl bond (M-OH).

In the next step condensation occurs between the hydroxyl and alkoxy ligand corresponding to the reaction (Equation 17):

$$(RO)_{x-1}M-OH+(RO)_xM \rightarrow (RO)_{x-1}M-O-M(RO)_{x-1}+ROH$$

Equation 17

or between two hydroxyl ligands as shown in following Equation 18:

$$(RO)_{x-1}M-OH+HO-M(RO)_{x-1} \rightarrow (RO)_{x-1}M-O-M(RO)_{x-1}+H_2O$$

Equation 18

The reactions above leads to the formation of the bridge metal - oxygen - metal, which form the skeleton structure for each oxide.

The advancing continuous condensation leads to an increase of the metal oxide density, up to the starting gelling point. The processes of hydrolysis and condensation takes place in parallel and depends on factors such as temperature and pH of the solution, the amount of solvent and water, and the type of catalyst. The particles in the sol[125] are partially polymerized, but the degree of polymerization is relatively low. Transition of sol to gel is accompanied by the increase in viscosity which corresponding to the agglomeration of the particles and associated with the formation of a three-dimensional structure as a result of the cross-linking and polymerization. The parameters are influenced by temperature, time, amount of water and the concentration of the precursor. The above reactions take place at room temperatures. The final stage of the process is the removal of the solvent by drying.

2.7.1 Sol gel preparation of NaCoO

The commercial available chemicals $NaNO_3$(99%), $Co(NO_3)_3 \cdot 6H_2O$(99%) and citric acid (99%) are used as a raw materials for sol gel synthesis[149]. The chemical reaction which occurs during the sol gel process can be written in following way (Figure 17):

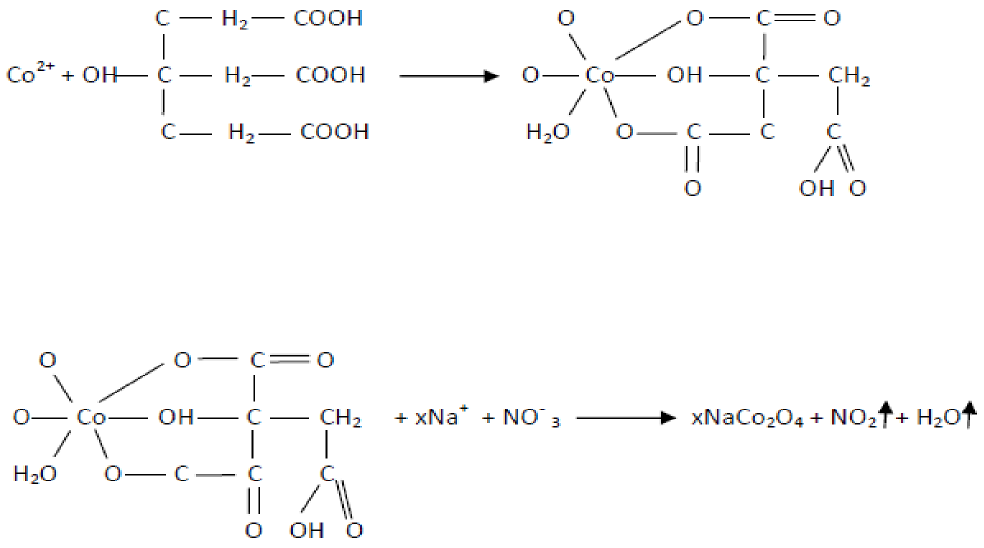

Figure 17 The chemical reaction occurring in the formation of sodium cobalt oxide using sol gel synthesis[88].

For the above reaction it can be noted that formation of sodium cobalt oxide by sol gel synthesis is accompanied by evaporation of NO_2 and H_2O[87].

2.8 Production of Ceramic Materials

The main stages in processing of ceramic materials are calcination and sintering. The heat treatment of ceramics is a process in which fine particles (powder) are transformed to a solid polycrystalline body. The process of preparing ceramics is divided into two stages of heat treatment as the reaction products generally have a different volume than the reactants, which lead to stresses in the system. These stresses could lead to cracking due to the brittle nature of the ceramic phase. So large microstructural changes can hamper the proper sintering and homogenization of the system. Therefore, the sintering of the polycrystalline ceramic is preceded by calcination in which the desired phase is first formed[126].

The free energy of the system is minimised due to the redistribution of atoms and interdiffusion to form new phases, to eliminate pores and increase grain size and so minimise the surface area. The fabrication involves a number of stages: preparation of powder, forming powder into shape, densification and finishing.

The preparation of powders begins with the mixing of reagents to reduce the particle size and eliminate aggregates. The most commonly used method is wet ball-milling. The next step is the calcination heat treatment. Calcination leads to the creation of the final phases. These may not be completely formed but the remaining starting components should assist sintering. Nevertheless the calcination should lead to a very coherent product. This thermal treatment is very popular due to the economic attractiveness as well as ease of transformation of the appropriately selected mixture of minerals or chemicals to yield a final product of the desired phase composition.

After calcination the powder has a non-uniform grain size, and therefore is subjected to milling to make the powder suitable for shaping. Pressing takes place in rigid moulds consisting of a die and punches, which exert pressure on the powder forming it into a shape. There are two methods, distinguished by the manner in which the compression force is applied: one- sided (pressure takes place on one side) and double-sided pressing (when the pressing force is applied on both sides). This method allows materials with a simple and symmetrical shape characterised by a relatively high relative density to be obtained.

The next important step in the formation of ceramic bodies is densification. Better compacted powder should sinter more effectively due to the removal of a smaller amount of pores. The process of compaction also affects packing homogeneity of particles. The agglomerates and aggregates formed during synthesis are conducive to the formation of pores in the compact. The presence of pores has a negative impact on the entire sintering process reducing final density and homogenisation of system. This can be explained on the basis of the theory proposed by Kingery and Francois in 1967. The thermodynamic considerations showed that only the pore with a coordination number (CN) that is smaller than a certain critical value (CN_c), dependent on the dihedral angle, can shrink and disappear. The coordination number (CN) represents the number of grains surrounding the pore (Figure 18). When pores with $CN \geq CN_c$ reach a certain equilibrium volume they do not shrink further. The pores with the largest coordination numbers are typically located between agglomerates.

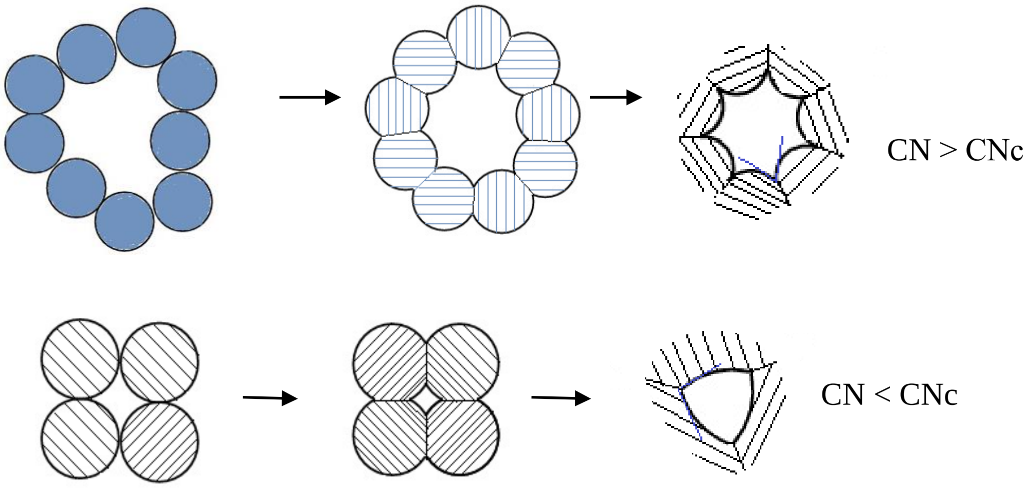

Figure 18 Illustrated stages of sintering of powder. Pores of $CN < CN_c$ may disappear, while pores $CN > CN_C$ shrink only to a certain value and may exhibit a change in the coordination number as a result of grain growth (with an indication of dihedral angle).

Assuming that the smallest value of coordination number of a pore is 4, the volume fraction of the pores, which may be lost, can be expressed with the formula[127] (Equation 19):

$$V_{CNc} = \int_{4}^{CNc} V(CN)d(CN)$$

Equation 19

Further production of ceramics is accompanied by the sintering process which is also recognizable as a high temperature consolidation process by which the dispersed material (usually powder) is converted into a well crystallized solid phase. This transformation is accompanied by shrinkage, which is considered to be the macroscopic evidence that the mass transfer processes occurs during the sintering. These processes include the grain rearrangement, diffusion and sometimes the plastic deformation and creep of grains. The kinetics of the sintering process are controlled by phenomena occurring at the interface between grains. The first contact between grain boundaries occurs during pressing. Further consolidation, leading to an increase in the degree of filling of the space occurs during sintering, and is thermally activated. The source of the driving force of particle rearrangement process is the reduction in energy associated with the grain surface. With the supplied heat the vibration energy of atoms (including atoms on the surface of the grains) increases, which leads to the creation of chemical bonds between the atoms from two different grains. With an increases in the number of bonds the momentary contact point between grains is transformed into a permanent junction. The increase in the number of junctions with increasing boundary area "stiffens" the arrangement of grains, leading consequently to a limit of the grain/particle mobility until they completely prevent their mutual movement. During sintering of the solid grains diffusion takes place mainly in the direction ensuring movement of atoms into the reaction zone (from one grain to another). In general, the rate of transport of two grains of different composition is not the same. Therefore grains whose matter diffuses slowly swell and the grain whose matter exhibits higher mobility shrink[127]. At this stage the mass transfer taking place in the junction area leads to a change of grain shape and further eliminate the pores, thus begins "appropriate sintering".

In this study, ceramic materials were fabricated from micro and nanometer size powders.

2.8.1 Sintering of nanopowders

In the case of nanopowders the speed of shrinkage during sintering are varied, which can lead to the generation of stress and in some cases where the stresses are high cracks between the agglomerates may form. These cracks can be considered as pores, which are surrounded by coordination numbers greater than the critical value that makes it impossible for them to be removed during sintering. Therefore it is important to use un-agglomerated powders. However, in the case of nanoparticles it is difficult because with the decrease in the sizes of particles the tendency to create agglomerates is increased. At a certain grain size the dispersion forces acting between grains /particles (eg, Van der

Waals forces) begin to be larger than the effect of gravity resulting in the connection of particles into larger clusters.

Grain growth is one of the factors which increase the volume fraction of the pores with a small coordination number leading to loss of pore volume as shown in Figure 18.

The effectiveness of the forming process is confirmed by the degree of compaction[128] and grain size in the sintered material. Therefore, similar to the macro scale, it is essential to achieve good compaction before the sintering process. The easiest way to consolidate the powders is through pressing. However the reduction in the effectiveness of pressing, induced by high intermolecular friction of small particles, leads to an inhomogeneous degree of compaction. Therefore effective consolidation of nanopowders with pressing requires the use of higher pressures. The application of higher pressures leads to the destruction of the agglomerates, shifting of grains and hence reduction of pores. The stresses arising during pressing should take into account by selection of pressure, to prevent the destruction of the mold[127].

The changes in the structure during the process of ceramics processing are shown schematically in Figure 19.

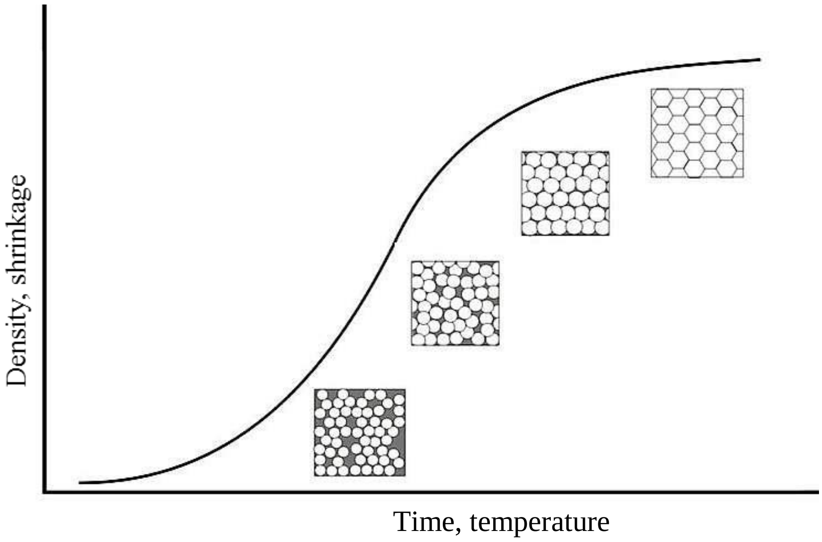

Figure 19 Schematic representation of the change in the structure during processing of ceramics leading to an increase in density.

Transformation of the material from powder to a polycrystalline form is accompanied by a change of material properties, such as density, porosity, hardness, strength, colour, and dielectric permittivity.

2.9 Films

The increase in performance of thermoelectric materials are connected with improvements of efficiency of thermoelectric devices. By the use of nanoscale materials, especially the production of films, the production of such high-performance thermoelectric materials is expected[129].

The use of nanostructured materials can increase the density of interfaces (which should be high as possible). The most commonly used techniques for preparation of the layers are: electrolytic deposition, and vapour deposition, wherein there are two methods of vapour deposition (PVD-Physical Vapour Deposition), and chemical vapour deposition (CVD-Chemical Vapour Deposition). There are several techniques for obtaining films by CVD coating methods among others the metallorganic CVD (MOCVD) used in electronics for the deposition of semiconductors with very thin epitaxial layers. Another possibility is the use of plasma with plasma assisted CVD (PACVD) which results in layers produced at lower temperatures with more control of stoichiometry and purity of coatings. Low-temperature techniques also include laser CVD (LCVD) technology. A vapour phase epitaxy (VPE) deposition technique is mainly used for producing oriented crystal layer microelectronic semiconductors.

In the PVD methods the metal or compound vapours are deposited on a cold or warm surface. Techniques of generating the vapor include: vacuum evaporation, ion plating, ion sputtering and magnetron sputtering.

Easier and cheaper methods to deposit films include: immersion, or spraying[130], jet printing, stamp printing and the spin coating method. The latter is used in this work and will be described further in the following section.

2.9.1 Spin coating technique

Spin coating[131] is a technique for the production of thin films and can be split into four stages. This includes deposition, spin up and spin off stages which occur one after the other. During all the above mentioned steps in the processing of films, evaporation occurs as a further stage.

The deposition stage involves the application of the appropriate amount of fluid on to a stationary or slowly spinning substrate.

During the spin up cycle, as a result of increase of centrifugal forces, fluid is spread all over the substrate, leaving a relatively even layer[132].

In the spin-off stage the discharge of excessive solvent from the surface of the substrate occurs. During this time the viscosity of the fluid increases until the liquid ceases to move, this process starts at approximately 10 seconds after spin up.

Evaporation is a complex process in which part of the excess solvent is absorbed into the atmosphere. Sometimes a skin layer forms on the surface which prevents evaporation and thus causes the destruction of the layer.

With this method, it is possible to deposit layers of different thickness depending on processing parameters[133].

2.9.2 $Na_xCo_yO_z$ films

The thermal, mechanical, electrical and magnetic properties of ceramics, sintered metals, and composites are improved significantly with decreasing particle size. Therefore, it is important to optimize the cheap and simple technology for the production of good thermoelectric material. To date, just a few methods have been reported on preparation thin films of $Na_xCo_2O_4$ using technique such as: electrospinning[102] or epitaxial deposition[103]. The properties depend on the density of the electron state and enhanced behaviour can be achieved with an increase of interface density.

Krochenberger et al.[134] have grown Na_xCoO_2 single phase thin films by pulsed laser deposition. The films were grown on $SrTiO_3$ substrates and when x=0.58 showed metallic behaviour. The highest resistivity has been found when x=0.54. Epitaxial films of Na_xCoO_2 were grown by pulsed laser deposition and topotaxial Na_xCoO_2 thin films were prepared by annealing epitaxial Co_3O_4 in Na vapour[103].

Single-phase superconducting $Na_{0.3}CoO_2 \cdot 1.3D_2O$ epitaxial thin films have been grown by pulsed laser deposition[135]. Superconductivity was found for x=0.3 and y =1.3 sample (for $Na_xCoO_2 \cdot yD_2O$). The result obtained show that the films can be produced with good Na homogeneity.

Brinks et al. reported films grown by pulsed laser deposition with an epitaxial structure on Al_2O_3 and textured crystal structure grown on $LaAlO_3$ (001)[136]. For textured Na_xCoO_2 thin films at room temperature a resistivity of 99 μΩm, Seebeck coefficient of 69 $\mu V\ K^{-1}$ were observed.

2.9.3 Crystals

In recent decades, many studies have been conducted on oxide semiconductors because of their unique properties as well as their wide range of applications, among others in electronics. Particular attention was given to their use on the nanotechnology scale where, depending on the applications, the shape, size as well as ease of production are important. Hence the one-dimensional[137] nanostructures (such as nanowires, nanorods, nanotubes, and nanobelts) have received wide attention as the materials are expected to play a critical role in the technologies of future electronic and optoelectronic devices. Much attention is paid to the processes of growth of different nano shapes. One can distinguish several basic mechanisms for growth of nano rods: vapour-liquid-solid (VLS)[138,139] supercritical fluid-liquid-solid (SFLS)[140], vapour-solid (VS)[141,142], screw dislocation as oxide-assisted growth (OAG)[143,144]. The growth mechanism consists of two stages: nucleation and growth[145]. These mechanisms are used as a way to produce increasingly diverse and valuable materials at the nano scale.

By the strong electron-electron correlation sodium cobaltite shows promising thermoelectric properties. A large Seebeck coefficient has been reported assigned to an unusual lattice as also low thermal conductivity due to the presence of sodium cations[146].

To date just a few methods have been reported on the preparation of Na_xCoO_2 nanowires[147,148,149]. Some details is provided in the following section.

2.9.3.1 Single crystal sodium cobalt oxide

The first crystal growth was reported in 1997 by Terasaki et al. with the largest size of crystal 1.5x1.5x0.01 mm^3 by the flux method. Fujita et al[150] described two layers γ-Na_xCoO_2 grown from molten materials of NaCl as the flux, results in the crystal size of 1.5x1.5x0.03 mm^3. The flux method was used by many researchers[151,152].

Another method for the growth of Na_xCoO_2 is the floating-zone technique[153,154,150].

A $Na_{0.75}CoO_2$ crystal was also prepared by a rapid heat up technique with enhancement of thermopower by reducing the resistivity[1]. A Seebeck coefficient value of 120 μV/K was obtained at 300K.

The thermal conductivity is of single crystals higher compared to the polycrystal and reported to be ~2W/mK, κ~5W/mK for polycrystal and single crystals respectively.

Fujita et al.[155] measured the in-plane electrical resistivity (ρ), the thermoelectric power (*PF*) and the in-plane thermal conductivity (κ) in the range of 300K to 800K. The results with comparison to the polycrystal $N_{ax}CoO_{2-\delta}$ phase, and typical p-type material $Si_{0.95}Ge_{0.05}$ are gathered and presented in Figure 20.

From the extensive literature review carried out on sodium cobalt oxide, it is clear that multiple phases of crystal structure exist and that a small change in elemental concentration results in a significant change in material properties (Figure 11). It is therefore paramount to develop a repeatable, material processing route that ensures the manufacture of this chemical compound with exact stoichiometric ratios.

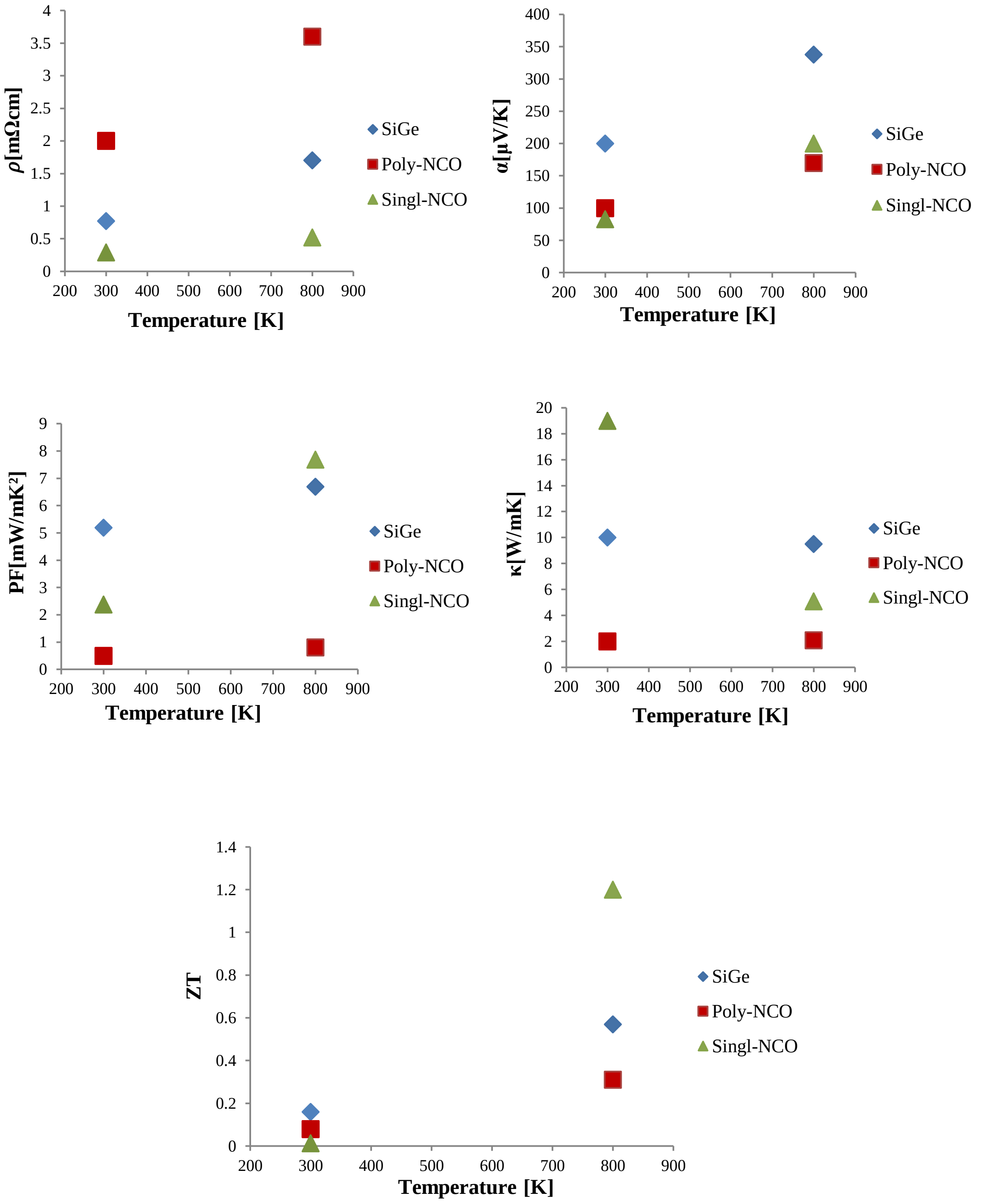

Figure 20 Comparison of polycrystal and single crystal Na$_x$CoO$_{2-\delta}$ phase, with typical p-type material Si$_{0.95}$Ge$_{0.05}$ in temperatures of 300K and 800K. Measurement of resistivity ρ, Seebeck coefficient S, thermal conductivity κ, and figure of merit ZT[155].

Chapter 3 Experimental procedures

3.1 Introduction

This chapter describes the techniques of characterisation used during the analysis of $NaCo_2O_4$ powders, films and pellets.

3.2 Synthesis of powder

3.2.1 Powders preparation

In the present research two types of powders were used for the preparation of $NaCo_2O_4$ bulk disc compacts (pellets). Powder produced by the Solid State Reaction (SSR) method and prepared using a sol gel (SG) method.

3.2.1.1 Solid State Reaction (SSR) powder

To produce SSR (Solid State Reaction) pellets: sodium carbonate Na_2CO_3 (Aldrich Sigma 99,5%) and cobalt oxide (II,III) Co_3O_4 (Aldrich Sigma powder < 10μm) were used as a starting reagents. These substrates were mixed with the molar ratio 1:2. Powders were accurately weighed using a digital balance (10^{-6} g) and the components were immersed in propan-2-ol (Aldrich Sigma propan-2-ol ($C_5H_{11}OH$)). The mixture was then placed together with zirconia balls in a ball mill, where the components were mixed and pulverized for up to 24 hours at room temperature. Afterwards, the slurry was dried in an oven over night at 70 – 80˚C, with the final powder being a grey colour. The calcination process was carried out in an alumina crucible were the powder was exposed at 850^{o}C in an air furnace.

3.2.1.2 Sol Gel (SG) powder

An aqueous solution of cobalt (II) nitrate hexahydrate [$Co(NO_3)_2 \cdot 6H_2O$], sodium nitrate $NaNO_3$ and citric acid was prepared. 0.11 mol of $Co(NO_3)_2 \cdot 6H_2O$, 0.094 mol $NaNO_3$ and 0.13 mol $C_6H_8O_7$ were dissolved in distilled water to obtain a 0.3M solution. The solution was constantly stirred at 80°C for 1.5 hour to achieve a homogenous solution. The resulting mixture was light red in colour and was allowed to cool while being stirred. The prepared $NaCo_2O_4$ producing sol was dried in an oven at 70 - 90˚C overnight. The resulting powder was a light pink colour. Dried and crushed powder was calcined at 700ºC for 6 hours with a ramp rate of 4 ºC/min.

3.3 Preparation of Na-rich pre-treatment and pure $NaCo_2O_4$ pellets

In the stage of production of pellets the SSR powder was ball milled with zirconia balls, for 24 hours in two kinds of solution: propan-2-ol or aqueous sodium hydroxide for this purpose 2 weight % (relative to the $NaCo_2O_4$ powder mass) of NaOH dissolved in distilled water. Solutions were placed in the bottle in the weight ratios 1:2:1- reagents; milling media; fluid. The obtained slurry was dried overnight in an oven. The dried powder after the ball mill in propane-2-ol was then divided in to the three parts for preparation of 3 kinds of pellets:

One type was crafted from solid state reaction powder, with the two remaining parts of the powders being subjected to two methods of saturation with sodium.

I. (Infiltrated - Inf) Initially calcined powder was pressed into pellets using a hydraulic press at a pressure of 1.3 MPa before being infiltrated with aqueous NaOH (). Pellets were dried in order to avoid distortions during sintering at higher temperatures. Such prepared samples were sintered for 1, 2, 6 and 12 hours in order to determine the optimal process conditions.

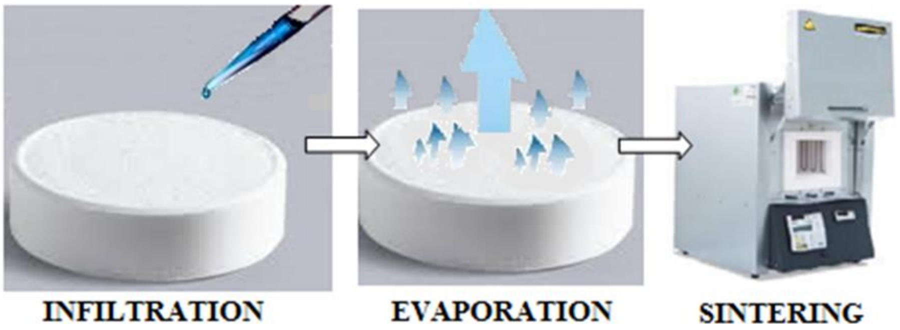

Figure 21 Schematic of preparation of infiltrated pellets.

II. The pre-calcined powder was balled mill in propan-2-ol for 48 hours and dried in the oven at 70°C - before being mixed with NaOH solution and redried at

70°C. The resulting powder was then used to produce pellets. The mixed pellets were prepared in the following procedures in accordance with the model shown in Figure 22.

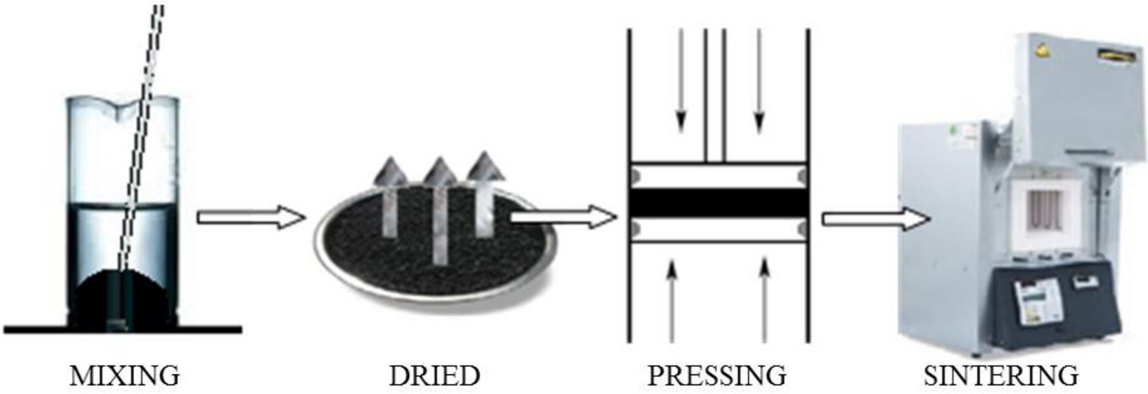

Figure 22 Schematic of preparation of powder to produce mixed pellets.

III. (Ball milled – BM) The ball milled pre-treatment of pellets was significantly differed from the other Na rich preparations. Namely, the calcined powder was ball milled in an aqueous NaOH solution instead of propan-2-ol as was employed for the previously described Na rich pre-treatments. The ball milled pellets were then prepared according to the scheme shown in Figure 23.

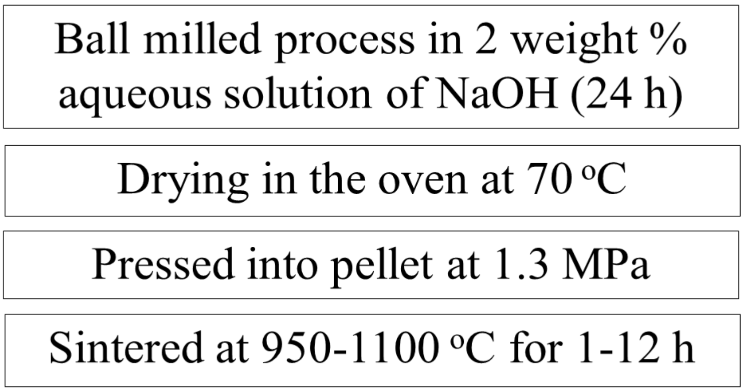

Figure 23 Preparation stages of ball milled pellets.

Each powder was crushed in a pestle and mortar in order to break down all aggregates, before being balanced and placed in the pressing machine (3 cm diameter) in order to obtain the flat pellets, the pressing force used was equivalent to 1.3 MPa. The formed pellets were sintered at high temperatures between 950 – 1100°C for various time periods between 1, 2, 6 and 12 hours respectively with a ramp rate of 4 C min^{-1}. A schematic diagram of the different stages used for the pellet production is shown in Table 5.

Table 5 Processing stage for production of different types of SSR pellets

	SSR **(Solid State Reaction)**	**INF** **(Infiltrated) I**	**M** **(Mixed) II**	**BM** **(Ball Milled) III**
Mixed:Na_2CO_3 + Co_3O_4 (1:2 mol ratio)	x	x	x	x
Ball milled process (24 h)	x	x	x	x
Calcinated at 850°C, for 12h	x	x	x	x
Ball milled process (24 h) in propan-2-ol	x	x	x	
Ball milled process (24 h) in NaOH aqueous solution				x
Mixed powder with NaOH aqueous solution and dryied			x	
Pressed in to pellet	x	x	x	x
Covering the surface of pellets with NaOH aqueous solution and then drying		x		
Sintered at 950-1100°C for 1-12 h	x	x	x	x

Sol gel powder after calcination was weighed and subjected to pressing in order to produce the SG pellets. The preparation maintained with the same parameters that have been used during production of SSR pellets. Table 6 shows in detail the stages of SG pellet preparation.

Table 6 Processing stages for production of two types of SG pellets

	SG **(Sol Gel powder Pellet)**	**SG-BM** **(Sol Gel powder pellet with additional NaOH)**
Mixed: 0.11 mol $Co(NO_3)_2 \cdot 6H_2O$, 0.094 mol $NaNO_3$ and 0.13 mol $C_6H_8O_7$	x	x
Dried in an oven at 70 - 90˚C	x	x
Calcinated at 700°C, for 6h	x	x
Ball milled process (24 h) in NaOH aqueous solution, dried in oven at 70°C		x
Pressed in to pellet	x	x
Sintered at 950-1100°C for 1-12 h	x	x

3.4 Preparation of films

As previously mentioned, two kinds of powder were used for the preparation of $NaCo_2O_4$ films. A deposition method for the thick films was done by spin coating using a sol prepared as 3.2.1.2 and ink 3.4.1.

3.4.1 Preparation of ink

To produce composite slurry-inks, both the SSR powders and SG powders, were used. Powder and sol were mixed together in a 1:2 weight ratio. Then 2 wt. % (relative to the $NaCo_2O_4$ powder mass) of dispersant (SURFYNOL CT 151 or SURFYNOL CT 324) was added to ensure thorough dispersion. To obtain a homogeneous ink, the ink was milled for 2 - 7 days with zirconia grinding media in a borosilicate glass bottle.

3.4.2 Film deposition

The slurry-ink and sol were deposited on alumina, pure silicon and on titanium-platinum coated (Nordiko Magneton Sputter machine) Si wafer. The wafers were cleanedwith distilled water, then acetone and dried with compressed air, then heated on a hot plate at 150ºC. The $NaCo_2O_4$ films were built up by covering the wafer sequentially with the slurry-ink and sol. The spin coating procedure was carried out according to the schematic process illustrated in Figure 24. Sol solutions were passed through a 0.2µm Whatman filter and were spun between 2000 - 3000 rpm for 30s using a spin coater. The individual applied layers were heated at 200ºC for 60s and pyrolysed at between 450 - 700ºC for 60s. The spin coated wafers were then subjected to a thermal annealing process in a furnace (Carbolite ELF 11/68). The thermal treatment was conducted at temperatures between 550-850ºC for 5 and 15min.

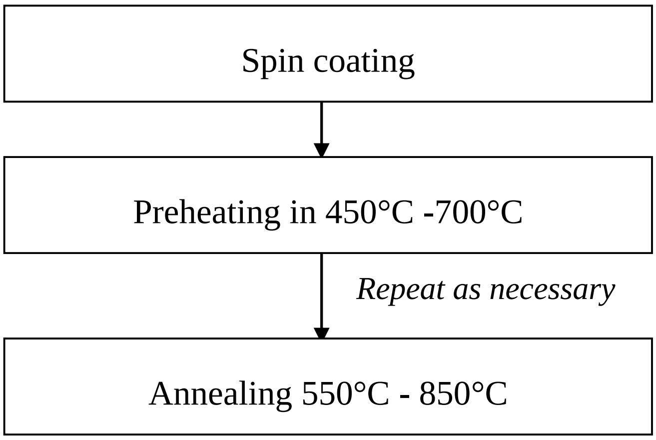

Figure 24 Scheme of procedure for film preparation using spin coating and various temperature treatments.

Different $NaCo_2O_4$ films were obtained by depositing 1, 2, 3 and 4 layers.

The layers were gradually built up in order to optimize parameters production. For effective TE performance it is important to maintain a temperature difference across the thermoelectric material. This requires the use of thick films (< 10µm) which can be produced at relatively low temperatures using the modified sol gel route[168]. In this study the following layers were produced:

- single sol layer (sol)
- single ink layer (1 ink)
- 1 ink + 1 sol layer
- 1 ink + 2 sol layers
- 2x (1 ink + 2 sol) layers
- 3x (1 ink + 2 sol) layers
- 4x (1 ink + 2 sol) layers

Each film was deposited in the sequences presented in Figure 24. The standard heat treatment of 700°C and time of 30 min were based on earlier work for PZT films by Dorey et al.[168],[156]. The standard procedure was adopted and later modified as described in a later section of this thesis.

Sodium cobalt oxide thin films were deposited on a Si wafer, which was previously prepared by plasma sputtering layers of Pt and Ti, as also Si on Al_2O_3 wafers. Such prepared films were heated at different temperatures and observations on whether these treatments have an effect on the phase changes were made.

3.5 Characteristics of the microstructure of the tested materials

The phase composition of the tested samples was determined using X-ray diffraction (XRD) (Siemens 5005) with Cu Kα source. Samples were scanned at angles of incidence between 10 and 90° with the step size of 0.05. XRD results were evaluated using XRD Evaluation software and compared to JCPDS patterns.

A scanning electron microscope (FEI XL30 SFEG) and environmental scanning electron microscope (FEI XL30 ESEM) were used to investigate the microstructure. Additionally, ESEM micrographs in back-scattered (BSE) and secondary electron (SE) were obtained to observe microstructural changes on the surface of the as prepared samples. The Energy Dispersive X-Ray Spectroscope (EDX) (Oxford ISIS series) attached to the SFEG was used to perform elemental analysis.

For investigation of crystal structure transmission electron microscopy (TEM - CM20 Philips) with attached the EDX Spectroscopy was used. The crystals were prepared for testing by collecting them on a scalpel, before being dispersed in water and lifted onto a carbon coated copper grid for analysis.

The d-spacing were calculated from the selected area diffraction image by dividing the camera constant for a particular voltage by the measured radius from the diffraction image.

Thick and thin films of sodium cobalt oxide formed on three different substrates were examined using a reflected light optical microscope (Nikon Optiphot). The use of this microscope allowed a study of the whole surface area of the films. A confocal scanning laser microscope (Olympus Lext OLS3100) was used to check roughness and surface topography of the prepared films.

3.5.1 Density of pellets

The size of prepared samples was determined in order to calculate the density. Each sample was weighed on an electronic scale in order to determine the actual weight. By using Equation 20 the density (p) of pellets was calculated.

$$p = \frac{m}{V}$$

Equation 20

Where m is the measured weight of material, and V is the mathematically calculated volume.

3.6 Electrical and thermal measurement of materials properties

3.6.1 Electrical measurement at low temperatures

The electrical properties were measured using a 4 point probe test.The measurements were taken by passing a current through two outer probes, with a probe spacing of 1.5 mm, and measuring the voltage across the inner probes.

For bulk samples the electrical resistivity was calculated using Equation 21:

$$\rho = \frac{V}{I}\frac{\pi t}{ln\left(\frac{sinh\left(\frac{t}{s}\right)}{sinh\left(\frac{t}{2s}\right)}\right)}$$ Equation 21

where t is thickness of a sample, s the probe spacing, V is the voltage measured, and I is the current applied.

For films the electrical resistivity (ρ) of the samples was then calculated using Equation 22:

$$\rho = \frac{\pi}{ln\,(2)}t\left(\frac{V}{I}\right) = 4.523t\left(\frac{V}{I}\right)$$ Equation 22

where t is thickness of a film, V is the voltage measured, and I is the current applied.

3.6.2 Seebeck coefficient and thermal conductivity measurement at low temperatures

3.6.2.1 Preparation of pellets for thermoelectric measurement at low temperatures

The bulk ceramic material was prepared for thermoelectrical testing at low temperatures by application of silver conductive paint (RS Components 186-3593) on both faces of the pellets.

3.6.2.2 Seebeck coefficient in low temperature

The thermoelectric measurements were conducted at low temperature in a range between 30ºC and 100ºC using a Thermoelectric Characterisation Rig (TC-Rig)

A hot plate with temperature controller (±1°C) acts as the heat source on one side of the sample. The opposite side of the sample was cooled down by a CPU cooler, to maintain a temperature gradient across the sample. In order to ensure uniform temperature across the heater and cooling system a copper disk was used. Each copper disk had a thermocouple embedded in its centre to allow temperature measurements to be made.

To measure the Seebeck coefficient the prepared samples were sandwiched between two squares of copper foil. In order to measure the voltage output, wire was soldered onto the copper foil to allow connection to an electrical meter. The sample, and foil structure was placed between two thermocouples where the temperature at the hot and cold sides of test pellet was recorded. The temperature of the heat source was increased to obtain multiple voltage readings for different temperature differences. The voltage was recorded by a high precision electrical meter (Keithley). To obtain accurate readings each measurement was taken over 5 minutes at a rate of 4/sec and the average value calculated. The Seebeck coefficient was calculated using Equation 2.

$$\alpha = \frac{\Delta \mathrm{V}}{\Delta \mathrm{T}}$$

3.6.2.3 Thermal conductivity

To determine the thermal conductivity of the disc shape pellets prepared, a comparative bar method was used. Glass pieces with known thermal conductivity were used as reference sample. The TC rig was modified as shown in Figure 25. The sample being measured was sandwiched between two glass reference samples with 4 thermocouples embedded into copper disks placed at end of each sample as shown in Figure 25.

Measurements of the 4 thermocouples were at different set temperatures once thermal equilibrium has been attained. Within the multilayer stack the heat transferred through each layer is assumed to be equal. The approach presented assumes that no heat is lost at the edges of the samples. Such heat loss was minimised by using samples with a low aspect ratio (<4) and external insulation.

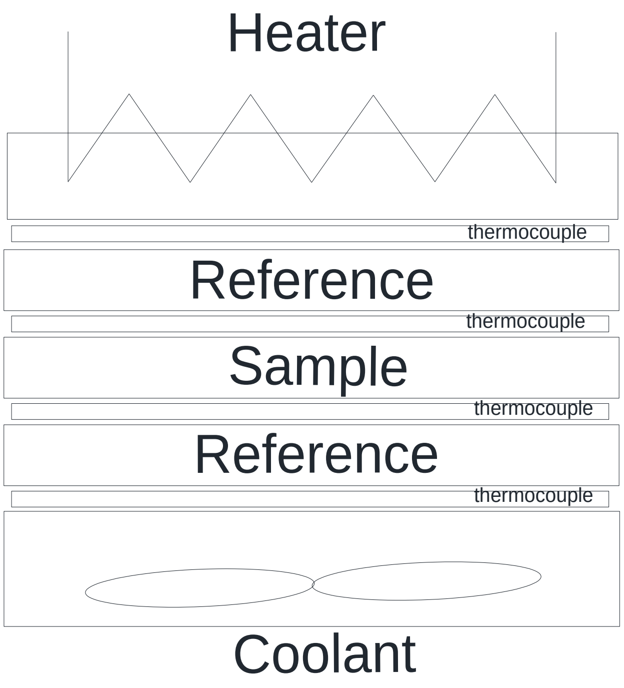

Figure 25 Diagram of used thermal conductivity setup.

The heat quantity transferred through the reference glass was calculated from measurements of the differences in temperature between the two ends of the conductor, and the known thermal conductivity. The thermal conductivity of the test material was then calculated from the calculated heat flux and temperature difference across the sample. Equation 23 describes the calculation used:

$$\kappa_s \frac{\Delta T_s}{L_s} = \kappa_r \frac{\Delta T_1 + \Delta T_2}{2} \frac{1}{L_r}$$

Equation 23

Where Q is the heat flux, A is the cross sectional area, κ_s the thermal conductivities of the sample, κ_r the thermal conductivity of the reference samples, and L_s and L_r are the thicknesses of the sample and reference, respectively.

3.6.3 Seebeck coefficient and electrical resistivity measurement at high temperature

The Seebeck coefficient and electrical resistivity tests were performed on the high temperature self-constructed measurement equipment at the heating rate of 3 º C/min – the dwell temperature relates to the cold side temperature. The hot side was around 5º C higher than the cold side. The sample was heated from the bottom in a vacuum. The measurements were conducted at Queen Mary, University of London.

Chapter 4 Synthesis of $NaCo_2O_4$ ceramics

4.1 Powder production

A sodium cobalt oxide precursor was obtained by ball milling Na_2CO_3 and Co_3O_4 (1.1:2 molar ratio) in propan-2-ol followed by calcination at different temperatures and times using a heating ramp rate of 4 °C min^{-1}. The different treatments are in Table 7:

Table 7 The name of the materials used in this study up to date

Sample ID	**Calcination temperature [˚C]**	**Calcination time [h]**
P-800-4	800	4
P-800-6	800	6
P-800-12	800	12
P-850-4	850	4
P-850-6	850	6
P-850-12	850	12
P-900-4	900	4
P-900-6	900	6
P-900-12	900	12

4.2 Result and discussion

The prepared powders were analyzed in order to determine the purity of the calcination product. The results of XRD analysis are shown in Figure 26, Figure 27, Figure 28 showing a comparison of calcined powder for different times calcined at set-point temperatures of 800°C (Figure 26), 850°C (Figure 27) and 900°C (Figure 28), respectively. Under the influence of high temperature, transformations have occurred which led to well-crystallized structures. For comparison the XRD pattern of the starting powder before calcination is also shown.

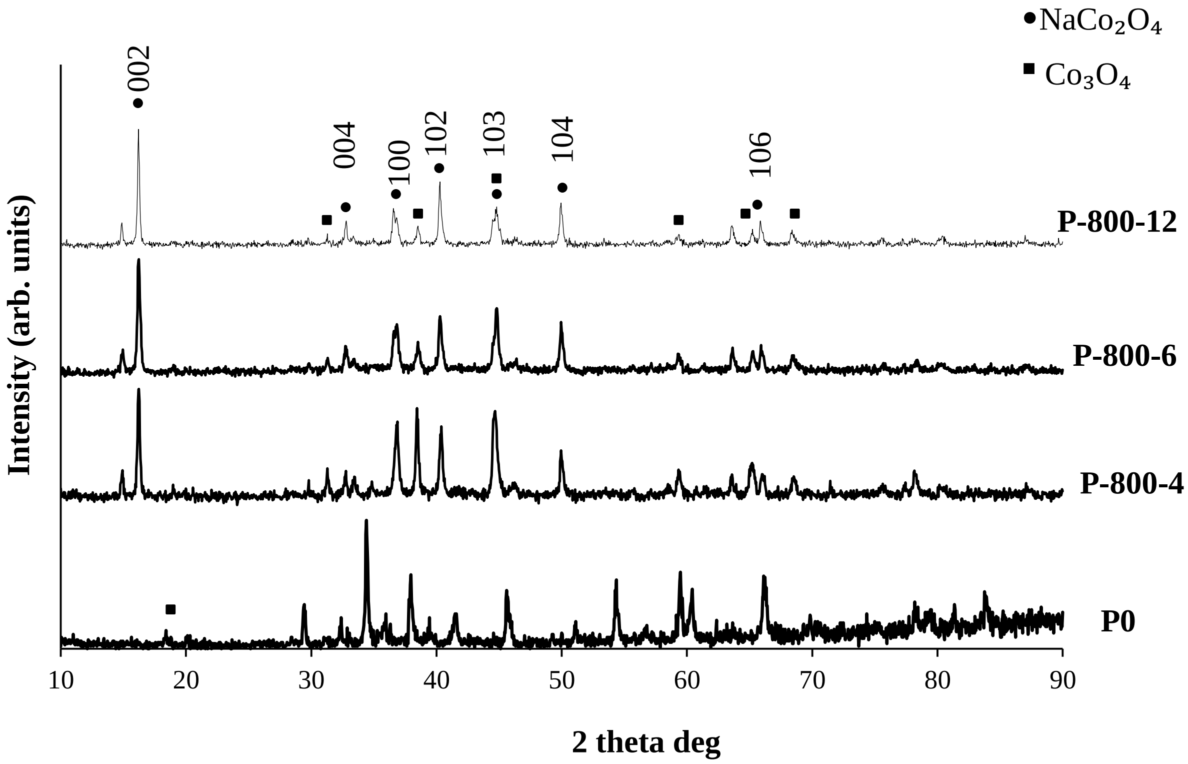

Figure 26 XRD spectrum of powders after 1st stage of calcination at 800°C for 4, 6 ,12 hours and reference powder after 1st ball milling.

The formation of a $NaCo_2O_4$ phase is visible and reveals the presence of characteristic peaks assigned to $NaCo_2O_4$ (JCPDF no.27 0682). In ambient atmosphere calcination of particles is additionally supported by oxygen partial pressure (pO_2). However, in powder calcined at 800°C additional peaks are visible which are identified with the phase Co_3O_4. The weak peak related to Co_3O_4 may suggest an unfinished reaction between Na and Co sources caused by the use of too low a temperature. At low temperatures the formation of $NaCo_2O_4$ is reported to be inhibited due the presence of CO_2 (byproduct) retarding the reduction of Co_3O_4[85].

From the XRD patterns it can be seen that with increased time of calcination the intensity of impurity peak decreases due to reduction of Co_3O_4 content.

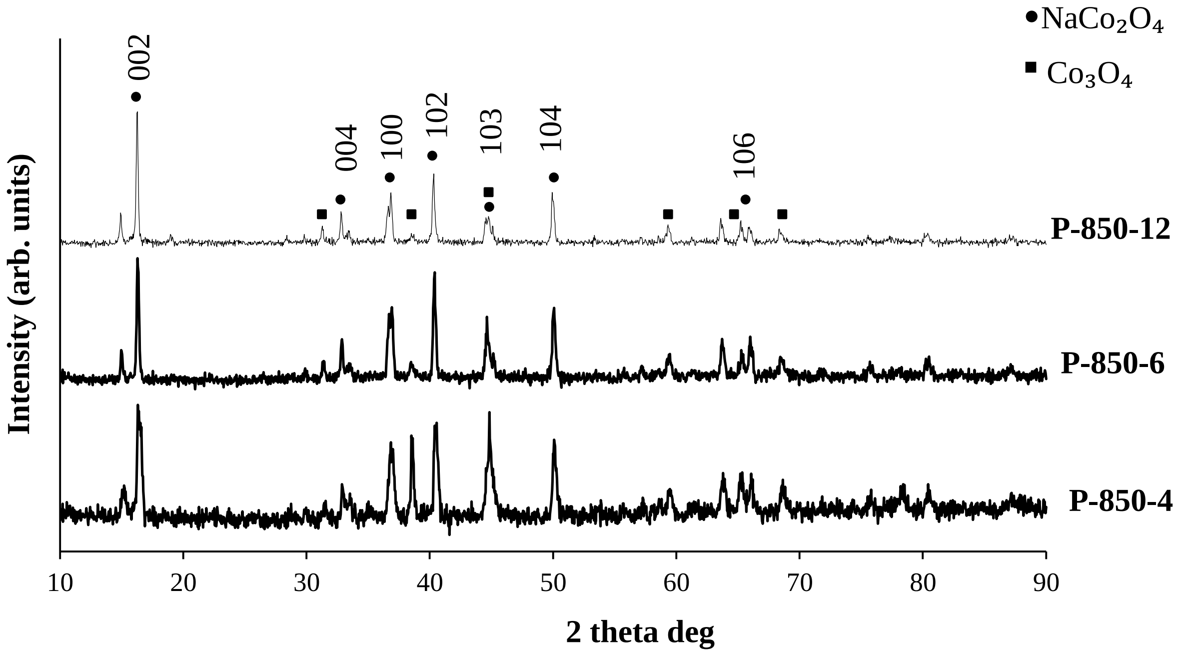

Figure 27 XRD patterns of the powders after 1st stage of calcination at 850°C of the 4,6, 12 hours.

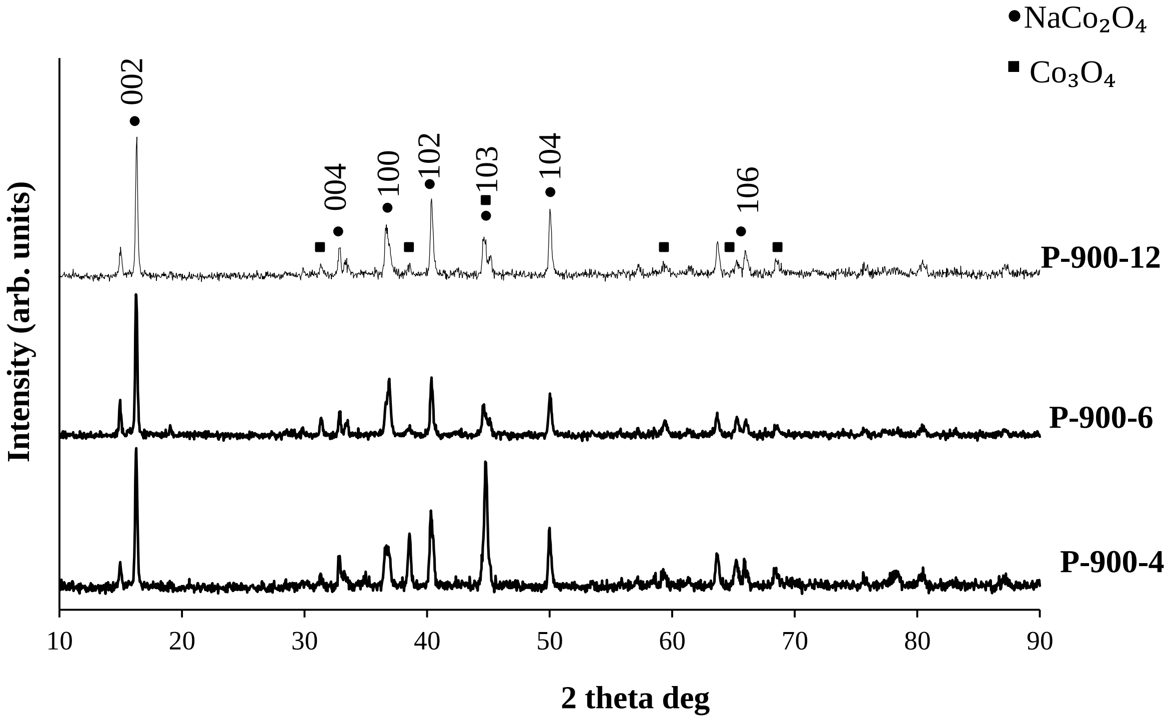

Figure 28 XRD patterns of the powders after 1st stage of calcination at 900°C of the 4,6, 12 hours.

Figure 29 shows SEM micrographs of the 9 powders after the 1st stage of calcination at different times and temperatures. Due to the long process time, single particles form aggregates. Increasing powder particle size is observed with increasing temperature as well as with an increases in the time of the process.

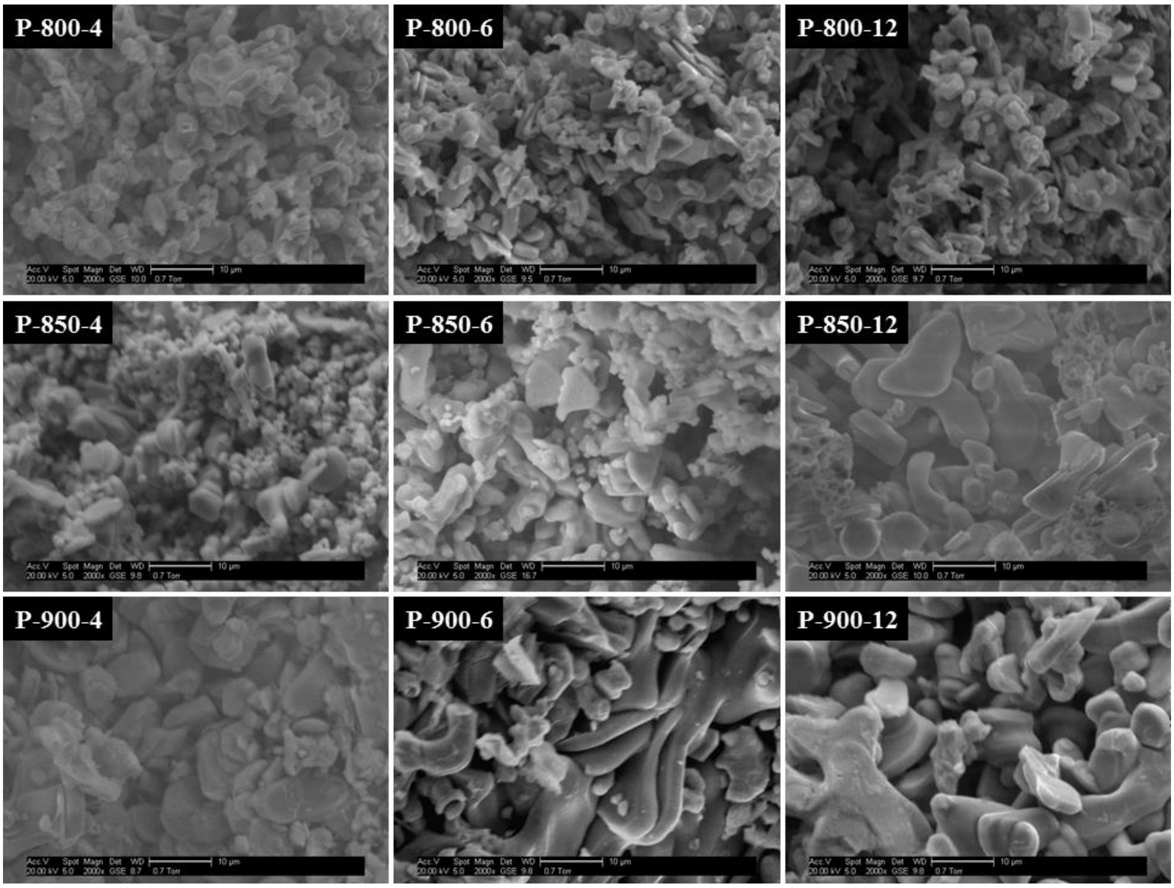

Figure 29 SEM micrographs of 9 powders after 1st stage of calcination at 800°C, 850°C 900°C for 4, 6 and 12hrs.

The size for powders calcined at 800°C was 4.9 µm, 5.5 µm and 6.1 µm for 4, 6, and 12 hours, respectively. Increasing the temperature by 50°C resulted in average calcined powder sizes of 5.1 µm, 5.6 µm and 9.3 µm. The particles size of powder calcined at 900°C were found to be around 9.5µm, 10.5 µm and 13.2 µm for powders as shown in Table 8 The increasing particle size during calcination is consistent with the general principles of the method of synthesis from solid state reaction.

Table 8 Average particles size of powder calcined at different temperature and time.

	4 hours	**6 hours**	**12ouhrs**
800°C	~4.9 µm	~5.5 µm	~6.1 µm
850°C	~5.1 µm	~5.6 µm	~9.3 µm
900°C	~9.5 µm	~10.5 µm	~13.2 µm

The temperature and time of calcination also had an effect on the chemical composition of the product. The EDX analysis performed on the powder calcined at different temperature and time are shown in Table 9.

Table 9 EDX analysis of powders calcined at different conditions, results in atomic % .

Sample ID	**Atomic% Na**	**Atomic% Co**
P-800-4	10.47	27.58
P-800-6	14.08	31.88
P-800-12	14.04	28.51
P-850-4	12.83	26.28
P-850-6	18.26	38.74
P-850-12	15.86	28.41
P-900-4	14.72	31.88
P-900-6	14.62	36.4
P-900-12	13.38	26.46

A satisfactorily pure $NaCo_2O_4$ phase, as well as stability of the Na content was achieved by calcinating at 850°C for 12 hours (Figure 30).

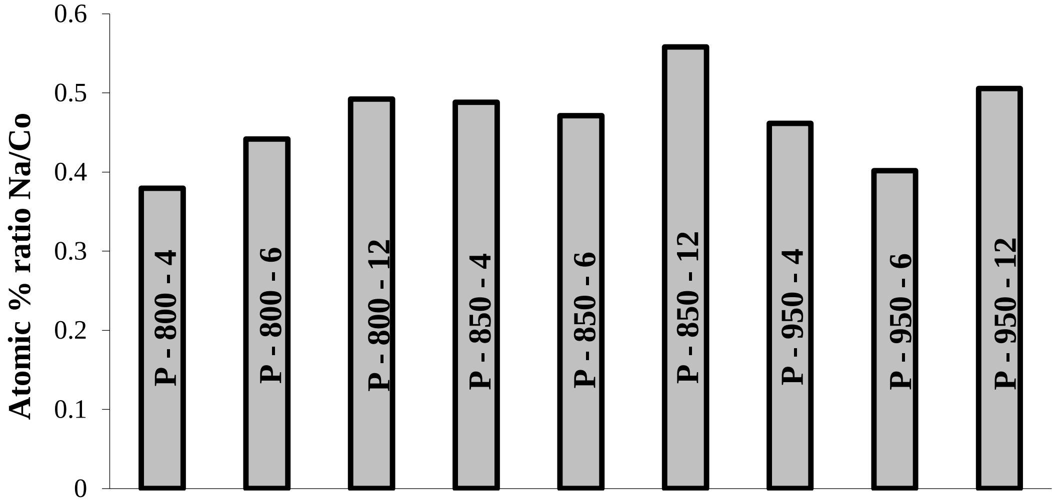

Figure 30 Atomic percentage ratio of Na/Co of EDX result from 9 of calcined powders.

4.3 Solid State Reaction pellets

4.3.1 Formation of pellets

Previously calcined powder was ball milled in propan-2-ol in order to increase the uniformity of grain size – breaking agglomerates. Subsequently the slurry was dried the powder compacted to produce pellets. After preparation of the pellets they were sintered at different temperatures between 950 - 1100°C with the heating ramp rate of 4°C min^{-1}. The increment in sintering temperature was 50°C and times used were 1, 2, 6 and 12 hours according to the schematic shown in Figure 31.

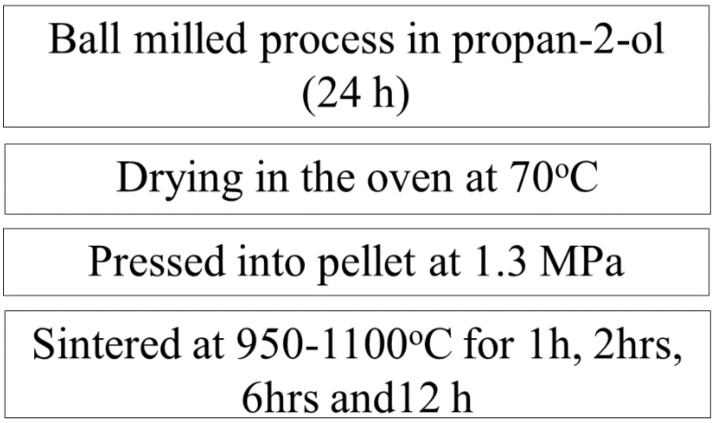

Figure 31 Schematic process of solid state reaction (SSR) pellets preparation after calcination of powder.

4.3.1.1 Results and discussion

The XRD patterns (Figure 32) show the presence of two phases: $NaCo_2O_4$ and Co_3O_4. A reduction in Co_3O_4 content with increasing sintering time can be seen. At higher temperatures the peaks corresponding to peaks $NaCo_2O_4$ are reduced in intensity. For the pellets sintered at 950°C peaks corresponding to the Co_3O_4 phase can be seen for each of test time examined. The Co_3O_4 phase disappears when pellets are sintered at 1000°C and after 12 hours sintering completely disappearance can be noted. At sintering temperatures of 1050°C after 12hours it can be noted that only one phase of $NaCo_2O_4$ is present. At temperatures 1100°C after 1h and 2 hours of sintering the $NaCo_2O_4$ phase is still visible. Longer sintering times at 1100°C causes melting of the pellets and as well as the loss significant amounts of sodium which is confirmed by the disappearance of the peaks corresponding to the phase of NaC_2O_4 on the XRD diffraction pattern.

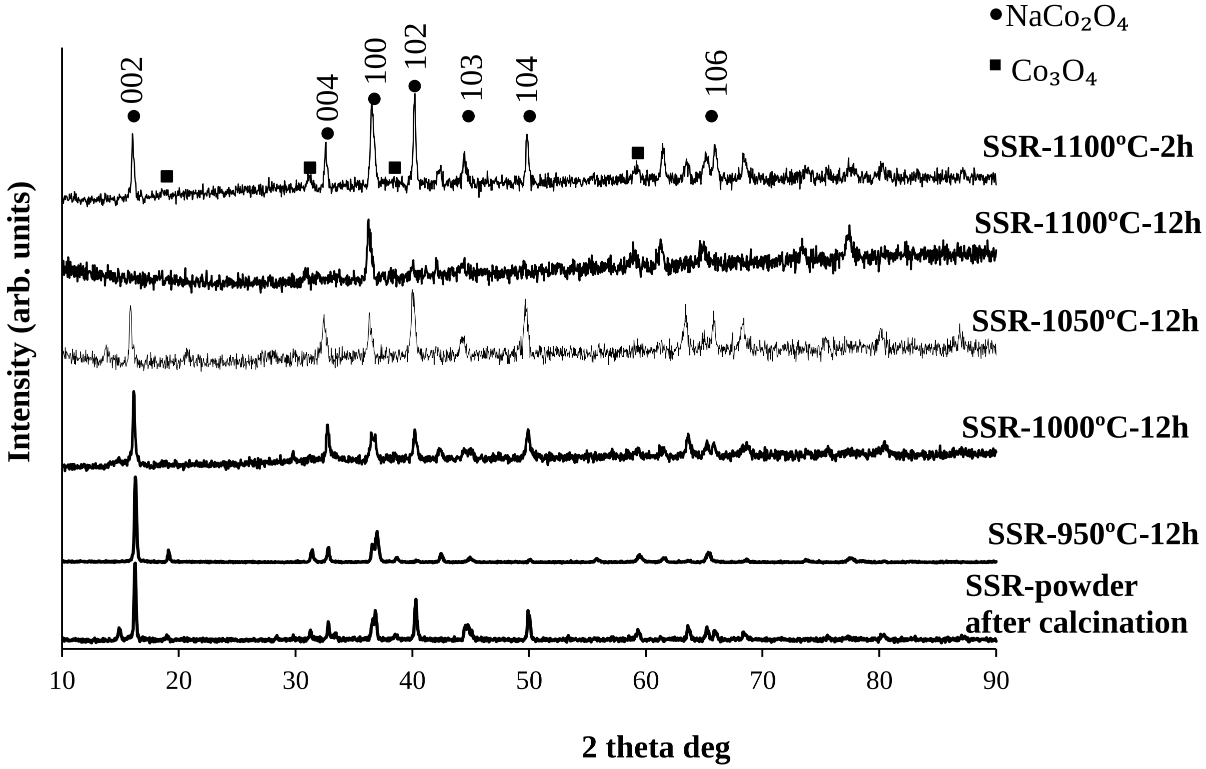

Figure 32 XRD patterns of SSR sintered pellets sintered at different temperatures and times.

EDX analysis indicates high purity of materials. A change in composition (Figure 33) also found with increasing temperature as well with increased sintering time.

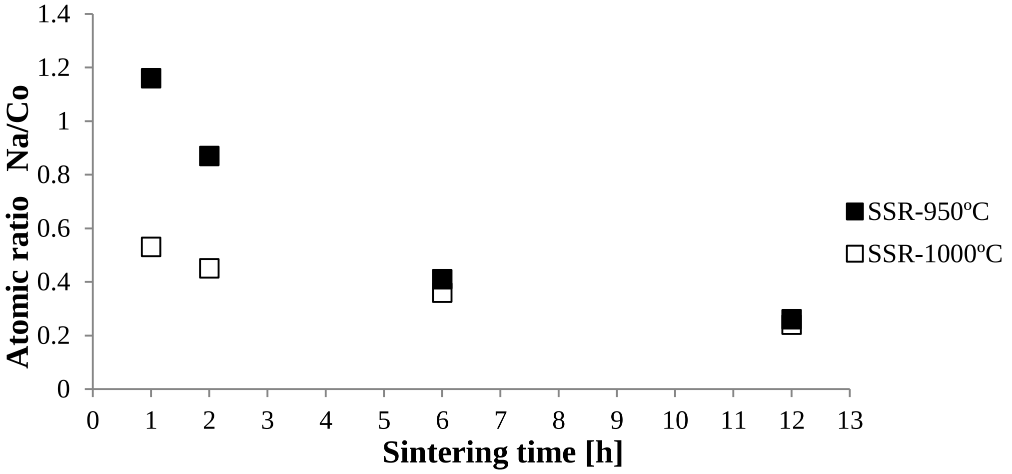

Figure 33 The dependence of Na/Co atomic% ratio on sintering duration and temperature for solid state reaction samples.

The samples show an increasing density with increased sintering temperature and processing time, especially evident at higher sintering temperatures (Figure 34). The increase of density is due to enhanced sintering of the ceramic, leading to increased mechanical strength.

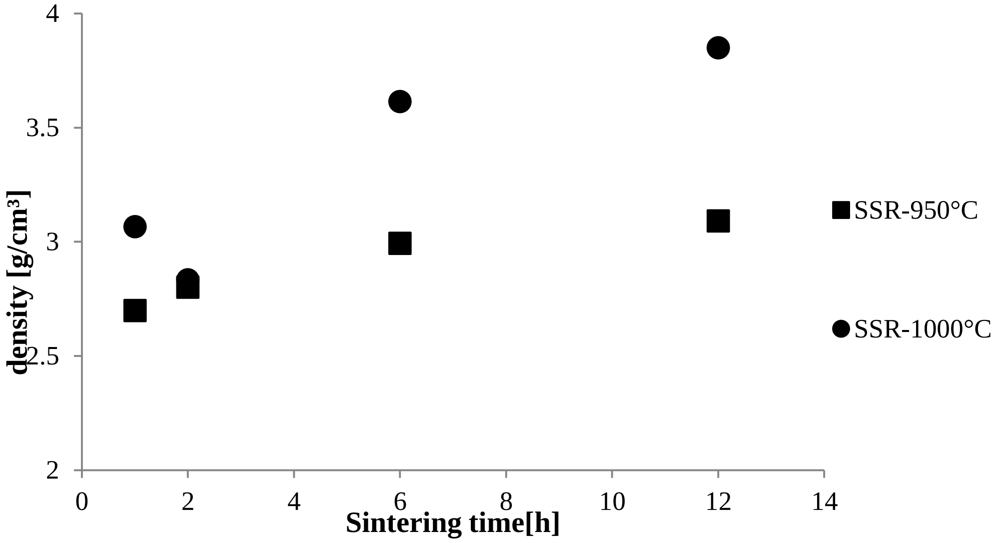

Figure 34 Evolution of density as a function of sintering time, temperature of solid state reaction pellets.

XRD data indicates that the unit cell dimensions are not changing significantly. Any density changes due to composition would be associated with relative changes in the levels of Na, Co and O. Such that loss of Na would lead to an increase in density due to the higher atomic mass of Co with respect to Na. The exact calculation of such a change is difficult due to the multivalent state of Co and the variability in oxygen content. At long sintering times the relative change in Na/Co levels is small while changes in density are large indicating that composition changes have a little effect on density. The changes in density can be seen in the micrographs shown in Figure 35. The absence of visible pores, as well as smooth, and dense surfaces sintered at 1050°C and 1100°C pellets could be an effect of a certain amount of liquid-phase created as a result of the high-temperature process.

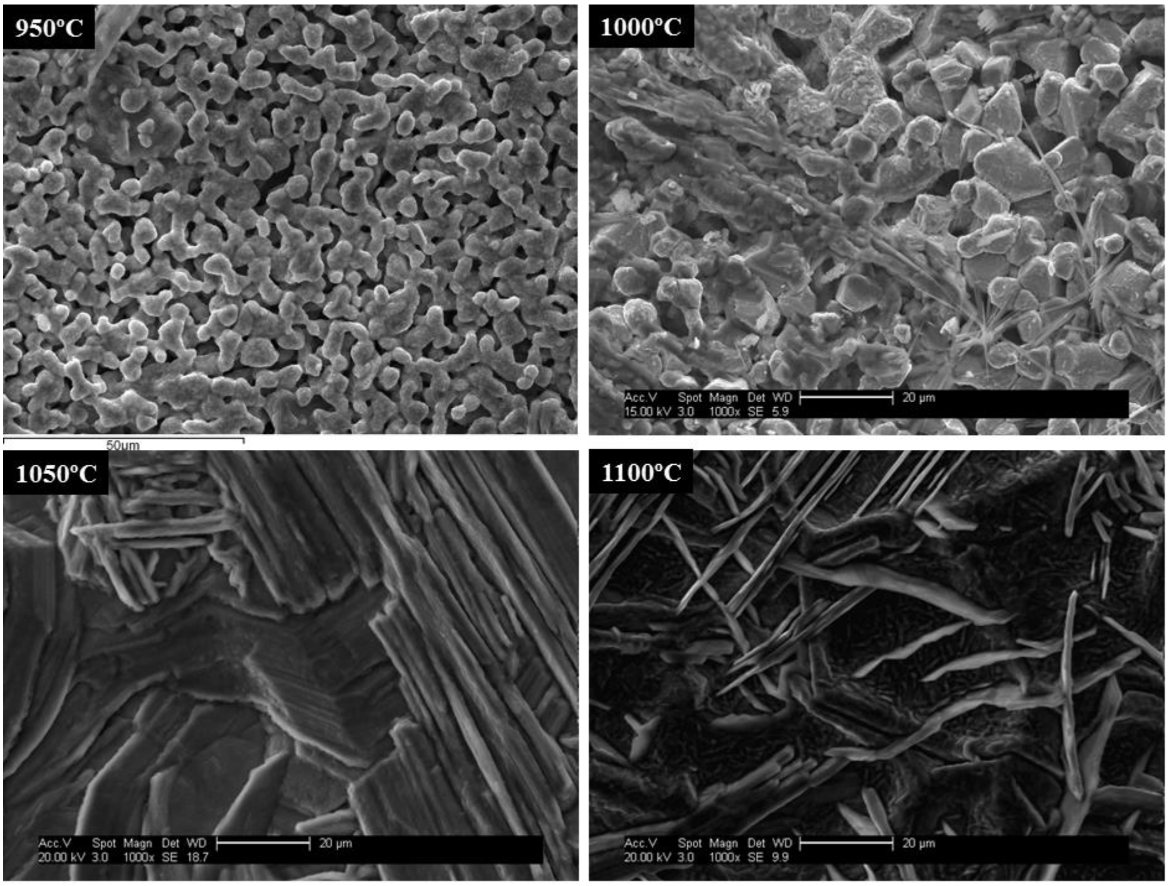

Figure 35 SEM micrographs of the surface of pellets sintered at 950 ºC, 1000ºC, 1050ºC and 1100ºC for 6 hours.

SFEG micrographs shown in Figure 36 shows the cross section of the pellets produced at different temperatures. Visible microstructural changes can be seen indicating atomic transport during the sintering. The atomic diffusion or material from inside the grain into the pores leads to the densification of the body.

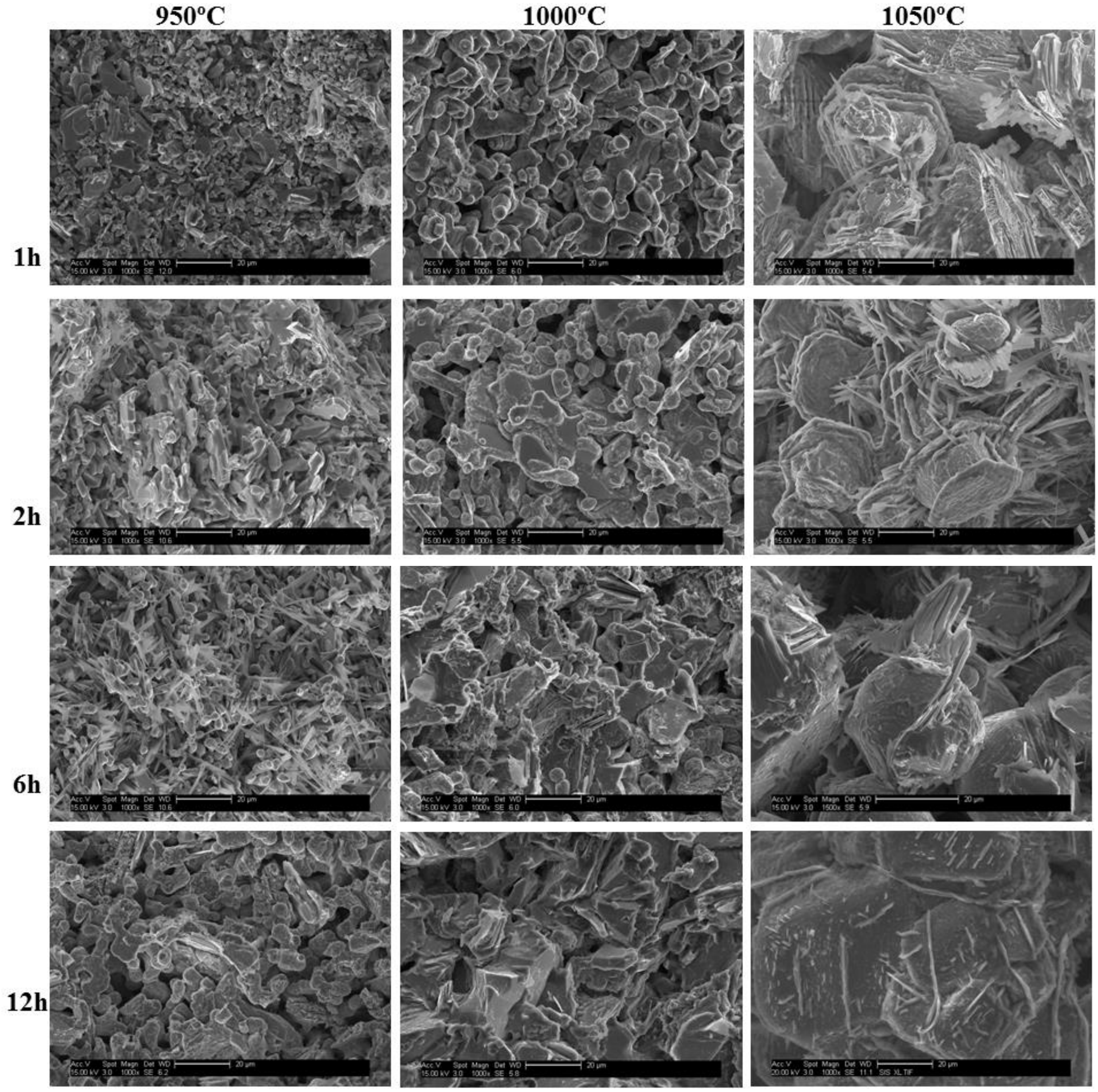

Figure 36 SFEG fracture of SSR pellets sintered at 950ºC, 1000ºC and 1050ºC for 1, 2, 6 and 12 hours.

The thermal conductivity of SSR pellets were evaluated at low temperatures in the range of 45°C - 80 °C. Then the value of thermal conductivity was determined by the Equation 23 and summarized in Figure 37.

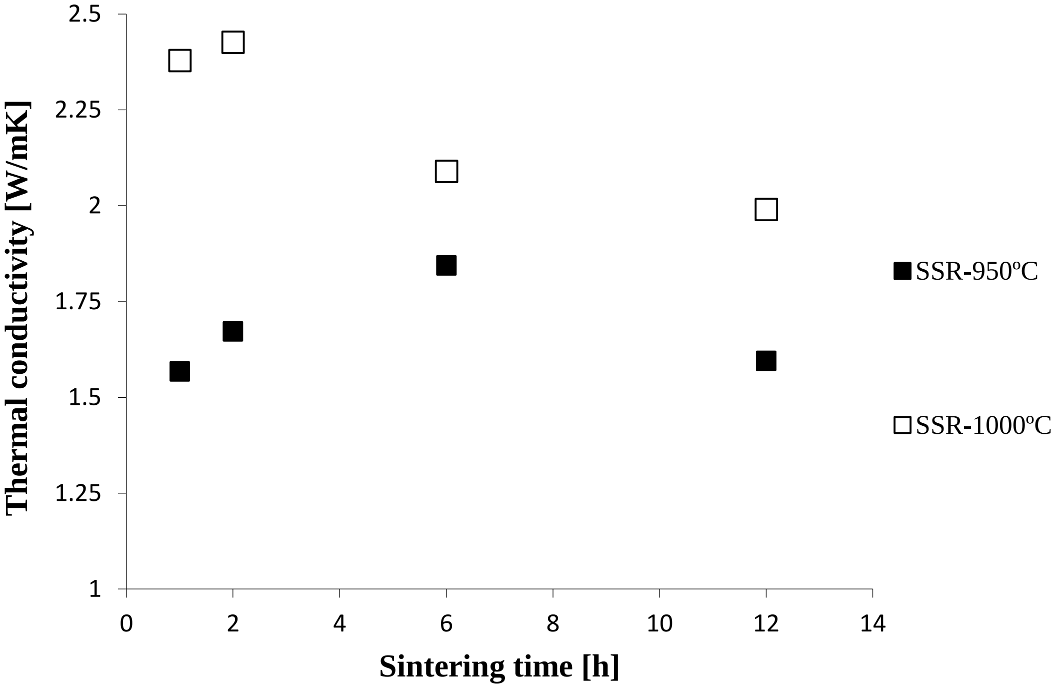

Figure 37 Average thermal conductivity for SSR pellets sintered under different conditions.

The thermal conductivity depends on temperature, for pellets sintered at 950°C, the results show lower levels of thermal conductivity which may be caused by an insufficient sintered porous body. Figure 38 shows the variation in Seebeck coefficient for the samples sintered at 950°C and 1000°C for 6 hours. In this small temperature range the Seebeck coefficient increased with increasing temperature confirming metallic behaviour of sintered pellets with the relatively low value of ~20 µV/K[157].

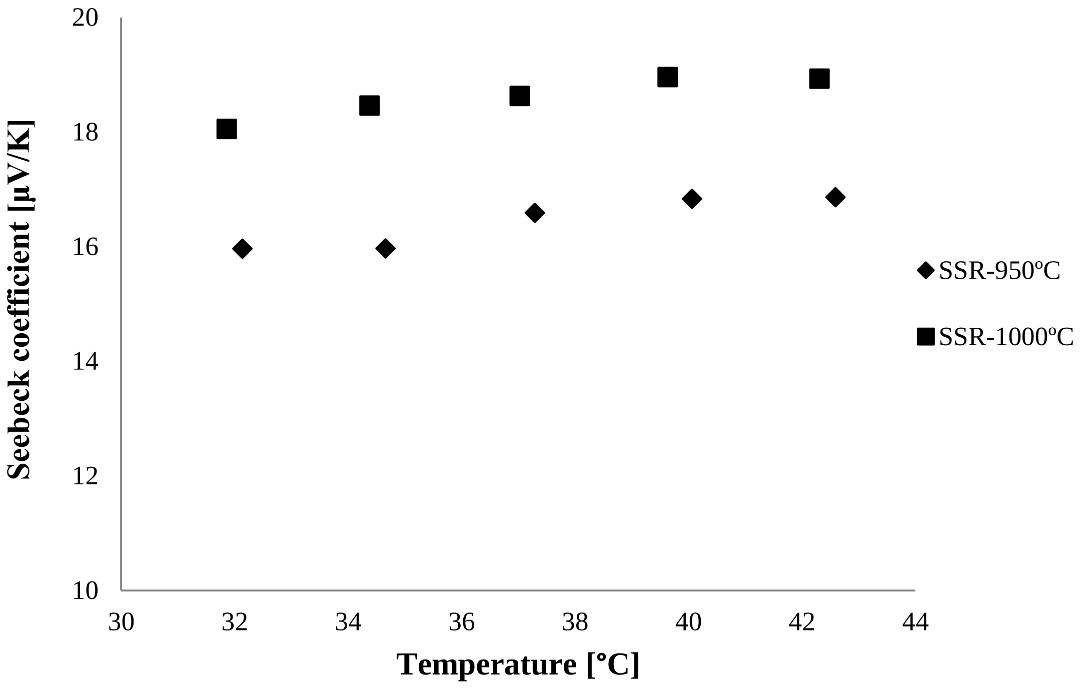

Figure 38 Seebeck coefficient obtained during measurement of SSR Pellets at lower temperatures between 45°C - 80°C.

Examples of obtained results from measurements on pellets calcined at 1000°C for 1 hour are shown in Table 10.

Table 10 Example of results obtained during measurement of Seebeck coefficient on SSR-1000-1h pellet.

dT (avg) K	Sample Temperature Cº	Seebeck-average (µV/K)	Avg voltage output (mV)
12.3	34.2	22.2	0.3
14.9	36.9	20.3	0.3
19.8	42.1	21.5	0.4
24.8	47.2	22.1	0.5
29.5	52.5	23.2	0.7
20.2	**42.6**	**21.9**	**0.4**

Electrical conductivity measured using four point probe technique also revealed slight differences between samples (Figure 39).

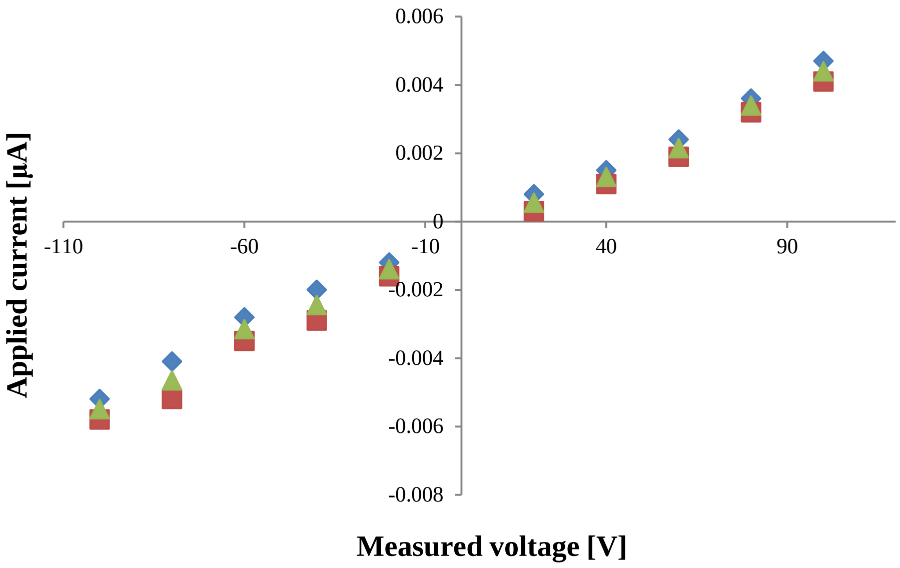

Figure 39 An example of results obtained from measurements carried out using the 4 point probe for pellets sintered at 950 C for 1 hour.

Electrical conductivity measurements in Figure 39 show a linear dependence between current and voltage. The electric conductivity slightly decreases with increasing sintering temperatures and times (Table 11).

Table 11 Measured electrical resistivity of infiltrated samples after sintering in various at 950°C and 1000°C for 1-12 hours. Error in measurements (+/-0.2)

Sintering temperature Sintering time	950°C	1000°C
1 hour	273 [μΩcm]	288 [μΩcm]
2 hours	267 [μΩcm]	283 [μΩcm]
6 hours	204 [μΩcm]	279 [μΩcm]
12 hours	271 [μΩcm]	285 [mΩcm]

A high temperature thermoelectric measurement was conducted on sample sintered at 1000 for 6 hours. The results are shown in Figure 40.

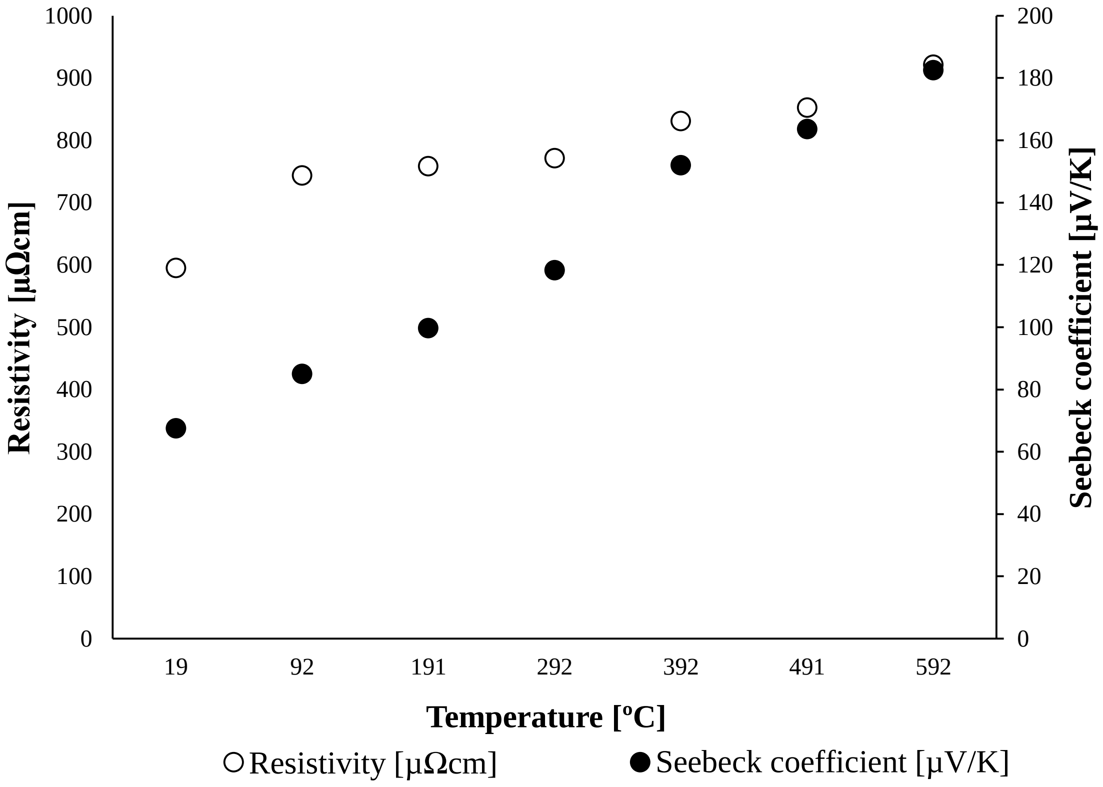

Figure 40 The temperature dependence of the electrical resistivity and Seebeck coefficient for the solid state reaction sample sintered at 1000ºC for 6 hours (SSR-1000-6).

The Seebeck coefficient shows linear dependence on temperature and tends to increase with increased temperature. The value was found to be ~70 μV/K at around 300K and increased up to 182 μV/K at around 860K. The electrical resistivity increases also with increased temperature at start point the value was found to be around 600 μΩcm and at 860K was increased to 920 μΩcm.

The thermoelectric figure of merit ZT was determined by the Equation 9. The value of ZT at around 300K was found to be $0.37 \cdot 10^{-2}$ and tends to increase with increase temperature the value of ZT for 350K was found to be $0.75 \cdot 10^{-2}$.

4.4 Summary

It was shown that sodium cobalt oxide could be obtained with a wide range of calcination temperatures with an increase in temperature leading to a more crystallized structure.

It was found that sintering at temperature > 900°C a well-crystallized phase of NaCo2O4 was obtained. Powder calcined at 850°C resulted in spherical grains with the size of ≤ 10 μm.

This study showed that ceramics that exhibited good thermoelectric behaviour, could be obtained through the use of high-temperatures and short sintering times. The maximum sintering temperature for this type of material is 1050°C. Increasing the sintering temperature up to 1100°C result in melting of the material.

Chapter 5 The sodium rich pre-treatment of $NaCo_2O_4$ ceramics

5.1 Introduction

Chapter 4 showed that loss of Na is a significant issue during processing of $NaCo_2O_4$. This chapter will examine routes to stabilize the level of Na during processing of $NaCo_2O_4$ through the use of Na-rich pretreatments.

Among the many thermoelectric materials sodium cobaltite still attracts attention because of is promising thermoelectric parameters. To produce usable thermoelectric materials powders need to be shaped and sintered to produce homogeneous bulk materials. The requirement of the sintering process is to bring about densification through high temperatures. However the use of high temperatures has a deleterious effect on composition due to the volatile nature of sodium. A number of Na rich pre-treatments are proposed to both compensate for sodium loss and reduce the sintering temperature. This chapter presents the results of three sodium rich pre-treatments: infiltration, mixing and ball milling. The general instruction of preparation of pellets was presented in experimental chapter of this thesis. As a reminder, each of the sections presenting new methods of Na rich pre-treatment has been preceded by a short preface, which shows the illustrated versions of the methods of introducing the additional amount of sodium.

5.2 Infiltration

5.2.1 Characterisation

5.2.1.1 XRD analysis

The sintered pellets were subjected to XRD analysis. Results are shown in Figure 41. The XRD pattern exhibited a strong diffraction peak from (002) planes for each of the sintered samples. The detected peaks indicate that a well-crystallized structure of sodium cobalt oxide is visible for each sintering temperatures. Increasing sintering temperature results in an increase in the relative intensity of the (100) peak which confirms observations described by Seetawan at al.[101]. However, a few diffraction peaks of unknown phase(s) can also be observed. The appearance of an extra phase(s) in the sample exposed to the long action of high temperature treatment could be explained by presence of energy which leads to higher reaction activity. The activity may result in side reactions and creation of additional phases.

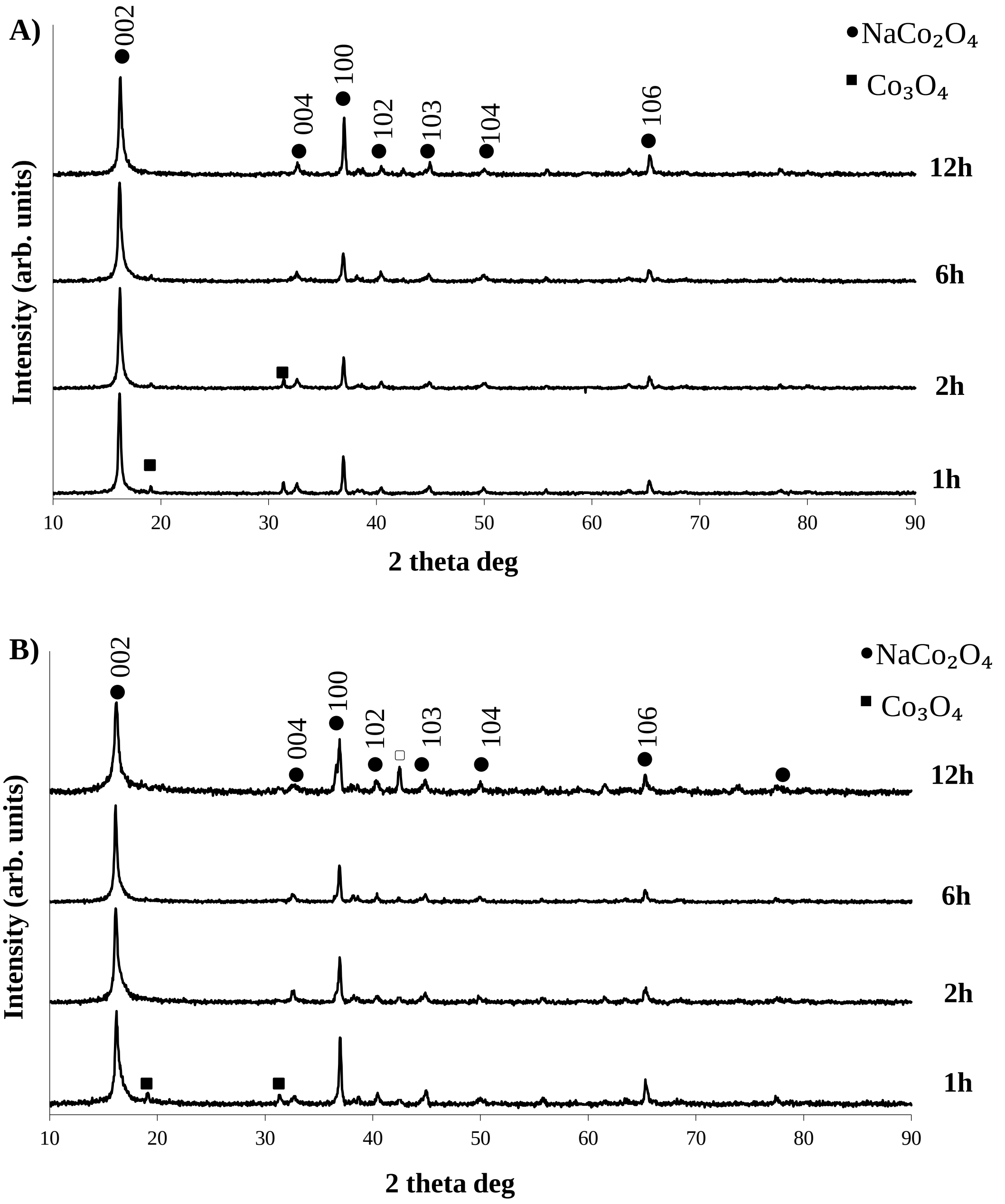

Figure 41 XRD patterns of the surface of pellets infiltrated with NaOH solution sintered at A) 950°C and B) 1000°C for 1, 2, 6 and 12 hours respectively. The empty square symbol corresponds to unidentified phase.

Comparing the XRD data to that of un-infiltrated $NaCo_2O_4$ (Figure 32) shows that infiltrated exhibit lower levels of Co_3O_4. It can be inferred that the increase of Na content enabled to creation of crystalline $NaCo_2O_4$ in a shorter period of time. It should be noted that rising the temperature to 1050°C resulted in the partial melting of pellets. At 1100°C visible pellet fusion/penetration of the substrate was observed (Figure 42).

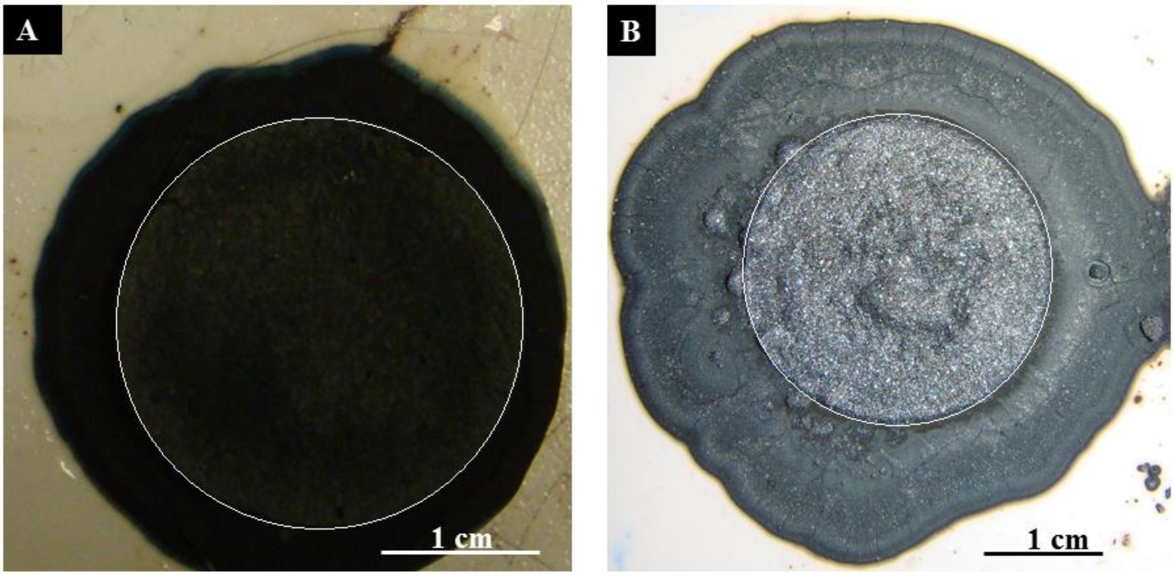

Figure 42 Images of melted NaOH solution infiltrated sample after sintering for 12 hours at A) 1050°C and B) 1100°C.

The addition of sodium hydroxide solution reduces the melting point of system such that full tests for pellets sintered at the highest temperatures (>1050°C) were not conducted because of the interaction with the substrate (Al_2O_3). The melting point was reduced due to the molten NaOH acting as a flux.

5.2.1.2 Microstructural analysis

The microstructure of pellets were observed using a SFEG electron microscope. Micrographs of pellet surfaces and cross-sections at various magnifications were analysed to determine the microstructural changes. Figure 43 presents the surface microstructure of infiltrated samples after sintering for 12 hours at 950°C, 1000°C and 1050°C, respectively. The high porosity and small grain size can be observed for samples sintered at 950ºC. Increasing the sintering temperature acts to lower the porosity.

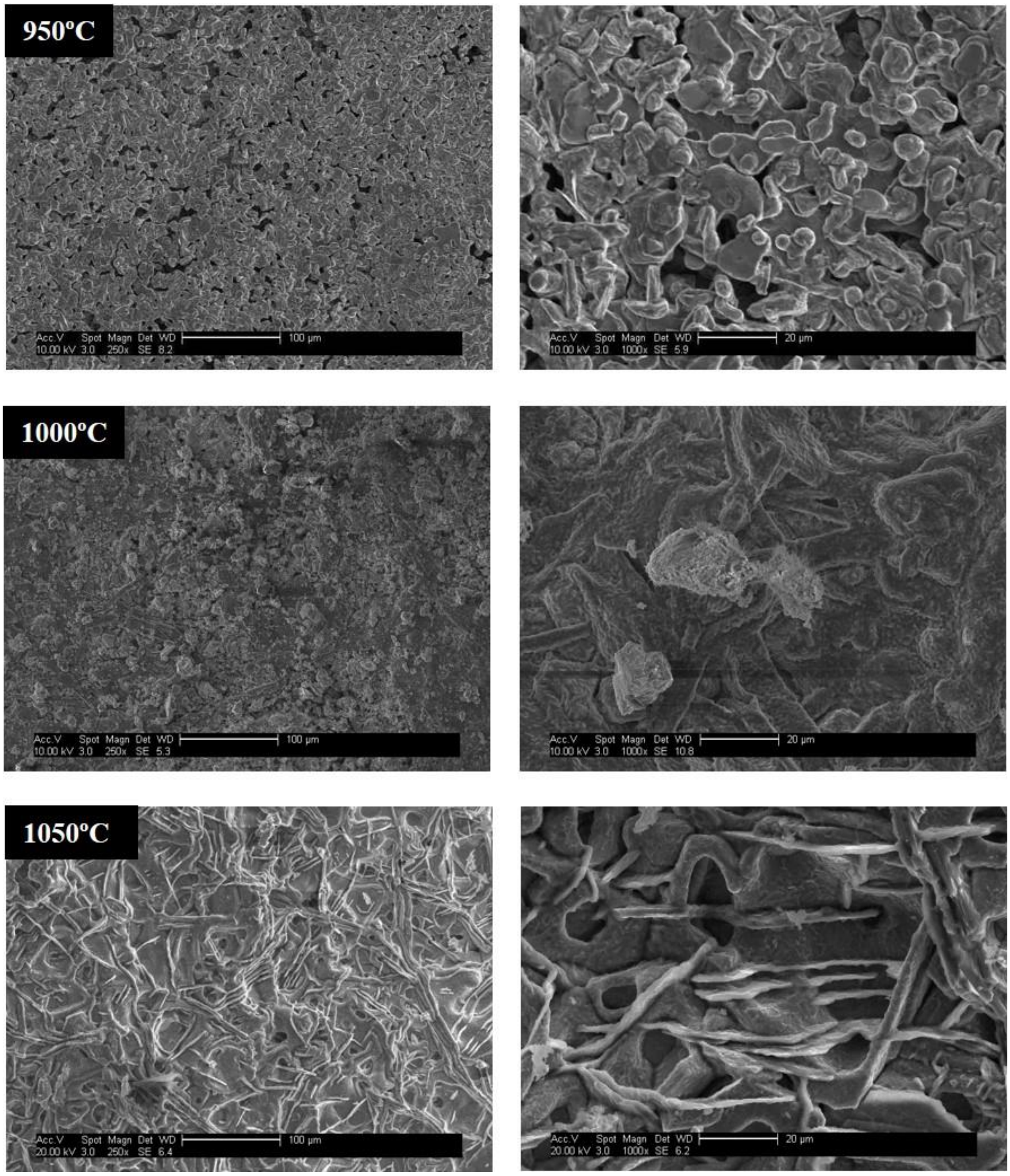

Figure 43 SEM micrographs showing the surface morphology of infiltrated (INF) pellets after sintering for 12 hours at: 950°C, 1000°C and 1050°C, respectively.

Densification is also noticeable on the cross sectional images of samples sintered for different times (Figure 44) where density increases with increased sintering time.

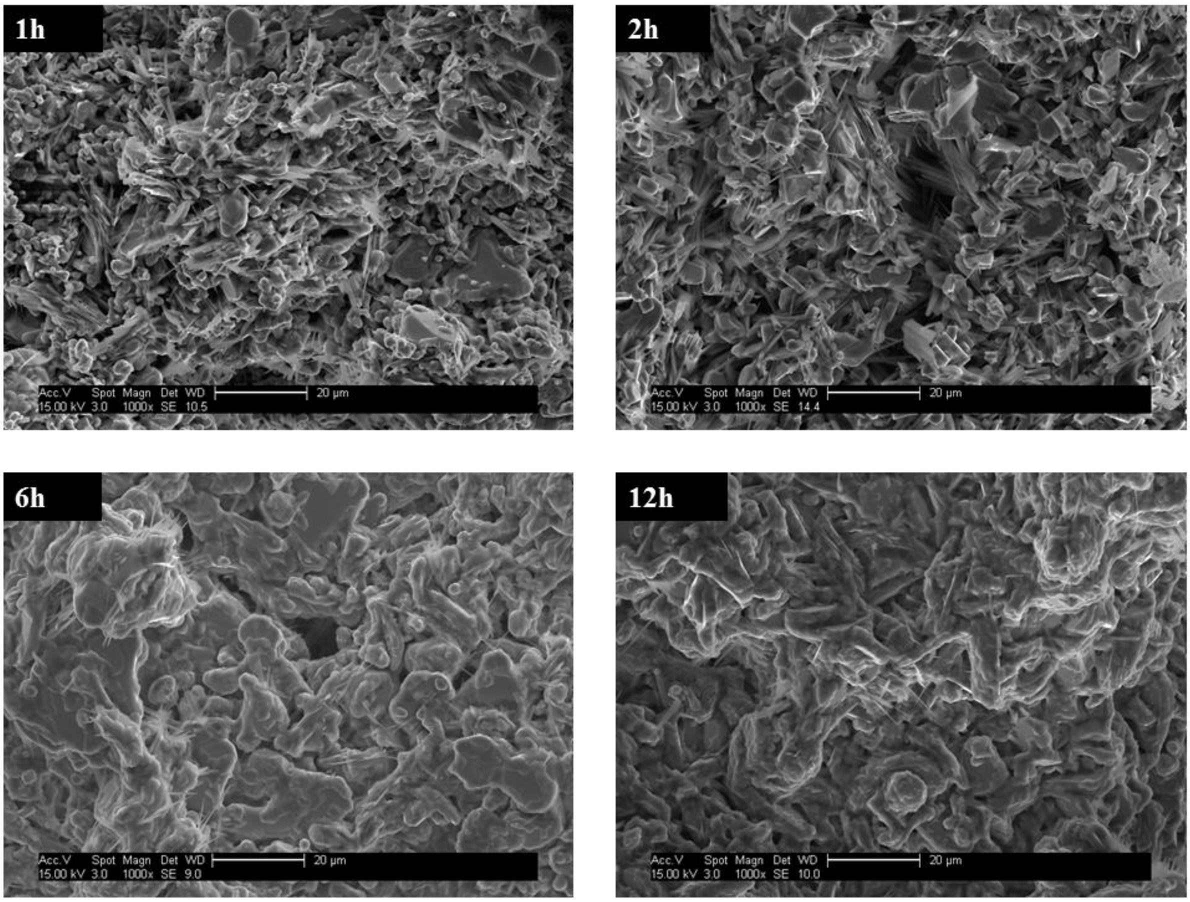

Figure 44 The cross sectional SFEG micrographs of infiltrated pellets sintered for 1, 2, 6 and 12 hours at 950°C.

At 950°C with increasing duration of sintering the particles merge to become aggregates. Figure 45 shows micrographs of pellets after different sintering times at 1000°C. It should be noted that the well-defined, plane-like grains were visible in all samples sintered at 1000ºC.

At temperatures above 1000°C the formation of hexagonal plate structures arranged forming tight rosettes or layered structures can be seen (Figure 46).

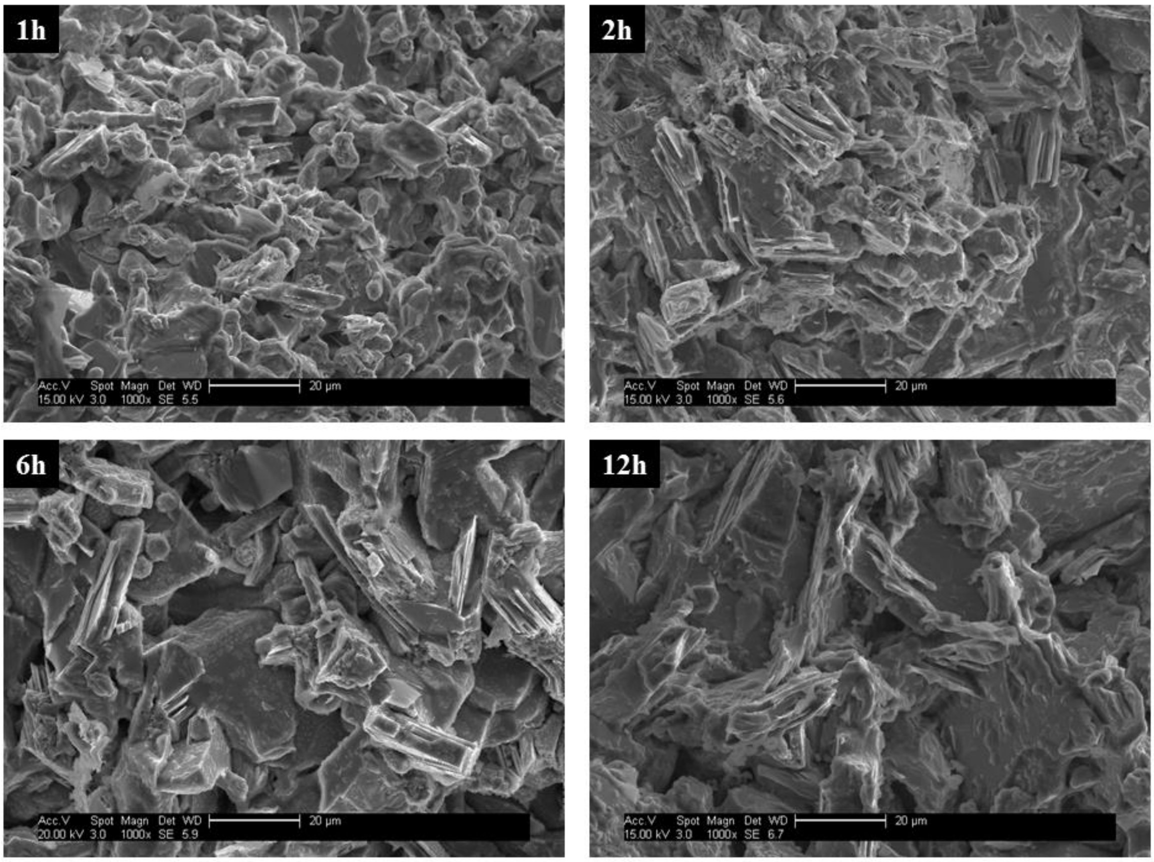

Figure 45 The cross section SFEG micrographs of infiltrated pellets sintered for 1, 2, 6 and 12 hours at 1000°C.

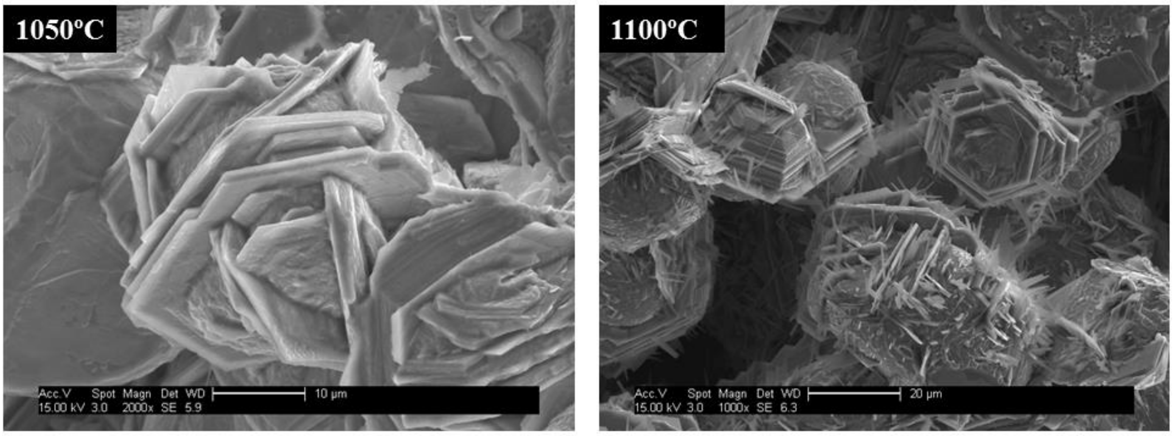

Figure 46 The cross section SFEG micrographs of infiltrated pellets sintered for 6 hours at 1050°C and 1100°C.

5.2.1.3 Density of samples

The measured densities of infiltrated samples sintered at various conditions are shown in Figure 47. Samples showed an increased density with increased sintering temperature and processing time, this was especially evident at higher sintering temperatures. It was found that the combination of SSR method and infiltration with an additional amount of sodium is useful for producing a dense sintered body. Without the infiltration process the maximum density (at room temperature) achieved was 3.84 g/cm^3 (Figure 34). The infiltrated samples, when compared with unpretreatment samples, were found to have densities up to 11% higher.

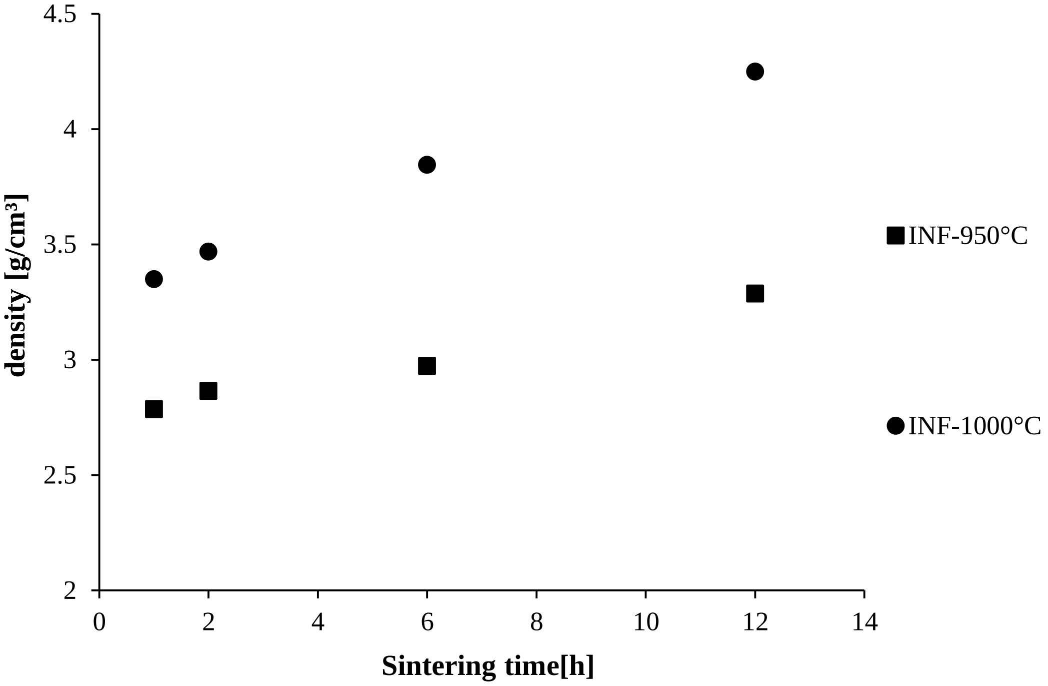

Figure 47 Evolution of density as a function of sintering time and temperature for NaOH pre-treatment infiltrated pellets.

5.2.2 Thermoelectric measurements at room temperature

5.2.2.1 Thermal conductivity

The thermal conductivity of samples sintered at 950°C and 1000°C were tested. Typical temperature readings obtained from the 4 thermocouples measurements are shown in Figure 48.

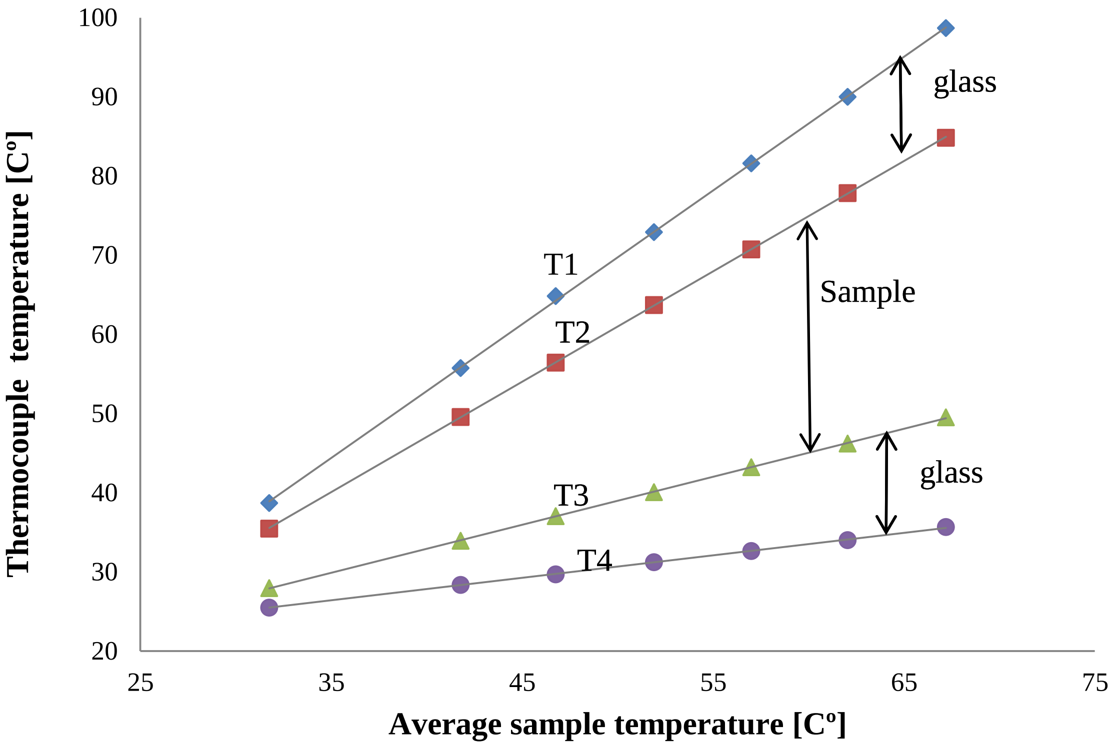

Figure 48 Example temperature measurements obtained from the 4 thermocouples during thermal conductivity measurements of infiltrated pellet sintered at 1000°C for 2 hours.

The linear increase of temperature in accordance with increasing set-point temperature: 45°C, 50°C, 60°C, 70°C and 80°C can be observed in graph (Figure 48). The calculated thermal conductivities for different samples are shown in Table 12. The results indicate that the thermal conductivity of the infiltrated samples was affected by both sintering time and sintering temperature.

Table 12 Thermal conductivity result for infiltrated samples sintered at 950°C and 1000°C**.**

Time and temperature of sintering **Set up temperature of measurements[°C]**	**Thermal conductivity κ[W/mK] (+/- 0.1)**							
	950 1h	**950 2hrs**	**950 6hrs**	**950 12hrs**	**1000 1h**	**1000 2hrs**	**1000 6hrs**	**1000 12hrs**
45	1.75	1.57	1.49	1.26	1.66	1.47	1.38	1.23
50	1.75	1.61	1.49	1.28	1.63	1.43	1.32	1.20
60	1.70	1.52	1.47	1.22	1.62	1.44	1.34	1.21
70	1.69	1.53	1.48	1.22	1.62	1.42	1.30	1.21
80	1.67	1.53	1.48	1.21	1.62	1.42	1.39	1.23

Thus the results indicate that lower thermal conductivity is achieved with higher density samples due to the creation of more interface structures with increasing of sintering temperature.

5.2.2.2 Electrical conductivity

The electrical conductivity tests were made using a four point probe. The electrical resistivities of infiltrated samples are shown in Table 13. An average electrical resistivity at room temperature for samples sintered at 950°C was found to be 307 μΩcm and for samples sintered at 1000°C was found to be 291 μΩcm.

Table 13 Measured electrical resistivity of infiltrated samples after sintering in various at 950°C and 1000°C for 1-12 hours. Error in measurements (+/-2)

Sintering temperature **Sintering time**	**950°C**	**1000°C**
1 hour	331 [μΩcm]	280 [μΩcm]
2 hours	312[μΩcm]	263 [μΩcm]
6 hours	283[μΩcm]	281 [μΩcm]
12 hours	301[μΩcm]	339 [μΩcm]

The results indicate that electrical conductivity increases with increasing density of pellets.

5.2.2.3 Seebeck coefficient

The Seebeck coefficients were measured at temperatures between 45°C - 80°C the two thermocouples record temperature at the cold and hot side of samples giving the temperatures difference. The measurements were performed through thickness under ambient cooling conditions. The Seebeck coefficient increases with increasing temperature difference across the samples as can be seen in Figure 49. The results indicate that the Seebeck coefficient was affected by sintering time and sintering temperatures. The Seebeck coefficient was found to be between 22-32 µV/K for samples sintered at 1000°C and 18-28 µV/K for samples sintered at 950°C.

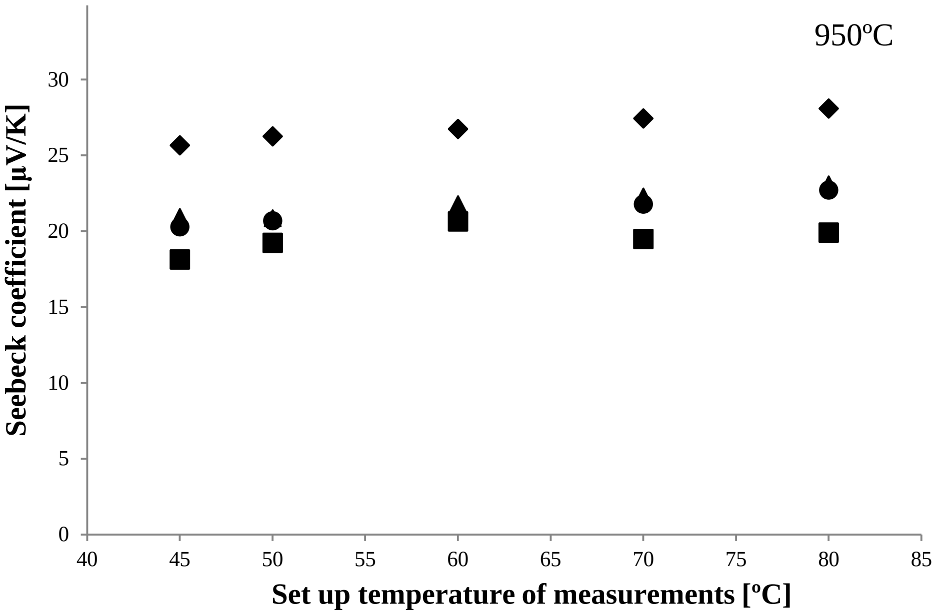

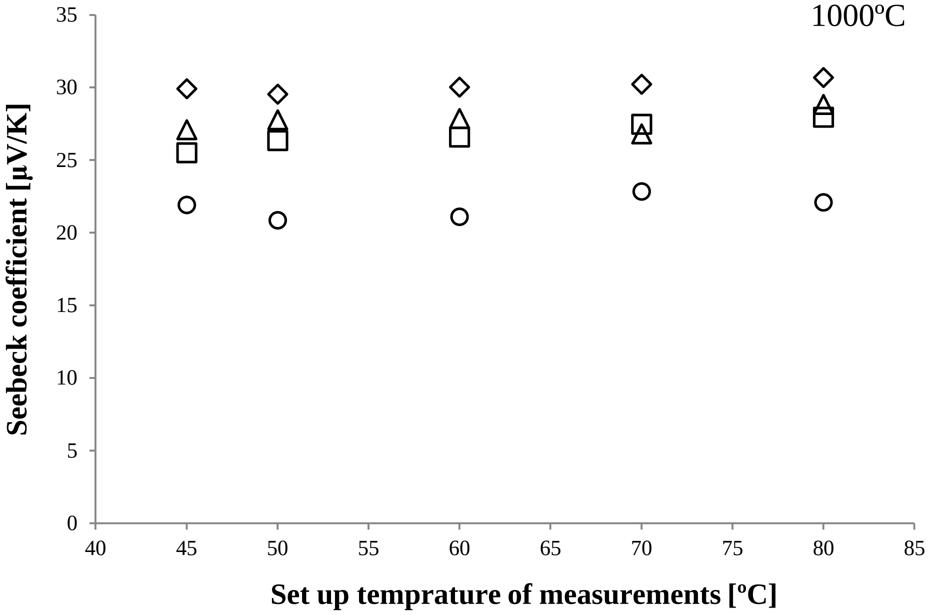

Figure 49 The Seebeck coefficient of infiltrated pre-treated $NaCo_xO_y$ pellets produced at 950°C and 1000°C.

5.2.3 Thermoelectric measurement at high temperature

For the study of thermoelectric properties at high temperatures, pellets sintered for 6 hours at 1000ºC were selected. The choice was based on the results obtained at low temperatures. Namely samples sintered at 1000ºC for 6 hours demonstrated relatively low electrical resistivity and thermal conductivity and are characterised by high measured density. High temperature measurements were conducted on in-plane direction of sample starting from room temperature. The electrical resistivity and Seebeck coefficient for the infiltrated pellet sintered at 1000ºC for 6 hours are shown on Figure 50.

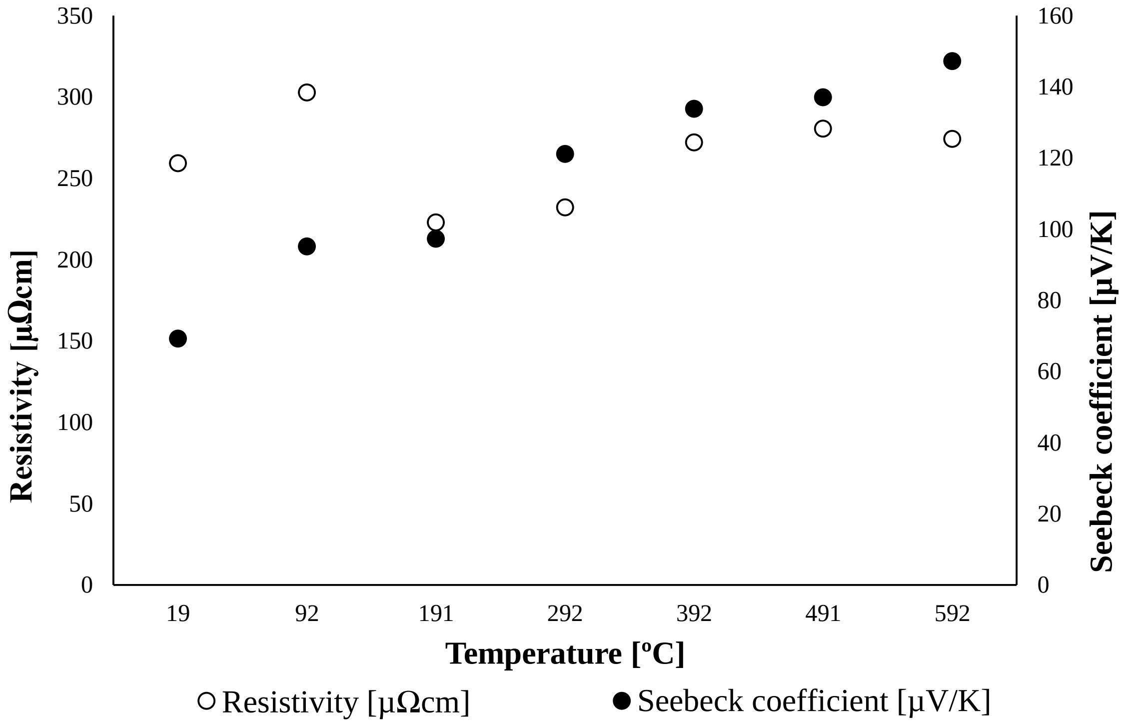

Figure 50 The temperature dependence of the electrical resistivity and Seebeck coefficient for the infiltrated sample sintered at 1000ºC for 6 hours (Inf-1000-6).

At low temperature, the lack of linearity of measurements can be noticed especially for electrical resistivity. This may suggest the presence of a partial hydrate phase due to storage of the sample under ambient conditions formed due to the absorption of water from air[164]. For temperatures above 200ºC a linear increase in electrical resistivity and Seebeck coefficient was observed. The value of the Seebeck coefficient is higher than reported in literature[158,100] which may suggest that the infiltration of the pellet with NaOH enhanced properties.

5.3 Mixing

5.3.1 Characterisation

5.3.1.1 XRD analysis

The XRD analysis of the sintered pellets is shown in Figure 51.

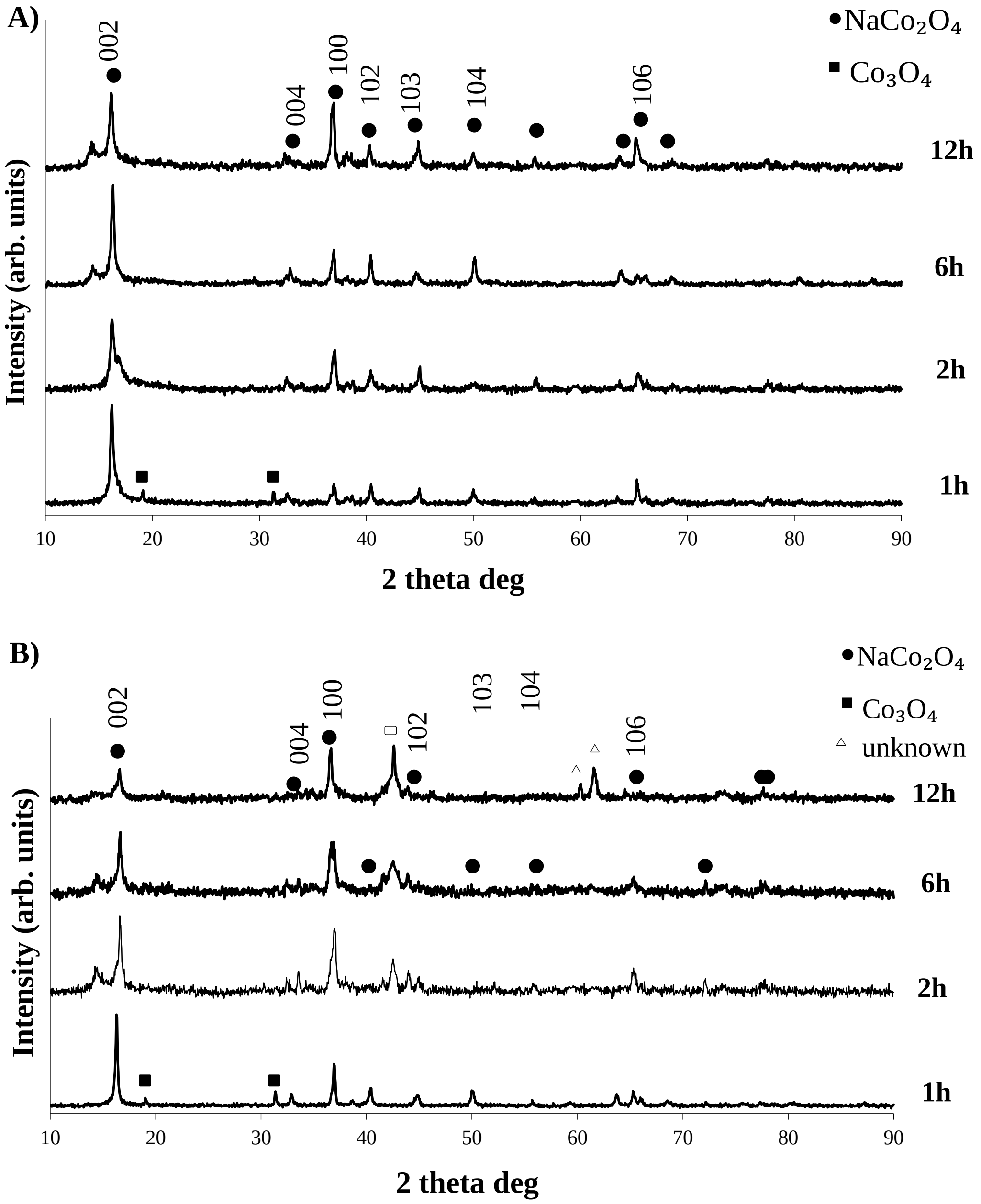

Figure 51 XRD patterns of mixed pellets sintered at A) 950°C and B) 1000°C for 1, 2, 6 and 12 hours, respectively. The empty square symbol corresponds to unknown phase.

In the mixed pellets a trace amount of Co_3O_4 phase, can be seen for pellets heat treated for 1 and 2 hours at 950°C. The evidence of weak peaks related to the mentioned Co_3O_4 phase can also be seen for pellets sintered at 1000°C for 1 and 2 hours. This evidence indicates that use of such short times may provide insufficient energy to drive the reaction entirely. Nevertheless, a well-crystallized structure of sodium cobalt oxide is visible for all samples. Peaks corresponding to the $NaCo_2O_4$ phase obtained after sintering at 1000°C for 12 hours were a changed intensity which can be attributed to the appearance of additional unknown peaks from possible side reactions.

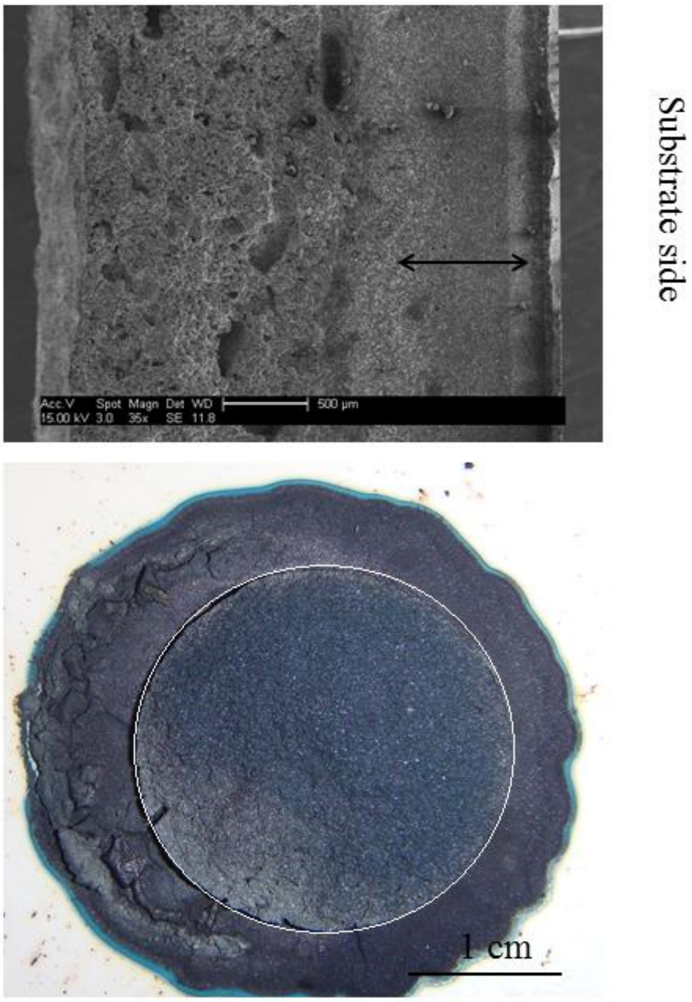

Figure 52 SEM micrograph of cross section of pellet with an arrow marking of diffusion area, photo of mixed pellet sintered at 1100°C for 6 hours.

The mixed pellets similar to infiltrated pellets, started to melt at temperatures above 1000°C as can be seen on Figure 52. Visible in the image is a blue border around the melted pellets suggesting the creation of a cobalt-aluminum spinel. The spinel is commonly known as Thenard's blue[159],[160] and is created around 1100°C. The EDX analysis confirms the diffusion of the elements and penetration into the substrate, the area where the Co, Na and Al elements were detected are marked with an arrow.

5.3.1.2 Microscopy analysis

Mixed pellets exhibit structural changes caused mostly by sintering temperature. It can be seen in Figure 53 that increases in sintering time result in the formation of various sizes and shapes of grains. The size and shape of grains becomes more uniform with increased sintering time.

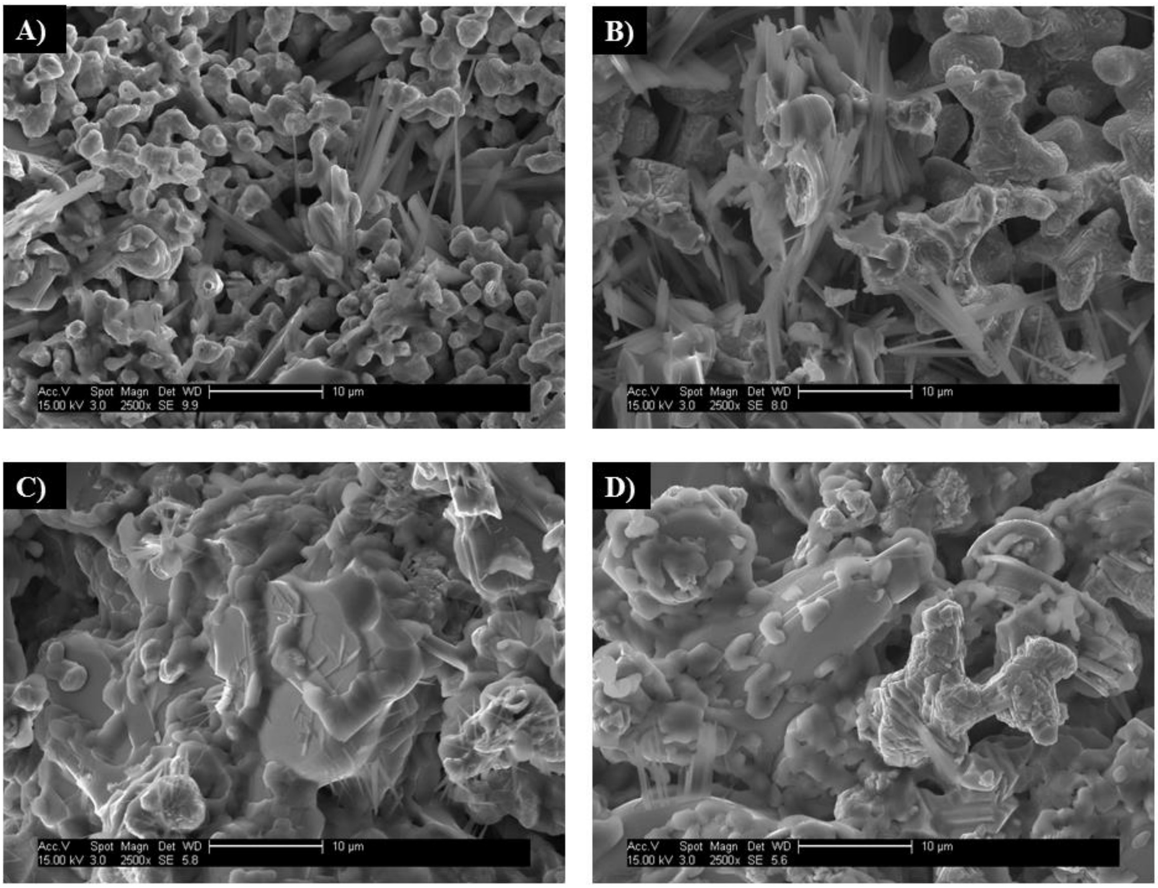

Figure 53 SFEG micrograph of mixed pellets sintered for A) 1 hour, B) 2 hours, C) 6 hours and D) 12 hours at 950°C.

The cross section of mixed samples shows the formation of compact structure and the aggregation of ovoid shapes covered with small forms in the shape of solidified droplets this is particularly evident after 1 hour as seen in Figure 54.

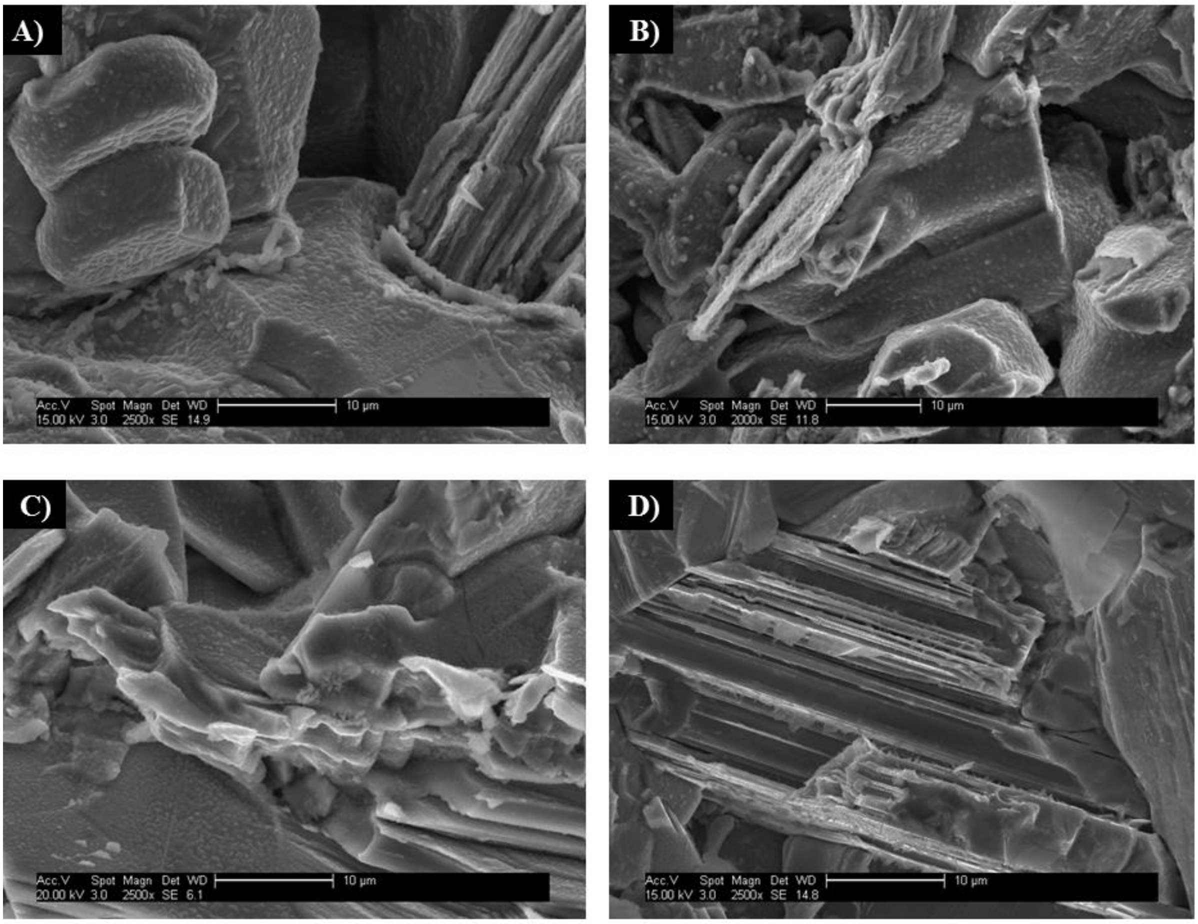

Figure 54 SFEG micrograph of mixed pellets sintered for A) 1 hour, B) 2 hours, C) 6 hours and D) 12 hours at 1000°C.

At higher temperatures the formation of extremely, precise shaped microstructure is apparent. Figure 55 shows typical example microstructure of pellets sintered at 1050°C for 2 and 6 hours respectively.

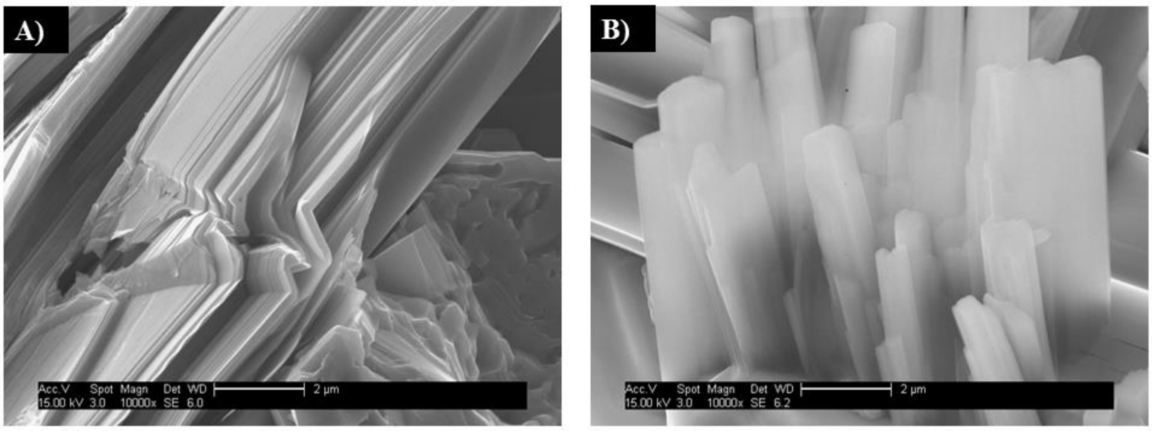

Figure 55 SFEG micrograph of mixed pellets sintered for A) 2 hours, B) 6 hours at 1050°C

5.3.1.3 Density of samples

The ceramic mixed samples containing higher levels of sodium show a measured density close to the theoretical density (4,6 g/cm^3)[161] in particular after sintering at the higher (1000ºC) temperature (Figure 56). That may indicate well-chosen parameters of sintering for this kind of Na rich pre-treatment.

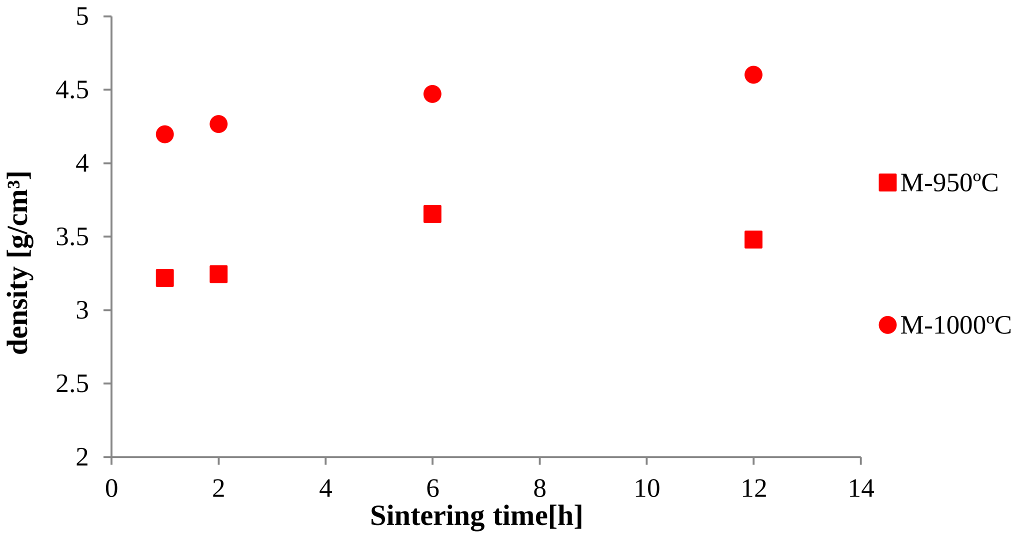

Figure 56 Evolution of density as a function of sintering time, temperature for NaOH pre-treatment infiltrated pellets.

Similarly to the infiltrated pellets, the density increases with increased sintering time and temperature.

5.3.2 Room temperature measurements

5.3.2.1 Thermal conductivity

Thermal conductivity was measured at low temperatures between 45 - 80ºC. The results obtained for mixed samples sintered in different conditions are presented in Table 14.

Table 14 Thermal conductivity of mixed samples sintered at 950°C and 1000°C for different period of time.

Time and temperature of sintering **Set up temperature of measurements[ºC]**	**Thermal conductivity κ[W/mK] (+/- 0.1)**							
	950 1h	**950 2hrs**	**950 6hrs**	**950 12hrs**	**1000 1h**	**1000 2hrs**	**1000 6hrs**	**1000 12hrs**
45	1.6	2.0	2.0	1.8	2.3	2.0	1.8	1.4
50	2.2	1.9	1.7	1.5	2.1	1.8	1.6	1.3
60	2.1	2.0	1.6	1.6	2.1	1.8	1.5	1.3
70	2.3	1.8	1.8	1.7	2.3	1.7	1.5	1.2
80	1.9	1.8	1.7	1.6	2.1	1.8	1.6	1.3

From the results can be seen that the longest sintering time results in the lowest values of thermal conductivity. Decreasing thermal conductivity can be attributed to structural changes of material. With increasing temperature and time of sintering the samples become denser and the formation of multi-interfaces was observed. The creation of plane like grains may also improve thermoelectric properties. On the other hand the formation of unknown phases may also have an impact on lowering thermal conductivity. Samples sintered at 1000°C for 12 hours exhibited lowest value of κ.

5.3.2.2 Electrical resistivity

The measured electrical resistivity is presented in Table 15. The average electrical resistivity was found to be 261 μΩcm for samples sintered at 950°C and 293 μΩcm for samples sintered at 1000°C.

Table 15. Measured electrical resistivity of mixed samples after sintering in various at 950°C and 1000°C for 1-12 hours. Error in measurements (+/-2)

Sintering temperature **Sintering time**	**950°C**	**1000°C**
1 hour	291 [μΩcm]	272 [μΩcm]
2 hours	299 [μΩcm]	257 [μΩcm]
6 hours	211 [μΩcm]	298 [μΩcm]
12hours	245 [μΩcm]	345 [μΩcm]

The result show that the pellets sintered at low temperatures and for long time exhibit reduced electrical resistivity. Enhanced densification results in slightly increased electrical resistivity.

5.3.2.3 Seebeck coefficient

Table 16 presents the average value of out-of-plane Seebeck coefficient measurements carried out at between 45°C and 80°C. All materials produced a positive Seebeck coefficient that confirming p-type behaviour.

Table 16 Average value of Seebeck coefficient obtained on mixed pellet in plane direction, testes at between 45-80°C.

Sintering temperature **Sintering time**	**Seebeck coefficient [µV/K]** **(+/- 0.1)**	
	950°C	**1000°C**
1 hour	21.44	18.78
2 hours	19.06	19.73
6 hours	19.43	20.65
12 hours	20.64	17.23

For samples sintered at higher temperatures EDX analysis detected trace amounts of Si which probably had an effect on lowering the value of Seebeck coefficient, according to the results obtained for pellet sintered at 1000°C for 12 hours.

5.3.3 Thermoelectric measurements at high temperature

The electrical resistivity and Seebeck coefficient as a function of temperature for mixed pellets sintered at 1000°C for 6 hours (M-1000-6) sample is shown in Figure 57.

The in plane electrical resistivity was found to be ~600 µΩcm at low temperatures (~20°C) and at high temperatures at around 600°C reached value of ~400 µΩcm. Similar to the infiltrated pellet, the Na rich pre-treatment tends to maintain the value of electrical resistivity at a constant level with varying temperatures. The Seebeck coefficient of the M-1000-6 pellet increased with increasing temperature.

This trend is characteristic for sodium cobalt oxide which metallic behaviour, what indicates higher Na content. It should be noted that the value of Seebeck coefficient was found to be higher than presented in literature for conventional SSR samples.

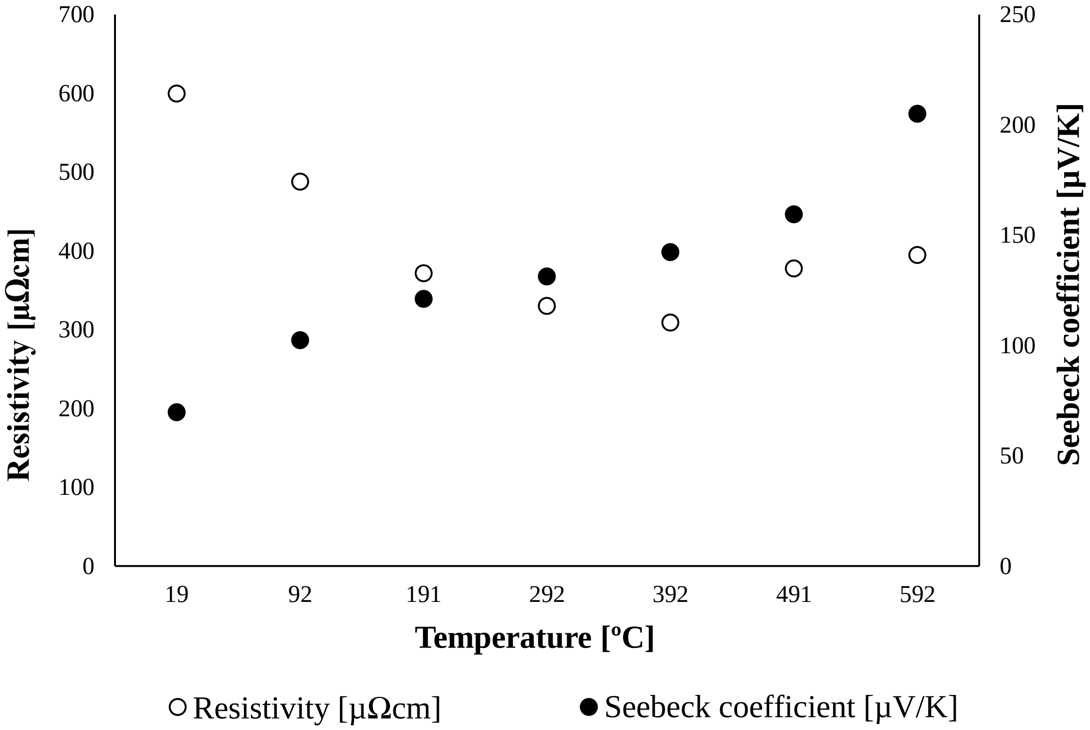

Figure 57 Temperature dependence of the electrical resistivity and Seebeck coefficient for mixed sample sintered at 1000°C for 6 hours (M-1000-6).

Starting from a value of ~70 μV/K which is comparable to literature at low temperature[90] and increases up above 200 μV/K at 800K. The Na rich pre-treatment used in this work appears to have enhanced the Seebeck coefficient of $NaCo_2O_4$ pellets by 38% when compared to literature[90].

5.4 Ball Milled

5.4.1 Characterisation

5.4.1.1 XRD analysis

The XRD analysis of the sintered pellets is shown in Figure 58. The presence of additional peaks indicated the presence of two phases $NaCo_2O_4$ and Co_3O_4 for samples sintered at 950°C for 1 and 2 hours (Figure 21).

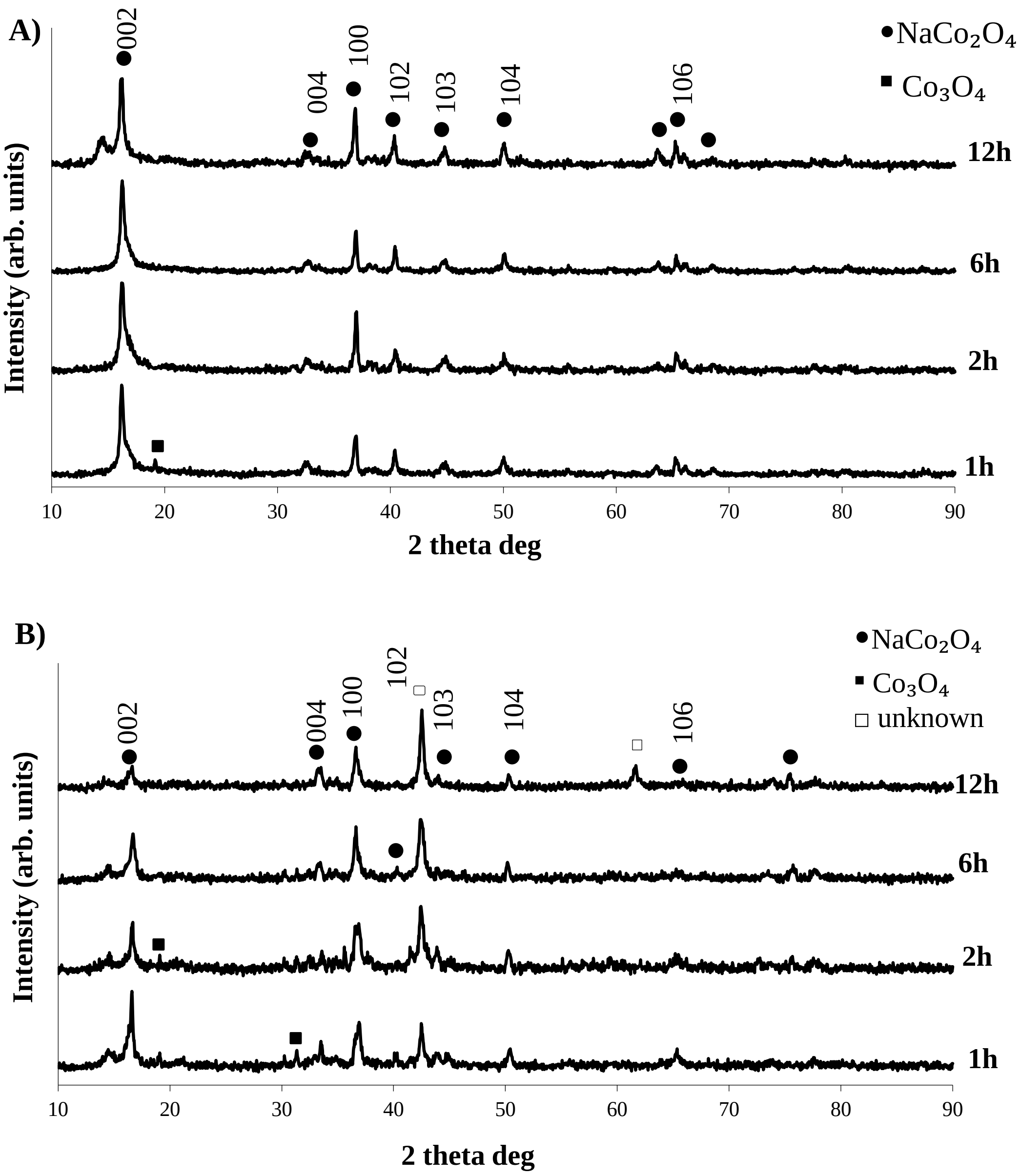

Figure 58 XRD patterns of ball milled pellets sintered at A) 950°C and B) 1000°C for 1, 2, 6 and 12 hours respectively. The empty square symbol corresponds to unknown phase.

It was found that the diffraction patterns also show coexistence of two phases for samples sintered at 1000°C for the longest time. The peak at around 42 theta degrees is characteristic of sodium cobalt oxide with high sodium content. This can suggest the diffusion (probably together with partial melting of Na_xCoO_{2-y}) of atoms and creation of unknown phase as a result of prolonged exposure to high temperatures.

The detected peaks below 15 degrees may suggest partial hydration of Na_xCoO_{2-y} phase which was previously reported by Lin et al.[164] for samples stored under ambient conditions.

5.4.1.2 Microscopy analysis

Microstructure evolution of the sample due to heat treatment was examined by the scanning electron microscopy. The most diverse internal structure is visible for ball milled pellets at the nano and micro scale. Increases in sintering times at 950°C result in the growth of spiky crystal structures which reached the size of a few micrometers. However, in all samples sintered at 950°C the compact forms of aggregates are visible (Figure 59).

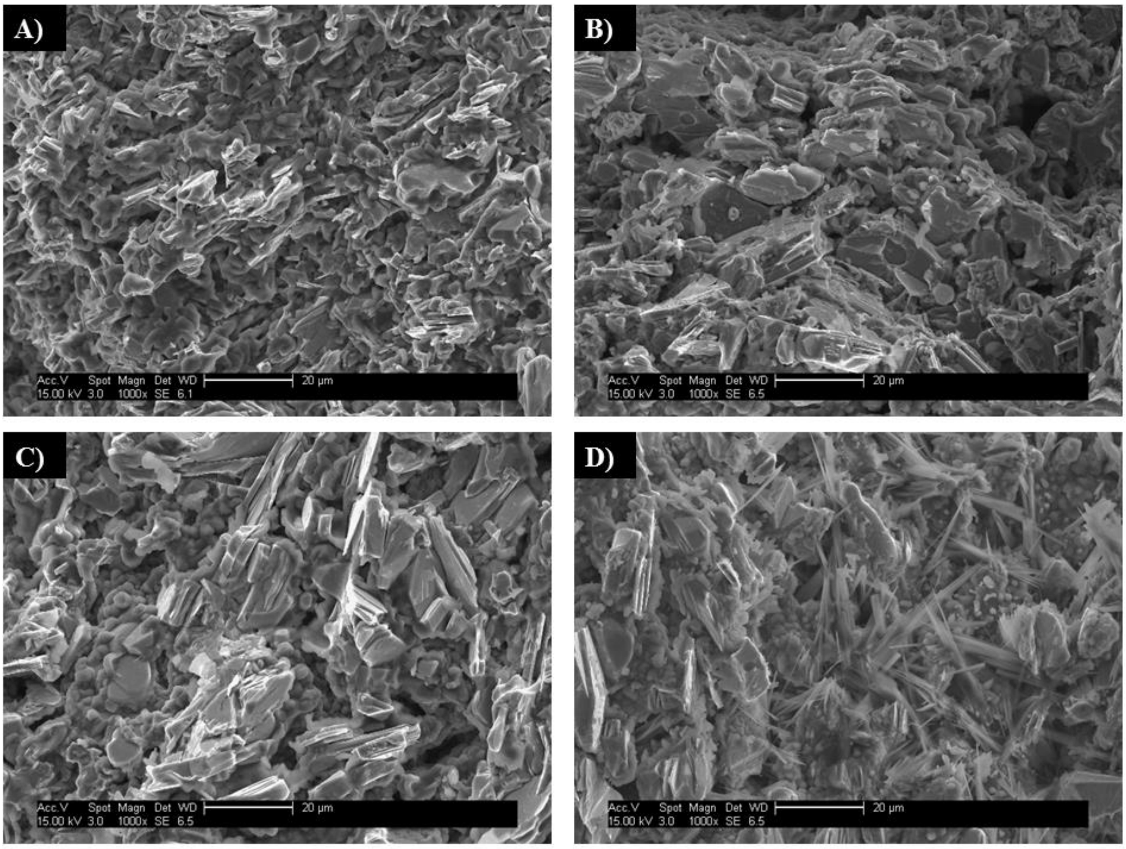

Figure 59 Microstructure cross section SFEG images of ball milled pellets sintered at 950°C for A) 1 hour, B) 2 hours, C) 6 hours and D) 12 hours.

It can be seen that ball milling in an aqueous solution of NaOH and sintering at 1000°C resulted in faceted solid aggregates (Figure 60).

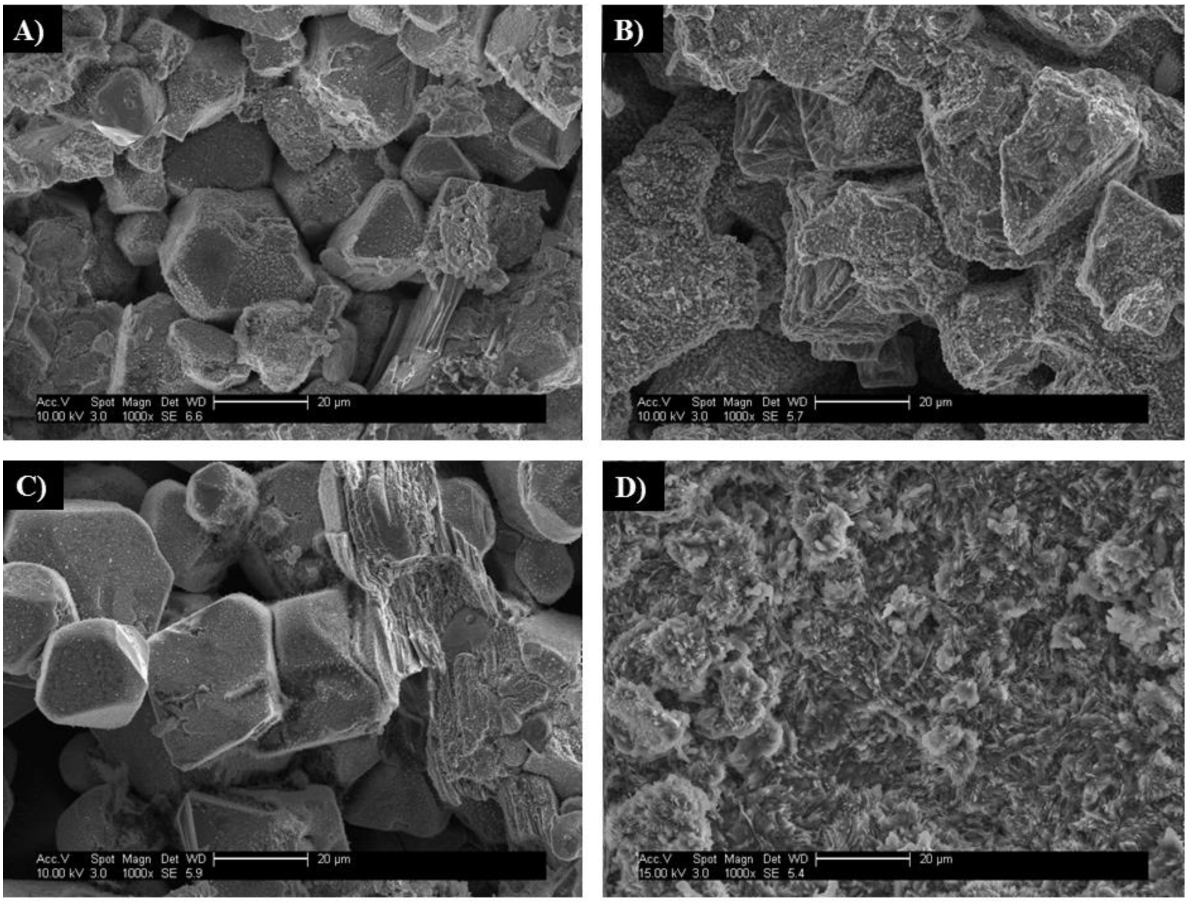

Figure 60 Microstructure cross section SFEG images of ball milled pellets sintered at 1000°C for A) 1 hour, B) 2 hours, C) 6 hours and D) 12 hours.

These grains are covered with nano-scale crystals. This kind of structure is visible for the sintering times of 1, 2 and 6 hours. When ball milling was conducted in a glass container such Si crystals were always evident (Figure 61) as identified by EDX.

These trace amounts of Si was found to be due to use of Pyrex glass during the milling stage. The present of NaOH during this pre-treatment process, contributes to the dissolution of this type of glass.

8.

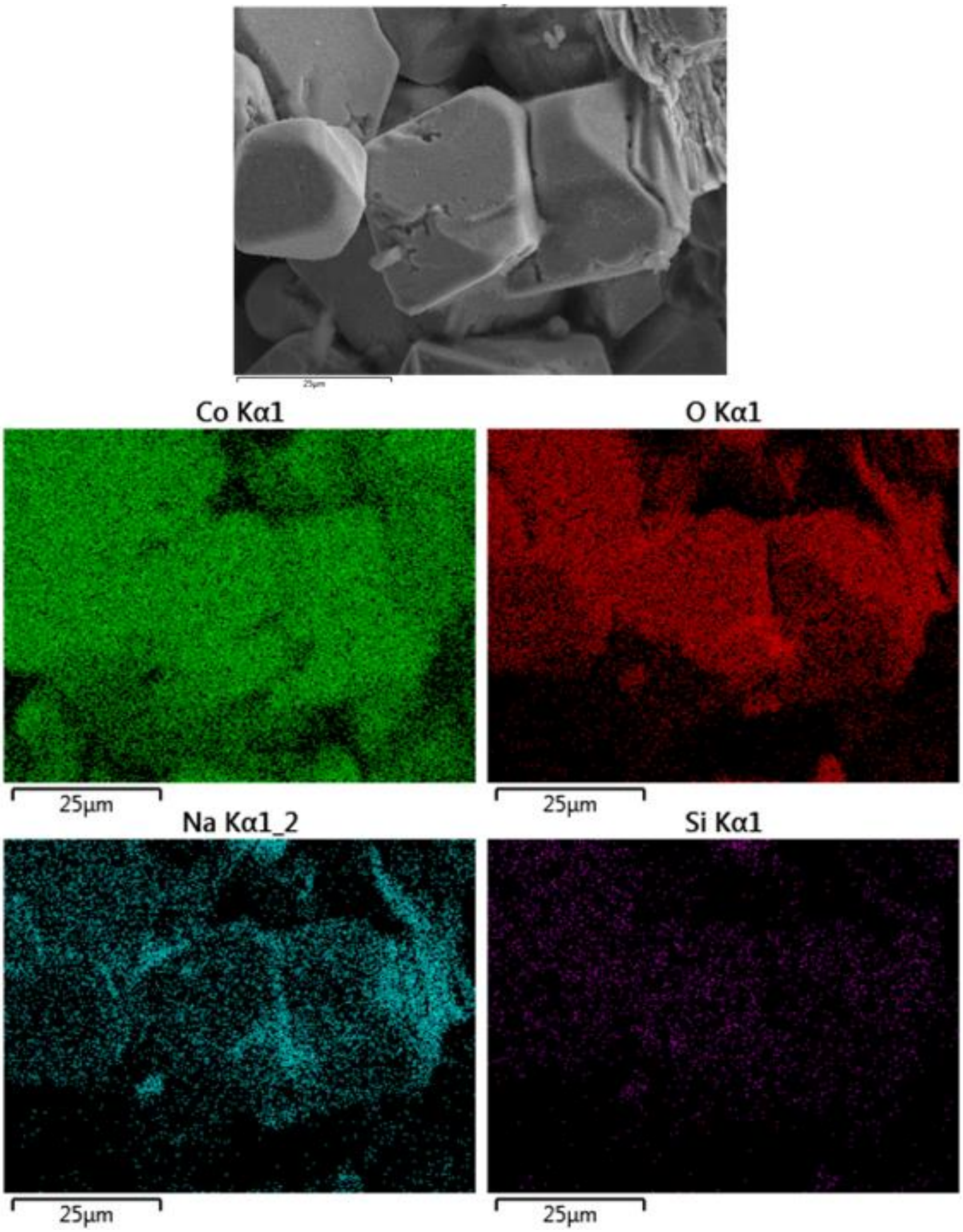

Figure 61 EDX mapping analysis for a pellet sintered at 1000°C for 6 hours showing Co, O, Na and Si.

The presence of silicon in conjunction with the processing conditions initiated the growth of Si containing crystals. This phenomenon will be exanimated more closely in Chapter 8.

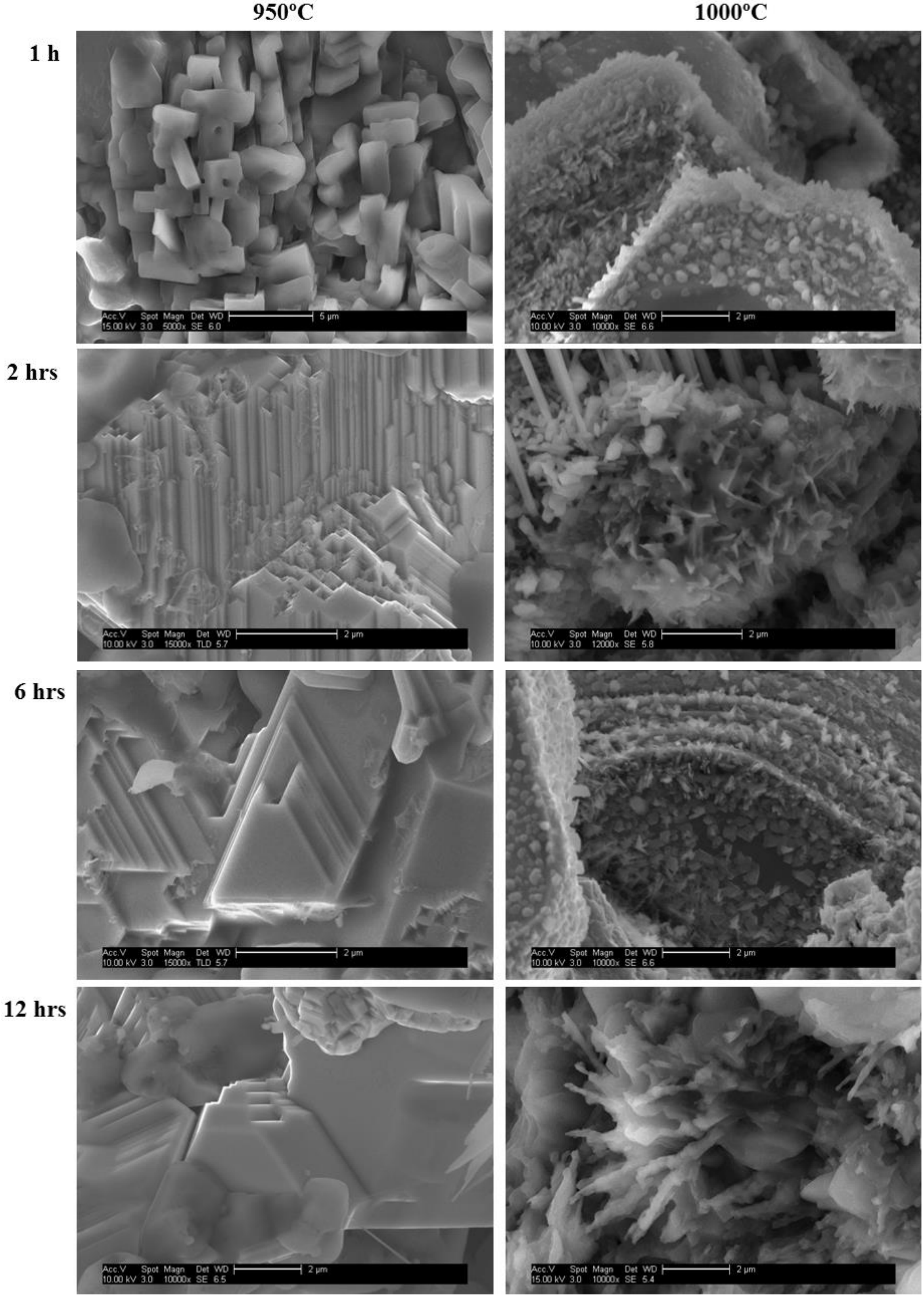

Figure 62 Example of various shapes created during sintering of ball milled pellets at 950°C for 1, 2, 6 and 12 hours, and at 1000°C for 1, 2 , 6 and 12 hours.

Figure 62 presents several of shapes in the structures throughout the cross-section. The formation of unusual shapes are visible especially for pellets sintered at 1000°C while the pellet sintered at 950°C temperature forms a compact structure. The pellets sintered at 1000°C exhibits structure of boulders, surrounded by a “layer” of different shaped crystals that are enriched in Na characterised. Changes in the appearance of the pellets surface that arise as a result of increasing of sintering temperature can also be noted. The SFEG image showing the surface morphology of as-prepared pellets is presented in Figure 63.

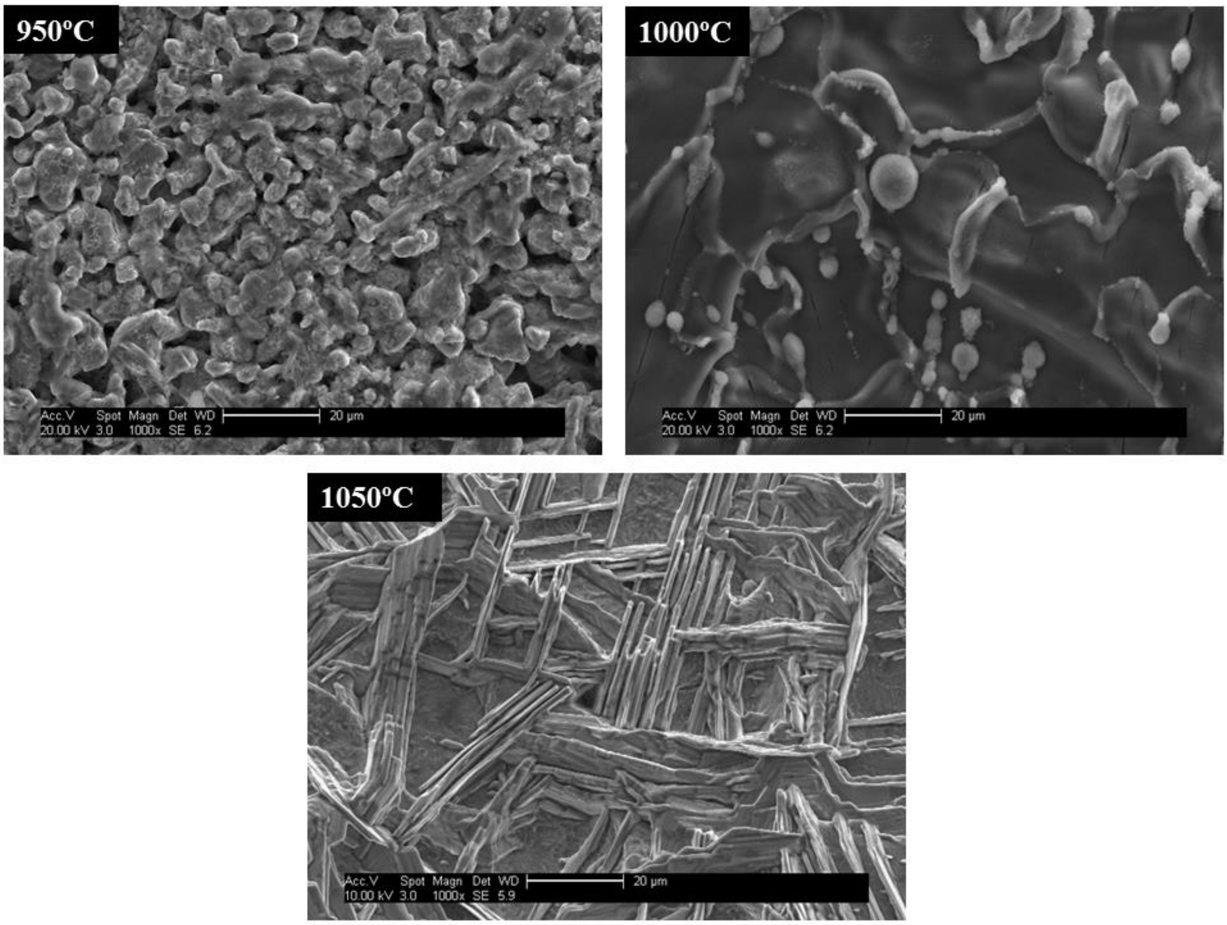

Figure 63 SFEG micrographs of surface morphology of pellets sintered at 950°C, 1000°C and 1050°C for 12 hours.

Differences were visible to the naked eye ranging from rough through a very smooth surface. No detectable changes of morphology were observed with changes in sintering time.

5.4.1.3 Density of samples

Structural changes coincide with the changes of density of the studied pellets as shown in Figure 64.

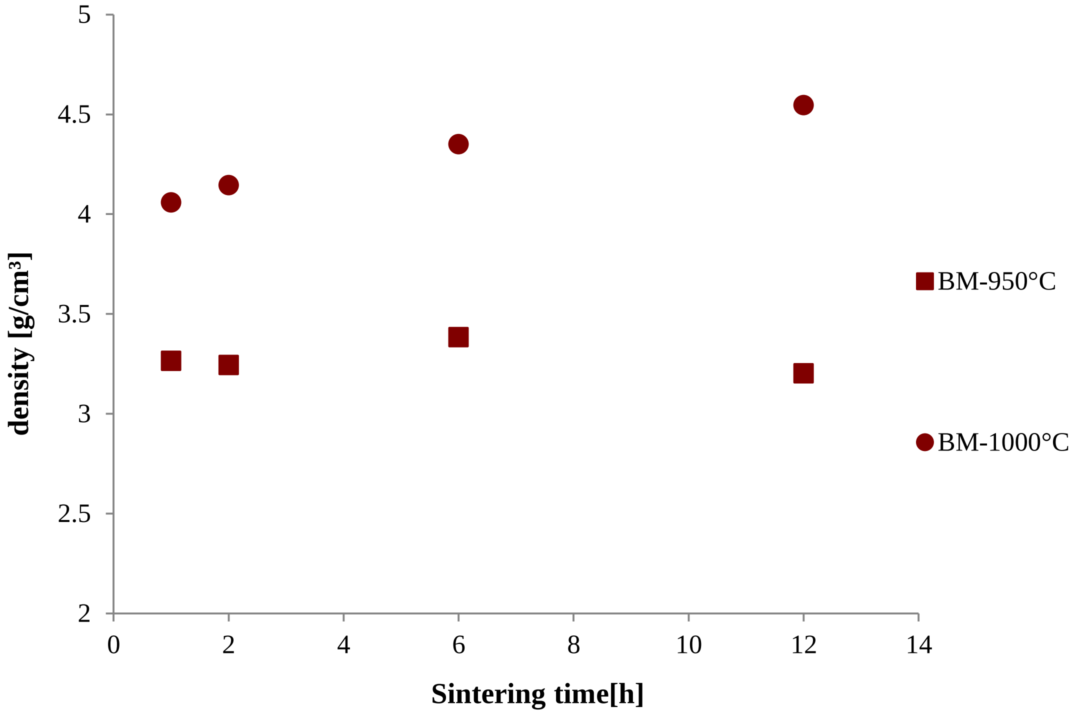

Figure 64 Evolution of density as a function of sintering time and temperature for NaOH pre-treatment ball milled pellets.

The ceramic samples pre-treated with additional sodium shows a measured density close to theoretical density (4.6 g/cm^3)[106]. Presented data for all sodium rich pre-treated pellets tends to show similar trend in density with increasing time and temperature of sintering.

5.4.2 Room temperature measurements

5.4.2.1 Thermal conductivity

The thermal conductivity decreases with increasing duration of sintering (Table 17). The values of thermal conductivity for samples sintered at temperatures of 950°C and 1000°C for 12 hours remain similar to each other.

Table 17 Average thermal conductivity obtained for ball milled pellets measured at between 45-80°C.

Time and temperature of sintering / **Set up temperature of measurements[ºC]**	**Thermal conductivity K[W/mK] (+/- 0.1)**							
	950 1h	**950 2hrs**	**950 6hrs**	**950 12hrs**	**1000 1h**	**1000 2hrs**	**1000 6hrs**	**1000 12hrs**
45	1.9	2.1	2.0	1.3	2.3	2.1	2.0	1.2
50	2.2	1.9	1.5	1.2	2.1	2.2	1.8	1.3
60	2.1	2.1	1.7	1.2	2.2	2.1	1.9	1.1
70	2.3	2.0	1.9	1.5	2.3	1.9	2.1	1.2
80	1.8	1.8	1.5	1.2	2.4	2.3	1.8	1.3

5.4.2.2 Electrical resistivity

The evolution of conductivity behaviour due to heat treatment of as-prepared ball milled samples was evaluated by 4 point probe measurements. The electrical resistivity at room temperature was measured in the in-plane direction.

The electrical resistivity is lower for samples sintered at a low (950ºC) temperature. From Table 18 it can be suggested that the electrical resistivity is strongly related to the structural changes occurring with the increases in density leading to increased electrical resistivity.

Table 18 Measurement of in plane electrical resistivity for ball milled samples

Sintering temperature / **Sintering time**	**Electrical resistivity (+/- 5)**	
	950°C	**1000°C**
1 hour	191 [μΩcm]	245 [μΩcm]
2 hours	210 [μΩcm]	311 [μΩcm]
6 hours	205 [μΩcm]	295 [μΩcm]
12 hours	280 [μΩcm]	410 [μΩcm]

The high value of electrical resistivity which is characterized for sample sintered at 1000ºC for 12 hour can be explained by considering the effects affecting the conductivity as follows. From the SEM images can be seen that the grain size is decreased, which can increase on electrical resistivity due to increased grain boundaries. The behaviour can also be correlated to the presence of the second unknown phase which was detected. This would be especially important if this second was concentrated at the grain boundaries forming a higher insulating layer.

5.4.2.3 Seebeck coefficient

The ball milled pellets showed the biggest variation in the value of Seebeck coefficient (Table 19) of all the Na rich pre-treatment pellets. The Seebeck coefficient was measured at temperatures between 45°C - 80°C. The ball milled samples exhibit unusual microstructure which was found to effect the value of Seebeck coefficient.

Table 19 Seebeck coefficient measured at low temperatures for ball milled samples sintered at different conditions.

Time and temperature of sintering / **Set up temperature of measurements[°C]**	**Seebeck coefficient [µV/K] (+/- 0.1)**							
	950 1h	**950 2hrs**	**950 6hrs**	**950 12hrs**	**1000 1h**	**1000 2hrs**	**1000 6hrs**	**1000 12hrs**
45	24.61	18.94	22.54	21.13	20.77	23.81	25.52	22.32
50	25.14	22.52	20.57	24.95	21.02	20.82	24.16	21.86
60	26.25	20.24	23.94	20.62	22.36	22.17	22.58	22.93
70	28.01	20.94	19.61	22.78	23.26	23.70	21.81	22.46
80	29.75	22.15	20.42	22.39	24.61	22.28	22.31	23.49

5.4.3 Thermoelectric measurement at high temperature

The measurement was conducted in in-plane direction in vacuum conditions at range of temperatures. The measurement was obtained for Ball Milled pellet sintered at 1000°C for 6 hours (BM-1000-6). The Seebeck coefficient results show a general trend characteristic of the metallic behaviour of sodium cobalt oxide (Figure 65).

The ball milling pre-treatment enhances the Seebeck coefficient compared to the other Na-rich pre-treatments. The highest value of Seebeck coefficient was found to be 230 µV/K. However this pre-treatment also resulted in an increase in the electrical resistivity. The value was similar throughout the temperature range with an average of 430 µΩcm.

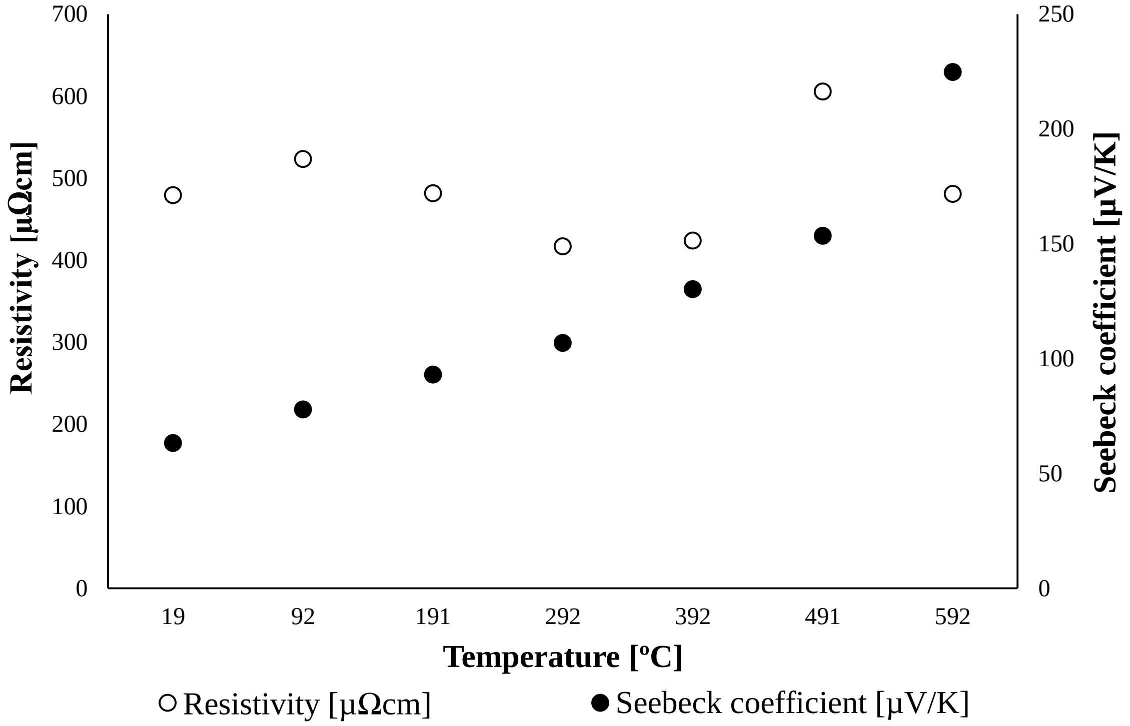

Figure 65 Temperature dependence of the electrical resistivity and Seebeck coefficient for the ball milled sample sintered at 1000ºC for 6 hours (BM-1000-6).

5.5 Overview summary discussion

All of the prepared pellets contained $NaCo_2O_4$ (JCPDF no.27 0682) in addition to residual Co_3O_4. A reduction in Co_3O_4 content was observed with increasing sintering time. Samples showed high purity. Nevertheless, the pre-treated pellets sintered at 1000ºC for 12 hours shows the presence of additional phase that can indicated that the Na rich pretreatments can be fabricated at low temperature and short time that consequently results in a reduction of pellet production costs.

All samples showed an increasing density with increased sintering temperature and processing time (Figure 66).

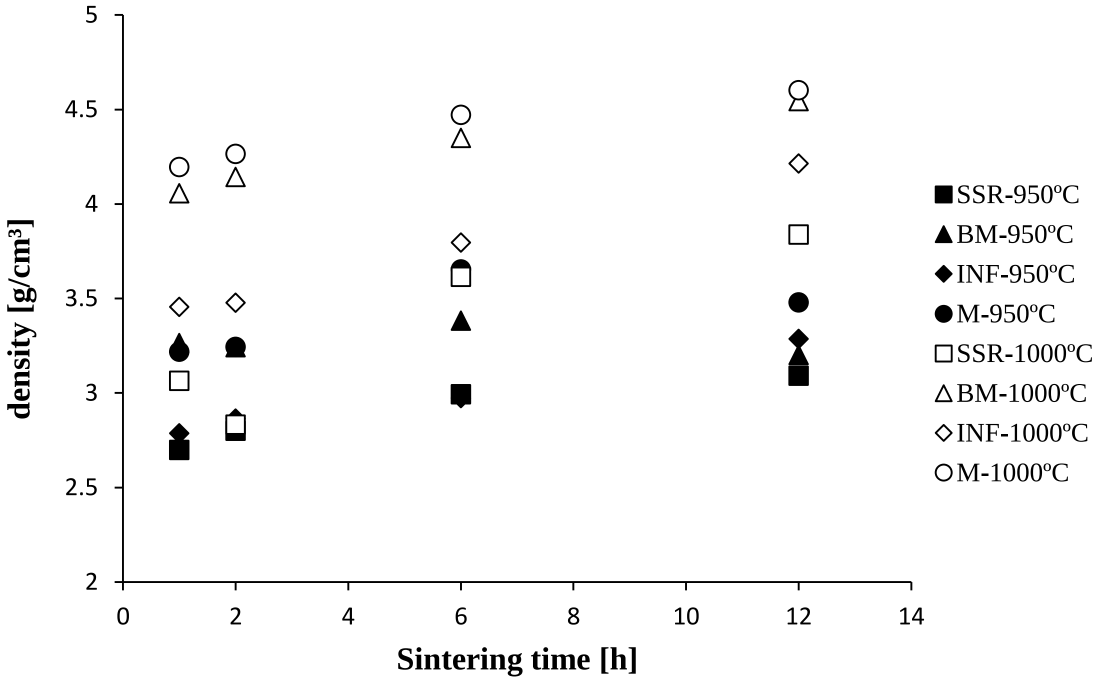

Figure 66 Evolution of density as a function of sintering time and temperature of ball milled (BM), mixed (M), infiltrated (INF) and solid state reaction (SSR) pellets.

The measured density was found to be close to the theoretical density in particular after sintering at 1000ºC. When compared with conventional SSR samples, for which the highest value of density was found to be 3.84 g/cm^3 after sintering at 1000ºC for 12 hours, the pre-treatment leads to an improvement in density of between 10-20%. For INF-1000-12 the density was found to be 4.25 g/cm^3. The ball milled and mixed pre-treated samples show the closest value to the theoretical (~4.6 g/cm^3 for BM-1000-12 and M-1000-12 pellets).

Despite increases in density corresponding increases in thermal conductivity were not observed. With increasing temperature and time of sintering the samples become dens and the formation of multi-interfaces is observed. Therefore, decreasing thermal conductivity can be attributed to structure changes. The comparison of thermal conductivity for all types of pre-treatments along-side conventional SSR samples are presented in Figure 67.

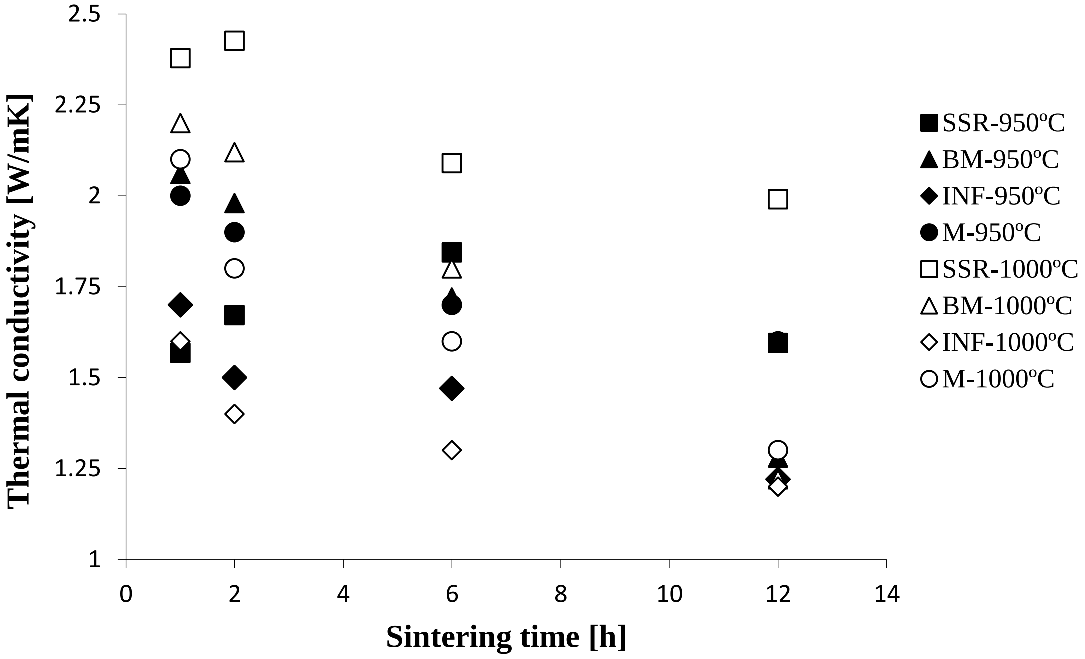

Figure 67 Evolution of thermal conductivity as a function of sintering time and temperature of ball milled (BM), mixed (M), infiltrated (INF) and solid state reaction (SSR) pellets

The compilation of results proves that the Na rich pre-treatment leads to a reduction in thermal conductivity. For pellets sintered at 950ºC and 1000ºC for 1 , 2 , 6 and 12 hours the value of thermal conductivity was found to be between for infiltrated pre-treated samples 1.2 – 1.75 W/mK, for ball milled pre-treated samples 1.1 – 2.4 W/mK, for mixed pre-treated samples 1.2 – 2.3 W/mK and for conventional SSR pellets 1.5 – 2.5 W/mK. The lowest value of thermal conductivity for SSR pellets was found to be for samples sintered at 950ºC which may be caused by inadequate sintering resulting in porous material. For all types of pre-treatments the lowest values of thermal conductivity was exhibited by the most dense pellets. Lowering the value of thermal conductivity may have a great impact on improving the efficiency of the thermoelectric material. The evolution of density and thermal conductivity are presented in Figure 68.

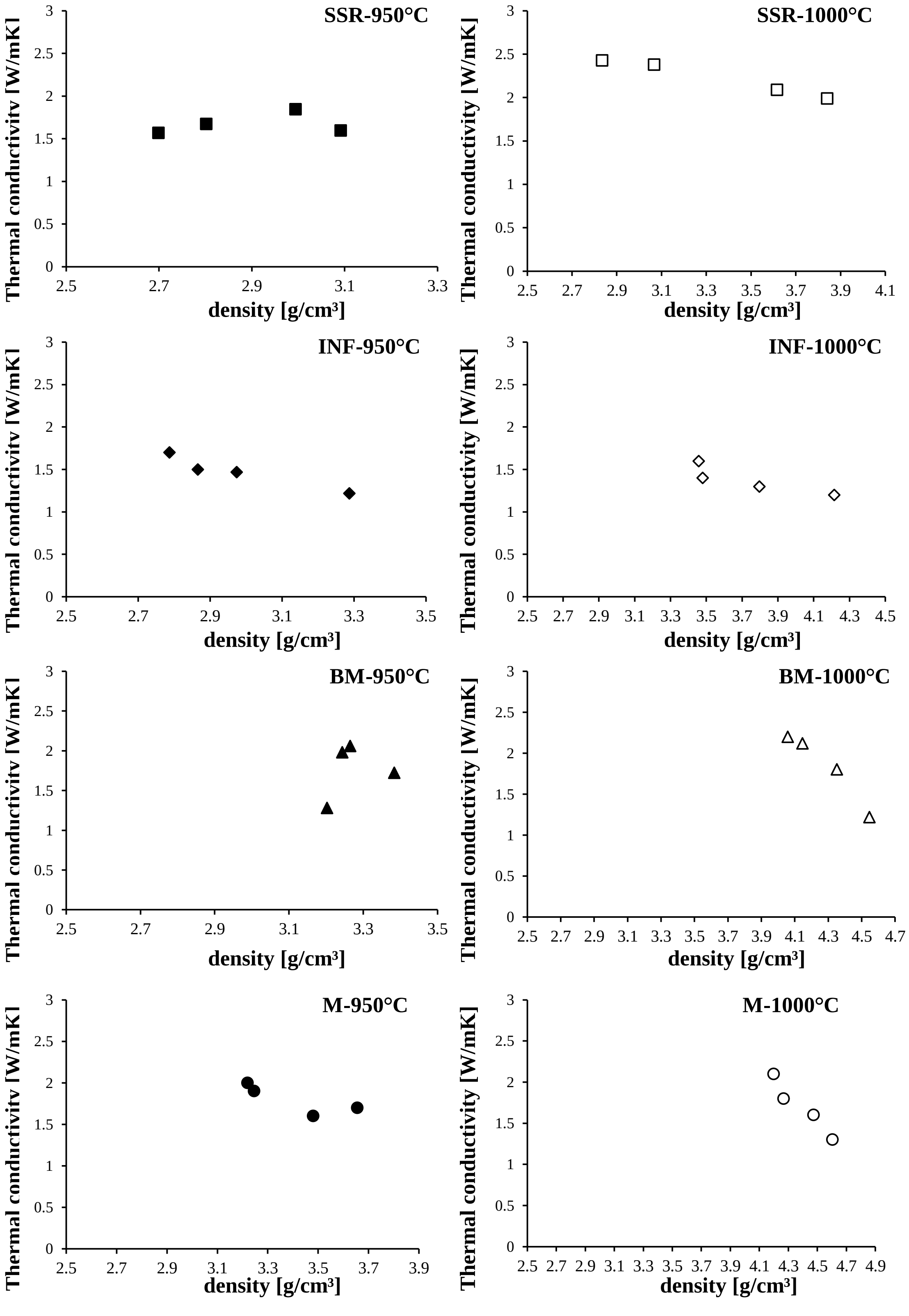

Figure 68 Evolution of density (black colour) and thermal conductivity (grey colour) as a function of sintering time for ball milled (BM), mixed (M), infiltrated (INF) and solid state reaction (SSR) pellets after sintering at 950ºC, and 1000 ºC.

Along-side the creation of multi-layered structures, the formation of plate like grains, which were also encountered in the pre-treated pellets, suggests another mechanism for improving thermoelectric properties. The study shows that the pre-treatment of samples affects the thermoelectric properties to a large degree with the Seebeck coefficient increasing with sodium pre-treatment. Moreover all materials produced a positive Seebeck coefficient that confirms p-type behaviour.

For pellets sintered for 1, 2, 6 and 12 hours the value of Seebeck coefficient measured at room temperature, was found to be:

- 20 – 27 μV/K for infiltrated samples sintered at 950ºC and 22 - 31 μV/K for pellets sintered at 1000ºC;
- 21 – 19 μV/K for mixed samples sintered at 950ºC and 17-20 μV/K for samples sintered at 1000ºC;
- 29 – 19 μV/K for ball milled pellets sintered at 950ºC and 25 – 20 μV/K for samples sintered at 1000ºC;

The biggest differences in the thermoelectric properties, arising from the method of preparation, are visible in the results of studies conducted at high temperatures. The measurements of Seebeck coefficient at high temperatures are presented in Figure 69.

The results show that the mixed sample exhibits a Seebeck coefficient starting from a value of ~70 μV/K and increasing to above 200 μV/K at ~600ºC. The ball milled pellet was found to have a similar value at low temperature with the highest value of 230 μV/K at ~600ºC. The infiltrated pellet also showed an increase in Seebeck coefficient with increasing temperature but the value was relatively low when compared with the other Na-rich pre-treated samples and was found to be 70 μV/K at 20ºC and 150 μV/K at ~600ºC. For conventional SSR pellets the value of Seebeck coefficient was found to be 67 μV/K at 20ºC increasing to 190 μV/K at ~600ºC.

All pre-treatments shows the same value of Seebeck coefficient at 20ºC with the SSR pellet showing a slightly lower value at the same temperature.

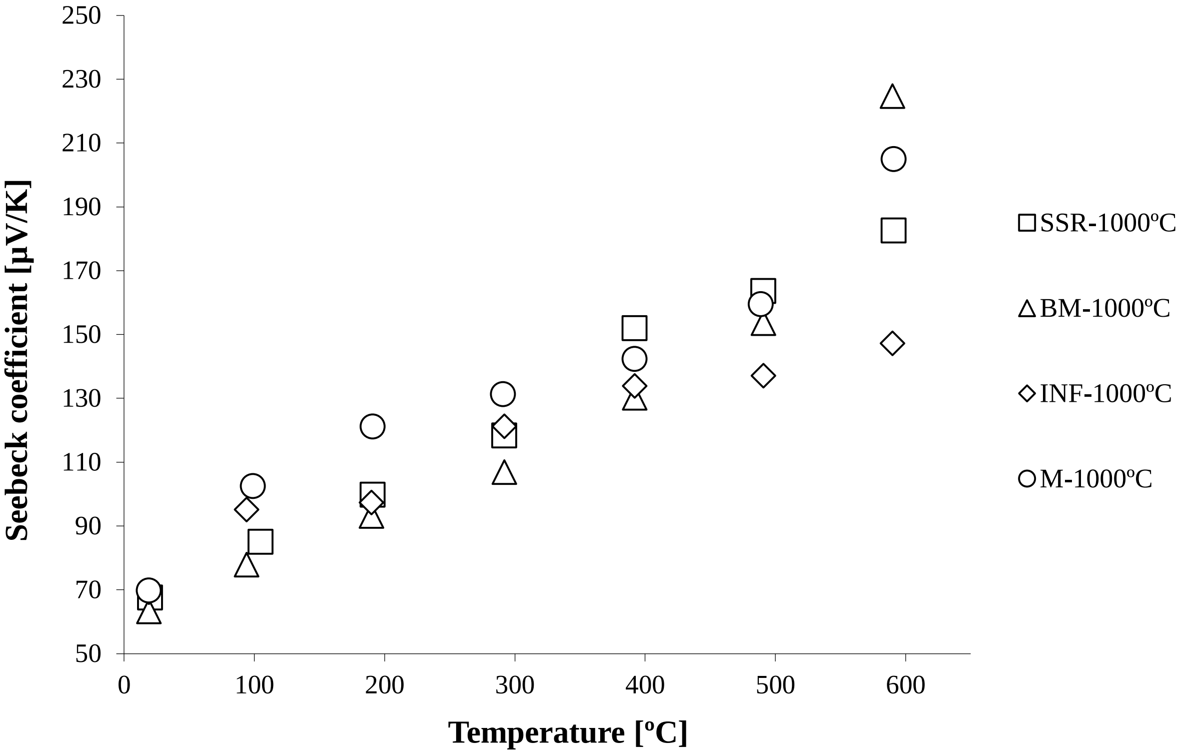

Figure 69 The temperature dependence of the Seebeck coefficient for the solid state reaction (SSR), ball milled (BM), infiltrated (INF) and mixed (M) pellets sintered at 1000 ºC for 6 hours.

The comparison of electrical resistivity of the different samples is shown in Figure 70.

Additionally the results show that the mixed and ball milled pre-treated samples exhibit the highest value of Seebeck coefficient, above 200 µV/K at ~600ºC.

The electrical conductivity was found to be strongly affected by the synthesis method. From the results one can notice that use of all types of pre-treatments lead to a decrease in electrical resistivity.

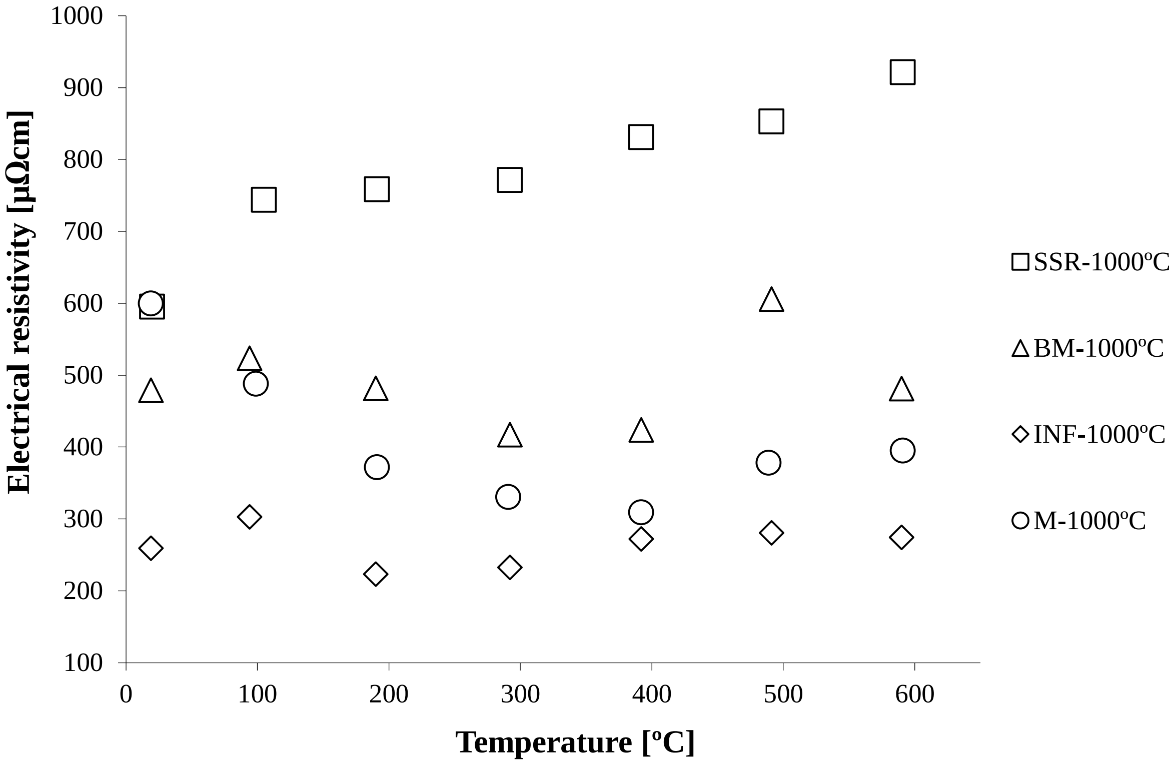

Figure 70 The temperature dependence of the electrical resistivity for the solid state reaction (SSR), ball milled (BM), infiltrated (INF) and mixed (M) pellets sintered at 1000 ºC for 6 hours.

The electrical resistivity for the M-1000-6 sample was found to be higher at low temperatures, with the value of 600 μΩcm, and decrease with increasing temperature resulting in value of 400 μΩcm. The infiltration pre-treated sample exhibits the lowest value of electrical resistivity around 270 μΩcm compared, for example, with the ball milled pre-treated sample with the value of around 500 μΩcm at 600ºC. Additionally in the case of INF-1000-6 the value was similar over the whole range of temperatures measured. The electrical resistivity for ball milled sample was found to be between 400 μΩcm and 600 μΩcm which is similar to mixed pre-treated sample.

The comparison of reported value of electrical resistivity and Seebeck coefficient with the results obtained in this work are presented in Table 20.

Table 20 Comparison of reported value of Seebeck coefficient and electrical resistivity with results obtained during this work.

Electrical resistivity [μΩcm]	**Seebeck coefficient [μV/K]**	**T [K]**	**Material Ref.**
200-600		300	[105]
200-260	120-140	500	[5]
265	145	300	[90]
150	118	500	[106]
103	85-135	500	[3]
380	150	600	[108]
320	150	300	[113]
200-900	70-180	300-600	SSR
230-300	70-150	300-600	INF
200-600	70-220	300-600	BM
300-600	70-230	300-600	M

It is worth adding that the most consistent composition (Na/Co=1/2) was exhibited by the infiltrated (INF) pellets which could explain the similar results regardless of sintering temperature and time in comparison to the other types of pre-treatments.

Finally the figure of merit ZT for all samples was determined by the Equation 8 and is summarized in Figure 71. The calculated value of ZT was obtained for low temperature measurements below 100°C.

Despite the small temperature differences considered the ZT can be seen to increase with increasing temperature. The results show that all pre-treatments enhance the thermoelectric performance of the sintered body at 350K. The biggest improvement was exhibited by the infiltration pre-treated samples which exhibited the highest value of ZT even at room temperature (~290K).

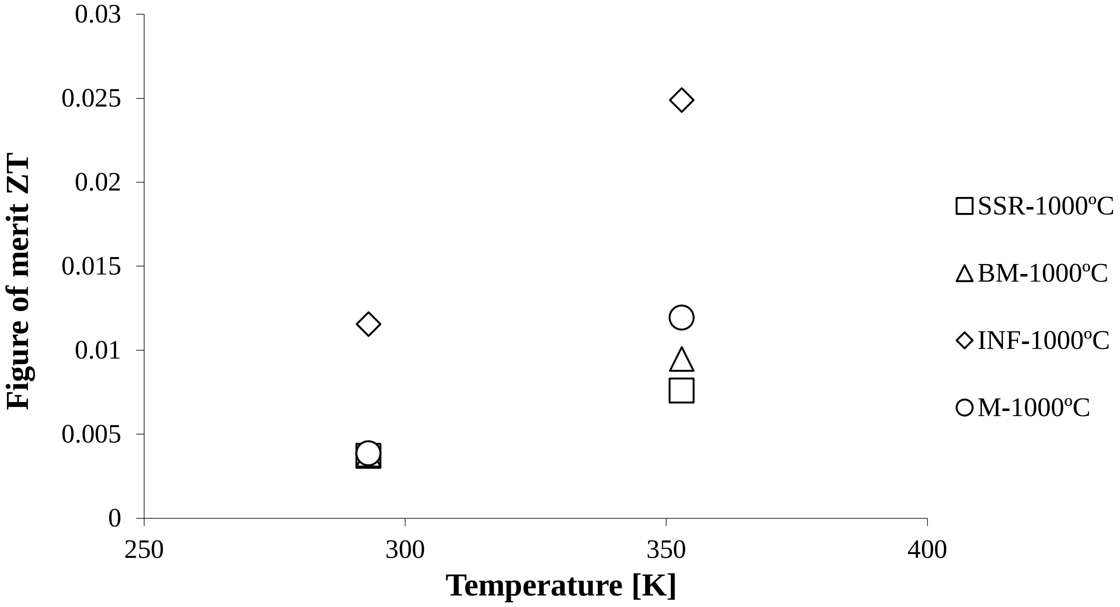

Figure 71 Figure of merit, ZT, of sodium cobalt oxide pellets produced using solid state reaction (SSR) synthesis powder and different Na rich pre-treatments: mixed (M), ball milled (BM), infiltrated (INF).

5.6 Summary

The use of Na pre-treatments enhances the thermoelectric properties of sintered $NaCo_2O_4$. The microstructural changes caused by the ball milled (BM) pre-treatment are enhanced densification and grain growth offset against the formation of grain boundary phases resulting in increased Seebeck coefficient and a relatively low value of thermal conductivity. Mixed (M) pre-treatment results in densification, without grain growth, and the formation of a grain boundary second phase resulting in an increase in ZT. The infiltrated (INF) pre-treatment results in minimal changes to the microstructure relative to that SSR samples of with a slight grain boundary disruption resulting in a decrease in thermal conductivity and relatively low value of Seebeck coefficient together with electrical resistivity and thermal conductivity. The results suggest that the infiltration treatment is the most effective method for improving thermoelectric performance of $NaCo_2O_4$.

Chapter 6 The sol gel preparation of $NaCo_2O_4$ ceramics

6.1 Introduction

The thermoelectric performance of polycrystalline sodium cobalt oxides is assumed to be strongly correlated with particle morphology, particle geometry and size. The existing research results indicate that the thermoelectric properties of sintered a bulk body may be enhanced by producing highly oriented crystals. The mentioned properties are strongly determined by the preparation method. The sol gel method is one of the most efficient production methods resulting in high homogeneity and purity of the as-formed powders. Small particle size of final powders and low synthesis temperatures are characteristics of this method. High efficiency of thermoelectric power generation requires low thermal conductivity and at the same time high electrical conductivity. The pH of the reaction environment should be kept below 6 during the preparation of $Na_xCo_2O_4$ by sol gel method[162]. Such conditions are necessary to avoid the formation of $Co(OH)_2$ due to the reaction of Co^{2+} with the solvent. The work dedicated to enhancing the thermoelectric properties of $NaCo_2O_4$ using sol gel powder synthesis have been presented in this chapter. The starting part describes the produced powder, selection of production parameters and material properties such as grain size and purity. Subsequent sections are dedicated to the study of sintered sol gel pellets with detailed description of the morphology and thermoelectric properties. The modification of the sol gel preparation method with Na enrichment, and its influence on the properties of prepared oxide ceramic materials, is also considered.

6.2 Sol gel powder

The first stage is the sol gel powder synthesis method described in the experimental section of this thesis. Sodium cobalt oxide powders prepared by sol gel method followed by calcination were examined using X-ray diffraction. Figure 72 shows the diffraction patterns of powders calcinated at different temperatures. The diffraction patterns of dry sol gel powder show peaks of an intensities that indicate the presence of Co_3O_4. The diffraction peaks indicate that powder calcined at 450 °C consists of sodium cobalt oxide in addition to cobalt oxide phases. All organic compounds and acids were removed at temperatures below 400°C. The increase of temperature of calcination results in a change in diffraction pattern. The diffraction patterns of powder calcined at 700°C show peaks corresponding to those assigned to $NaCo_2O_4$ (JCPDS no.27 0682). The results demonstrate that the calcination of powder at 700°C results in crystallised $NaCo_2O_4$-type structures.

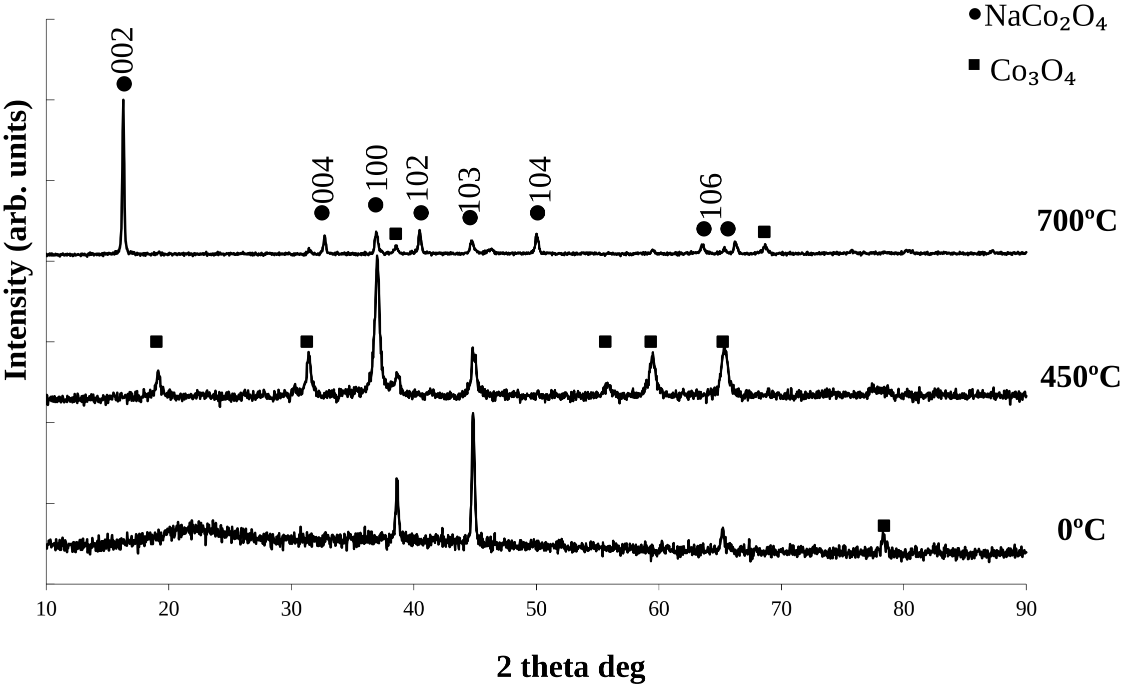

Figure 72 X-ray diffraction patterns of sol gel syntheses powder calcined at 450°C and 700°C the lowest pattern corresponding to the dry pink-coloured sol powder.

The next stage of the research involved the analysis of microstructures, together with a quantitative analysis (EDX) of the obtained powder. As shown in Figure 73 the microstructure of the powder formed a compact structure for the dry sol powder and a delicate openwork for the calcined powder. The powders calcined at 450°C and 700°C show a similar structure. The use of a relatively low calcination temperature made it possible to maintain a similar level of sodium as detected during EDX analysis.
When compared to the solid state reaction powder it can be seen that the same level of Na has been measured in two types of powder using EDX analysis (Table 21).

Table 21 EDX analysis of powders produced by the Solid State Reaction method (SSR powder) and Sol Gel method (SG powder).

Name of sample	Na content (atomic %)	Co content (atomic %)
SSR powder	15.89	29.91
SG powder	16.04	32.05

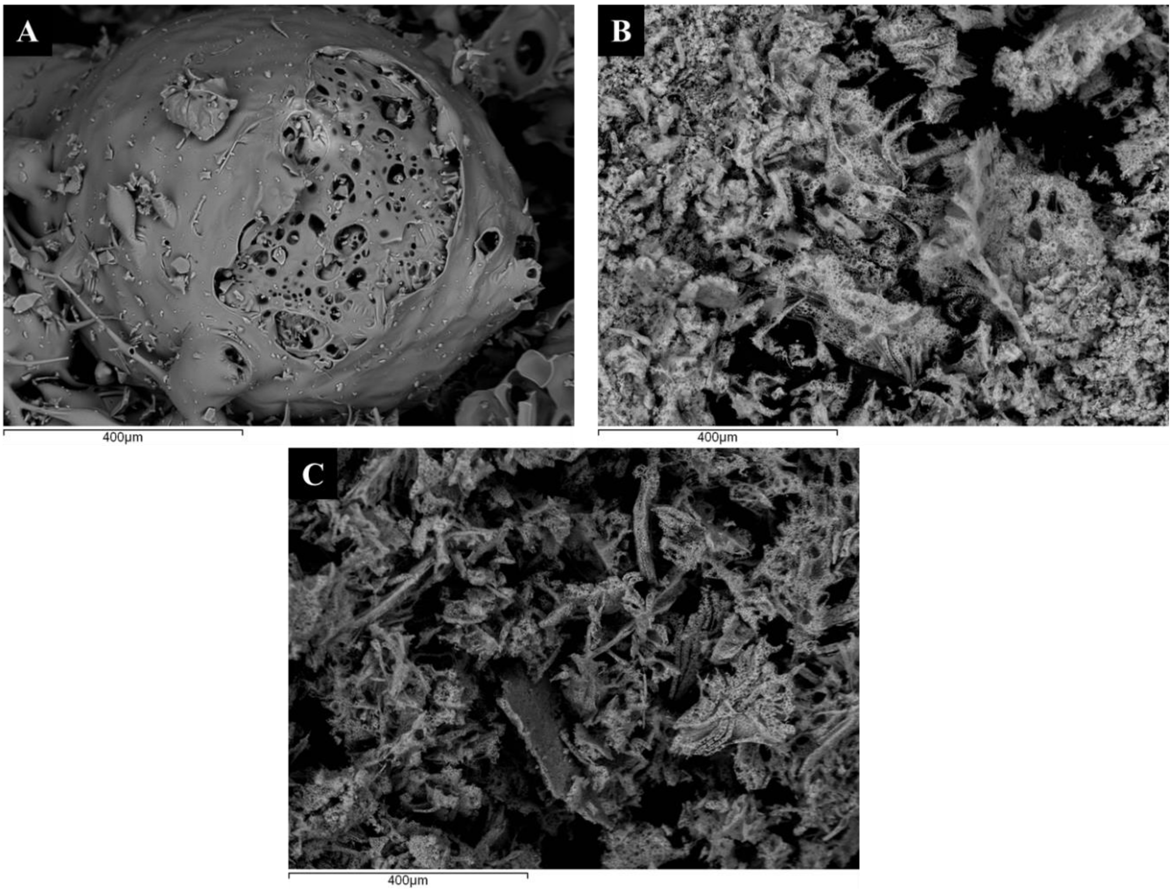

Figure 73 Micrograph of sol gel prepared powder; A) as-prepared powder before calcination, B as-prepared powder after calcination at 450°C for 6 hours in air, C) as-prepared powder after calcination at 700°C for 6 hours in air.

The higher magnification image presented in Figure 74 exhibit a polycrystalline structure with the grain size in the range of nano meters. The grains have a sheet like appearance due to the layered structure of the oxides[74]. As presented in Figure 74 the particle size of the sol gel synthesized powder was found to be less than 1 μm. The high magnification SEM images (Figure 74) indicates noticeable grain growth after processing at 700°C with an open structures. That confirms the characteristic behaviour of ceramics under the influence of heat treatment.

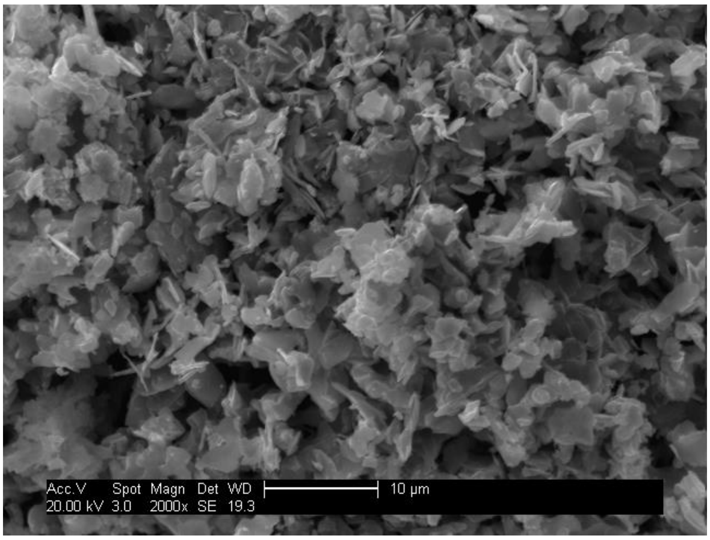

Figure 74 SEM micrograph of the calcinated powder synthesized by sol gel method after heat treatment at 700°C for 6 hours.

The parameters of synthesis were chosen for the further research on the basis of the obtained results and the comparison to powder obtained by the solid state reaction method. It was considered that powder calcined at 700°C for 6 hours gave sufficient purity and nano-scale grain size.

6.3 SG pellets

6.3.1 Introduction

As in the case of production of the SSR pellets the effects of time and sintering temperature on structural changes and thermoelectric properties have been studied. In order to compare with SSR pellets the same parameters of preparation were used for pellets prepared from powders SG. Namely, each of the pellets were prepared from 6 grams of powder, which was crushed in a mortar, then compressed using a 2 ton load for a period of 2 min. Before being subjected to a high temperature treatment at 950°C and 1000°C for 1, 2, 6 and 12 hours respectively. As the powders obtained by the sol gel method are characterized by a small grain size thus high densification can be achieved at lower temperatures, therefore, for comparison pellets sintered at 850°C for 6h were also prepared.

6.3.2 Microstructure characterisation

6.3.2.1 XRD analysis

Figure 75 shows the XRD pattern for $Na_xCo_2O_4$ pellets sintered at 950°C and 1000°C. It can be seen that except for the diffraction pattern of $NaCo_2O_4$ no additional peaks were detected, indicating that the formation reaction of $NaCo_2O_4$ was completed. Prolonging the sintering time demonstrating that the $NaCo_2O_4$ was synthesized successfully even for the shortest time of sintering of 1h. Increasing sintering temperature together with prolonging the time of sintering resulted in $NaCo_2O_4$ and in an additional peak below 16 (2Θ) angle. A peak in this region is often described in literature as the effect of storage of the sample in the air and its partial hydration or decomposition[163]

The appearance of peaks at lower angles is often accompanied by a reduction in intensity of peaks corresponding to $NaCo_2O_4$, in particular associated with (002). In this work, the appearance of the peaks in these regions was found to be characteristic for pellets sintered at the higher temperature of 1000°C. This observation suggests that pellets exposed to the 1000°C temperature treatment for a 12 hours exhibit a more moisture-sensitive nature then others. Comparison of diffraction pattern corresponding to as-sintered $NaCo_2O_4$ pellets obtained by the solid state reaction (described in chapter 4) and the sol gel method (presented here) confirms that the powder preparation method is also important during the preparation of the final product. Maintaining appropriate synthesis parameters is decisive for the quality of the resulting compound. Residual Co_3O_4 was detected in SSR pellets sintered at 950°C while when the same temperature was used for sintering SG pellets only $NaCo_2O_4$ was observed affirming that the use of SG powder when preparing $NaCo_2O_4$ pellets can lower the production costs due to decreased temperatures and time required to obtain the $NaCo_2O_4$ phase.

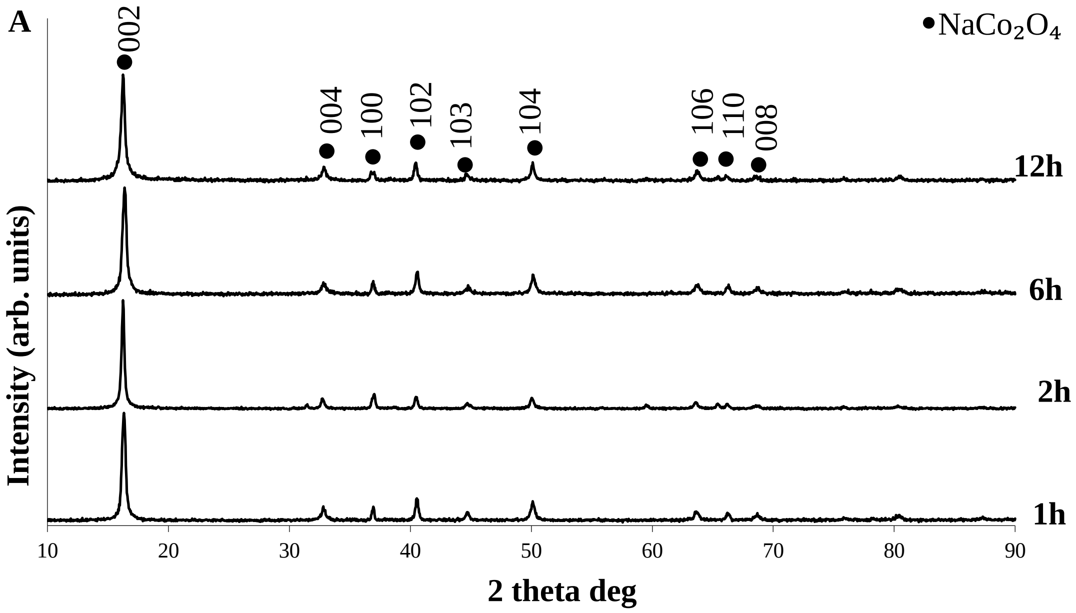

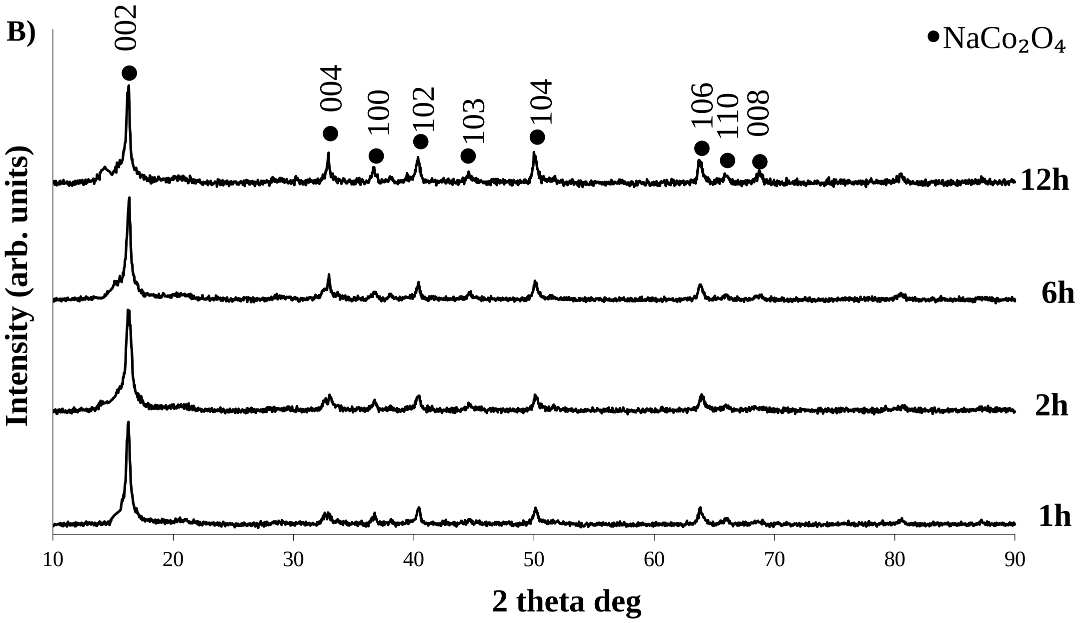

Figure 75 X-ray diffraction patterns of $NaCo_2O_4$ sol gel powder pellets sintered at A) 950°C and B) 1000°C for 1, 2,6 and 12 hours, respectively. Presence of characteristic peaks assigned to $NaCo_2O_4$ (no.27 0682) is indicated.

6.3.2.2 Microscopy analysis

The temperature dependence of the microstructural changes was determined by scanning electron microscopy. The powder synthesized by the sol gel method was found to contain nanoscale particles as can be seen from the SEM images, which demonstrates the grain size at the micron level, and that sintering affects the morphology of polycrystalline ceramic.

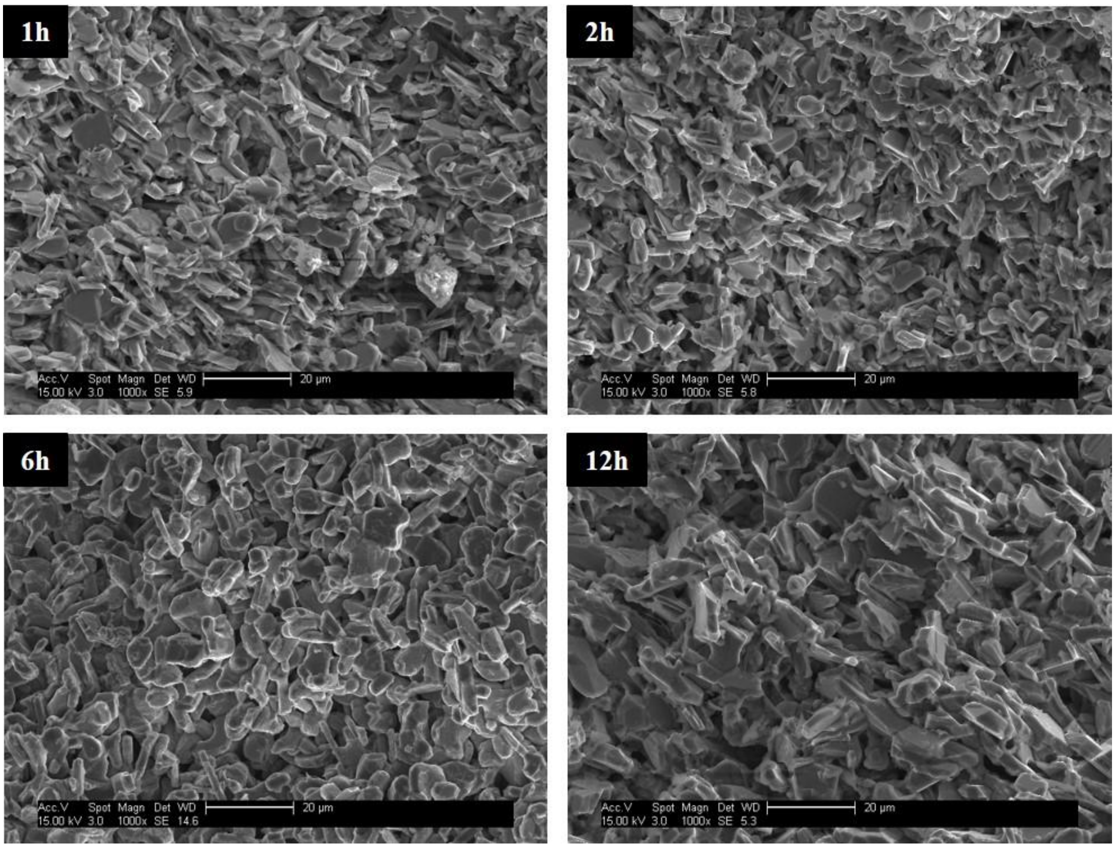

Figure 76 Cross-section micrographs of ceramics sintered at 950°C. Influence of increasing time on the microstructure with visible change.

The microstructure of pellets sintered at 950°C shows a fine grained and relatively dense structure in the whole range of sintering time (Figure 76). When compared to the conventional SSR samples (Figure 36), the porous structure is not as obvious as with SG pellets. The presence of pores has a strong effect on the properties of oxides materials. Pores can lead to deterioration of electrical and thermal conductivity and consequentially to lower thermoelectric performance of oxide material. Therefore the study of the microstructural changes is very important due to its impact on the properties. The influence of sintering temperature was the next step of this research, however pellets sintered at 1000°C over a range of times were not examined (Figure 77).

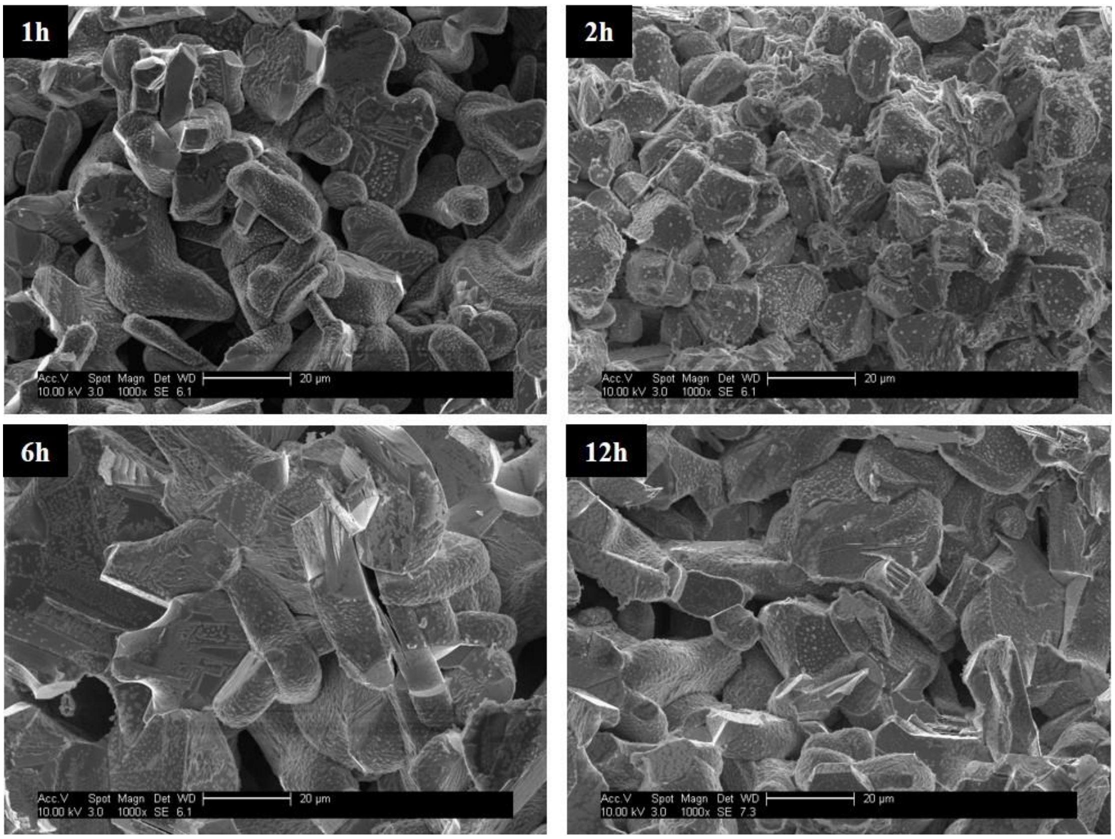

Figure 77 SEM micrograph of cross sections of pallets sintered at 1000°C prepared from powder synthesized by the sol gel method with visible influence of prolongation of sintering time.

As shown in Figure 76 and Figure 77 the pellets exhibited elongated of the powder grains during densification. However the grain elongated of samples sintered at 1000°C was emphatically stronger than these sintered at 950°C. This occurrence may explain the improvement of densification of pellets under the influence of increase of sintering temperature. Moreover the grain thickness of the pellets sintered at 950°C was found to be smaller than these sintered at 1000°C. The increase in size of grains in two dimensions under the influence of heat treatment is more visible in the Figure 78. The presented cross sectional micrographs reveal that the microstructure changes from a fine grained structure when sintering at 850°C to the higher density structure as a result of sintering at 1000°C.

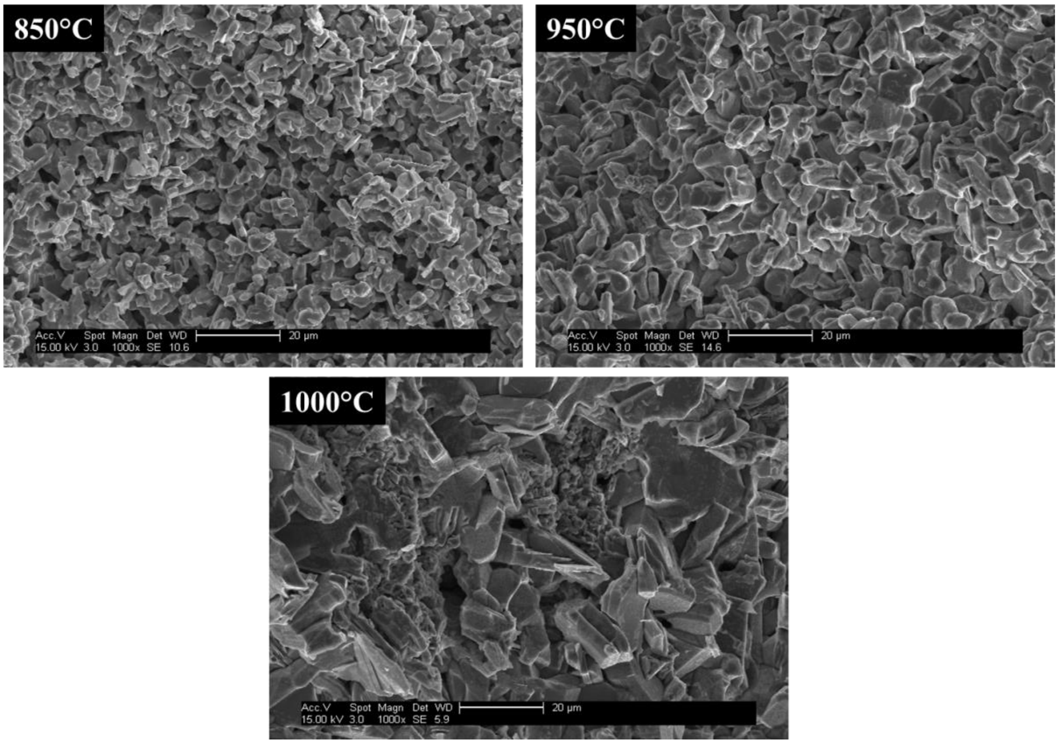

Figure 78 Cross sectional micrographs of sol gel synthesized pellets showing the change due to sintering at 850°C, 950°C and 1000°C for 6 hours.

Increases in the density of the pellets under the influence of sintering temperature were visible to the naked eye since each of the sintered disks had a different diameter. The most visible shrinkage of the sintered pellets was found to be after heat treatment at 1000°C for above 2 hours and particularly in the case of pellets sintering for 12 hours where the diameter was found to be ~4 mm smaller than the size prior to sintering. Moreover the calculated density was found to be close to the theoretical density of sodium cobalt oxide, with density increasing with increasing sintering temperature.

6.3.3 Room temperature measurements

6.3.3.1 Thermal conductivity

Thermal conductivity was measured at low temperatures between 45 - 80ºC in plane direction. The results obtained from SG samples sintered under different conditions are presented in Table 22. The results indicate that the highest values of thermal conductivity are exhibited by pellets SG-950-1 and SG-1000-12. Pellet SG-950-1 represents a disk sintered at 950ºC for 1 hour. This pellet was found to be characterised by a small grain size and the lowest relative density. The SG-1000-12 sample, which corresponds to pellet sintered at 1000 ºC for 12 hours, is characterized by strong grains elongated together with a density close to theoretical density. However from the XRD pattern this sample can be seen to contain additional phases. The presence of an additional phase can result in an increase in of thermal conductivity. Nevertheless, when compared with solid state reaction samples, the sol gel samples clearly show lower values of thermal conductivity. This observation confirms the reduction in thermal conductivity in connection with the use of a different method of preparation. A high thermal conductivity which is characteristic of pellets sintered at 950°C for 1 hour can be explained by low level of sintering and the formation of a granular structure. With increases in sintering time, and further densification, the thermal conductivity decreases, with excess sintering (1000°C/12h) thermal conductivity once again increases.

Table 22 Variation in thermal conductivity of sol gel (SG) samples sintered at 950°C and 1000°C for different period of time.

Time and temperature of sintering **Temperature of measurements[ºC]**	**Thermal conductivity K[W/mK] (+/- 0.1)**							
	950 1h	**950 2hrs**	**950 6hrs**	**950 12hrs**	**1000 1h**	**1000 2hrs**	**1000 6hrs**	**1000 12hrs**
45	1.3	1.0	0.9	0.7	0.6	0.9	0.7	1.2
50	1.3	1.0	1.0	0.7	0.6	0.5	0.8	1.2
60	1.3	1.2	1.0	0.7	0.6	0.5	0.7	1.2
70	1.3	1.4	1.0	0.6	0.6	0.5	0.8	1.2
80	1.3	1.3	0.9	0.6	0.6	0.6	0.7	1.2

6.3.3.2 Electrical conductivity

The electrical conductivity results, obtained using the four point probe method are shown in Table 23. The result show that pellets sintered at a low temperatures and short time exhibit a reduced electrical conductivity. Enhanced densification results in an improvement of electrical conductivity. The measured value was found to be relatively low.

Table 23 In plane electrical resistivity for sol gel (SG) samples sintered at different times and temperatures.

Sintering temperature **Sintering time**	**Electrical resistivity (+/- 3)**	
	950°C	**1000°C**
1 hour	311 [μΩcm]	261 [μΩcm]
2 hours	279 [μΩcm]	257 [μΩcm]
6 hours	255 [μΩcm]	246 [μΩcm]
12 hours	252 [μΩcm]	257 [μΩcm]

6.3.3.3 Seebeck coefficient

The Seebeck coefficient measurements were carried out at low temperature (45°C - 80°C) in plane direction. Over such a small temperature range no trend was observed for each of the examined samples with values remaining at a similar level within the range of measurement error. Table 24 therefore reports the average value of Seebeck coefficient obtained for measurements temperature between 45°C - 80°C.

Table 24 Seebeck coefficient measured at low temperatures (45°C - 80°C) for sol gel samples sintered under different conditions.

Sintering temperature / **Sintering time**	**Seebeck coefficient [µV/K] (+/- 0.1)**	
	950°C	**1000°C**
1 hour	30.1	29.8
2 hours	34.1	33.0
6 hours	34.3	34.1
12 hours	34.9	33.4

The results show small differences of measured value in the range between ~30 µV/K and 35 µV/K values of Seebeck coefficient were found to increase with increasing sintering time. With the exception of the pellet sintered at 1000°C for 12hours which exhibited a decrease in Seebeck coefficient. The values obtained from sol gel derived samples was found to be higher than that for samples produced using the conventional solid state reaction method described in Chapter 4. In addition, all of the pellets tested have a positive value of Seebeck coefficient which confirms p-type behaviour.

6.3.4 High temperature thermoelectric measurement

The in-plane electrical resistivity was found to be similar over almost the entire temperature range of measurement and remained at the level of ~270 µΩcm. The lowest value of (250 µΩcm) was measured at a temperature around 100°C and a the highest value of ~280 µΩcm was noted at around 200°C as presented in Figure 79. The temperature dependence of the Seebeck coefficient for sol gel derived samples is plotted in Figure 8 and shows an increasing value with increasing temperature. The lowest value of 83 µV/K was obtained at the starting temperature and the highest value of 140 µV/K was read at around 600°C.

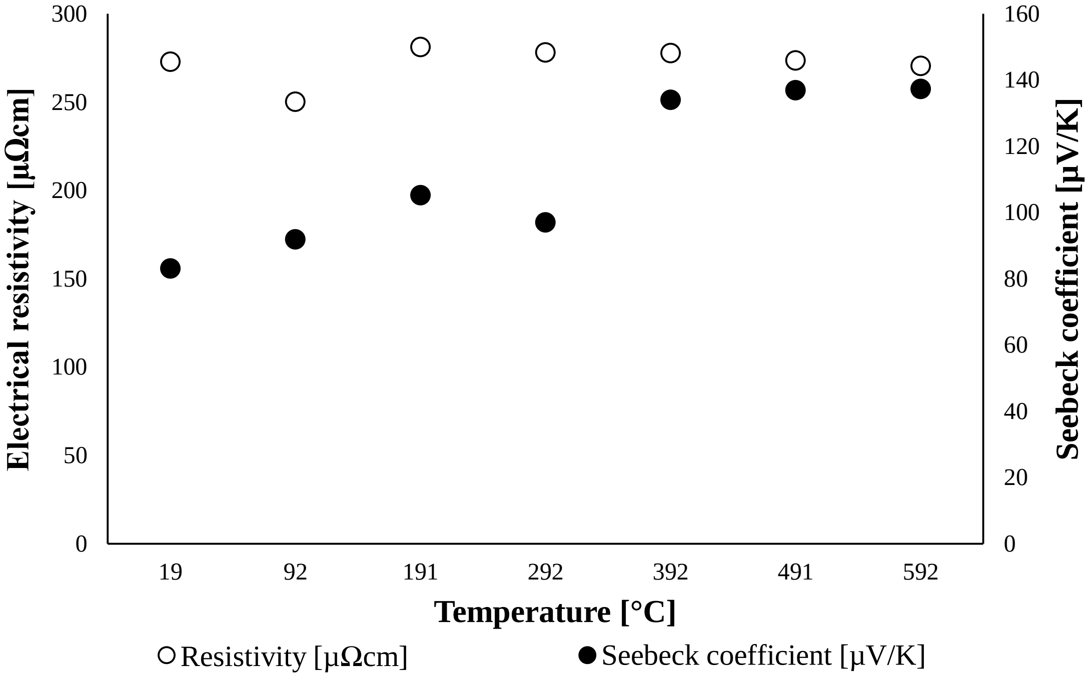

Figure 79 Temperature dependence of the electrical resistivity and Seebeck coefficient, as a function of temperature, for sol gel sample sintered at 1000ºC for 6 hours (SG-1000-6).

6.4 Sol gel ball milled pellets

6.4.1 Introduction

The next stage of the research was to verify the influence of the Na rich pre-treatment on the behaviour of sintered ceramic bodies made from sol gel powder. For this purpose the method that brought the most effective change for pellets made from SSR powder was chosen. To prevent Si contamination during the ball milling stage of preparation plastic bottles were used. The sequences of steps for preparation were described in earlier chapters. The modification of production method and its influence on the structure and properties is the main theme of this section.

6.4.2 Microstructure characterisation

6.4.2.1 XRD analysis

Figure 80 shows the XRD pattern for $Na_xCo_2O_4$ sol gel Na enriched pellets sintered at 950°C and 1000°C. It can be seen that except for $NaCo_2O_4$ peaks no additional peaks were detected in the XRD pattern for pellets sintered at 950°C indicating that the formation of $NaCo_2O_4$ was competed at this temperature. This observation is similar to results from standard sol gel pellets presented in the previous section of this chapter. For pellets sintered at 1000°C there are visible changes in intensify of peaks especially after 12 hours. The most mixed phase diffraction pattern resulted from the pellet sintered at 1000°C for 12 hours. The appearance of intense peaks in the region of the 2Θ angle of 42.5° with concomitant reduction of the intensity of the (002) peak can be noticed. In addition, the peak separation at the 2Θ angle of 16° can be seen that may suggest the appearance of another phase which was created due to length of time at high temperature. Further X-ray analysis has demonstrated the presence of a delicate peak associated with a hydrated phase[164] at a lower angle region of 2Θ for pellets sintered at 1000°C. This observation suggests that the presence of additional peak is a result of sintering at higher temperature (1000°C) resulting in a greater moisture-sensitive nature of the resultant pellets. These observations indicate a greater chemical stability of pellets sintered at 950°C.

On the basis of the observation of the diffraction pattern it is expected that SGBM-1000-12 pellets will behave differently.

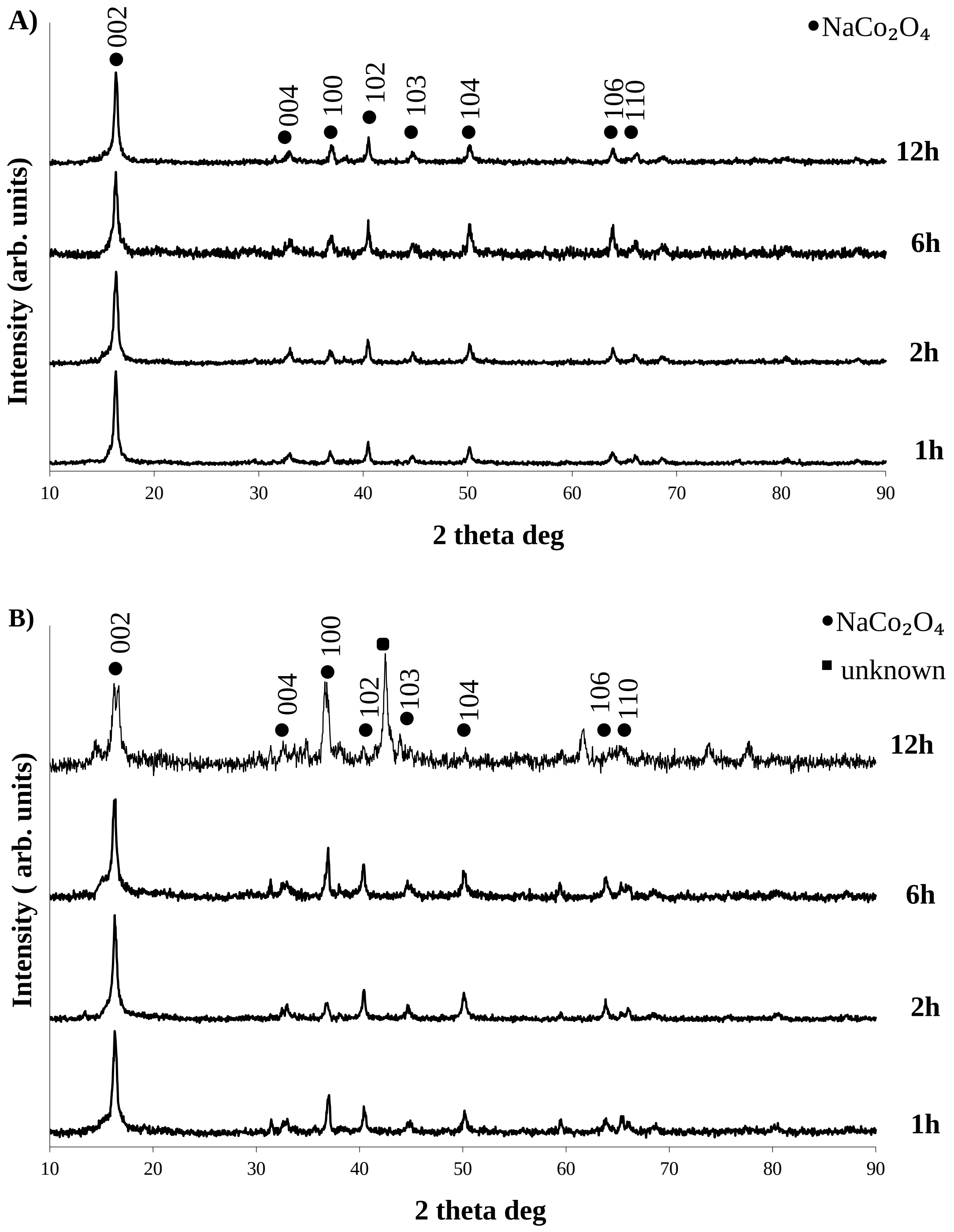

Figure 80 X-ray diffraction patterns of $NaCo_2O_4$ sol gel powder prepared pellets sintered at A) 950°C B) 1000°C for 1, 2,6 and 12 hours respectively. Presence of characteristic peaks assigned to $NaCo_2O_4$ (no.27 0682).

6.4.2.2 Microscopy analysis

The microstructural dependence on sintering temperature and time was determined by scanning electron microscopy. The influence of time on the microstructure is shown in Figure 81.

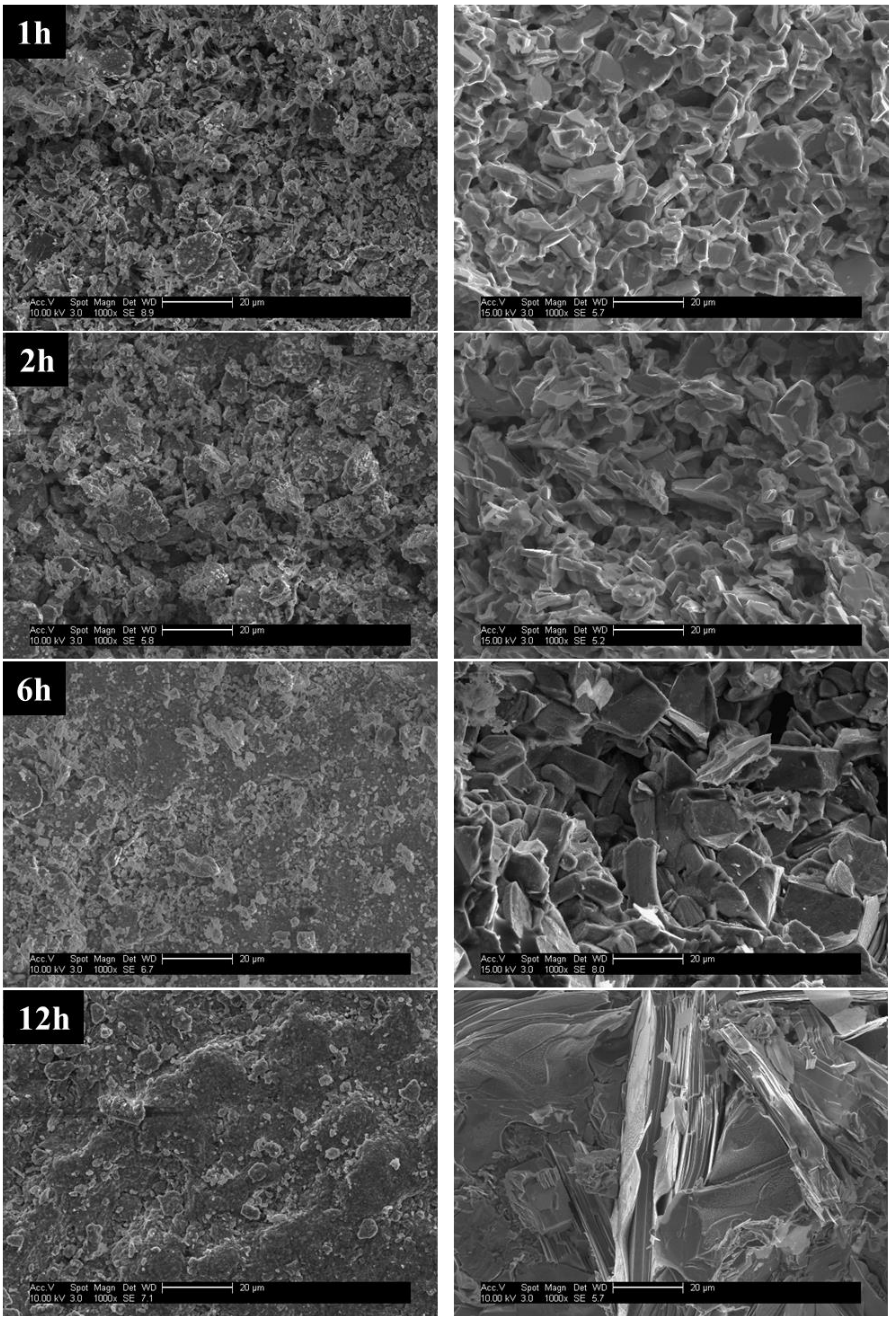

Figure 81 SFEG micrographs of surface and cross-section of pellets sintered at 950°C for 1, 2, 6, and 12 hours.

Changes are noticeable in the internal structure as well as on the surface of the sintered pallets especially for pellets sintered at 950°C. Therefore for pellets sintered at 950°C additional microstructure images of the surfaces and cross section have been presented. With increases in sintering time a smoothing of the surface of the sintered pellets can be noticed. These differences are visible even to the naked eye. The micrographs of the cross sections indicate an increase in grain size and the creation of more dense structure with increases in sintering time. When compared to previously described pellets made of sol gel powder, the Na rich pre-treatment pellets exhibit greater grain size together with higher density. Along with the increase of sintering temperature further smoothing of the surface can be seen, however these differences are small with increasing sintering time. For this reason for pellets sintered at 1000°C the micrograph of sample cross sections are shown in Figure 82.

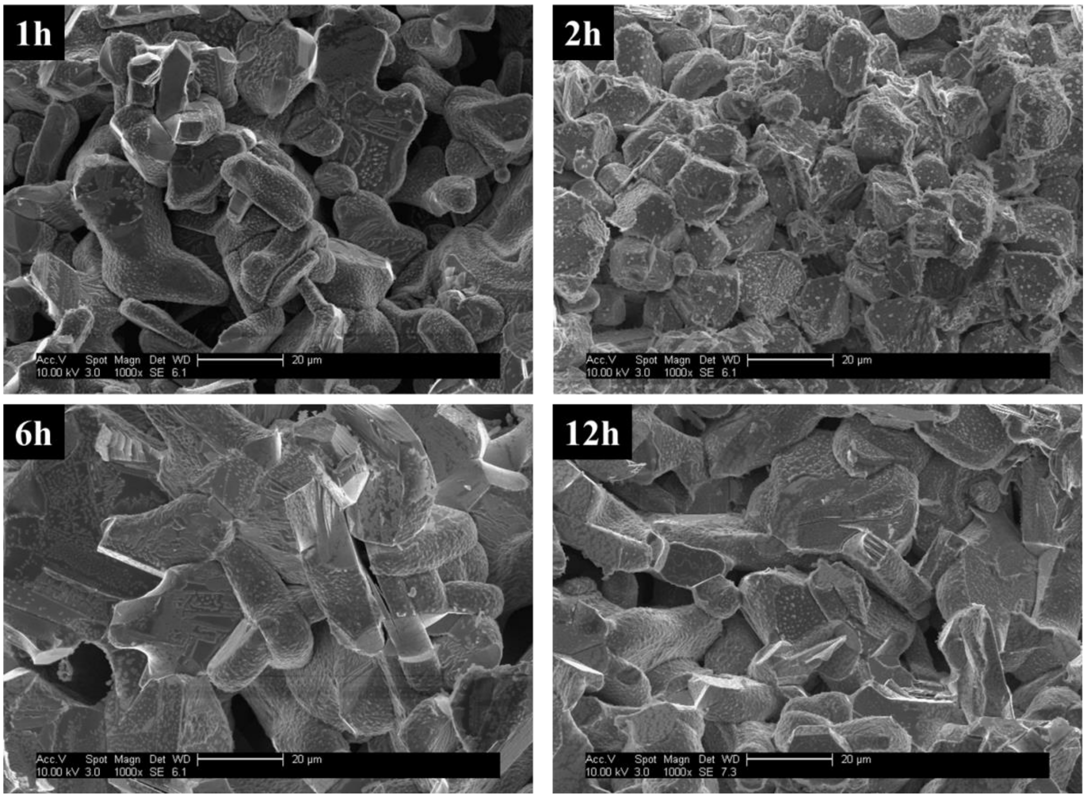

Figure 82 Micrographs of cross-sections of ceramics sintered at 1000°C showing influence of sintering time and visible effect on the microstructural changes.

Increasing of the time and temperature of sintering was found to result in densification of pellets, observed via microscopic analysis, changes and the observed decrease in the volume of the sintered pellets.

In order to study the effect of temperature over a wider range pellets were also sintered at temperatures of 850°C, 950°C and 1000°C for 6 hours. A sintering time of 6 hours was chosen on the basis of studies showing that the most pure and well crystallized phase of $NaCo_2O_4$ was obtained with this time. The influence of sintering temperature on the structural changes is presented in Figure 83. From the micrographs of cross sections of pellets sintering can be observed with a visible change in the structure starting from finely granular, through sintered aggregates and ending with the uniform dense layers. Besides the obvious different in grain size there also is change in the shape of the grains with different sintering temperatures.

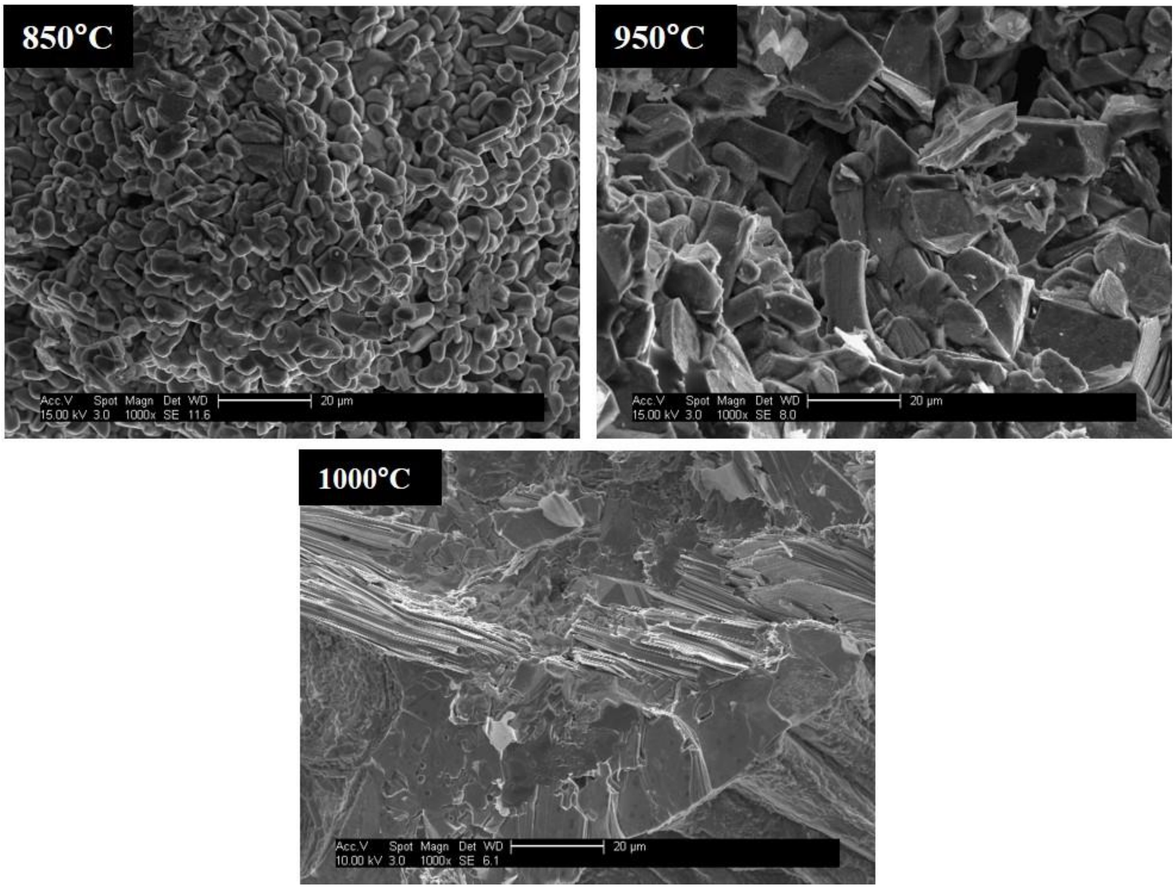

Figure 83 Micrograph of cross-section of $NaCo_2O_4$ ceramics sintered at 850°C, 950°C and 1000°C for 6hours.

Pellets sintered at a temperature of 850°C are characterised by a granular structure and the average grain size is approximately 10 μm. All grains were found to be oval-shaped. For sintering temperatures of 950°C the pellets were demonstrated to be denser with grains that are sharper multi-shaped in excess of 20 μm in size. After sintering at 1000°C the pellets exhibit a more complex structure. The cross-sections show well densified, almost forming a single body, giant grains, which when broken show a multi-layered structure. Each of these layers has nanometric dimensions.

6.4.3 Room temperature measurement

6.4.3.1 6.4.2.1 Thermal conductivity

Thermal conductivity was measured at low temperatures between 45-80ºC in the through thickness direction. The results obtained for ball milled sol gel samples (SGBM) sintered using different conditions are presented in Table 25. The results indicate that for samples sintered at 950°C longer sintering times reduce thermal conductivity. The highest value of κ can be observed for sintering times of 1 hour and 2 hours and was found to be close to 1 W/mK. For pellets sintered for 6 hours and 12 hours the thermal conductivity was found to be 0.7 W/mK. The low value can be assigned to the large-grained structure. As shown in the microscopic examinations of the structure the interior of the larger grains consists of multiple layers. Such a complex structure can slow down the flow of heat and results in the low value of thermal conductivity. For pellets sintered at 1000°C for 12 hours the thermal conductivity was found to be at the same value (0.7 W/mK) as for pellets sintered at 950°C for the same period of time (12 hours). Such low values of κ may also be due to the presence of the additional phase which was detected in the XRD pattern. In contrast, the thermal conductivity of the untreated sol gel powder pellets was found to be lower. This suggests that the Na rich pre-treatment is an effective method to enhance the thermal conductivity of sodium cobalt oxide ceramics.

Table 25 Thermal conductivity of ball milled NaOH pre-treated sol gel samples sintered at 950°C and 1000°C.

Time and temperature of sintering / **Average sample temperature[°C]**	**Thermal conductivity κ[W/mK] (+/- 0.1)**							
	950 °C **1h**	**950** °C **2hrs**	**950** °C **6hrs**	**950** °C **12hrs**	**1000** °C **1h**	**1000** °C **2hrs**	**1000** °C **6hrs**	**1000** °C **12hrs**
45	0.9	1.0	0.7	0.7	0.7	0.7	0.9	0.7
50	0.9	1.0	0.7	0.7	0.9	0.8	0.9	0.7
60	1.0	1.0	0.7	0.7	0.8	0.8	0.9	0.7
70	0.9	1.1	0.7	0.7	0.9	0.7	1.0	0.7
80	0.9	1.0	0.7	0.7	1.0	0.8	0.9	0.7

6.4.3.2 Electrical resistivity

The electrical resistivity tests made using the four point probe method are shown in Table 26.

Table 26 In plane electrical resistivity of sol gel ball milled (SGBM) samples sintered for different times and temperatures.

Sintering temperature / **Sintering time**	**Electrical resistivity [μΩcm] (+/- 3)**	
	950°C	**1000°C**
1 hour	283	255
2 hours	261	247
6 hours	218	211
12 hours	199	309

The results show that the use of short times has the effect of reducing the electrical resistivity. The increase of sintering time result in densification and reduces electrical resistivity. Moreover the measured value of electrical resistivity shows that the use of the ball mill NaOH pre-treatment for sol gel powders leads to a reduction in electrical resistivity.

6.4.3.3 Seebeck coefficient

The Seebeck coefficient measurements were performed at low temperatures in the through thickness direction. When compared to the untreated sol gel pellets the Na rich pre-treated pellets exhibit slightly higher values of Seebeck coefficient (Table 27). Pellets sintered at 950°C exhibit similar values with no clear trend. In the case of pellets sintered at 1000 °C for short periods of time the Seebeck coefficient was found to be 34 μV/K-35 μV/K. However, this value decreased in the case of pellets sintered for longer times. The pellets sintered at 1000 °C for 12 hours exhibit unusual behaviour with noticeably lower values of Seebeck coefficient. This behaviour can be the result of the presence of an additional phase which was observed in the diffraction pattern.

Table 27 Seebeck coefficient measured at low temperatures for NaOH ball milled pre-treated sol gel powder samples sintered using different conditions.

Sintering temperature **Sintering time**	**Seebeck coefficient [μV/K] (+/- 0.1)**	
	950°C	**1000°C**
1 hour	32.9	35.4
2 hours	34.2	34.2
6 hours	32.5	29.2
12 hours	35.1	(Figure 13)

The Seebeck coefficients, measured at different temperatures (45°C-80°C), of pellets sintered at 1000°C for 12 hours exhibited a large degree of variation and are shown in Figure 84. From the graph it can be seen that at the lowest temperature (45°C) the

Seebeck coefficient is negative which corresponds to n-type behaviour. When measurements above 50°C are made, the Seebeck coefficient changes sign to a positive value which corresponds to p-type material behaviour. A positive Seebeck coefficient is characteristic for sodium cobalt oxide. Such changes in behaviour of this specific prepared pellet are possibly caused by the presence of additional phases.

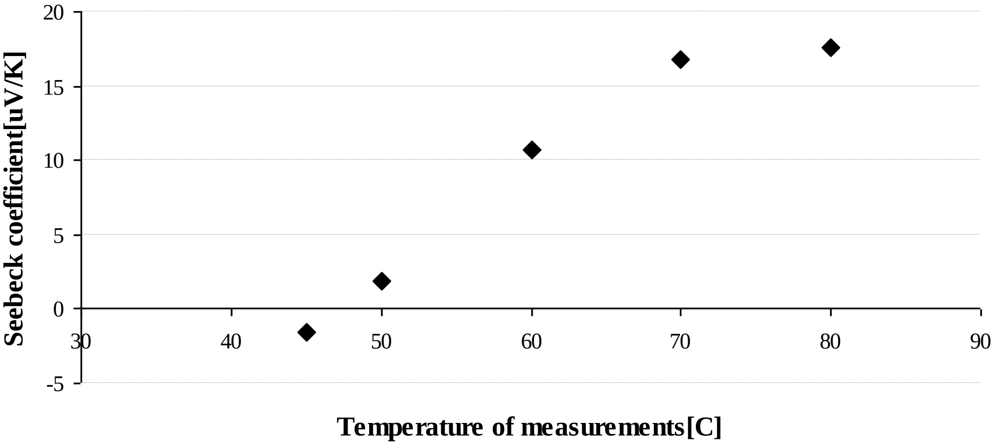

Figure 84 Temperature dependence of the Seebeck coefficient for ball milled sol gel samples sintered at 1000ºC for 12 hours (SGBM-1000-12).

6.4.4 High temperature thermoelectric measurement

The high temperature measurement of Seebeck coefficient and electrical resistivity was conducted in the in- plane direction. The results are presented in Figure 85.

The electrical resistivity drops slightly at temperatures between 100ºC -200ºC then increases and from around 390ºC reminds at approximately the same level of 270 μΩcm. The in- plane electrical resistivity was found to be 270 μΩcm – 300 μΩcm at low temperature and at around 600°C reached a value of 270 μΩcm. Similar to the results presented for mixed oxide pellets, the Na rich pre-treatment tends to stabilise the value of electrical resistivity at a similar level through varying temperatures. The

Seebeck coefficient SGBM-1000-6 pellets increases with increasing temperature. This trend is characteristic for sodium cobalt oxide with metallic behaviour.

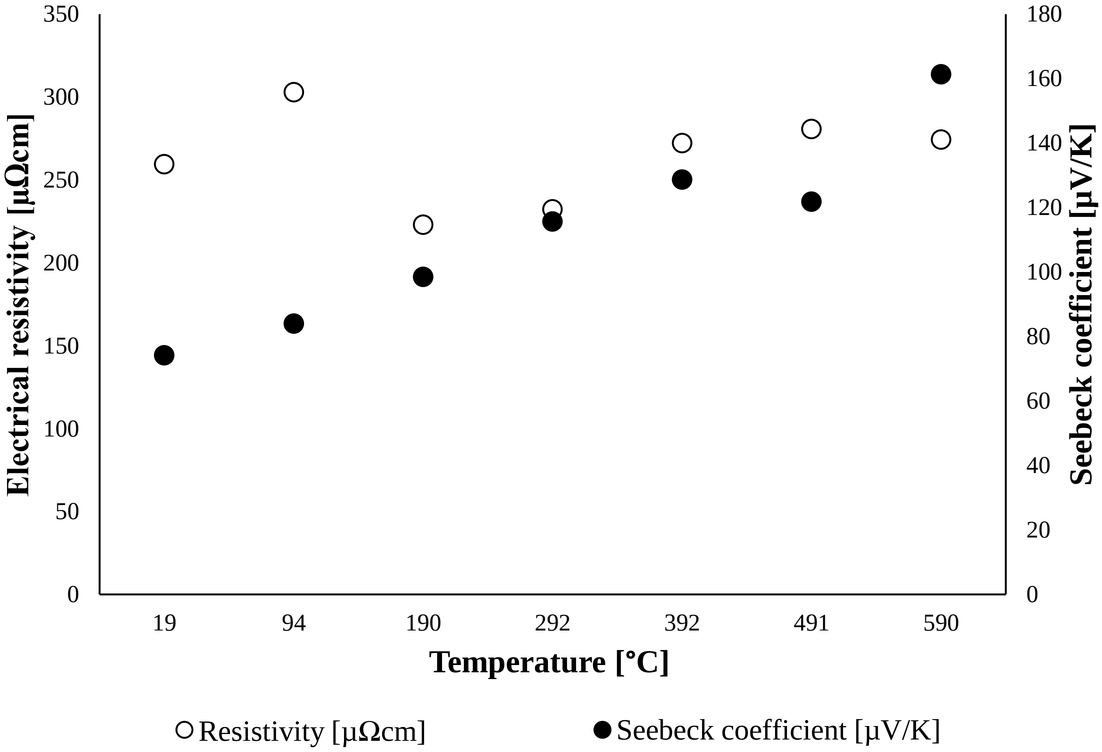

Figure 85 Temperature dependence of the electrical resistivity and Seebeck coefficient for ball milled NaOH pre-treated sol gel sample sintered at 1000ºC for 6hours (SGBM-1000-6).

The Seebeck coefficient was found to be higher than pellets prepared from untreated sol gel powder. That may confirm that the Na rich pre-treatment proposed in this work enhances the Seebeck coefficient.

6.5 Thermoelectric figure of merit ZT

The figure of merit ZT for all samples was determined by the Equation 8 and is shown in Figure 86. The calculated value of ZT was obtained for room temperature measurements.

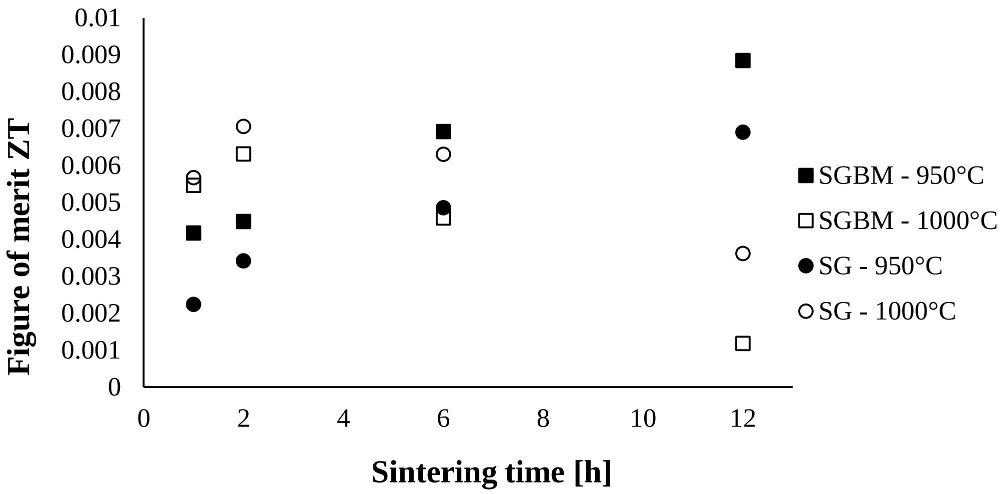

Figure 86 Figure of merit, ZT, of sodium cobalt oxide pellets produced using sol gel synthesis powder pellets and Na rich pre-treated sol gel samples, sintered at 950ºC and 1000ºC for 1, 2, 6 and 12 hours.

The results show that the NaOH ball milling pre-treatment enhances the thermoelectric performance of pellets especially at 950ºC. The biggest improvement was exhibited by the SGBM sample sintered at 950ºC for 12 hours and exhibited the highest value of ZT (0.009) at room temperature. From the results one can notice that the ZT value for both type of samples sintered at 950ºC increase with longer sintering time. The results shown that for untreated and Na pre-treated pellets, prepared from synthesized sol gel powder, when sintered at 1000ºC show changes in the ZT value. Increase sintering time at 1000ºC result in decrease of thermoelectric figure of merit ZT. System sintered at 1000ºC exhibited a maximum figure of merit at intermediate processing times due to competing phoneme that arise at elevated temperatures.

6.6 High temperature multi layered structure

Observations made during the microstructural studies of SGBM pellets sintered at 1000ºC showing the layered structure, led to a more detailed study of the structural change. The study showed that for pellets made from untreated sol gel powder as well as from NaOH ball milled pre-treated sol gel powder and sintered at 1000°C a characteristic a layered structure was formed. However, the layers were found to have different morphology depending on the method of preparation. These observations indicate the extremely important role played by the production route in creating the final microstructure as well as the nature and consequently the behaviour of the prepared pellets. Based on the results obtained in this work and literature it can be definitely concluded that each of the different stages of the production has a tremendous impact on the final properties of the material produced. The presented micrographs of, and measurements conducted on, sol gel (SG) powder pellets, show that with changes in duration of sintering the layers form different widths. The longer the sintering time, the greater the connection of layers. Changes in the structure caused by the use of different lengths of sintering times for SG pellets are shown in Figure 87. The measurements show that the SG pellet layered structure after 1hour of sintering have the thinnest layers with the average measured value of 167 nm. Pellet sintered for 2 hours have shown layers an average thickness of 225 nm. The pellet sintered for 6 hours exhibits the thickest layers at 260 nm.

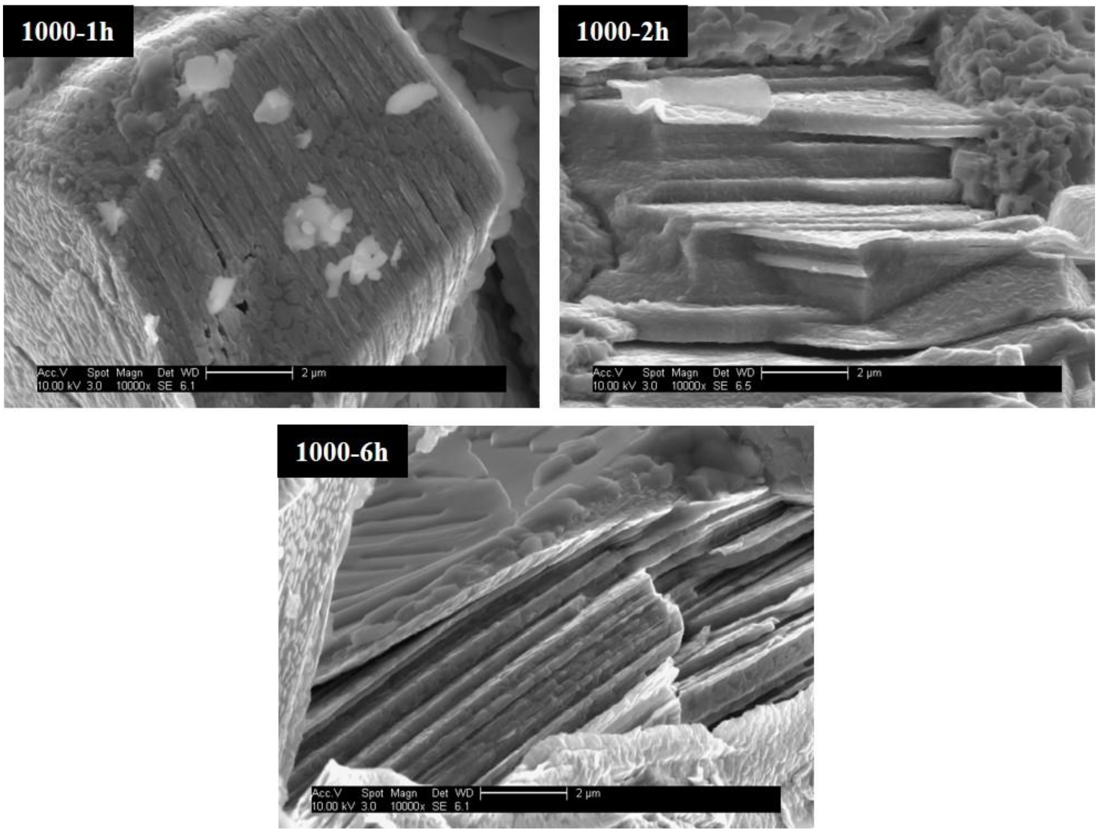

Figure 87 Micrographs of cross sections of SG pallets sintered at 1000°C at 1, 2 and 6 hours.

The opposite was found to occur with sol gel ball milled (SGBM) pellets sintered at the same temperature and for the same lengths of time as SG pellets with the thickness of layer decreasing with increased duration of sintering. It was also observed with SGBM pellets the presence of frequent breaks between the layers. The delamination seen in the layered structure is likely to be a result of the fracturing of the sample during preparation for microstructural analysis. The higher magnification micrographs presented in Figure 88 show the layered morphology of the SGBM pellets for different sintered times. The created layers after 1 hour of sintering were found to be of around 56 nm thick. Pellets sintered for 2 hours were characterised by narrower layers of an average value of 23.5 nm. The thinnest layers were found in pellets sintered for 6 hours.

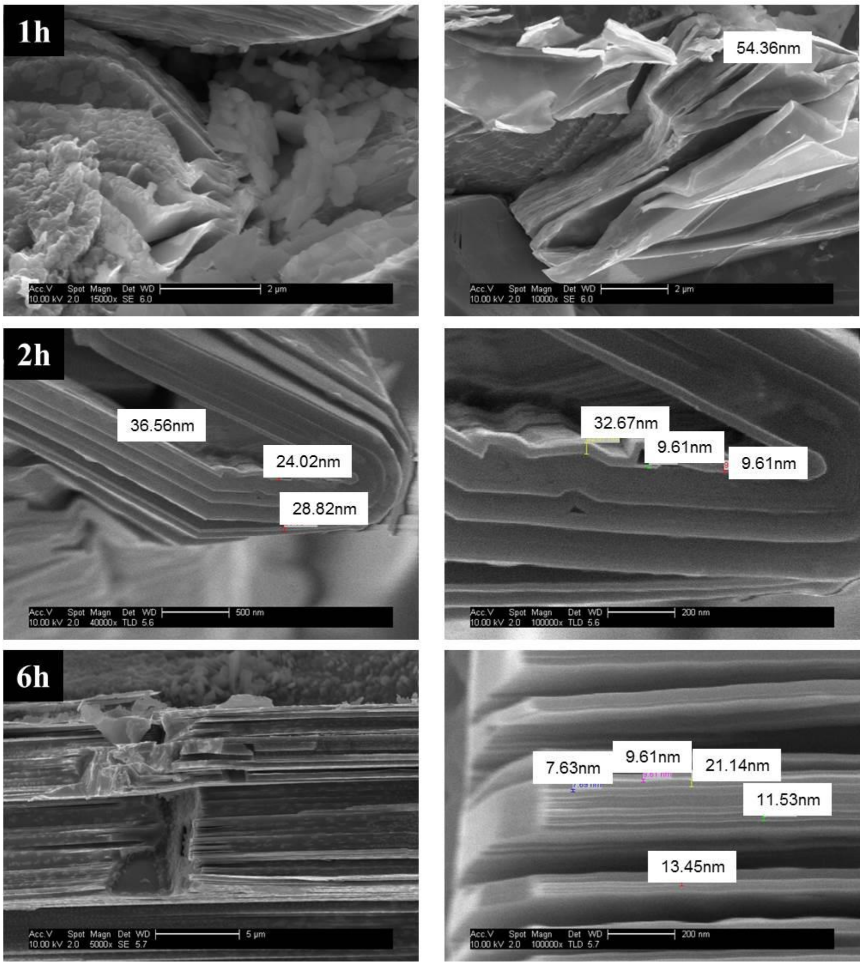

Figure 88 Micrographs of SGBM pellets sintered at 1000°C for 1hour, 2 hours and 6 hours.

The width of these layers, created after 6 hours of sintering, was found to be 12.5 nm. For pellets sintered at 1000°C for 12 hours the creation of large “grains” was observed. These were found to have a complex layered structure. A comparison of microstructures of samples produced with and without NaOH treatment are presented in Figure 89 in which the morphology differences can be clearly seen. In the case of SG pellets the large “grains” created were found to be longitudinal solids block oriented perpendicular to the pressing direction. In case of SGBM pellets the large “grains” were found to be solids blocks with a visible, repeated shape

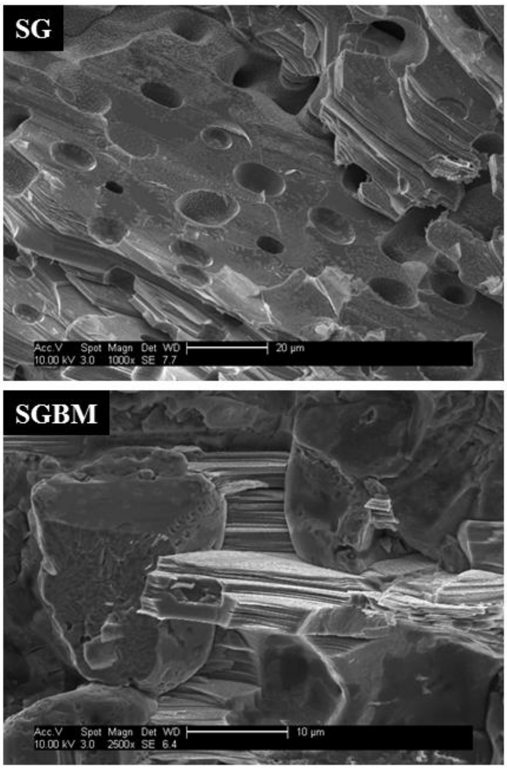

Figure 89 SFEG micrograph of a SG pellet sintered at 1000°C for 12 hours and a SGBM pellet sintered at 1000°C for 12 hours.

6.7 Summary

Two types of pellets were prepared from previously synthesized sol gel powder. Quantitative analysis demonstrated that the starting powders obtained by sol gel method and the traditional solid state reaction method had approximately the same composition.

The pellets referred to as SG were made from pure sol gel powder and SGBM pellets were made from sol gel powder that had previously been ball milled in an aqueous solution of NaOH. Both type of pellet exhibited changes in the microstructure with sintering time and additional differences were seen with increasing sintering temperature. Increasing the time and temperature of sintering was found to result in densification of the pellets for both SG and SGBM pellets. The microstructure of SG pellets after sintering at 950°C consists of a fine grained and relatively compact structure over the whole range of sintering times. The pellets exhibited alignment of the grains during. The increase the size of grains in only two dimensions under the influence of heat treatment was observed. The thermal conductivity was found to decrease with increasing sintering time and temperature and found to between 0.6 W/mK and 1.3 W/mK. The exception to this trend was found to be for pellets sintered at 1000°C for 12 hours which exhibited a value of 1.2 W/mK. However, when compared with pellets produced using the solid state reaction powder, the sol gel derived pellets clearly showed lower values of thermal conductivity. The measured Seebeck coefficient at low temperature showed small differences in the range 30 μV/K - 35 μV/K. The value was found to increase with longer sintering times. When increasing the temperature no significant changes in the value were observed. High temperature measurements of in-plane electrical resistivity found it to be 270 μΩcm – 300 μΩcm and the Seebeck coefficient showed a metallic behaviour with increasing temperature of measurement, with the highest value of 140 μV/K at around 600°C. SGBM pellets, when compared to SG pellets, exhibited larger grains size together with increased densification. With the increase of sintering temperature further smoothing of the surface of the SGBM pellets was observed. The Seebeck coefficients exhibited similar values with no trends. The value was found to be around 34 μV/K - 35 μV/K except for pellets sintered at 1000°C for 12 hours. It was observed that the increase of sintering time lead to a reduced thermal conductivity especially for samples sintered at 950°C. The highest value of κ, close to 1 W/mK was found for sintering time of 1 hour and 2 hours. For pellets sintered for 6 hours and 12 hours the thermal conductivity was found to be 0.7 W/mK. When compared with SG pellets the increase of thermal conductivity is visible. The electrical resistivity measured at high temperature was found to be 270 μΩcm which is similar to that observed in SG pellets. The Seebeck coefficient was found to be higher than seen for SG pellets with the highest value of 170 μV/K. The electrical resistivity measured at low temperature indicated that the use of Na rich ball milling as a pre-treatment favoured the enhancement of thermoelectric figure of merit due to the low value of electrical resistivity and thermal conductivity together with the higher value of Seebeck coefficient. This behaviour may be due to the material having a more complex structure.

For both types of pellets increasing the sintering temperature has been found to create a complex layered structure. Increasing of the sintering time affects the thickness of those layers. In the case of SG pellets the prolonging of sintering time increases the thickness of the layers, while for SGBM a reduction of layer thickness was observed.

The use of high temperature sintering for 12 hours with SGBM pellets leads to the creation of an additional phase which consequently affects the properties of the final bulk ceramic material.

6.8 Conclusion

$Na_xCo_2O_4$ pellets can be fabricated through the use of a sol gel derived powder sintered at between 950°C and 1000°C for 1-12 hours. The NaOH pre-treatment enhances the thermoelectric figure of merit by increasing the Seebeck coefficient by 17% and reducing electrical conductivity by 4% and thermal conductivity by 58% when compared with unpretreatment samples (SG). The thermoelectric figure of merit is maximised when SGBM pellets are sintered at 950°C for 12 hours.

Chapter 7 Sodium cobalt oxide thick films

7.1 Introduction

In the available literature not much work could be found on the sodium cobalt oxide films. The films are generally prepared by a flux method[165], epitaxial growth[166] or electrospun[147]. Chia-Jyi Lui described the fabrication of superconductivity films using sol-gel spin deposition[115]. The main objective of the work presented in this chapter is to produce thin and thick layers of sodium cobalt oxide by spin coating. The deposition method was initially established by Barrow et al.[167] and enhanced by Dorey et al.[168]. To improve the quality of the films several parameters were considered: inclusion of sol based layers, influence of used substrate, and use of different dispersant and application of different heat treatment.

7.2 Results of multilayer's deposition

7.2.1 Sol based films

EDX analysis has the greatest changes in chemical composition occur at low temperatures corresponding to chemical decomposition, pyrolysis (S. Katsuyama et al.[90]) and finally the formation of sodium cobalt oxide with more stable stoichiometric ratio. SEM micrograph and EDX graph obtained from sample heat treated at 700ºC for 30 minutes are shown in Figure 90. The heat treatment of sol based films at 550°C and 700°C did not affect the chemical composition and the atomic % ratio of Na to the Co atom is approximately 0.2 for these two mentioned temperatures.

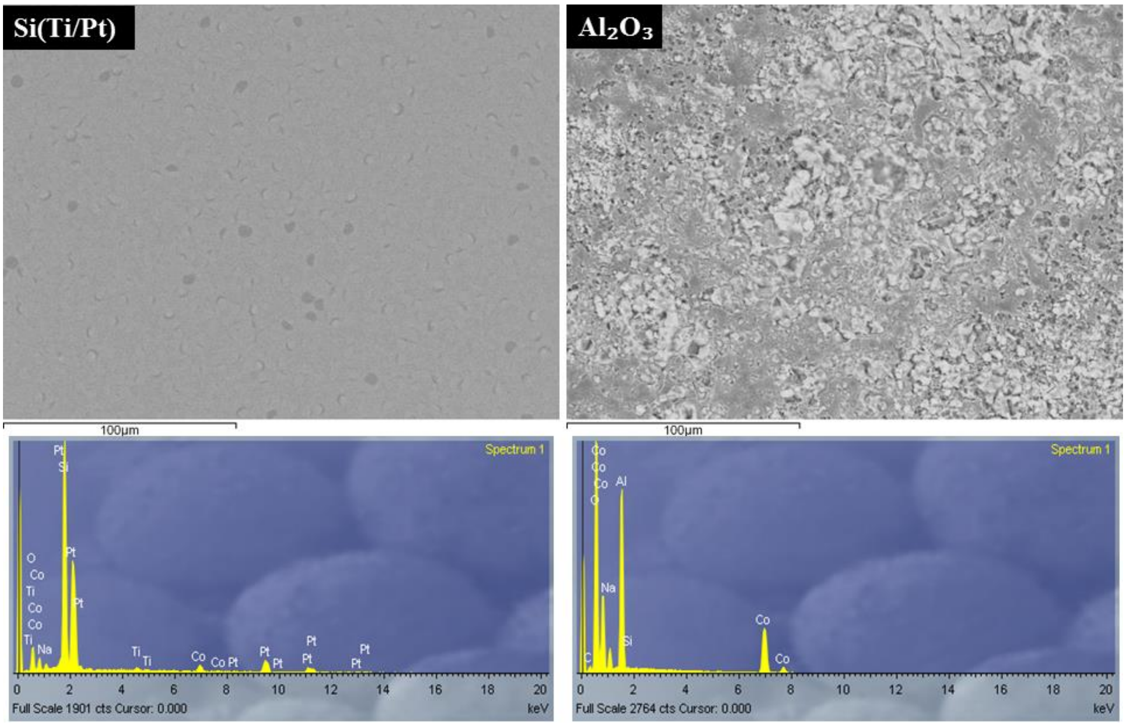

Figure 90 SEM micrographs and EDX analysis graph for single sol layers deposited on Si(Pt/Ti) and Al_2O_3 wafers heat treated at 700ºC for 30 minutes.

The X-ray diffraction analysis shows evidence of a well-crystallized phase apparent for films subjected to sintering at higher temperature. The X-ray analysis of the films indicated that the formation of sodium cobalt oxide phase occurs regardless of the substrate being used. The heat treatment of 450°C was found to be too low and the most characteristic peak for sodium cobalt oxide, corresponding to Miller indices (002), was not observed (Figure 91).

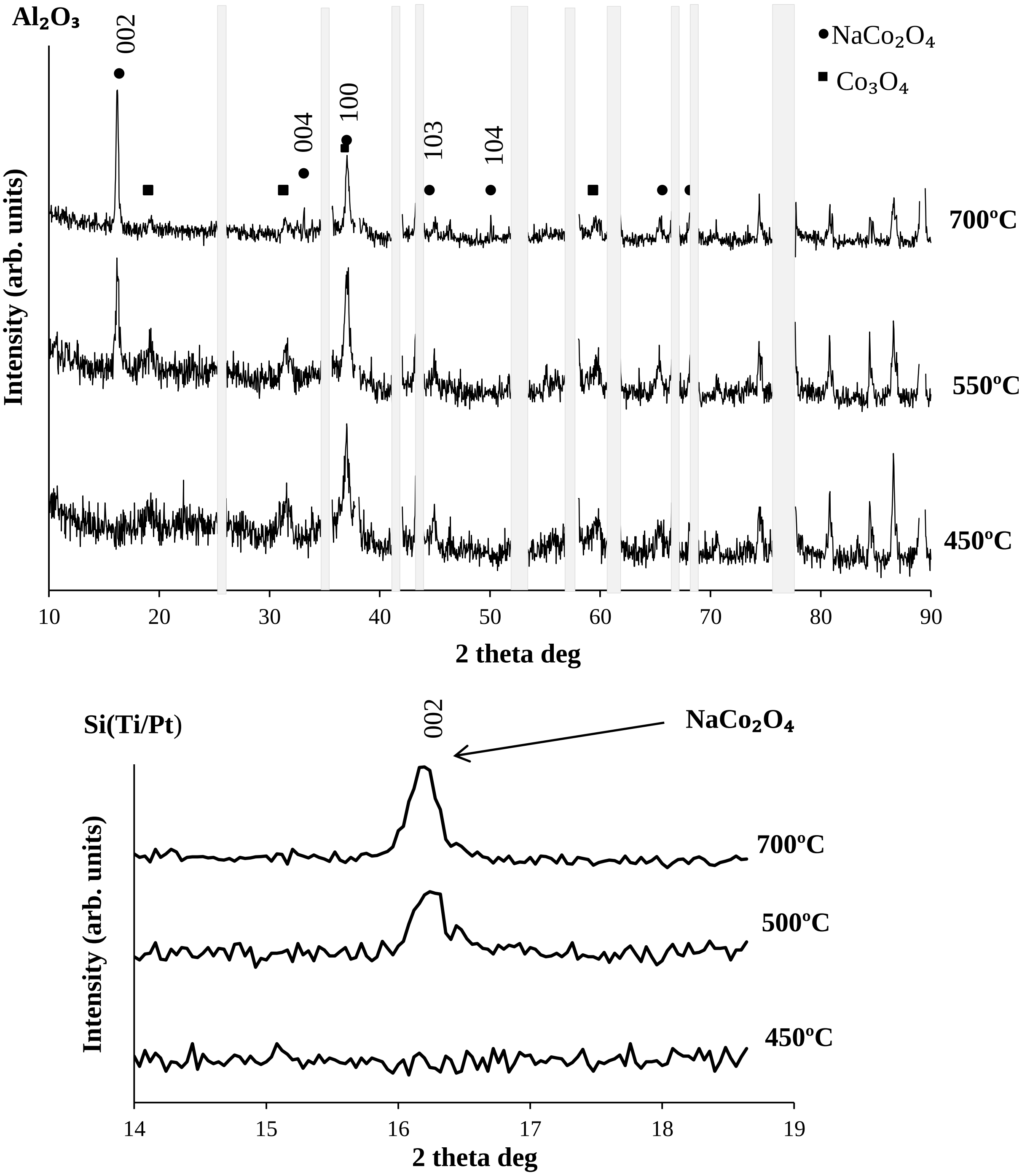

Figure 91 XRD diffraction patterns for sol films deposited on Al_2O_3 and Si(Pt/Ti) wafers heat treated at 450ºC, 550ºC and 700ºC for 30 minutes (light gray lines correspond to peaks from the substrate used).

The thickness of single sol layer deposited on Si(Pt/Ti) and Al_2O_3 was found to be around 200 nm. This study indicates crystalline sodium cobalt oxide layers can be prepared successfully using spin coating and a thermal treatment at 700°C. These processing conditions will be used as the basis for further work for the preparation of thicker layers.

7.2.2 Comparison of the sequence of building layers

The XRD analysis of dried ink (SSR powder + sol solution) confirmed the presence of sodium cobalt oxide phase as well as the presence of additional phases of possibly reacted and unreacted material (Figure 92).

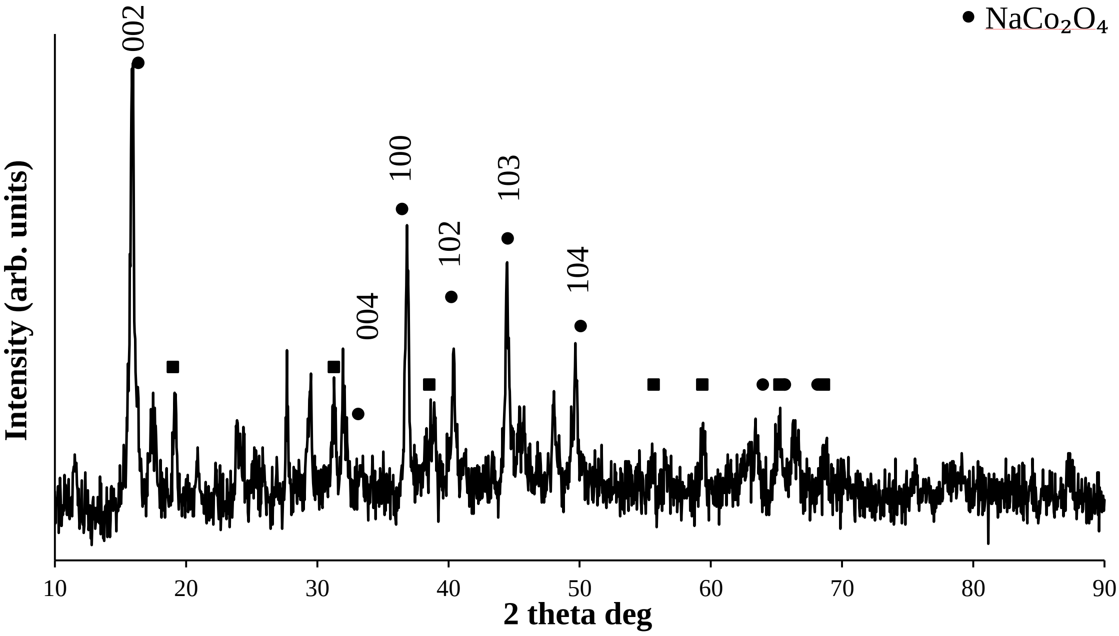

Figure 92 XRD pattern of dry ink (SSR powder +sol solution) without heat treatment with visible $NaCo_2O_4$ phase marked with black circle.

Presence of peaks corresponding to Co_3O_4 (JCPDF no.43 1003) was expected as it occurs in the powder used. The visible multiple peaks in the angular range between 20 and 36 correspond to cobalt nitrate hydrate (JCPDF no.01 0317).

A range of film thicknesses were achieved. Ranging from 200 nm for single sol film up to ~ 32 µm for 4 (ink + 2 sol layers) films. The structure of the films was found to depend on processing conditions.

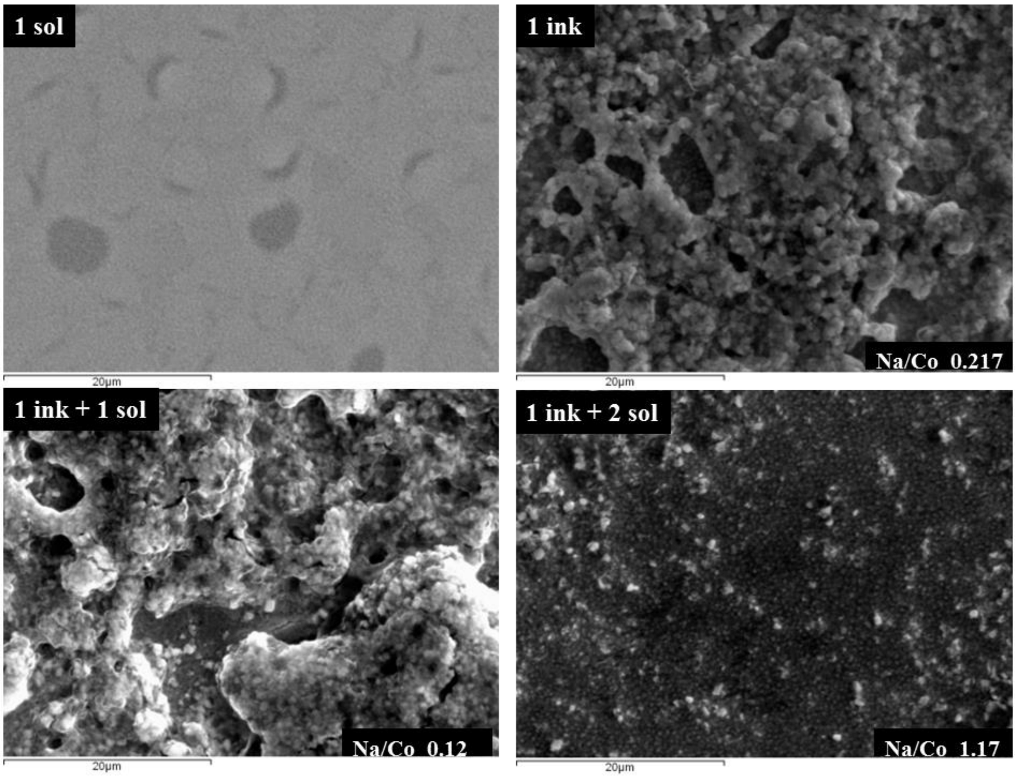

Figure 93 Figure SEM micrograph of effect on infiltration on surface of layered $Na_xCo_2O_4$ films spin coated on platinium/titanium coated silicon wafer.

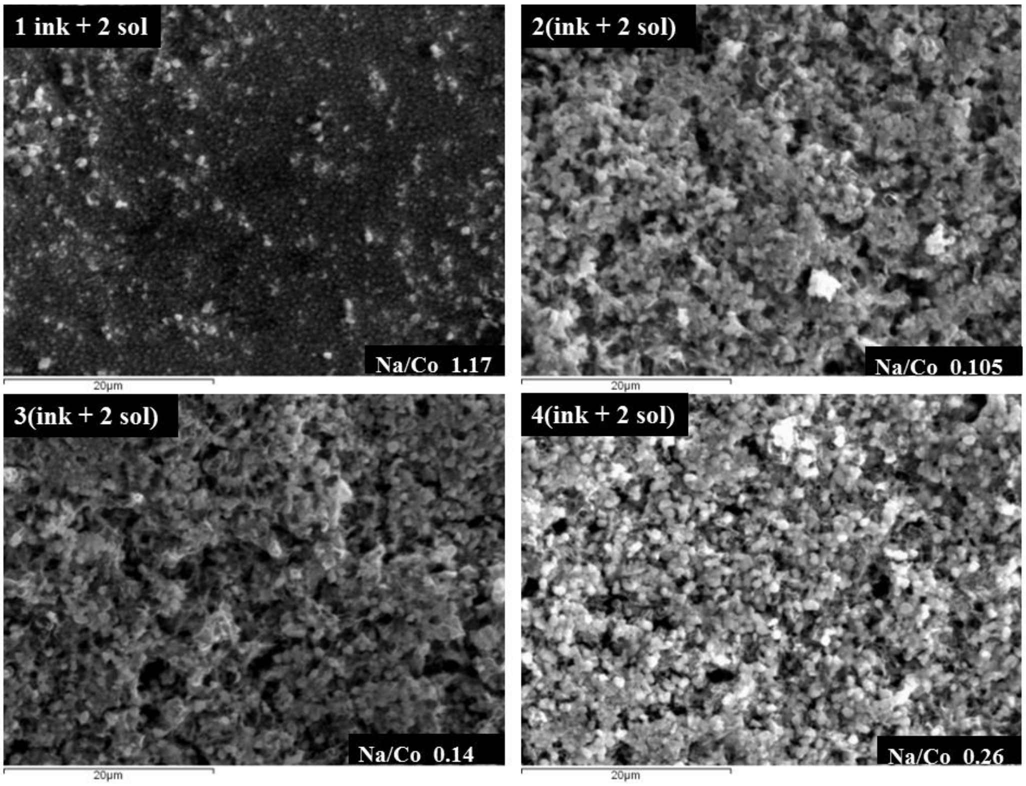

Figure 94 SEM micrograph of surface of layered $Na_xCo_2O_4$ films on platinium/titanium coated silicon wafer.

As shown in Figure 93 layers of pure sol exhibit a smooth surface, while the ink based films are rough and destroyed. That may indicate too short or too low heating time resulting in the presence of an unfavorable components. Infiltration of coatings with sol increases the density[168]. Sol infiltration of each layer also increases the wettability of inks which improves the inter-layer adhesion which consequently leads to a better quality of films (Figure 94).

7.2.3 Effect of powders on film quality

$NaCo_2O_4$ powders prepared by sol gel (SG) and solid state reaction (SSR) were used to prepare thick films. SEM micrographs of both powders are shown in Figure 95. The SSR particles are spherical in shape and have an average size of 9.5 μm while SG particles are ~1 μm in diameter and appear more plate-like.

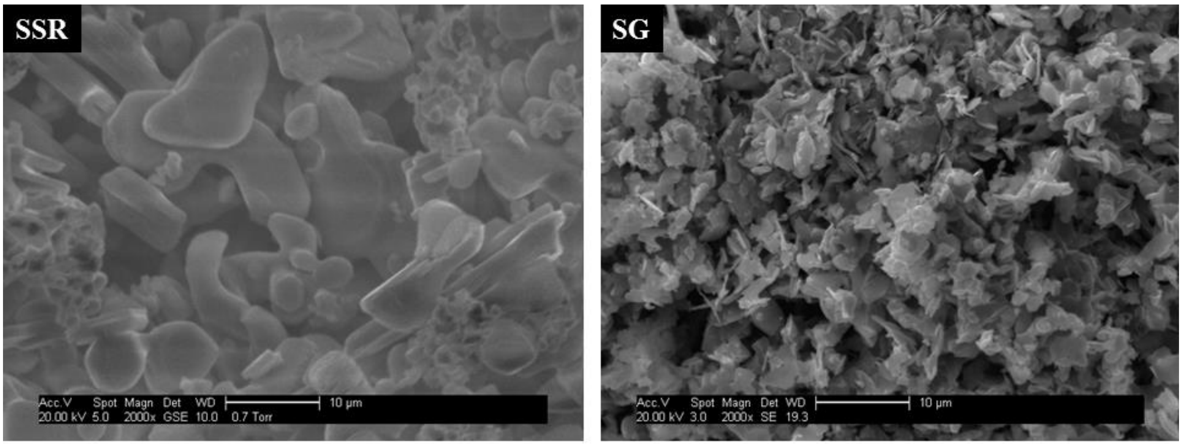

Figure 95 SEM micrographs of two powders a) SSR b) SG after calcination.

The XRD patterns obtained from SSR and SG powders are shown in Figure 96 and reveal the presence of characteristic peaks associated with $NaCo_2O_4$ (JCPDF no.27 0682).

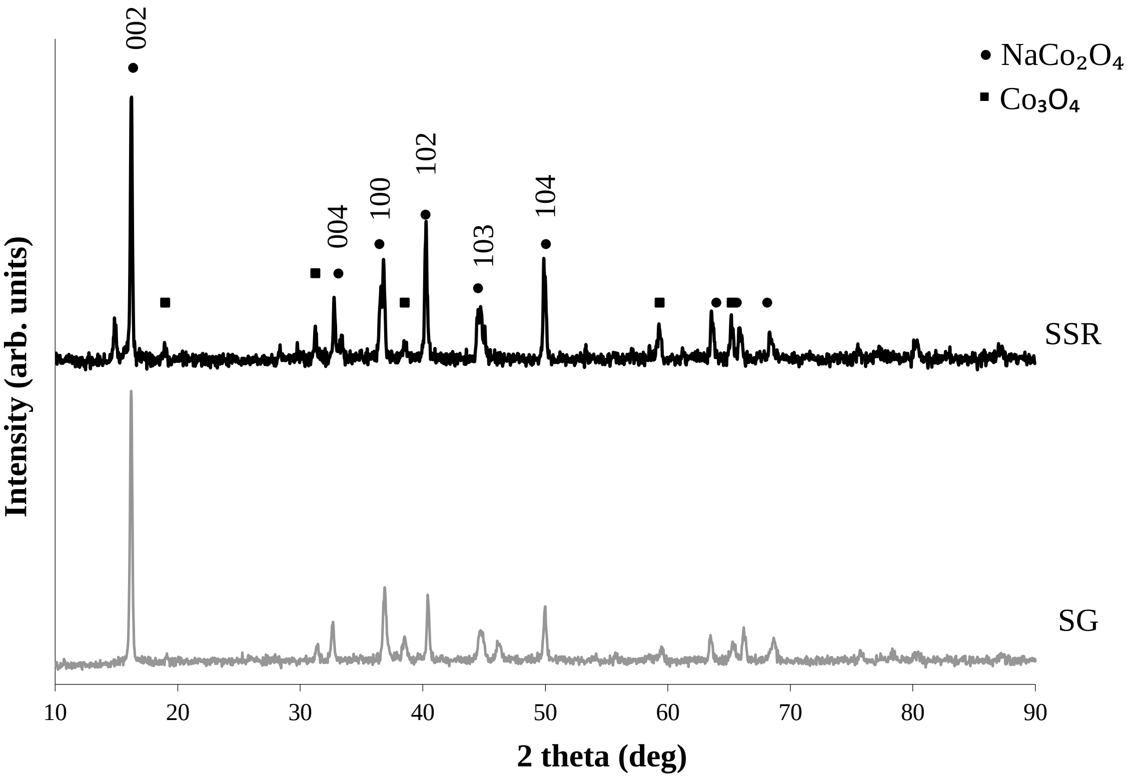

Figure 96 XRD spectrum of the selected powders (SSR, SG)

Figure 97 shows the SEM microstructure of $NaCo_2O_4$ films made using SSR and SG powders, and different dispersant (SURFYNOL CT 151 and 324) deposited on Si(Pt/Ti) substrate. The particles presented in the SG film are uniform in size and small (~2µm) forming homogenous layer of the film. The large range of particle size (2-10µm) presented in the SSR film results in a homogenous structure.

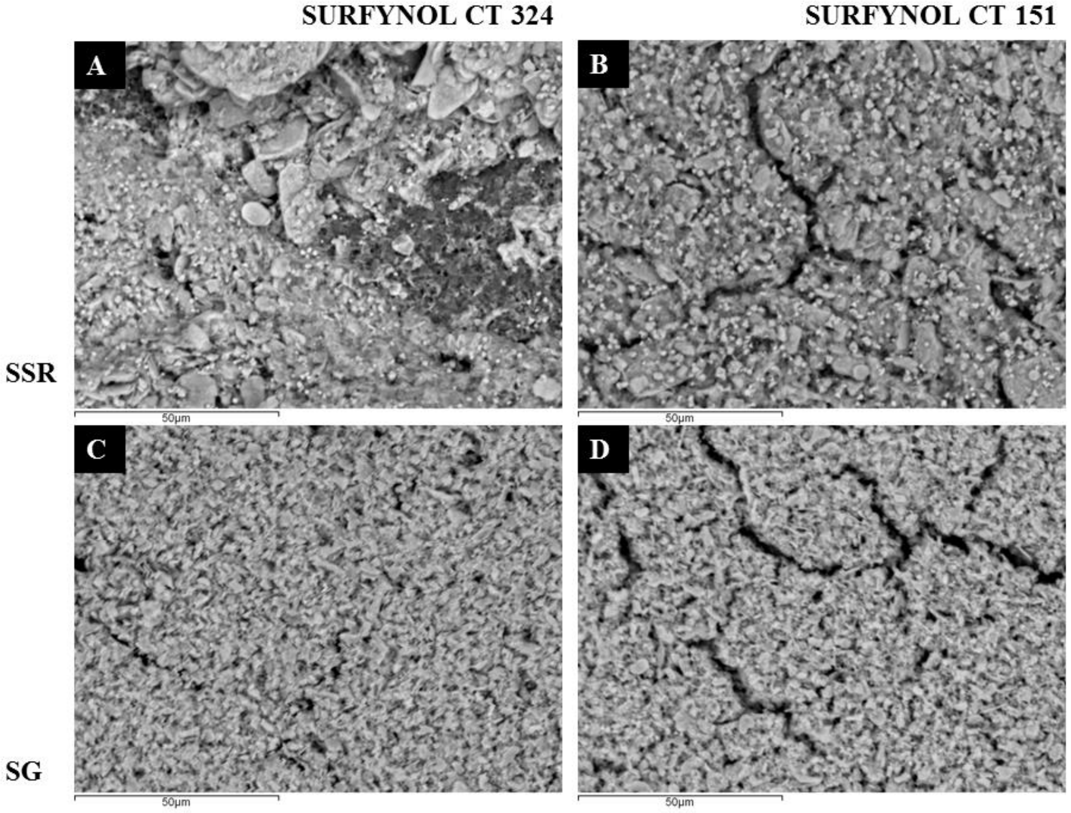

Figure 97 SEM microstructure of 4(ink + 2 sol) films on Al_2O_3 substrate prepared from: A) SSR-324 ink, B) SSR-151-ink, C) SG-324-ink and D) SG-151-ink. Layers were preheated at 450°C and annealing at 700°C.

Trace quantities of sodium carbonate which was present in the SSR powder in contact with the acidic sol environment formed CO_2[85] which result in crumbling and flaking of layers. It is known that the thermal decomposition of sodium citrate occurs at temperatures > 230°C. Therefore with the increase of sintering temperature the reduction of sodium content could be observed especially for SSR inks (Table 28) as the sodium nitrate decomposes.

Table 28 EDX analysis for 4(ink+2sol) layers sintered at 550°C and 700°C with a preheating of 450°C.

SSR 550°C			
	Na	**Co**	**Na/ Co atomic ratio**
Spec 1	11.63	24.19	0.48
Spec 2	11.52	27	0.43
Spec 3	11.38	25.67	0.44
SSR 700°C			
Spec 1	4.29	39.41	0.11
Spec 2	4.24	38.27	0.11
Spec 3	3.66	31.44	0.12

7.2.4 Effect of dispersant on deposited layers

There was a noticeable difference in the appearance of the film depending on which dispersant was used (SURFYNOL CT 151 and 324). These visible differences are shown above in Figure 97.

In order to maintain the good electric properties of the final product, it is important to control not only the microstructure of the film but also the amount of Na which should be maintained at the appropriate level. It has been found that the presence of dispersant affects the content of Na in the final film. The same content of Na was observed in the two starting powders during EDX analysis where no dispersant was presented. Using SURFYNOL CT 324 as a dispersant the amount of Na was 7.27 at % for SG-powder films and 1.36 at% for SSR-powder films while in case of 151 was 4.32 at % for SG-ink and 5.35 at% for SSR-powder films thermal treated at 700°C for 30 min (Table 29).

Table 29 EDX analysis of powder produced by Solid State Reaction method (SSR powder) and Sol Gel method (SG powder) and EDX analysis of films produced from inks with SURFYNOL CT 324 and SURFYNOL CT 151 dispersant and the two powder types.

Type of dispersant / powder	**Na atomic %**	**Co atomic %**	**Na/Co atomic ratio**
SSR powder	15.89	29.91	0.53
SG powder	16.04	32.05	0.5
SURFYNOL CT 324 – SG ink	7.27	35.31	0.2
SURFYNOL CT 324- SSR ink	1.36	36.7	0.04
SURFYNOL CT 151-SG ink	4.32	38.94	0.11
SURFYNOL CT 151- SSR ink	5.35	35.89	0.14

From XRD analysis (Figure 98) can be deduced that for both the used dispersant, SURFYNOL CT 151 and SURFYNOL CT 324 the phase of sodium cobalt oxide was identified.

The results indicated that the two dispersants have no significant effect on the chemical composition but nevertheless when the micrographs are compared (Figure 97) the SG-324 is distinguished as the most homogeneous structure of the films.

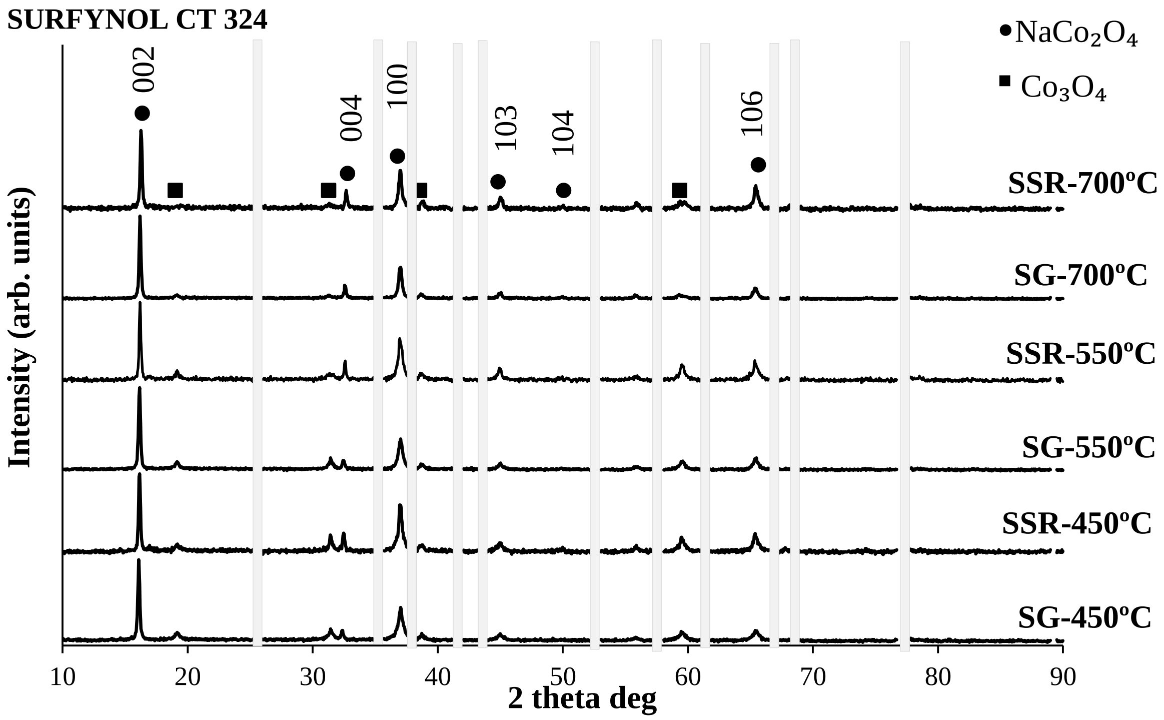

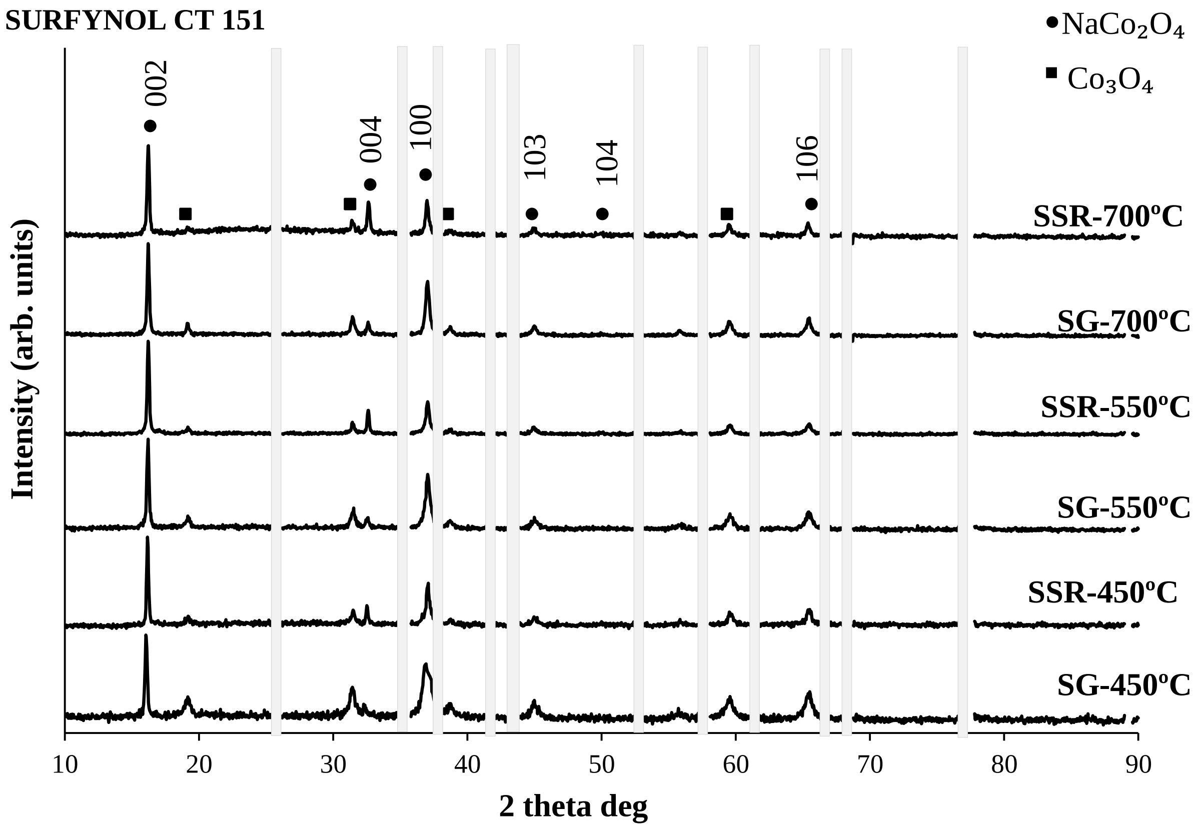

Figure 98 XRD analysis on sintered at different temperatures films produced from SSR ink and SG ink using SURFYNOL CT 324 and SURFYNOL CT 151 as dispersant (light gray lines correspond to peaks from the substrate used).

Based on the results obtained, SG powder and SURFYNOL CT 324 dispersant were chosen for further research.

7.2.5 Influence of temperature treatment

7.2.5.1 Preheating temperature:

The appearance of the films depended strongly on the preheating temperature used. Figure 99 shows SEM micrographs of the cross section for SG-324 films on Si (Pt/Ti) preheated at A) 450ºC and B) 700ºC both films were annealed at 700ºC. With preheating at 700ºC pores appeared along with pore-penetrating networks. Differences in particle size were also observed when the preheating temperature was changed. At 450ºC the size of the particles was 2µm while smaller (0.8µm) and more spherical particles were obtained at 700ºC.

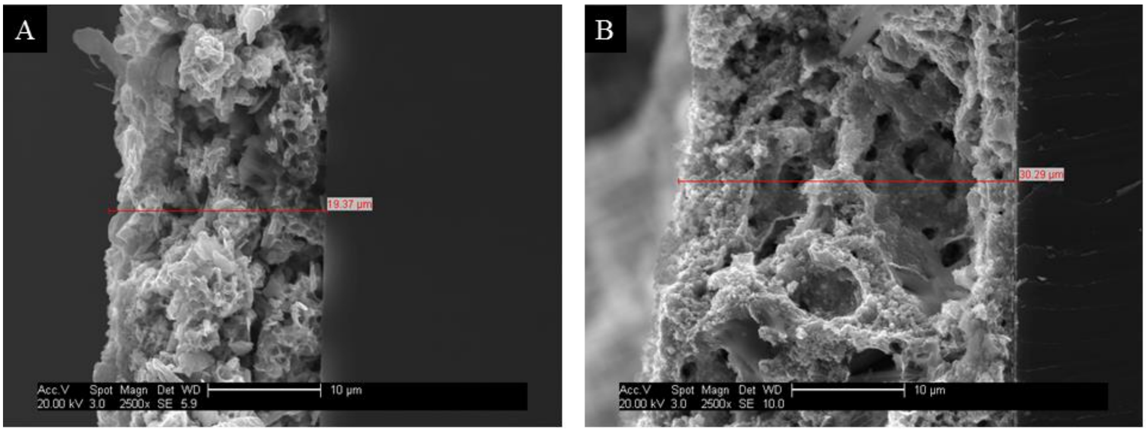

Figure 99 SEM micrographs of cross section for SG-324 films on Si(Pt/Ti): A) preheated at 450°C and annealing at 700°C, B) preheated at 700°C and annealed at 700°C.

The changes in the microstructure affected the electrical conductivity of these materials. Table 30 shows the results from electrical measurements of the prepared films. Preheated at 450ºC, 550ºC, 650ºC and 700ºC, as the preheated temperature was increased the resistivity decreases form 496.2µΩcm to 257.9µΩcm. Porous structures are usually is accompanied by an increase in electrical resistance. The opposite behaviour is observed in the present study indicating the creation of electrically conducting networks. The resulting network stabbing structure of pores is working as a kind of connection between the layers which allows facilitating transport property.

Table 30 Electrical properties of $NaCo_2O_4$ films preheated at different temperatures and annealed at 700°C.

Temperature of preheating	**Electrical resistivity ρ [μΩcm]**	**Electrical conductivity σ [S/cm]**
450°C	496	$2.01 \cdot 10^{-2}$
550°C	371	$2.70 \cdot 10^{-2}$
650°C	307	$3.25 \cdot 10^{-2}$
700°C	258	$3.88 \cdot 10^{-2}$

7.2.5.2 Annealing temperature.

The annealing process did not significantly affect the size of the grain structure, but it does did affect the Na content of $Na_xCo_2O_4$ films especially for SSR based inks, (Figure 101). Annealing temperature also affected the surface of the films. With increasing temperature cracks appeared and the surface of the layers became rougher. From the EDX analysis it is know that with increasing temperature the Na contents decreases. Increasing the temperature above 800 °C would accelerate this effect as at temperatures above 800°C Na becomes very volatile[149]. This increased evaporation and accompanying reduction in volume of Na led to the delamination of film as shown on Figure 100.

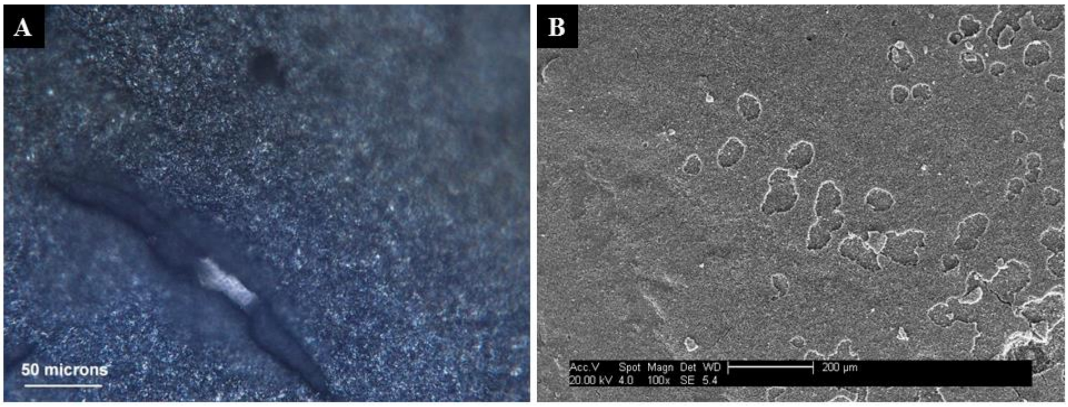

Figure 100 Images bringing to the fore the destruction of the surface of films under influence of temperature A) optical image of surface of $Na_xCo_2O_4$ – [4(ink+2 sol)] film, B) SEM image of surface of $Na_xCo_2O_4$ – [4(ink+2 sol)] film after annealing at 800 ºC.

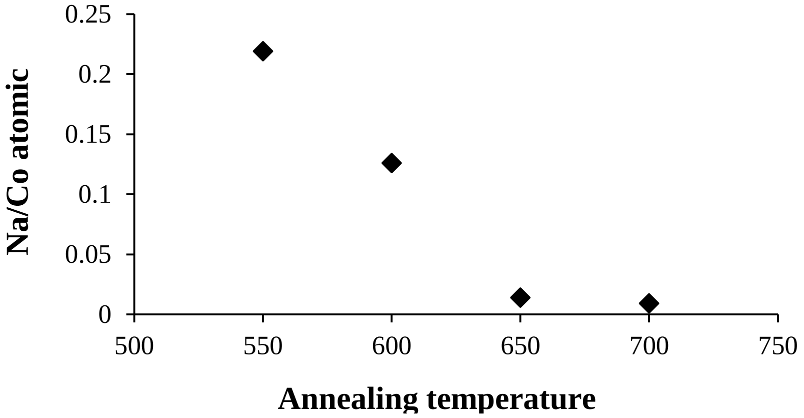

Figure 101 Variation in Na:Co atomic ratio as a function annealing temperature for $Na_xCo_2O_4$ films prepared by spin coating as a 4(ink+2sol) layers using a SSR-151-ink.

The lowest film resistivity was obtained from films annealed at 700ºC. The resistivity of films annealed at this temperature was calculated to be 257.9 μΩcm.

It was found that the preheating temperatures as well as the annealing temperatures have an impact on the roughness of final films.

Figure 102 shows the variation in surface finish of films obtained using different preheating and annealing temperatures.

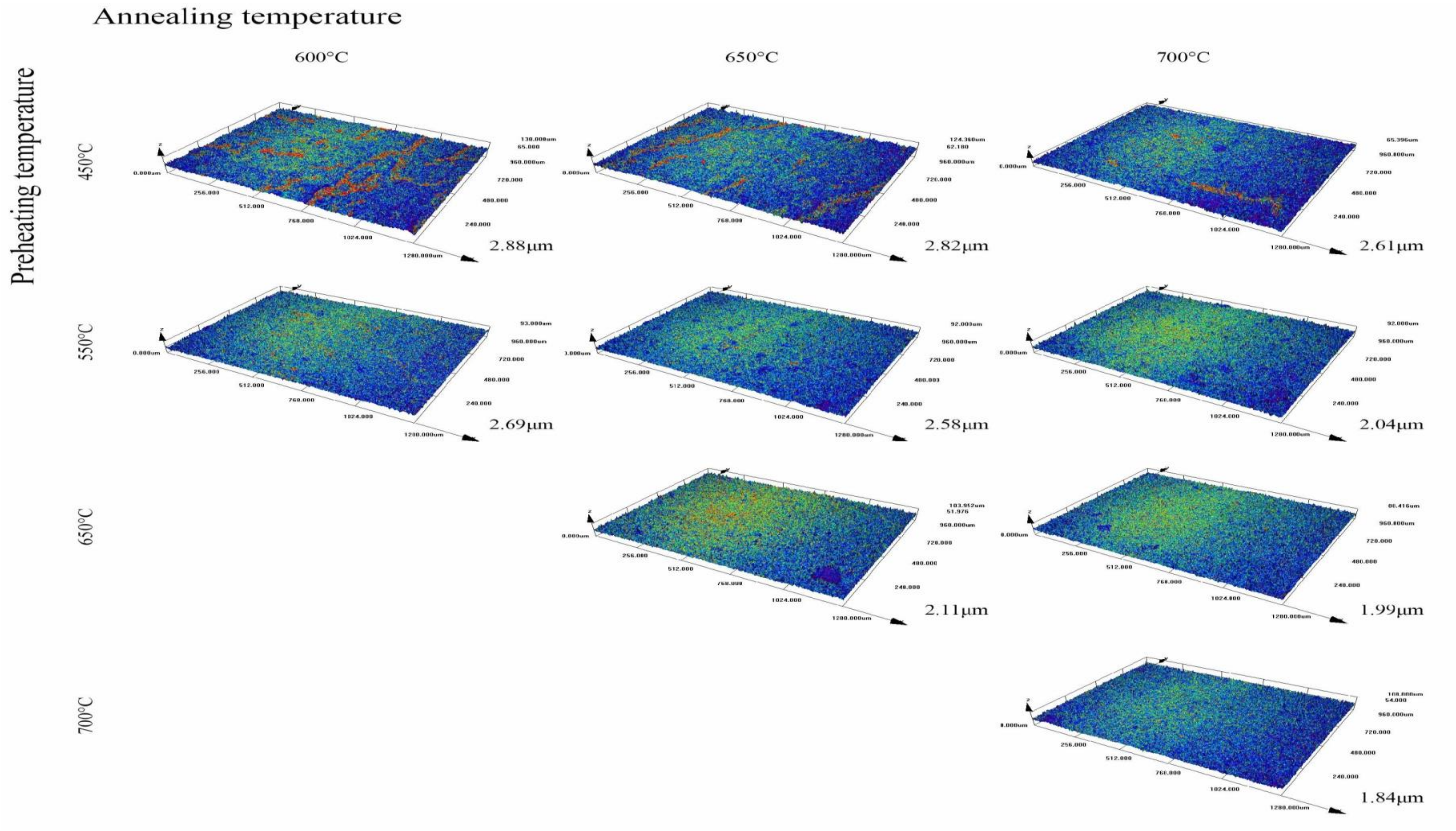

Figure 102 Confocal microscope micro-topography and surface roughness of obtained films under different preheated and annealing heat treatment.

The results obtained reaffirm a marked decrease in roughness with increase of both treatment temperatures. The reduction in roughness of films may be due to total decomposition of components during the preheating stage that eliminates the later release of gases and as a consequence cracking and chipping of the upper layers.

7.2.6 Effect of duration of temperature treatment on final films

The duration of annealing (5, 15, 30 minutes) during preparation of films does not significantly affect the properties of films. It was found that the microstructures as well as the Na content were not changed markedly under the influence of time. As an example Figure 103 shows variation of Na content in SG-324-4(ink + 2 sol layers) films after annealing at 550°C and 700°C for 5 and 30 min.

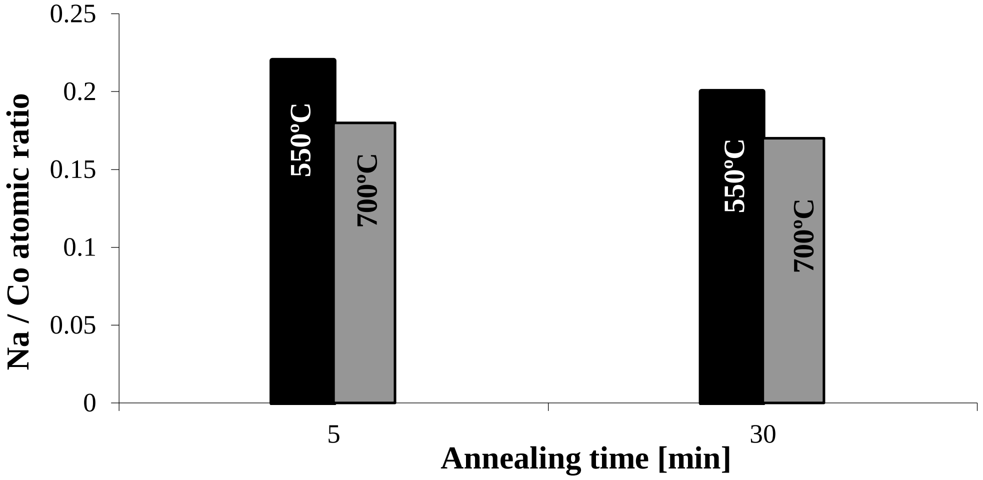

Figure 103 Dependence of chemical composition on temperature and time of the annealing process.

7.2.7 Effect of substrate on the film composition

Figure 104 shows the variation in Na/Co atomic ratio for 4(ink+2 sol) films obtained on Si, Ti/Pt coated Si and Al_2O_3 wafers.

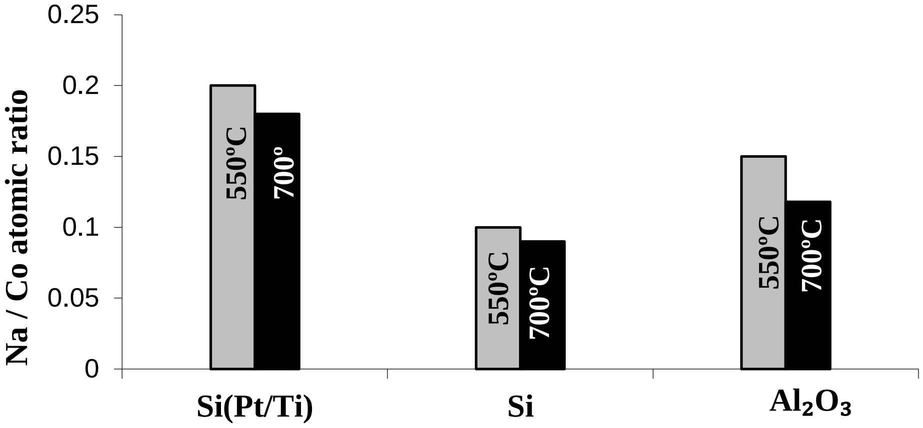

Figure 104 The dependence of Co/Na atomic ratio of 4 (ink + 2 sol) films sintered at 550°C and 700°C on a silicon, Ti/Pt coated silicon and Al_2O_3.

The changes in the stoichiometry can be due to evaporation of sodium or diffusion into the wafer what can explain the apparent dependence on Figure 104.

In order to verify adhesion of sol on different substrates the contact angles were measured and compared with that on glass (Figure 105).

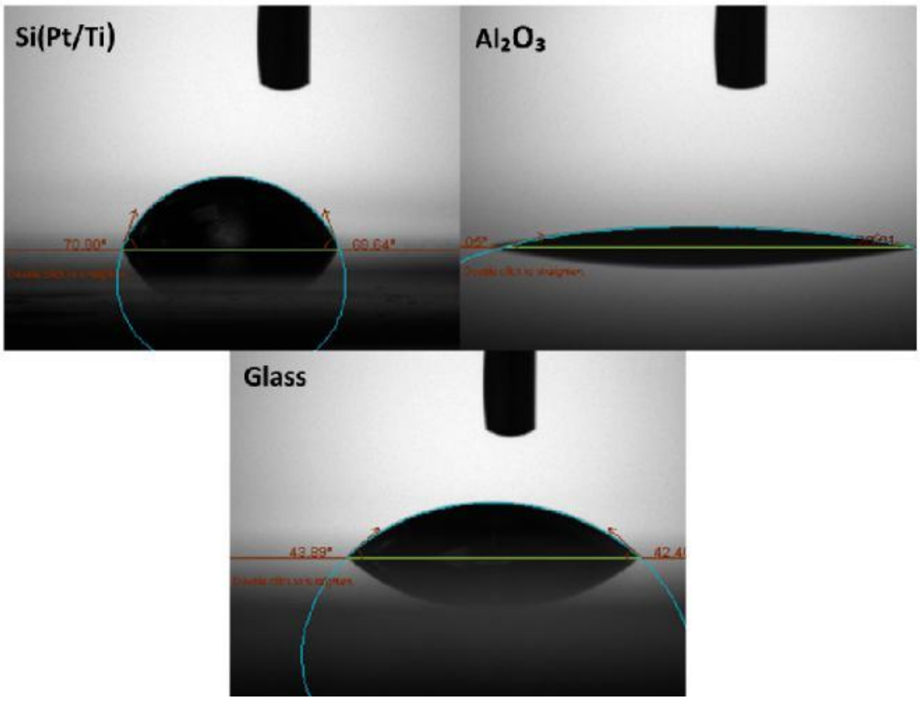

Figure 105 The image of contact angle between sol drop and substrate.

The contact angle between the sol and substrate for Ti/Pt coated silicon was found to be 70° for aluminia 20° and for silicon with no electrode was found to be very similar to glass at to 40° and 43°, respectively. The best wetting by the sodium cobalt oxide was on aluminia substrates. The same behaviour was observed for the ink as it is a water based ink. All polar liquids including, water have strong intermolecular interactions and exhibit high surface tensions, which is ascribed to the hydrogen bonding[169].

7.3 Conclusion

Thick and thin $Na_xCo_2O_4$ films can be fabricated through the use of a spin coating technique on silicon, Ti/Pt coated silicon and Al_2O_3 substrates. The quality of films can be enhanced due to reduction of cracking by increasing temperature treatment, reduction of roughness due to use of SG powder for inks preparation and by sol saturation of sequenced layers. The films show good electrical properties range from 257.92 to 496.22 μΩcm.

Chapter 8 Sodium cobalt oxide nanostructures

8.1 Introduction

A range of different Na-rich pretreatments have been evaluated to determine their effect on microstructure and properties of $NaCo_2O_4$ thermoelectric materials. Following processing it was found that samples produced using the milling pretreatment in borosilicate glass bottles developed a nanoscale candle-like structure. Observation are reported in this chapter.

8.2 Formation of sodium cobalt oxide candle nanostructures

The prepared products were characterised with high resolution field emission gun scanning electron microscopy (SFEG), energy dispersive X-ray spectroscopy (EDX) attached to the SFEG, as well as field-emission transmission electron microscopy (TEM).

Electron microscopy revealed the presence of many elongated nanostructures (Figure 106) with EDX indicating the presence of Na, Co, O and Si. The presence of trace amounts of Si can be attributed to the use of the borosilicate glass bottles used during the ball milling pre-treatment with NaOH solution. The elongated nanostructures only formed in samples that had been milled in borosilicate glass bottles and where Si was observed indicating that the presence of Si is critical for their formation.

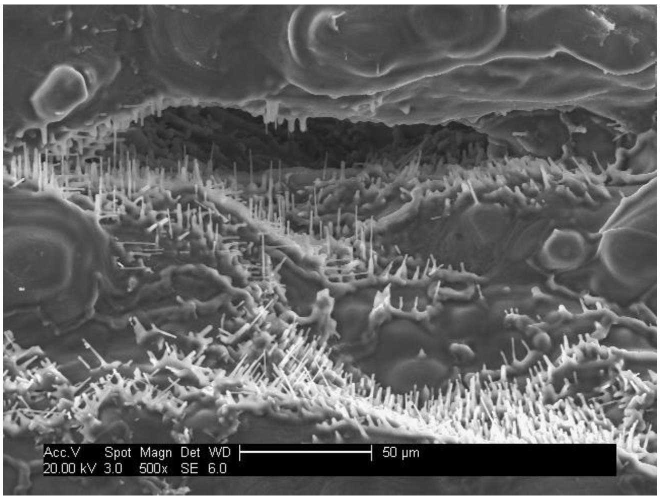

Figure 106 SFEG micrograph of columnar structures created on the surface of $NaCo_2O_4$ grains after treatment at 1000°C for 1 hour.

Higher magnification micrographs showed the columnar structures to resemble a candle with a fine protrusion visible at the upper tip (Figure 107).

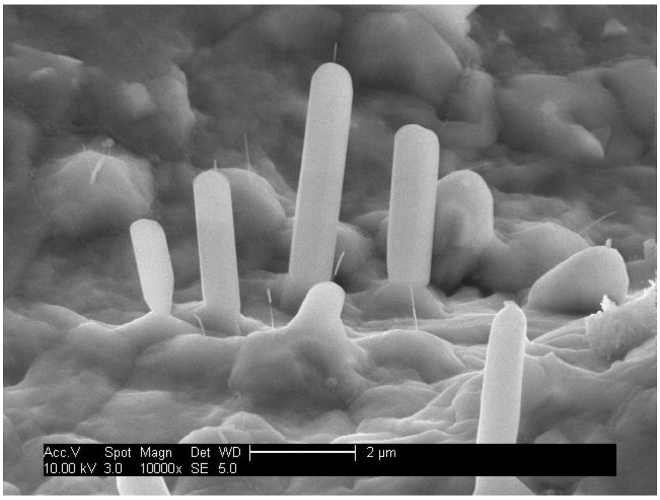

Figure 107 High magnification SFEG micrograph of columnar structure formed on the surface of $NaCo_2O_4$ grains after sintering at 1000°C for 1 hour.

The high magnification images show that the candle wick-like structure develops in the centre of the end of each columnar structure. Such wick-like structures appear irrespective of the length of the column. In each case the character of the filament structure is independent of the column structure. The studies also showed that with increasing temperature, longer and filaments were obtained. The filaments were found to be 700 nm long with a 50 nm diameter for samples sintered at 1000ºC and longer (≥1µm) but with the same diameter (~50 nm) for samples sintered at 1050ºC (Figure 108). The diameter of the candle-like structures does not change significantly over the entire length and when sintered at 1000ºC the bases are between 1µm and 1.5µm in diameter while when sintered at 1050ºC the diameter decreases and is less than 1µm (Figure 108).

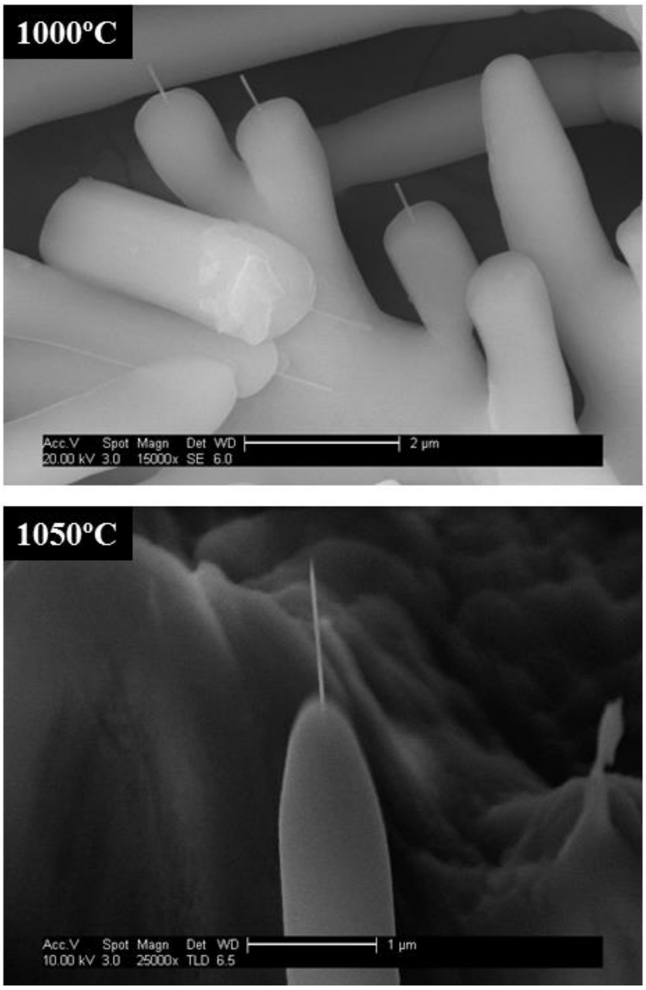

Figure 108 SFEG micrographs of sodium cobalt oxide candles-like structures created: at 1000ºC after sintering for 1h and at 1050 ºC after sintering for 1h.

Two distinctly different structures are observed when samples are sintered for less than 1 hour. In the initial stages (< 25 min) a raised or humped structure is observed (Figure 109 A). Later (~ 40 min), columnar growths are visible on the surface of those humps (Figure 109 B).

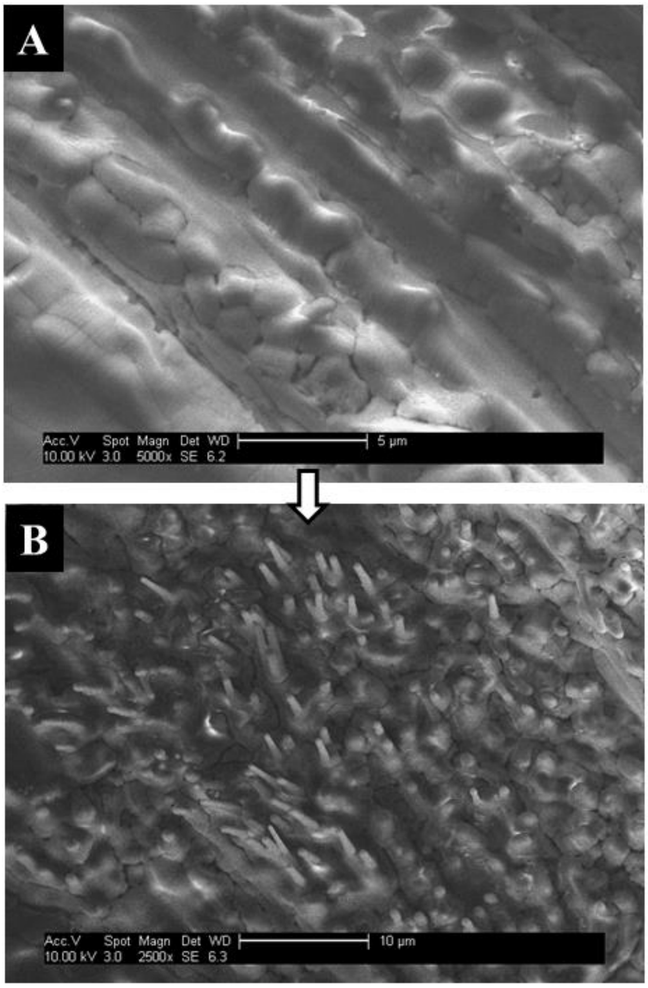

Figure 109 Micrograph of features formed on the surface of $Na_xCo_2O_4$ grains sintered at 1000ºC for A) < 25 min and B) 40 min.

Based on the observations it is possible to hypothesise a growth mechanism for the formation of the candle-like structure. In the first stage of growth the formation of humps on the surface of the grains occurs. From each of those humps one micro scale rod grows. Nano scale wick-like features are observed on roads of different lengths, and even in the absence of rods indicating their formation may be part of a separate growth mechanism.

EDX analysis shows that the silicon content is greater at the end of wick-like features (Figure 110).

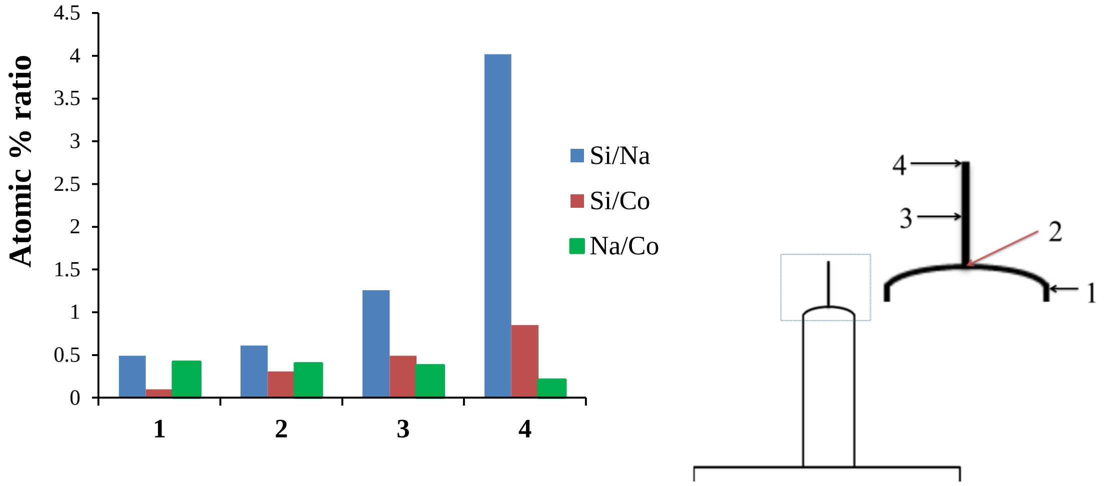

Figure 110 EDX composition analysis illustrating the change in the proportion of Na, Co and Si through the length of candle-like structure, numbers corresponding to the analysed areas as shown in B.

The results obtained from TEM show rods and filaments to be crystalline with the crystal lattice unchanged over the entire length of the filament (single crystal pattern) and rods (polycrystalline patterns).

The only difference between these samples and comparable ball mill pre-treated samples is the use of borosilicate milling vessels during the preparation and the presence of Si in the elemental analysis. It is therefore reasonable to assume that it is the presence of Si that has led to the formation of the candle-like structures. Samples were also prepared at 950˚C however no visible form of nano candle-like structures were observed. Temperatures above 1100˚C resulted in significant distortion of the substrate surface and large scale of melting.

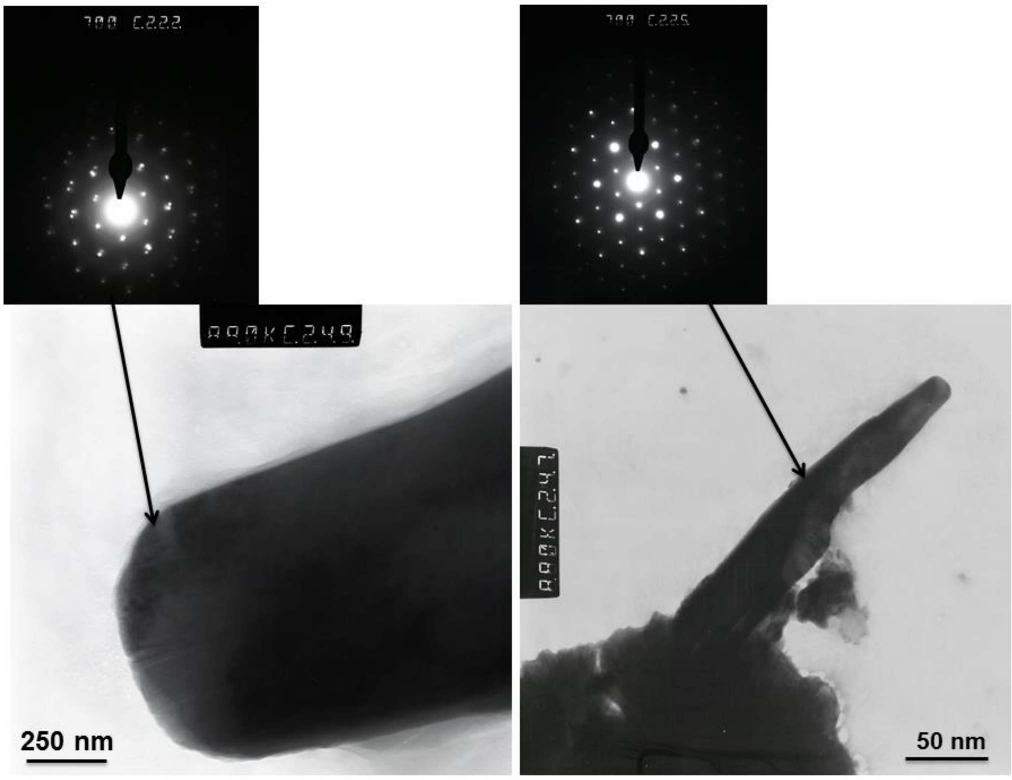

Figure 111 TEM image of single rods and filament and TEM diffraction pattern.

The form of the humps (Figure 109A) indicate the presence of a liquid phase during the formation process. While no phase diagram was available for oxides of Si, Co and Na the SiO_2-Na_2O phase diagram (Figure 112) shows that a liquid phase form over a wide composition range at temperatures around 1000°C, this can lead to a hypothesis that the formation of the candle-like structures is reliant on the presence of a liquid phase.

In the early stage a Si-Na rich liquid phase is formed on the surface of grains and body of the compact. As sintering process and Co and Na are dissolved and redistributed as part of the liquid phase sintering process reprecipitation leads to the formation and growth of the columnar structures.

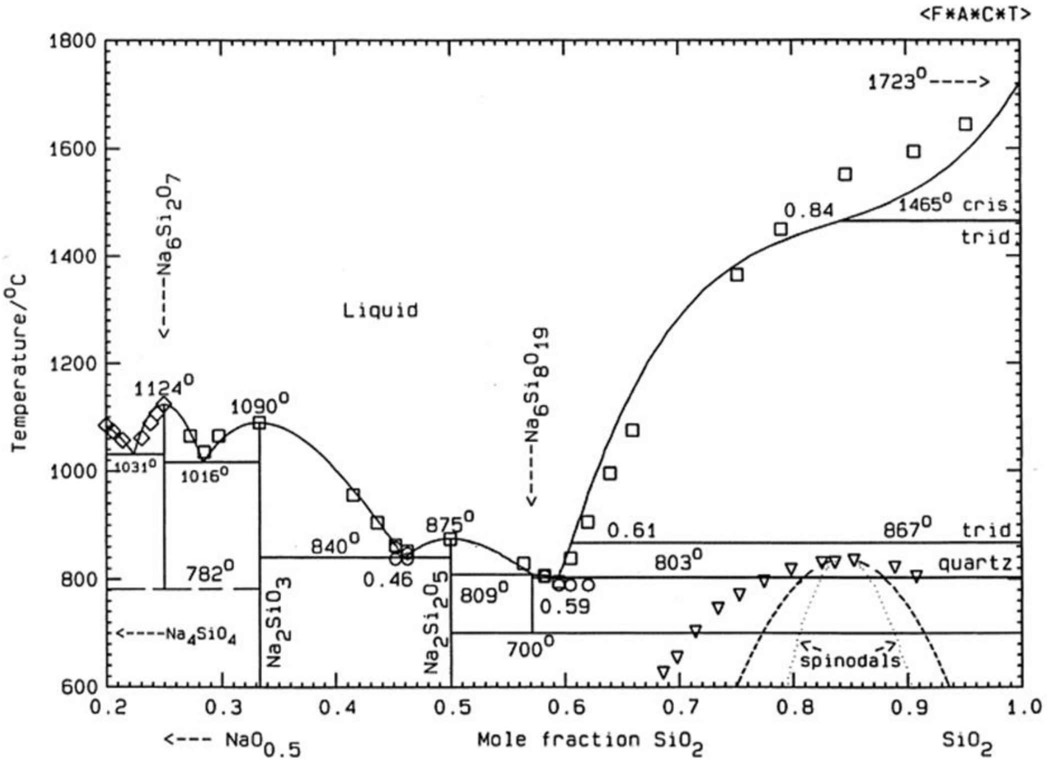

Figure 112 The SiO_2-Na_2O phase diagram[170].

As the formation of nano wicks-like does not appear reliant on the presence of a rod, and that these wicks-like structures are very rich in Si, it is possible that they form as cooling as a result of a dendrite growth mechanism.

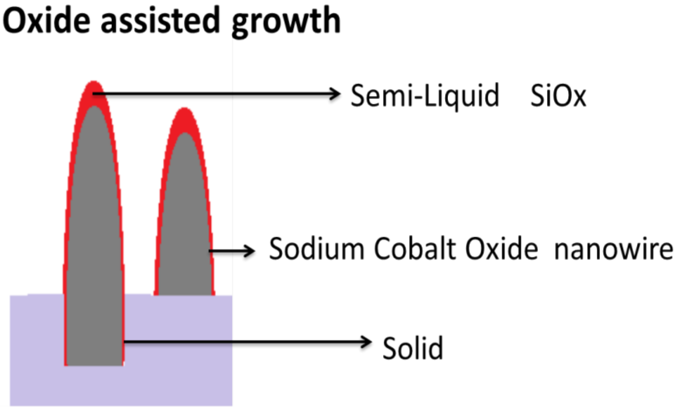

Figure 113 Schematic diagram of oxide-assisted growth (OAG) methods.

8.2.1 Conclusion

In conclusion, the high quality sodium cobalt oxide nanostructured candle-shapes were successfully synthesized on sodium cobalt oxide substrate. Straight and long nanowires ~50nm in diameter and hundreds of nanometre in length were obtained while the rods of candle-like structure were more varied in width as well as in length. TEM diffraction patterns taken from along the length of the filament are essentially the same implying a single-crystal of homogeneous crystallographic nature.

Chapter 9 Conclusion and future work

9.1 General conclusion

The aim of this project was to develop an inexpensive, reproducible processing route to fabricate a high temperature thermoelectric material. The work presented focuses on the synthesis of sodium cobalt oxide. A variety of preparation techniques and analysis methods were used to study the electrical and thermal conductivity and the thermoelectric properties the materials produced.

9.1.1 Influence of time and temperature on microstructure and composition of sodium cobalt oxide.

A solid state reaction (SSR) method was initially selected as suitable powder route synthesis.

- Sodium cobalt oxide was synthesised at 800ºC for 4, 6 and 12 hours with particle sizes between 5 and 6 μm. The average Na to Co atomic ratio was found to be 0.4.
- For the sintering temperature of 850ºC after 4, 6, and 12 hours of heat treatment the particle size was between 5 and 9 μm with an average Na to Co atomic ratio of 0.5.
- Sintering at 900ºC for 4, 6 and 12 hours resulted in spherical particles with diameters between 9 and 13 μm with an average Na to Co atomic ratio of 0.4.

Sintering at 850ºC for 12 hours was selected as the best powder synthesis condition for later production of pellets.

9.1.2 Influence of a powder synthesis route on microstructure and composition of material

The sodium cobalt oxide powders have been prepared through the solid state reaction and sol gel method. For the sol gel (SG) method a calcination temperature of 450ºC was found to be too low for the creation of the desired sodium cobalt oxide phase. The sol gel powder calcined at 700ºC for 6 hours was found to have a similar stoichiometric ratio to the powder prepared by solid state reaction process (850ºC 12h), and for this reason was chosen as the optimal preparation route. The calcined sol gel powder has spherical particles with a size less than 1µm.

Besides the influence of powder synthesis route, the microstructural changes and composition of the material during fabrication of pellets were also investigated. It was shown that sodium cobalt oxide could be obtained over a wide range of sintering temperatures with an increase in temperature leading to a more dense structure. High purity of materials was found for pellets prepared from SG powder over the whole range of sintering temperatures (850ºC - 1000ºC) while when prepared from SSR powder the pellets showed high purity when sintered at 1000ºC and above. When sintered at 950ºC the Co_3O_4 phase was still detected. The maximum sintering temperature for this type of material is 1050°C. Increasing the sintering temperature to 1100°C result in melting of the material.

9.1.3 Development of a novel Na rich pre-treatment.

Studies were made to improve the physical properties through changing the preparation route by incorporating different types of Na rich pre-treatment processes. The possibility to control microstructural changes of material during sintering of pellets has also been investigated. The microstructural changes caused by a ball milled (BM) pre-treatment are increased densification and grain growth offset against the formation of grain boundary phases. The infiltrated (INF) pre-treatment resulted in minimal changes to the microstructure relative to that of SSR samples with a slight grain boundary phase formation. The use of mixed (M) pre-treatment resulted in the formation of a grain boundary phase and in densification of material with increased sintering time and temperature. Pellets prepared by ball milled and mixed pre-treatments and sintered at 1000ºC formed boulders structures. Infiltrated pre-treatment, when sintered above 1000°C, led to the formation of hexagonal plate structures forming tight rosette or layered structures. All pre-treatments resulted in lowering of the melting point of the material.

9.1.4 The influence of processing and powder on thermal and electrical properties.

Sodium cobalt oxide pellets were fabricated using of a sol gel powder and solid state reaction powder at between 950ºC and 1000ºC for 1-12 hours. In the case of both powders, the Na rich pre-treatment led to increased thermoelectric figure of merit by enhancing the Seebeck coefficient and reducing the electrical resistivity and thermal conductivity (Table 20). This study confirmed that ceramics that exhibited good thermoelectric behaviour could be obtained through the use of different Na rich pre-treatments as well as higher-temperatures and shorter sintering times.

9.1.5 Evolution of inks and films

A new contribution to sodium cobalt oxide synthesis, the production of spin coated film was developed.

The sodium cobalt oxide ink was successful prepared.

The development of this method allowed films to be produced on different substrates.

Spin coating was successfully used to deposit films with a range of thicknesses (200 nm for single sol film up to ~ 32µm for 4 (ink + 2 sol layers) films).

The cracking and surface roughness was reduced by increasing the temperature of thermal treatment.

The electrical resistivity was also reduced (496.22 to 257.92 μΩcm) through the use of heat treatment temperatures.

9.1.6 Summary of main findings

The inexpensive, reproducible processing route using solid oxide synthesis combined with Na rich pretreatments it has been demonstrated that it is possible to produce $NaCo_2O_4$ ceramic material with stable Na:Co ratios. Processing at 1000°C for 6 hours with an infiltrated treatment yielded ceramics that exhibited Seebeck coefficient, electrical resistivity and thermal conductivity of 150 μV/K, 270 μΩcm, 1.3 W/mK, respectively showing promises for applications as high temperature TE materials.

9.2 Future work

The Na rich pre-treatment is a very promising technique for the synthesis of sodium cobalt oxide bulk materials which shows improvement of thermoelectric properties. The use of such pre-treatments could be interesting in the preparation of future thermoelectrics for use at higher temperatures (above 600ºC). The use of pre-treatments led to the formation of grain boundary phases which has impact on thermal and electrical conduction. The observed reduction of thermal conductivity and higher Seebeck coefficient could be further improved by other modifications such as the use of different reaction environments (gas flow, pressure, temperature etc.). The deeper understanding of the structural or lattice changes would be helpful in the development of new preparation routes.

The powders synthesised by the SSR and SG methods were high purity. The use of dopants could be used to improve the properties. Additional dopants could be added in both the sol gel and solid state reaction powder preparation methods, or introduced as a new method of pre-treatment.

To obtain more uniform films further work is required. Improvement in powder and ink could reduce surface roughness and appearance of cracks in the annealed samples and could lead to improved properties of the final product. Further investigation of factors such as the particle size, viscosity and surface tension of fluids, as well as pre-preparation of substrates, might be helpful in obtaining uniform sodium cobalt oxides film by the method proposed in this work. The influence of preparation factors on thermoelectric properties should to be investigated

It is worth noting the candle-like structures produced during these studies and potential to investigate their behaviour and possible uses.

Despite the constant development of promising thermoelectric candidates, some major issues should be taken in to consideration in the future:

- The performance of n-type materials still needs improvements:
- The classic semiconductors theories cannot fully explain the mechanism of electrical and thermal conduction and thermoelectric performance of complex oxides systems. Development of this knowledge and deeper understanding would support the discovery and production of higher performance materials:
- Last but not least, the problems with fabrication of thermoelectric devices are still to be considered.

REFERENCES

[1] Motohashi, T., Naujalis, E., Ueda, R., Isawa, K., Karppinen, M. and Yamauchi, H. (2001), "Simultaneously enhanced thermoelectric power and reduced resistivity of $Na_xCo_2O_4$ by controlling Na nonstoichiometry", *Applied Physics Letters*, vol. 79, no. 10, pp. 1480-1482.

[2] Ohta, H., Sugiura, K. and Koumoto, K. (2008), "Recent progress in oxide thermoelectric materials: P-type $Ca_3Co_4O_9$ and n-Type $SrTiO_3$ -", *Inorganic chemistry*, vol. 47, no. 19, pp. 8429-8436.

[3] Seetawan, T., Amornkitbamrung, V., Burinprakhon, T., Maensiri, S., Tongbai, P., Kurosaki, K., Muta, H., Uno, M. and Yamanaka, S. (2006), "Effect of sintering temperature on the thermoelectric properties of $Na_xCo_2O_4$", *Journal of Alloys and Compounds*, vol. 416, no. 1–2, pp. 291-295.

[4] Erdal, M., O., Uslu I., Aytimur, A., Koyuncu, M., ”Synthesis and Characterization of $Na_xCo_2O_4$ Thermoelectric Material Using PVA Polymerized Complex” *International Journal of Material Science and Electronics Research*, vol. 1, no. 2, July-Dec. 2010, pp. 55-59

[5] Ito, M., Nagira, T., Tsuchiya, Y., Katsuyama, S., Majima, K. and Nagai, H. (2002), "Microstructure and thermoelectric properties of $NaxCo_2O_4$ synthesized by spark plasma sintering", *Funtai Oyobi Fummatsu Yakin/Journal of the Japan Society of Powder and Powder Metallurgy*, vol. 49, no. 5, pp. 406-411.

[6] He, J., Liu, Y., Funahashi, R., (2011), “Oxide thermoelectrics: The challenges, progress, and outlook “,*Journal of Materials Research*, vol. 26 , no 15 , pp 1762-1772

[7] Ioffe, A. F. (1957), Semiconductor thermoelements, and Thermoelectric cooling, Rev a supplement for the English ed, Infosearch, ltd, London.

[8] D.M. Rowe, Ph.D., D.Sc. “Thermoeloectric Handbook Macro to Nano” (2006).

[9] Heikes, R. R. and Ure, R. W. (1961), “Thermoelectricity: science and engineering”, Interscience Publishers, New York.

[10] Koshibae, W., Tsutsui, K. and Maekawa, S. (2000), "Thermopower in cobalt oxides", *Physical Review B - Condensed Matter and Materials Physics*, vol. 62, no. 11, pp. 6869-6872.

[11] Koshibae, W. and Maekawa, S., (2009), “Thermoelectric effect in transition metal oxides”, *NATO Science for Peace mand Security Series B: Physics and Biophysics*, pp.69-79.

[12] Dresselhaus, M. S., Chen, G., Tang, M. Y., Yang, R., Lee, H., Wang, D., Ren, Z., Fleurial, J. -P. and Gogna, P. (2007), "New directions for low-dimensional thermoelectric materials", *Advanced Materials*, vol. 19, no. 8, pp. 1043-1053.

[13] Yang, R., Chen, G. and Dresselhaus, M. S. (2005), "Thermal conductivity of simple and tubular nanowire composites in the longitudinal direction", *Physical Review B - Condensed Matter and Materials Physics*, vol. 72, no. 12.

[14] Leonov, V. and Vullers, R. J. M. (2009), "Wearable thermoelectric generators for body-powered devices", *Journal of Electronic Materials*, vol. 38, no. 7, pp. 1491-1498.

[15] El-Genk, M. S. and Saber, H. H. (2003), "High efficiency segmented thermoelectric unicouple for operation between 973 and 300 K", *Energy Conversion and Management*, vol. 44, no. 7, pp. 1069-1088.

[16] http://voyager.jpl.nasa.gov/spacecraft/instruments_rtg.html

[17] Lofy, J. and Bell, L. E. (2002), "Thermoelectrics for environmental control in automobiles", *Thermoelectrics, 2002. Proceedings ICT '02. Twenty-First International Conference on*, pp. 471.

[18] Singh, R., Tundee, S. and Akbarzadeh, A. (2011), "Electric power generation from solar pond using combined thermosyphon and thermoelectric modules", *Solar Energy*, vol. 85, no. 2, pp. 371-378.

[19] Wojciechowski, K. T., Bucko, M. M., Obla¸kowski, J., Fuc, P. and Merkisz, J. (2006), "A new concept of reducing nitrogen oxides emissions in a combustion engine - combination of ceramic oxygen conductors and thermoelectric materials", *International Conference on Thermoelectrics, ICT, Proceedings*, pp. 706.

[20] Zhao, L. -D., Dravid, V. P. and Kanatzidis, M. G. (2014), "The panoscopic approach to high performance thermoelectrics", *Energy and Environmental Science*, vol. 7, no. 1, pp. 251-268.

[21] Kavei, G. and Karami, M. A. (2006), "Fabrication and characterization of the p-type $(Bi_2Te_3)_x(Sb_2Te_3)_{1-x}$ thermoelectric crystals prepared via zone melting", *Bulletin of Materials Science*, vol. 29, no. 7, pp. 659-663.

[22] Bejenari, I., Kantser, V. and Balandin, A. A. (2010), "Thermoelectric properties of electrically gated bismuth telluride nanowires", *Physical Review B - Condensed Matter and Materials Physics*, vol. 81, no. 7.

[23] Singh, A., Bhattacharya, S., Thinaharan, C., Aswal, D. K., Gupta, S. K., Yakhmi, J. V. and Bhanumurthy, K. (2009), "Development of low resistance electrical contacts for thermoelectric devices based on n-type PbTe and p-type TAGS-85 $((AgSbTe_2)_{0.15}(GeTe)_{0.85})$", *Journal of Physics D: Applied Physics*, vol. 42, no. 1.

[24] Rowe, D. J. and Kortshagen, U. R. (2014), "Boron- and phosphorus-doped silicon germanium alloy nanocrystals - Nonthermal plasma synthesis and gas-phase thin film deposition", *APL Materials,* vol. 2, no. 2.

[25] Rodríguez, J. E. and Moreno, L. C. (2011), "$La_{1-x}Sr_xCuO_{3-d}$ ceramics as new thermoelectric material for low temperature applications", *Materials Letters,* vol. 65, no. 1, pp. 46-48.

[26] Wojciechowski, K., Godlewska, E., Mars, K., Mania, R., Karpinski, G., Ziolkowski, P., Stiewe, C. and Müller, E. (2008), "Characterization of thermoelectric properties of layers obtained by pulsed magnetron sputtering", *Vacuum,* vol. 82, no. 10, pp. 1003-1006.

[27] Crane, D. T. and Jackson, G. S. (2004), "Optimization of cross flow heat exchangers for thermoelectric waste heat recovery", *Energy Conversion and Management,* vol. 45, no. 9-10, pp. 1565-1582.

[28] Xiao, F., Hangarter, C., Yoo, B., Rheem, Y., Lee, K. -H. and Myung, N. V. (2008), "Recent progress in electrodeposition of thermoelectric thin films and nanostructures", *Electrochimica Acta,* vol. 53, no. 28, pp. 8103-8117.

[29] Glosch, H., Ashauer, M., Pfeiffer, U. and Lang, W. (1999), "Thermoelectric converter for energy supply", *Sensors and Actuators, A: Physical,* vol. 74, no. 1, pp. 246-250.

[30] Wojciechowski,K., T., Oblakowsk, J., (2008) Preparation and characterization of nano-structured spherical powers for thermoelectric applications, *Solid State Ionics* 157, pp. 341 – 347.

[31] Lee, H. B., We, J. H., Yang, H. J., Kim, K., Choi, K. C. and Cho, B. J. (2011), "Thermoelectric properties of screen-printed ZnSb film", *Thin Solid Films,* vol. 519, no. 16, pp. 5441-5443.

[32] Böttner, H., Ebling, D., Kölbel, H., Schubert, A., Gavrikov, A., Mahlke, A. and Nurnus, J. (2007), "Formation of nanometerscale layers of V-VI (Bi_2Te_3-related) compounds based on amorphous precursors", *Proceedings of the Estonian Academy of Sciences: Engineering,* vol. 13, no. 4, pp. 354-362.

[33] Zahid, M., Arul Raj, I., Fischer, W., Tietz, F. and Alfaro, J. M. S. (2006), "Synthesis and investigations on the stability of $La_{0.8}Sr_{0.2}CuO_{2.4+d}$ at high temperatures", *Solid State Ionics,* vol. 177, no. 35-36, pp. 3205-3210.

[34] Jalan, B. and Stemmer, S. (2010), "Large Seebeck coefficients and thermoelectric power factor of La-doped $SrTiO_3$ thin films", *Applied Physics Letters,* vol. 97, no. 4.

[35] Mazo, G. N., Savvin, S. N., Petrykin, V. V. and Koudriashov, I. A. (2001), "Oxygen mobility in layered cuprates La2-xSrxCuO4-d", *Solid State Ionics,* vol. 141-142, pp. 313-319.

[36] Okinaka, N., Zhang, L. and Akiyama, T. (2010), "Thermoelectric properties of rare earth-doped SrTiO3 using combination of combustion synthesis (CS) and spark plasma sintering (SPS)", *ISIJ International,* vol. 50, no. 9, pp. 1300-1304.

[37] Ohta, H., Huang, R. and Ikuhara, Y. (2008), "Large enhancement of the thermoelectric Seebeck coefficient for amorphous oxide semiconductor superlattices with extremely thin conductive layers", *Physica Status Solidi - Rapid Research Letters,* vol. 2, no. 3, pp. 105-107.

[38] Usui, H., Shibata, S. and Kuroki, K. (2010), "Origin of coexisting large Seebeck coefficient and metallic conductivity in the electron doped $SrTiO_3$ and $KTaO_3$", *Physical Review B - Condensed Matter and Materials Physics,* vol. 81, no. 20.

[39] Mazo, G. N. and Savvin, S. N. (2004), "The molecular dynamics study of oxygen mobility in $La_{2-x}Sr_xCuO_{x-d}$", *Solid State Ionics,* vol. 175, no. 1-4, pp. 371-374.

[40] Nan, J., Wu, J., Deng, Y. and Nan, C. W. (2003), "Synthesis and thermoelectric properties of $(Na_xCa1_{-x})_3Co_4O_9$ ceramics", *Journal of the European Ceramic Society,* vol. 23, no. 6, pp. 859-863.

[41] Ito, M. and Matsuda, T. (2009), "Thermoelectric properties of non-doped and Y-doped $SrTiO_3$ polycrystals synthesized by polymerized complex process and hot pressing", *Journal of Alloys and Compounds,* vol. 477, no. 1-2, pp. 473-477.

[42] Shikano, M. and Funahashi, R. (2003), "Electrical and thermal properties of single-crystalline $(Ca_2CoO_3)_{0.7}CoO_2$ with a $Ca_3Co_4O_9$ structure", *Applied Physics Letters,* vol. 82, no. 12, pp. 1851-1853.

[43] Hecht, J., (2008), "Understanding Lasers: An Entry Level Guide" (IEEE Press Understanding Science & Technology Series), *Wiley-Blackwell, 3rd Edition edition*.

[44] Singleton, J., (2001), "Band theory and electronic properties of solids" *OUP Oxford*.

[45] Neamen, D. (2003), "Semiconductor Physics and Devices", *3rd ed. New York: McGraw-Hill*.

[46] Sze, S., M., (1981) "Physics of Semiconductor Devices", *2nd ed. New York: John Wiley & Sons*.

[47] Ohtaki, M., "Oxide Thermoelectric Materials for Heat-toelectricity Direct Energy Conversion", *Kyushu UniersityGlobal COE Program Novel Carbon Resources SciencesNewsletter,* vol 3,Special Issue.

[48] Matsumiya, M., Qiu, F., Shin, W., Izu, N., Murayama, N. and Kanzaki, S. (2002), "Thin-film Li-doped NiO for thermoelectric hydrogen gas sensor", *Thin Solid Films*, vol. 419, no. 1-2, pp. 213-217.

[49] Park, S. -S. and Mackenzie, J. D. (1996), "Thickness and microstructure effects on alcohol sensing of tin oxide thin films", *Thin Solid Films*, vol. 274, no. 1-2, pp. 154-159.

[50] Moharrami, F., Bagheri-Mohagheghi, M. -M., Azimi-Juybari, H. and Shokooh-Saremi, M. (2012), "Structural, electrical, optical, thermoelectrical and photoconductivity properties of the SnO_2-Al_2O_3 binary transparent conducting films deposited by the spray pyrolysis method", *Physica Scripta,* vol. 85, no. 1.

[51] Dynys, F., Sayir, A., Sehirlioglu, A., “Thermoelectric Properties of Self Assemble TiO_2/SnO_2 Nanocomposites “, *32nd International Conference & Exposition on Advanced Ceramics & Composites*; 27 Jan - 1 Feb 2008.

[52] Yanagiya, S., Nong, N. V., Sonne, M. and Pryds, N. (2012), "Thermoelectric properties of SnO_2-based ceramics doped with Nd, Hf or Bi", *AIP Conference Proceedings*, Vol. 1449, pp. 327.

[53] Terasaki, I., Sasago, Y. and Uchinokura, K. (1997), "Large thermoelectric power in $NaCo_2O_4$ single crystals", *Physical Review B - Condensed Matter and Materials Physics*, vol. 56, no. 20, pp. R12685-R12687.

[54] Bérardan, D., Guilmeau, E., Maignan, A. and Raveau, B. (2008), "In_2O_3:Ge, a promising n-type thermoelectric oxide composite", *Solid State Communications*, vol. 146, no. 1-2, pp. 97-101.

[55] Gregory, O. J., Amani, M. and Fralick, G. C. (2011), "Thermoelectric power factor of In_2O_3:Pd nanocomposite films", *Applied Physics Letters*, vol. 99, no. 1.

[56] Karim, D. P. and Aldred, A. T. (1979), "Localized level hopping transport in La(Sr)CrO_3", *Physical Review B*, vol. 20, no. 6, pp. 2255-2263.

[57] Weber, W. J., Griffin, C. W. and Bates, J. L. (1987), "Effects on cation substitution on electrical and thermal transport properties of YCrO//3 and LaCrO//3.", *Journal of the American Ceramic Society*, vol. 70, no. 4, pp. 265-270.

[58] Ohtaki, M., Koga, H., Tokunaga, T., Eguchi, K. and Arai, H. (1995), "Electrical Ohtaki, M., Koga, H., Tokunaga, T., Eguchi, K. and Arai, H. (1995), "Electrical Transport Properties and High-Temperature Thermoelectric Performance of $(Ca_{0.9}M_{0.1})MnO_3$ (M = Y, La, Ce, Sm, In, Sn, Sb, Pb, Bi)", *Journal of Solid State Chemistry*, vol. 120, no. 1, pp. 105-111.

[59] Lingner, J., Letz, M. and Jakob, G. (2013), "$SrTiO_3$ glass-ceramics as oxide thermoelectrics", *Journal of Materials Science*, vol. 48, no. 7, pp. 2812-2816.

[60] Tsubota, T., Ohtaki, M., Eguchi, K. and Arai, H. (1997), "Thermoelectric properties of Al-doped ZnO as a promising oxide material for high-temperature thermoelectric conversion", *Journal of Materials Chemistry*, vol. 7, no. 1, pp. 85-90.

[61] Ohtaki, M., Tsubota, T., Eguchi, K. and Arai, H. (1996), "High-temperature thermoelectric properties of $(Zn_{1-x}Al_x)O$", *Journal of Applied Physics*, vol. 79, no. 3, pp. 1816-1818.

[62] Tsubota, T., Ohtaki, M., Eguchi, K. and Arai, H. (1997), "Thermoelectric properties of ZnO doped with the group 13 elements", *International Conference on Thermoelectrics*, ICT, Proceedings, pp. 240.

[63] Tsubota, T., Ohtaki, M., Eguchi, K. and Arai, H. (1998), "Transport properties and thermoelectric performance of $(Zn_{1-y}Mg_y)_{1-x}Al_xO$", *Journal of Materials Chemistry*, vol. 8, no. 2, pp. 409-412.

[64] Ohtaki, M., Araki, K. and Yamamoto, K. (2009), "High thermoelectric performance of dually doped ZnO ceramics", *Journal of Electronic Materials*, vol. 38, no. 7, pp. 1234-1238.

[65] Tripathi, A. K. and Lal, H. B. (1982), "Electrical transport in light rare-earth orthochromites", *Journal of Materials Science*, vol. 17, no. 6, pp. 1595-1609.

[66] Sparks, T. D., Gurlo, A. and Clarke, D. R. (2012), "Enhanced n-type thermopower in distortion-free $LiMn_2O_4$", *Journal of Materials Chemistry*, vol. 22, no. 11, pp. 4631-4636.

[67] Bordeneuve, H., Guillemet-Fritsch, S., Rousset, A., Schuurman, S. and Poulain, V. (2009), "Structure and electrical properties of single-phase cobalt manganese oxide spinels $Mn_{3-x}Co_xO_4$ sintered classically and by spark plasma sintering (SPS)", *Journal of Solid State Chemistry*, vol. 182, no. 2, pp. 396-401.

[68] Klyndyuk, A. I. (2009), "Structure and properties of the layered compound $HoBaCuCoO_{5+d}$", *Inorganic Materials*, vol. 45, no. 7, pp. 806-808.

[69] Jia, Ch., Xifan, W., Annabella, S., ”Electronic structure and bonding properties of cobalt oxide in the spinel structure”, *Physical Review B*, (2011) vol. 83, Issue 24.

[70] Hamdani, M., Singh, R. N. and Chartier, P. (2010), "Co_3O_4 and co-based spinel oxides bifunctional oxygen electrodes", *International Journal of Electrochemical Science*, vol. 5, no. 4, pp. 556-577.

[71] Pollock, D., D., “Thermoelectricity: Theory, Thermometry, Tool”,(1985);

[72] Egli, P., H., (ed.), “Thermoelectricity” (John Wiley and Sons, New York, 1960);

[73] Takeuchi, T., Kondo, T., Takami, T., Takahashi, H., Ikuta, H., Mizutani, U., Soda, K., Funahashi, R., Shikano, M., Mikami, M., Tsuda, S., Yokoya, T., Shin, S. and Muro, T. (2004), "Contribution of electronic structure to the large thermoelectric power in layered cobalt oxides", *Physical Review B - Condensed Matter and Materials Physics*, vol. 69, no. 12, pp. 1254101-1254109.

[74] Masset, A. C., Michel, C., Maignan, A., Hervieu, M., Toulemonde, O., Studer, F., Raveau, B. and Hejtmanek, J. (2000), "Misfit-layered cobaltite with an anisotropic giant magnetoresistance: $Ca_3Co_4O_9$", *Physical Review B - Condensed Matter and Materials Physics*, vol. 62, no. 1, pp. 166-175.

[75] Miyazaki, Y., Onoda, M., Oku, T., Kikuchi, M., Ishii, Y., Ono, Y., Morii, Y. and Kajitani, T. (2002), "Modulated Structure of the Thermoelectric Compound $[Ca_2CoO_3]_{0.62}CoO_2$", *Journal of the Physical Society of Japan*, vol. 71, no. 2, pp. 491-497.

[76] Miyazaki, Y., Miura, T., Ono, Y. and Kajitani, T., (2003), “Crystal structure and thermoelectric properties of the composite crystal $[(Ca_{1-x}Sr_x)_2CoO_3]_\rho CoO_2$”, *Jurnal of the Japan Society of Powder and Powder Metallurgy*, vol. 50, pp. 475-479.

[77] Miyazaki, Y., Miura, T., Onoda, M., Uchida, M., Ishii, Y., Ono, Y., Morii, Y. and Kajitani, T. (2003), "Modulated Structure of Misfit-Layered Cobalt Oxide $[Ca_2(Co_{0.65}Cu_{0.35})_2O_4]$ 0.63CoO2", *Japanese Journal of Applied Physics, Part 1: Regular Papers and Short Notes and Review Papers*, vol. 42, no. 12, pp. 7467-7473.

[78] Maignan, A., Pelloquin, D., Hebert, S., Klein, Y. and Hervieu, M. (2006), "Thermoelectric power in misfit cobaltites ceramics: Optimization by chemical substitutions", *Boletin de la Sociedad Espanola de Ceramica y Vidrio*, vol. 45, no. 3, pp. 122-125.

[79] Zhou, Y., Matsubara, I., Shin, W., Izu, N. and Murayama, N. (2004), "Effect of grain size on electric resistivity and thermopower of $(Ca_{2.6}Bi_{0.4})Co_4O_9$ thin films", *Journal of Applied Physics*, vol. 95, no. 2, pp. 625-628.

[80] Iguchi, E., Katoh, S., Nakatsugawa, H. and Munakata, F. (2002), "Thermoelectric Properties (Resistivity and Thermopower) in $(Bi_{1.5}Pb_{0.5}Ca_{2-x}M_xCo_2O_{8-\delta}$ (M=Sc3+, Y3+, or La3+)", *Journal of Solid State Chemistry*, vol. 167, no. 2, pp. 472-479.

[81] Fujishiro, Y., Hamamoto, K., Shiono, O., Katayama, S. and Awano, M. (2004), "Synthesis and thermoelectric characterization of polycrystalline $Ni_{1-x}Ca_xCo_2O_4$ (x = 0-0.05) spinel materials", *Journal of Materials Science: Materials in Electronics*, vol. 15, no. 12, pp. 769-773.

[82] Tareen, J. A. K., Malecki, A., Doumerc, J. P., Launay, J. C., Dordor, P., Pouchard, M. and Hagenmuller, P. (1984), "Growth and electrical properties of pure and Ni-doped Co_3O_4 single crystals", *Materials Research Bulletin*, vol. 19, no. 8, pp. 989-997.

[83] Maignan, A., Flahaut, D. and Hébert, S. (2004), "Sign change of the thermoelectric power in $LaCoO_3$", *European Physical Journal B*, vol. 39, no. 2, pp. 145-148.

[84] Hébert, S., Flahaut, D., Miclau, M., Caignaert, V., Martin, C., Pelloquin, D., Maignan, A., “Search for New n-type Thermoelectric Oxides”, *8th European Workshop on Thermoelectrics*, (2004).

[85] Ohtaki, M. and Shouji, K. (2005), "Strong influence of CO2 partial pressure on inhomogeneous Na distributions and the thermoelectric performance of polycrystalline $NaCo_2C_4$", *International Conference on Thermoelectrics, ICT, Proceedings*, vol. 2005, pp. 472.

[86] Ito, M., Nagira, T., Furumoto, D., Katsuyama, S. and Nagai, H. (2003), "Synthesis of $Na_xCo_2O_4$ thermoelectric oxides by the polymerized complex method", *Scripta Materialia*, vol. 48, no. 4, pp. 403-408.

[87] Wang, W., Jiang, Y., Niu, M., Wang, L. and Cao, B. (2008), "Auto-ignition route to thermoelectric oxide $Na_xCo_2O_4$ powder with high compactibility", *Powder Technology*, vol. 184, no. 1, pp. 25-30

[88] Fouassier, C., Matejka, G., Reau, J.-. and Hagenmuller, P., (1973), “Sur de nouveaux bronzes oxygénés de formule $Na_{\chi}CoO_2$ (χ1). Le système cobalt-oxygène-sodium”, *Journal of Solid State Chemistry*, vol. 6, pp. 532-537.

[89] Cheng, J., Sui, Y., Fu, H., Lu, Z., Wei, B., Qian, Z., Miao, J., Liu, Z., Huang, X., Zhu, R., Wang, X. and Su, W. (2006), "Fabrication and thermoelectric properties of highly textured $NaCo_2O_4$ ceramic", *Journal of Alloys and Compounds*, vol. 407, no. 1-2, pp. 299-303.

[90] Katsuyama, S., Kishida, A. and Ito, M. (2006), "Synthesis of $Na_xCo_2O_4$ by the hydrothermal hot-pressing and its thermoelectric properties", *Journal of Alloys and Compounds*, vol. 414, no. 1-2, pp. 215-220.

[91] Tang, X., He, J., Aaron, K., Abbott, E., Kolis, J. K. and Tritt, T. M. (2008), "Single-crystal growth of $Na_xCo_2O_4$ via a novel low-temperature flux method", *Journal of Crystal Growth*, vol. 310, no. 3, pp. 665-670.

[92] Jansen, M., Hoppe, R.,“Notiz zur Kenntnis der Oxocobaltate des Natriums” Z. *Anorg. Allg. Chem*. 408 (1974) 104 – 106.

[93] Viciu, L., Bos, J. W. G., Zandbergen, H. W., Huang, Q., Foo, M. L., Ishiwata, S., Ramirez, A. P., Lee, M., Ong, N. P. and Cava, R. J. (2006), "Crystal structure and

elementary properties of Na_xCoO_2 (x=0.32, 0.51, 0.6, 0.75, and 0.92) in the three-layer $NaCoO_2$ family", *Physical Review B - Condensed Matter and Materials Physics,* vol. 73, no. 17.

[94] Roger, M., Morris, D. J. P., Tennant, D. A., Gutmann, M. J., Goff, J. P., Hoffmann, J. -., Feyerherm, R., Dudzik, E., Prabhakaran, D., Boothroyd, A. T., Shannon, N., Lake, B. and Deen, P. P. (2007), "Patterning of sodium ions and the control of electrons in sodium cobaltate", *Nature,* vol. 445, no. 7128, pp. 631-634.

[95] Huang, Q., Foo, M. L., Lynn, J. W., Zandbergen, H. W., Lawes, G., Wang, Y., Toby, B. H., Ramirez, A. P., Ong, N. P. and Cava, R. J. (2004), "Low temperature phase transitions and crystal structure of $Na_{0.5}CoO_2$", *Journal of Physics Condensed Matter,* vol. 16, no. 32, pp. 5803-5814.

[96] Huang, Q., Foo, M. L., Pascal Jr., R. A., Lynn, J. W., Toby, B. H., He, T., Zandbergen, H. W. and Cava, R. J. (2004), "Coupling between electronic and structural degrees of freedom in the triangular lattice conductor Na_xCoO_2", *Physical Review B - Condensed Matter and Materials Physics,* vol. 70, no. 18, pp. 1-7.

[97] Zhang, P., Capaz, R. B., Cohen, M. L. and Louie, S. G. (2005), "Theory of sodium ordering in Na_xCoO_2", *Physical Review B - Condensed Matter and Materials Physics,* vol. 71, no. 15.

[98] Koshibae, W. and Maekawa, S. (2003), "Effect of spin and orbital on thermopower in strongly correlated electron systems",*Journal of Magnetism and Magnetic Materials,* vol. 258-259, pp. 216-218.

[99] Terasaki, I. (2003), "Transport properties and electronic states of the thermoelectric oxide $NaCo_2O_4$", *Physica B: Condensed Matter,* vol. 328, no. 1–2, pp. 63-67.

[100] Tajima, S., Tani, T., Isobe, S. and Koumoto, K. (2001), "Thermoelectric properties of highly textured $NaCo_2O_4$ ceramics processed by the reactive templated grain growth (RTGG) method", *Materials Science and Engineering: B,* vol. 86, no. 1, pp. 20-25.

[101] Seetawan, T., Amornkitbamrung, V., Burinprakhon, T., Maensiri, S., Kurosaki, K., Muta, H., Uno, M. and Yamanaka, S. (2006), "Thermoelectric properties of $Na_xCo_2O_4$/Ag composites", *Journal of Alloys and Compounds,* vol. 414, no. 1–2, pp. 293-297.

[102] Uslu, I., Cetin, S. S., Aytimur, A., Yuceyurt, S. and Erdal, M. O. (2012), "Synthesis and Properties of Boron Doped $Na_xCo_2O_4$ Nanocrystalline Ceramics", *Journal of Inorganic and Organometallic Polymers and Materials,* vol. 22, no. 4, pp. 766-771.

[103] Venimadhav, A., Ma, Z., Li, Q., Soukiassian, A., Xi, X. X., Schlom, D. G., Arroyave, R., Liu, Z. K., Lee, M. and Ong, N. P. (2006), "Thermoelectric properties of epitaxial and topotaxial Na_xCoO_2 thin films", *Materials Research Society Symposium Proceedings,* vol. 886, pp. 65.

[104] Maensiri, S. and Nuansing, W. (2006), "Thermoelectric oxide $NaCo_2O_4$ nanofibers fabricated by electrospinning", *Materials Chemistry and Physics*, vol. 99, no. 1, pp. 104-108.

[105] Terasaki, I., Sasago, Y. and Uchinokura, K. (1998), "Large thermopower in a layered oxide $NaCo_2O_4$", *International Conference on Thermoelectrics, ICT, Proceedings*, pp. 567.

[106] Kurosaki, K., Muta, H., Uno, M. and Yamanaka, S. (2001), "Thermoelectric properties of $NaCo_2O_4$", *Journal of Alloys and Compounds*, vol. 315, no. 1-2, pp. 234-236.

[107] S.Tajima,T. Tani, S. Isobe, K. Koumoto,Thermoelectric properties of highly textured NaCo2O4 ceramics processed by the reactive templated grain growth (RTGG) method, Material Science and Engineering B86 (2001) 20-25;

[108] Ito, M. and Furumoto, D. (2008), "Effects of noble metal addition on microstructure and thermoelectric properties of $Na_xCo_2O_4$", *Journal of Alloys and Compounds*, vol. 450, no. 1-2, pp. 494-498.

[109] Ito, M. and Furumoto, D. (2008), "Microstructure and thermoelectric properties of $Na_xCo_2O_4$/Ag composite synthesized by the polymerized complex method", *Journal of Alloys and Compounds*, vol. 450, no. 1-2, pp. 517-520.

[110] Ito, M. and Furumoto, D. (2006), "Effects of mechanical milling and Ag addition on thermoelectric properties of $Na_xCo_2O_4$", *Scripta Materialia*, vol. 55, no. 6, pp. 533-536.

[111] Park, K., Jang, K. U., Kwon, H. -C., Kim, J. -G. and Cho, W. -S. (2006), "Influence of partial substitution of Cu for Co on the thermoelectric properties of $NaCo_2O_4$", *Journal of Alloys and Compounds*, vol. 419, no. 1-2, pp. 213-219.

[112] Zhang, L., Tang, X. and Gao, W., (2010), “Synthesis and electrical properties of γ-$Na_xCo_2O_4$ via a citrate sol-gel method with polyethylene glycol 400”, *Journal of Electronic Materials*, vol. 39, pp. 1429-1432.

[113] Mikami, M., Yoshimura, M., Mori, Y., Sasaki, T., Funahashi, R. and Shikano, M. (2003), "Thermoelectric Properties of Two Na_xCoO_2 Crystallographic Phases", *Japanese Journal of Applied Physics, Part 1: Regular Papers and Short Notes and Review Papers*, vol. 42, no. 12, pp. 7383-7386.

[114] Sugiura, K., Ohta, H., Nomura, K., Yanagi, H., Hirano, M., Hosono, H. and Koumoto, K. (2006), "Epitaxial film growth and superconducting behavior of sodium-cobalt oxyhydrate, $Na_xCoO_2 \cdot yH_2O$ ($x \sim 0.3$, $y \sim 1.3$)", *Inorganic chemistry*, vol. 45, no. 5, pp. 1894-1896.

[115] Liu, C.-J., Nayak, P.K. and Chen, Y.-Z., (2009), A simple approach of fabricating thermoelectric γ-NaxCoO$_2$ and superconductive Na$_x$(H$_2$O)yCoO$_{2-\delta}$ films using the sol-gel spin-coating method", *Thin Solid Films*, vol. 518, pp. 91-93.

[116] Hicks, L. D. and Dresselhaus, M. S. (1993), "Thermoelectric figure of merit of a one-dimensional conductor", *Physical Review B*, vol. 47, no. 24, pp. 16631-16634.

[117] Hicks, L. D., Harman, T. C. and Dresselhaus, M. S. (1993), "Use of quantum-well superlattices to obtain a high figure of merit from nonconventional thermoelectric materials", Applied Physics Letters, vol. 63, no. 23, pp. 3230-3232.

[118] Hicks, L. D., Harman, T. C. and Dresselhaus, M. S. (1993), "Use of quantum-well superlattices to obtain a high figure of merit from nonconventional thermoelectric materials", *Applied Physics Letters*, vol. 63, no. 23, pp. 3230-3232.

[119] Rabin, O., Lin, Y. -M. and Dresselhaus, M. S. (2001), "Anomalously high thermoelectric figure of merit in Bi$_{1-x}$-Sb$_x$ nanowires by carrier pocket alignment", *Applied Physics Letters*, vol. 79, no. 1, pp. 81-83.

[120] Chen, G., Zeng, T., Borca-Tasciuc, T. and Song, D. (2000), "Phonon engineering in nanostructures for solid-state energy conversion", *Materials Science and Engineering A*, vol. 292, no. 2, pp. 155-161.

[121] Dresselhaus, M. S., Dresselhaus, G., Sun, X., Zhang, Z., Cronin, S. B. and Koga, T. (1999), "Low-dimensional thermoelectric materials", *Physics of the Solid State*, vol. 41, no. 5, pp. 679-682.

[122] Rahaman, M. N. (1995), "Ceramic processing and sintering", *Marcel Dekker, New York.*

[123] Vinicius. C., Renan. S., (2010), "Nanomaterials: Properties, Preparation and Processes" *Nova Science Publishers.*

[124] Granqvist, C., Kish,L., Marlow, W., H., (2004), "Gas Phase Nanoparticle Synthesis" *Springer Science & Business Media.*

[125] Wilson, M., Kannangara, K., Smith, G., Simmons, M., Raguse, B., (2002) "Nanotechnology: Basic Science and Emerging Technologies", UNSW Sydney NSW.

[126] Ring, T., A., (1996) "Fundamentals of Ceramic Powder Processing and Synthesis" Academic Press-Technology & Engineering

[127] Pampuch, R., (2008), "Funkcjonalne materialy ceramiczne" Wydawnictwo Akademia Górniczo-Hutnicza.

[128] Jorand, Y., Taha, M., Missiaen, J. M. and Montanaro, L. (1995), "Compaction and sintering behaviour of sol-gel powders", *Journal of the European Ceramic Society,* vol. 15, no. 5, pp. 469-477.

[129] Sima, M., Vasile, E., Sima, M. and Matei, E. (2010), "Semiconductor hybrid structure: Nanowires embedded in a matrix from the same material", *ECS Transactions*, Vol. 25, pp. 155.

[130] Pham, N. P., Burghartz, J. N. and Sarro, P. M. (2005), “Spray coating of photoresist for pattern transfer on high topography surfaces”, *Journal of Micromechanics and Microengineering,* vol. 15, no. 4, pp. 691-697.

[131] Bornside, D. E., Macosko, C. W. and Scriven, L. E. (1987), " Modeling of spin coating”, *Journal of imaging technology,* vol. 13, no. 4, pp. 122-130.

[132] Carcano, G.; Ceriani, M.; and Soglio, F. "Spin Coating with High Viscosity Photoresist on Square Substrates," *Hybrid Circuits,* Vol. 32, Sept. 1993, p. 12.

[133] West, A. R. (1999), “Basic solid state chemistry”, 2nd ed, John Wiley & Sons, Chichester.

[134] Krockenberger, Y., Fritsch, I., Cristiani, G., Matveev, A., Alff, L., Habermeier, H. -U. and Keimer, B. (2005), “Epitaxial growth of Na_xCoO_2 thin films bypulsed laser deposition”, *Thin Solid Films,* vol. 486, no. 1-2, pp. 170-173.

[135] Krockenberger, Y., Fritsch, I., Christiani, G., Habermeier, H. -U., Yu, L., Bernhard, C., Keimer, B. and Alff, L. (2006), Superconductivity in epitaxial thin films of $Na_xCoO_2 \cdot y D_2O$, *Applied Physics Letters,* vol. 88, no. 16.

[136] Brinks, P., Heijmerikx, H., Hendriks, T. A., Rijnders, G. and Huijben, M. (2012), “Achieving chemical stability in thermoelectric Na_xCoO_2 thin films”, RSC Advances, vol. 2, no. 14, pp. 6023-6027.

[137] Fan, D., Zhang, R. and Wang, X. (2010), "Synthesis and optical property of ZnO nanonail arrays with controllable morphology", *Physica E: Low-Dimensional Systems and Nanostructures,* vol. 42, no. 8, pp. 2081-2085.

[138] Wagner, R. S. and Ellis, W. C. (1964), "Vapor-liquid-solid mechanism of single crystal growth", *Applied Physics Letters,* vol. 4, no. 5, pp. 89-90.

[139] Fortuna, S. A. and Li, X. (2010), "Metal-catalyzed semiconductor nanowires: A review on the control of growth directions", *Semiconductor Science and Technology,* vol. 25, no. 2.

[140] Davidson III, F. M., Wiacek, R. and Korgel, B. A. (2005), "Supercritical fluid-liquid-solid synthesis of gallium phosphide nanowires", *Chemistry of Materials,* vol. 17, no. 2, pp. 230-233.

[141] Hsu, Y. -J. and Lu, S. -Y. (2005), "Vapor-solid growth of Sn nanowires: Growth mechanism and superconductivity", *Journal of Physical Chemistry B,* vol. 109, no. 10, pp. 4398-4403.

[142] Fan, H. J., Werner, P. and Zacharias, M. (2006), "Semiconductor nanowires: From self-organization to patterned growth", *Small,* vol. 2, no. 6, pp. 700-717.

[143] Sekhar, P. K. and Bhansali, S. (2010), "Manufacturing aspects of oxide nanowires", *Materials Letters,* vol. 64, no. 6, pp. 729-732.

[144] Tang, C., Bando, Y. and Sato, T. (2002), "Oxide-assisted catalytic growth of MgO nanowires with uniform diameter distribution", *Journal of Physical Chemistry B,* vol. 106, no. 30, pp. 7449-7452.

[145] Kim, S. -H., Umar, A. and Hahn, Y. -B. (2005), "Growth and formation mechanism of sea urchin-like ZnO nanostructures on Si", *Korean Journal of Chemical Engineering,* vol. 22, no. 3, pp. 489-493.

[146] Chang, W. J., Hsieh, C. C., Chung, T. Y., Hsu, S. Y., Wu, K. H., Uen, T. M., Lin, J. -Y., Lin, J. J., Hsu, C. -H., Kuo, Y. K., Liu, H. L., Hsu, M. H., Gou, Y. S. and Juang, J. Y. (2007), "Fabrication and low temperature thermoelectric properties of Na_xCoO_2 (x=0.68 and 0.75) epitaxial films by the reactive solid-phase epitaxy", *Applied Physics Letters,* vol. 90, no. 6.

[147] Ma, F., Ou, Y., Yang, Y., Liu, Y., Xie, S., Li, J. -F., Cao, G., Proksch, R. and Li, J. (2010), "Nanocrystalline structure and thermoelectric properties of electrospun $NaCo_2O_4$ nanofibers", *Journal of Physical Chemistry C,* vol. 114, no. 50, pp. 22038-22043.

[148] Liu, C. -J. and Chen, Y. -Z. (2012), "Synthesis of submicron tubules of sodium cobaltate using a natural template of bamboo charcoal as supporting templates", *Materials Letters,* vol. 69, pp. 4-6.

[149] Liu, C.-J., Chen, S.-Y., Shih, L.-J. and Huang, H.-J., (2010), Fabrication of nanotubules of thermoelectric γ-$Na_{0.7}CoO_2$ using porous aluminum oxide membrane as supporting template", *Materials Chemistry and Physics,* vol. 119, pp. 424-427.

[150] Fujita, K., Mochida, T. and Nakamura, K. (2001), "High-temperature thermoelectric properties of Na_xCoO_{2-d} single crystals", *Japanese Journal ofApplied Physics, Part 1: Regular Papers and Short Notes and Review Papers,* vol. 40, no. 7, pp. 4644-4647.

[151] Wang, N. L., Zheng, P., Wu, D., Ma, Y. C., Xiang, T., Jin, R. Y. and Mandrus, D. (2004), "Infrared probe of the electronic structure and charge dynamics of $Na_{0.7}CoO_2$", *Physical ReviewLetters*, vol. 93, no. 23.

[152] Jin, R., Sales, B. C., Li, S. and Mandrus, D. (2005), "Dependence of the specific heat of Na_xCoO_2 yH_2O/D_2O on sodium and water concentrations", *Physical Review B - Condensed Matter and Materials Physics*, vol. 72, no. 6.

[153] Foo, M. L., Wang, Y., Watauchi, S., Zandbergen, H. W., He, T., Cava, R. J. and Ong, N. P. (2004), "Charge ordering, commensurability, and metallicity in the phase diagram of the layered Na_xCoO_2", *Physical Review Letters*, vol. 92, no. 24, pp. 247001-1.

[154] Luo, L. B., Zhao, Y. G., Zhang, G. M., Guo, S. M., Cui, L. and Luo, J. L. (2006), "Singular behavior observed in the low temperature electronic transport and thermodynamic properties of Mn doped $Na_{0.68}$ CoO_2", *Physical Review B - Condensed Matter and Materials Physics*, vol. 73, no. 24.

[155] Fujita, K., Mochida, T. and Nakamura, K. (2001), "High-temperature thermoelectric properties of Na_xCoO_{2-d} single crystals", *International Conference on Thermoelectrics, ICT, Proceedings*, pp. 168.

[156] Dorey, R. A., Rocks, S. A., Dauchy, F., Wang, D., Bortolani, F. and Hugo, E. (2008), "Integrating functional ceramics into microsystems", *Journal of the European Ceramic Society*, vol. 28, no. 7, pp. 1397-1403.

[157] Claeys, C., L., (2004) "Low Temperature Electronics and Low Temperature Cofired CeramicBased Electronic Devices", *Electrochemical Society, Inc, USA*

[158] Seetawan, T., Vora-Ud, A., Chainaronk, P., Thanachayanont, C. and Amornkitbamrung, V. (2010), "Evaluating Seebeck coefficient of Na_xCoO_2 from molecular orbital calculations", *Computational Materials Science*, vol. 49, no. 4 SUPPL., pp. S225-S230.

[159] http://pubs.rsc.org/en/Content/ArticleLanding/2013/DT/c3dt32828g#!divAbstract

[160] http://home.agh.edu.pl/~pwysz/surowce.pdf

[161] Kurosaki, K., Muta, H., Uno, M. and Yamanaka, S. (2001), "Thermoelectric properties of $NaCo_2O_4$", *Journal of Alloys and Compounds*, vol. 315, no. 1-2, pp. 234-236.

[162] Li, Y., Xu, G. and Jiang, M. (2006), "Thermoelectric characterization of $(Na_{1-y}M_y)_{1.6}Co_2O_4$ (M=K, Ca, Sr)", *Journal of Materials Science and Technology*, vol. 22, no. 4, pp. 526-528..

[163] Chen, C., Zhang, T., Donelson, R., Chu, D., Tian, R., Tan, T. T. and Li, S. (2014), "Thermopower and chemical stability of $Na_{0.77}CoO_2/Ca_3Co_4O_9$ composites", *Acta Materialia*, vol. 63, pp. 99-106.

[164] Lin, C. T., Chen, D. P., Lemmens, P., Zhang, X. N., Maljuk, A. and Zhang, P. X. (2005), "Study of intercalation/deintercalation of NaxCoO2 single crystals", *Journal of Crystal Growth*, vol. 275, no. 3-4, pp. 606-616.

[165] Kuno, S., Takeuchi, T., Ikuta, H., Kondo, T., Kaminski, A., Saito, Y. and Fujimori, S. (2007), "Electronic structure and thermoelectric properties of a layered cobalt oxide Na_xCoO_2 ($0.5 < x < 0.8$) investigated by angle-resolved photoemission spectroscopy", *International Conference on Thermoelectrics, ICT, Proceedings*, pp. 99.

[166] Sugiura, K., Ohta, H., Nomura, K., Yanagi, H., Hirano, M., Hosono, H. and Koumoto, K. (2006), "Epitaxial film growth and superconducting behavior of sodium-cobalt oxyhydrate, $Na_xCoO_2 \cdot yH_2O$ ($x \sim 0.3$, $y \sim 1.3$)", *Inorganic chemistry*, vol. 45, no. 5, pp. 1894-1896.

[167] Barrow, D. A., Petroff, T. E. and Sayer, M. (1995), "Thick ceramic coatings using a sol gel based ceramic-ceramic 0-3 composite", *Surface and Coatings Technology*, vol. 76-77, no. 1 -3 pt 1, pp. 113-118..

[168] Dorey, R. A., Haigh, R. D., Stringfellow, S. B. and Whatmore, R. W. (2002), "Effect of sol infiltrations on electrical properties of PZT", *British Ceramic Transactions*, vol. 101, no. 4, pp. 146-148.

[169] Kosmala, A., Wright, R., Zhang, Q. and Kirby, P. (2011), "Synthesis of silver nano particles and fabrication of aqueous Ag inks for inkjet printing", *Materials Chemistry and Physics*, vol. 129, no. 3, pp. 1075-1080.

[170] http://www.crct.polymtl.ca/fact/phase_diagram.php?file=Na-Si-O_Na2O-SiO2.jpg&dir=FToxid